

Processing 3d Materials for Electrochemical Analysis and Anode Applications

Zur Erlangung des akademischen Grades eines

DOKTORS DER NATURWISSENSCHAFTEN

(Dr. rer. nat.)

von der KIT-Fakultät für Chemie und Biowissenschaften

des Karlsruher Instituts für Technologie (KIT)

genehmigte

DISSERTATION

von

Umaira Shuaib, M. Chem.

1. Referentin: Prof. Dr. Annie K. Powell
2. Referent: Prof. Dr. Helmut Ehrenberg
Tag der mündlichen Prüfung: 20.04.2023



This document is licensed under a Creative Commons Attribution-NonCommercial-ShareAlike 4.0 International License (CC BY-NC-SA 4.0):
<https://creativecommons.org/licenses/by-nc-sa/4.0/deed.en>

Notes

The compounds shown in this thesis are not to scale. In figures showing crystal structures, the hydrogens are omitted for clarity of the core and packing. Colours used for atoms and ions are mentioned in figure captions. Yttrium is grouped with the lanthanides due to the similarity in chemical reactivity and size. All oxides were analysed against literature, ICSD and the Materials Projects database (referenced accordingly).

It must be mentioned that the active materials measured in this thesis are 'cathodes' in the half-cell reactions tested against lithium-metal foil. However, in full cells the oxides would replace graphite as the anode material. Further clarification is provided in chapters 2.5 and 4.

For diffraction patterns where certain reflections are assigned with grey squares, those specific reflections are instrument related and can be ignored (confirmed by additional synchrotron measurements).

In depth theory on the field of electrochemistry as a broad topic, as well as on individual systems within this field was studied from the following books: *Handbook of Batteries* (Lindon and Reddy)^[1], *Electrochemical Science and Technology. Fundamental and Applications*. (Oldham, Myland and Bond)^[2], and *Electrochemical Energy Storage* (Tarascon and Simon).^[3]

This thesis was prepared for submission on March 13th, 2023, at the Institute of Inorganic Chemistry, Faculty of Chemistry and Biosciences of the Karlsruhe Institute of Technology (KIT) under the supervision of Prof. Dr. Annie K. Powell.

Eidesstattliche Erklärung

Bei der eingereichten Dissertation zu dem Thema

Processing 3d Materials for Electrochemical Analysis and Anode Applications

handelt es sich um meine eigenständig erbrachte Leistung.

Ich habe nur die angegebenen Quellen und Hilfsmittel benutzt und mich keiner unzulässigen Hilfe Dritter bedient. Insbesondere habe ich wörtlich oder sinngemäß aus anderen Werken übernommene Inhalte als solche kenntlich gemacht.

Die Arbeit oder Teile davon habe ich bislang nicht an einer Hochschule des In- oder Auslands als Bestandteil einer Prüfungs- oder Qualifikationsleistung vorgelegt.

Die Richtigkeit der vorstehenden Erklärungen bestätige ich.

Die Bedeutung der eidesstattlichen Versicherung und die strafrechtlichen Folgen einer unrichtigen oder unvollständigen eidesstattlichen Versicherung sind mir bekannt.

Ich versichere an Eides statt, dass ich nach bestem Wissen die reine Wahrheit erklärt und nichts verschwiegen habe.

Karlsruhe, 13.03.2023

.....

Ort und Datum

.....

Unterschrift

Acknowledgments

Without Annie, I would never have contemplated pursuing a PhD, let alone moving abroad to do it. Being in Annie's supporting and nurturing environment for our group has benefited not only my scientific ability but also my personal growth. Sanjit's introduction to Annie led me into a professional path I had not before explored. I am genuinely grateful to you both for that, as well as the opportunity to work alongside some of the greatest scientists and people I have encountered. Gertraud Amschlinger for all her assistance, direction, and patience in organizing papers and managing my terrible German during my time at KIT. I would like to extend a special thanks to Professor Helmut Ehrenberg, for his input and for being my co-examiner.

I would like to thank the following academics for their experimental, analytical, and conversational contributions to this research:

Masooma Ibrahim for assisting me in settling down in Karlsruhe when I arrived on an Erasmus Scholarship for my MChem research project. You introduced me to some important people and helped me anytime I needed it. I genuinely appreciate the time we spent together at INT and everything I learned from you. I would like to thank Christopher Anson, Andreas Eichhöfer, Olaf Fuhr, and Dieter Fenske for their contributions to the crystallographic data and analysis in this thesis.

Luis Basche, Thomas Ruppert, and Jonas Braun for their help with data analysis when I was feeling out of my depth. Furthermore, their assistance in proofreading, editing, or preparing data for my thesis was really appreciated. Additionally, a special thanks to Hagen Kämmerer and Anthony Blue Carter for keeping me highly entertained throughout the years.

Sven Stahl for all elemental analysis measurements while based at INT. Sergei Lebedkin for showing me how to run Raman measurements. Thank you to Tessy Baby, Arjun Neyyathalla, and Surya Singaraju for assisting with the scanning electron microscopy measurements when I was unable to do it myself. In addition, I'd like to thank Arjun for his assistance with a thermogravimetric analysis/differential thermal analysis measurement. Kiran Chakravadhanula and Saleh Gorji for performing transmission electron microscopy on a material that, while not featured in this thesis, sparked fascinating discussions between us. Without a furnace, it would have been difficult to prepare these materials. I'd like to express my gratitude to Sylvio Indris, Lars Esmezjan, Raju Kante, and Sharali Malik for allowing me to use their furnaces when necessary.

Angelina, who watched over my electrochemical tests and cell preparations to ensure everything was done correctly, and who also gave me some lab space to create electrodes and chambers to measure my coin cells. Björn Schwarz was responsible for measuring the magnetic data as well as completing some of the Rietveld analyses given in this thesis. And thanks again to Sylvio for providing my initial introduction to battery chemistry and demonstrating typical procedures of working in a battery lab. Furthermore, our discussions on science, but mostly about life in general, were usually fruitful and engaging.

I am grateful to the group members of AK Ehrenberg who helped to measure my samples at the synchrotron since beamtimes are short, dense, and stressful. Finally, a huge thanks to the entire Powell group, past and present, for offering as much feedback as possible at our group meetings and throughout the thesis preparation process.

Abstract

This thesis highlights the need for different processing techniques and pyrolysis parameters to produce materials which can be used as the active material in the working electrode of a Li-ion battery. In general, it shows that there is still a scope for research on sustainable and readily available compounds including those materials which are already published for other applications.

Chapter 1 introduces the key concepts on which this thesis is based.

Chapters 2 and 3 focus on bringing the motivation of this research into perspective as the theory behind energy storage technologies is discussed, bringing to light some of the largest hurdle's academia and industry are facing in current times. Additionally, a focus is placed on lithium-ion batteries with significant points based on history, fundamental principles, challenges, and reported literature being highlighted.

Chapter 4 clarifies the use of the term's anode and cathode, what they represent, and how they are used in literature.

Chapter 5 provides an overview of the methods and measurements used to characterise data

As we transition into the research, Chapter 6 introduces the concept of lanthanide-induced polymorphism on commercially available activated-MnO₂. The addition of 5 mol% Y₂O₃, CeO₂, Dy₂O₃ and Yb₂O₃ was investigated to observe how different lanthanides yield different Mn_xO_y phases and morphologies. The addition of Y₂O₃ stabilises the charge/discharge cycles, albeit at the expense of the overall performance. The addition of Dy₂O₃ however gave an overall better performance, with a capacity of 412 mAh g⁻¹ after 239 cycles.

Continuing with manganese, Chapter 7 focuses the study on templating oxides from previously reported coordination complexes. The complexes were modified for some cases to improve their thermal stability and/or their electrochemical performance. For example, the coordination compound Mn₁₂ acetate was previously reported as the cathode material in the first molecular cluster battery with an initial discharge capacity of 200–250 Ah kg⁻¹ which dramatically decreased over the following 13 cycles measured.^[4] By pyrolysing this Mn₁₂ acetate and testing it as the working electrode in a lithium cell, a capacity of 368 mAh g⁻¹ (mAh g⁻¹ = Ah kg⁻¹) was recorded after 139 cycles.

Chapter 8 used an iron dinuclear system that forms a large, interconnected network with alkali-ions. This was thermally treated to form iron oxide. These oxides rapidly oxidised, resulting in decomposition after one month of storage under atmospheric conditions. These oxides were tested as the active material in the working electrode of lithium and sodium cells. After 140 cycles in a lithium cell, the capacity gradually began to increase from 128 mAh g⁻¹, suggesting the active material may have undergone a chemical change resulting in a material that is capable of a higher capacity (203 mAh g⁻¹ after 239 cycles). Three additional ligands were designed, prepared, and characterised, to outline a concept for future work on alkali-rich (preferably lithium or sodium) coordination complexes as electrode materials.

A summary is provided at the end of each chapter. Chapters 9 through 15 cover the experimental procedures, bibliography, resume, tables, instruments, and abbreviations.

Zusammenfassung

Diese Arbeit unterstreicht die Notwendigkeit unterschiedlicher Verarbeitungstechniken und Pyrolyseparameter, um Materialien herzustellen, die als aktives Material in der Arbeitselektrode einer Li-Ionen-Batterie verwendet werden können. Generell zeigt sich, dass es noch Raum für Forschung zu nachhaltigen und leicht verfügbaren Verbindungen gibt, einschließlich solcher Materialien, die bereits für andere Anwendungen veröffentlicht wurden.

Kapitel 1 stellt die Schlüsselkonzepte vor, auf denen diese Arbeit basiert.

In den Kapiteln 2 und 3 geht es darum, die Motivation dieser Forschung ins rechte Licht zu rücken, während die Theorie hinter Energiespeichertechnologien diskutiert wird und einige der größten Hürden ans Licht gebracht werden, mit denen Wissenschaft und Industrie derzeit konfrontiert sind. Darüber hinaus liegt ein Schwerpunkt auf Lithium-Ionen-Batterien, wobei wichtige Punkte basierend auf der Geschichte, Grundprinzipien, Herausforderungen und berichteter Literatur hervorgehoben werden.

Kapitel 4 erläutert die Verwendung der Begriffe „Anode“ und „Kathode“, was sie darstellen und wie sie in der Literatur verwendet werden.

Kapitel 5 bietet einen Überblick über die Methoden und Messungen zur Charakterisierung von Daten.

Während wir mit der Forschung beginnen, stellt Kapitel 6 das Konzept des Lanthanid-induzierten Polymorphismus bei kommerziell erhältlichem aktiviertem MnO_2 vor. Die Zugabe von 5 Mol-% Y_2O_3 , CeO_2 , Dy_2O_3 und Yb_2O_3 wurde untersucht, um zu beobachten, wie verschiedene Lanthanoide unterschiedliche Mn_xO_y -Phasen und Morphologien ergeben. Die Zugabe von Y_2O_3 stabilisiert die Lade-/Entladezyklen, allerdings auf Kosten der Gesamtleistung. Die Zugabe von Dy_2O_3 führte jedoch zu einer insgesamt besseren Leistung mit einer Kapazität von 412 mAh g^{-1} nach 239 Zyklen.

Im Kapitel 7 geht es um die Untersuchung von Templatoxiden aus zuvor beschriebenen Koordinationskomplexen aus Mangan. In einigen Fällen wurden die Komplexe modifiziert, um ihre thermische Stabilität und/oder ihre elektrochemische Leistung zu verbessern. Beispielsweise wurde bereits zuvor berichtet, dass die Koordinationsverbindung Mn_{12} -Acetat das Kathodenmaterial in der ersten molekularen Clusterbatterie war und eine anfängliche Entladekapazität von $200\text{--}250 \text{ Ah kg}^{-1}$ aufwies, die in den folgenden 13 gemessenen Zyklen dramatisch abnahm.^[4] Durch Pyrolyse dieses Mn_{12} -Acetats und dessen Test als Gegenelektrode in einer Lithiumzelle wurde nach 139 Zyklen eine Kapazität von 368 mAh g^{-1} ($\text{mAh g}^{-1} = \text{Ah kg}^{-1}$) aufgezeichnet.

In Kapitel 8 wurde ein zweikerniges Eisensystem verwendet, das mit Alkaliionen ein großes, miteinander verbundenes Netzwerk bildet. Dieses wurde thermisch behandelt, um Eisenoxid zu bilden. Diese Oxide oxidierten schnell, was nach einem Monat Lagerung unter atmosphärischen Bedingungen zur Zersetzung führte. Diese Oxide wurden als aktives Material in der Gegenelektrode von Lithium- und Natriumzellen getestet. Nach 140 Zyklen in einer Lithiumzelle begann die Kapazität allmählich von 128 mAh g^{-1} zu steigen, was darauf hindeutet, dass das aktive Material möglicherweise eine chemische Veränderung erfahren hat, die zu einem Material mit höherer Kapazität geführt hat (203 mAh g^{-1} nach 239 Zyklen). Drei zusätzliche Liganden wurden entworfen, hergestellt und charakterisiert, um ein Konzept für zukünftige Arbeiten an alkalireichen (vorzugsweise Lithium oder Natrium) Koordinationskomplexen als Elektrodenmaterialien zu skizzieren.

Am Ende jedes Kapitels finden Sie eine Zusammenfassung.

Die Kapitel 9 bis 15 behandeln die experimentellen Verfahren, die Bibliographie, den Lebenslauf, Tabellen, Instrumente und Abkürzungen.

Table of Contents

1	Introduction	1
2	Theory.....	2
2.1	Basic Introduction to Li-ion Battery (LIB) Systems	2
2.2	A General Overview of Energy Sources and Energy Storage Systems (ESSs): Principles and Problems	3
2.2.1	Energy Storage Systems	3
2.2.2	Energy Sources	6
2.3	The Theory and Subsequent Evolution of the Li-ion Battery	6
2.4	Fundamental Principles of Electrochemistry	9
2.5	Working Principles of the Lithium-ion Battery	14
2.6	Challenges	19
2.7	Interest in Na-ion Batteries (NIBs).....	24
2.8	Anode Materials	27
2.8.1	Graphite.....	28
2.8.2	Soft and Hard Carbons	29
2.8.3	Metal Oxides of Cobalt (Co), Iron (Fe), and Manganese (Mn) as Active Electrode Materials	30
2.8.3.1	Cobalt.....	30
2.8.3.2	Iron.....	32
2.8.3.3	Manganese	34
2.9	Importance of Lanthanides	36
2.9.1	Lanthanides in Energy Storage Devices.....	37
2.10	Crystal Field Theory (CFT).....	39
2.10.1	Jahn-Teller Distortion for Manganese Oxides	41
3	Motivation	42
4	Clarification of Terms	43
5	Materials, Methods, and Measurements	45
5.1	Preparation.....	47
5.1.1	Complex Synthesis	47
5.1.2	Thermal Treatment	47
5.1.3	Electrode Preparation	47
5.1.4	Coating on Cu-foil Current Collector	48
5.1.5	Coin Cell Preparation.....	48
5.2	Measurements	49
5.2.1	Powder X-ray Diffraction (PXRD).....	49

5.2.2	Scanning Electron Microscopy (SEM)	50
5.2.3	Brunauer-Emmet-Teller (BET) Surface Area Technique	51
5.2.4	Infrared Spectroscopy (IR).....	51
5.2.5	Raman Spectroscopy	51
5.2.6	X-ray Absorption Spectroscopy (XAS).....	52
5.2.7	Nuclear Magnetic Resonance (NMR)	52
5.2.8	Thermogravimetric/Differential Thermal Analysis (TGA/DTA)	53
5.2.9	Vibrating Sample Magnetometer (VSM)	53
5.2.10	Galvanostatic Charge-Discharge Cycling (GCD).....	53
5.2.11	Cyclic Voltammetry (CV)	54
6	Polymorphism of MnO ₂ Nanoparticles Induced by the Addition of Lanthanides	56
6.1	Manganese Dioxides.....	56
6.2	MnO ₂ Nanoparticles (MnO ₂ -NP).....	60
6.2.1	Phase and Morphological Analysis	60
6.2.2	Electrochemical Analysis in a Li-ion Coin Cell	62
6.3	MnO ₂ + 5 mol% Y ₂ O ₃ , 5 mol% CeO ₂ , 5 mol% Dy ₂ O ₃ , and 5 mol% Yb ₂ O ₃	.66
6.3.1	Addition of 5 mol% Y ₂ O ₃ – MnO ₂ Y-NP	72
6.3.1.1	Phase and Morphological Analysis	72
6.3.1.2	Electrochemical Analysis in a Li-ion coin cell	75
6.3.2	Addition of 5 mol% CeO ₂ – MnO ₂ Ce-NP	79
6.3.2.1	Phase and Morphological Analysis	79
6.3.2.2	Electrochemical Analysis in Li-ion Coin Cells.....	83
6.3.3	Addition of 5 mol% Dy ₂ O ₃ – MnO ₂ Dy-NP	86
6.3.3.1	Phase and Morphological Analysis	86
6.3.3.2	Electrochemical Analysis in a Li-ion Coin Cell.....	89
6.3.4	Addition of 5 mol% Yb ₂ O ₃ – MnO ₂ Yb-NP	91
6.3.4.1	Phase and Morphological Analysis	91
6.3.4.2	Electrochemical Analysis in a Li-ion Coin Cell.....	94
6.4	Summary and Conclusion	96
7	Manganese-based Templated Oxides	97
7.1	Manganese Formate: A Simple Carboxylate-bridged Mn ^{II} -MOF	97
7.1.1	Phase and Morphological Analysis	98
7.1.2	Electrochemical Analysis in a Li-ion Coin Cell	102
7.1.3	Magnetisation Studies	110
7.2	Mn ₁₂ Acetate: From an SMM to an Electrode.....	113
7.2.1	Phase and Morphological Analysis	114

7.2.2	Electrochemical Analysis in a Li-ion Coin Cell	118
7.2.3	Magnetisation Studies	120
7.3	Mn ₃ Ca ₃ Na ₃ : Templating from Stacked Sheets	122
7.3.1	Phase and Morphological Analysis	123
7.3.2	Electrochemistry	125
7.4	Mn ₂₁ Cluster: Azide-rich Complex to Oxide	127
7.4.1	Phase and Morphological Analysis	128
7.4.2	Electrochemical Analysis	132
7.5	Summary and Conclusion	135
8	Exploring a Di-nuclear Iron ^{III} Complex Electrochemically	136
8.1	Reproducing K ₆ Fe ₂ chnda ₂ and Na ₆ Fe ₂ chnda ₂	136
8.1.1	Ligand Preparation:	136
8.1.2	Synthesis of K ₆ Fe ₂ chnda ₂ and Na ₆ Fe ₂ chnda ₂	137
8.1.3	Pyrolysis to the Mixed Phase NaFe _x O _y -500	139
8.1.4	Electrochemical Analysis in a Li-ion Coin Cell	142
8.1.5	Electrochemical analysis in a Na-ion Coin Cell	145
8.2	Characterisation of Additional Ligands	148
8.3	Summary and Conclusions	150
9	Complete Experimental	151
10	Bibliography	157
11	Table of Figures	161
12	Table of Tables	171
13	Instruments Used	172
14	Abbreviations	173
14.1	General Terms	173
14.2	Chemicals	174

1 Introduction

As demand for portable technology and large-scale energy storage systems (ESSs) grows with the increasing population, optimisation of current materials and the innovation of new and exciting materials are at the forefront of research today. Amongst the many types of energy storage systems, electrochemical energy storage is a popular area of research, and the current commercial gold standard battery is in fact the Li-ion battery.

As with most technology, there is room for improvement. Concerning the chemistry within a battery, there are many obstacles that reduce performance of a cell, be it stability, aging, recyclability, environmental toxicity, availability of natural resources and temperature sensitivity. The hunt for better, safer, and cheaper materials continues with a focus not only on lithium-ion but also sodium-ion, solid-state electrolyte, and lithium-sulphur batteries, to name a few.

However, Li-ion is still one of the most commercialised batteries available in the market for mobile technologies and requires modification and optimisation until another battery is developed that is more sustainable and can surpass the performance of the Li-ion.

In the presented thesis, materials and coordination compounds were processed with the intention to modify and/or optimise their electrochemical performance as well as to show multi-functionality.

Most of the compounds presented in this thesis were analysed structurally using powder X-ray diffraction (PXRD) and scanning electron microscopy (SEM). Elemental analysis (EA) and infrared spectroscopy (IR) were carried out to support selected results. Electrochemical measurements such as the cyclic voltammetry (CV) and galvanostatic cycling (GC) were carried out on coin cells and Rietveld refinement and additional analysis of diffraction patterns were done using the FullProf software.

2 Theory

2.1 Basic Introduction to Li-ion Battery (LIB) Systems

This chapter will provide a general overview of the types of energy storage systems used for small- and large-scale application. It will state the limiting factors of such systems with a focus on sustainability and processes of sourcing critical materials as shown in Figure 2-1. Furthermore, it will emphasise on the progression made in the field of Li-ion batteries and touch on the transferability of knowledge to Na-ion batteries. By focusing specifically on electrode materials, a range of materials which have been processed to produce oxides for application as the active material in in the working electrode, will be discussed in detail.

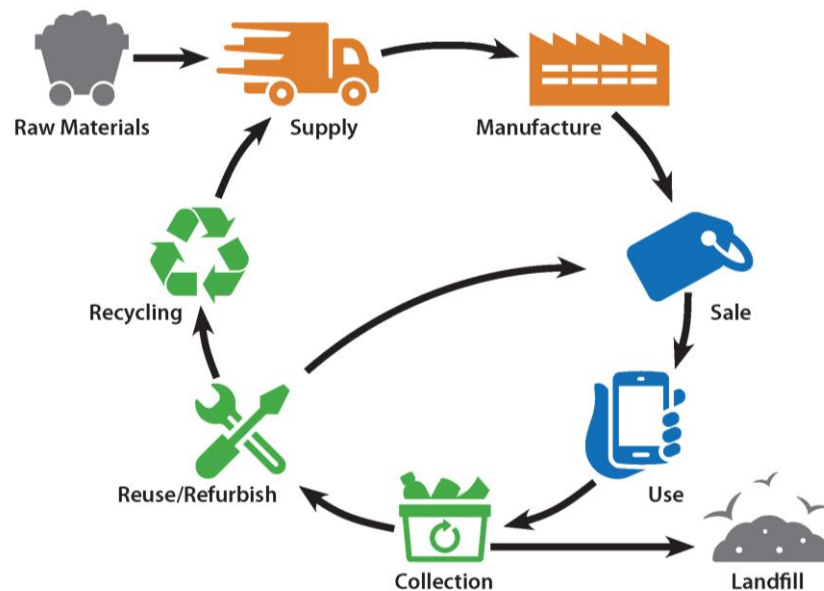


Figure 2-1 Lifecycle of Li-ion batteries.^[5]

2.2 A General Overview of Energy Sources and Energy Storage Systems (ESSs): Principles and Problems

2.2.1 Energy Storage Systems

Looking at ESSs, they can be classified in one of the following categories: thermal, mechanical, chemical, or electrical. A bridge between the latter two is called electrochemical energy storage and this is considered the honorary fifth member of the list. Within these subcategories, the five technologies can be broken down further into application-scale or bulk systems, from customer-specific use to transport electrification. The largest issue with ESSs is neither the recyclability nor sustainability, rather it is simply the inability to store enough energy on the grid. There is simply no single storage system that can hold all the electrical energy produced from the different sources, with some examples shown in Figure 2-2. It should also be noted that this categorisation is not definitive as many ESSs cross over or share categories. It is perhaps the biggest roadblock when mapping the future of energy storage and usage, to find a battery or capacitor capable of storing and efficiently releasing this energy for consumers. To control peak-time demands it is vital to search for alternative methods of storing large quantities of energy. Ultimately, there will be a global reliance on these non-fossil fuel resources, so storage optimisation is considered an imperative area of research as of the 21st Century.

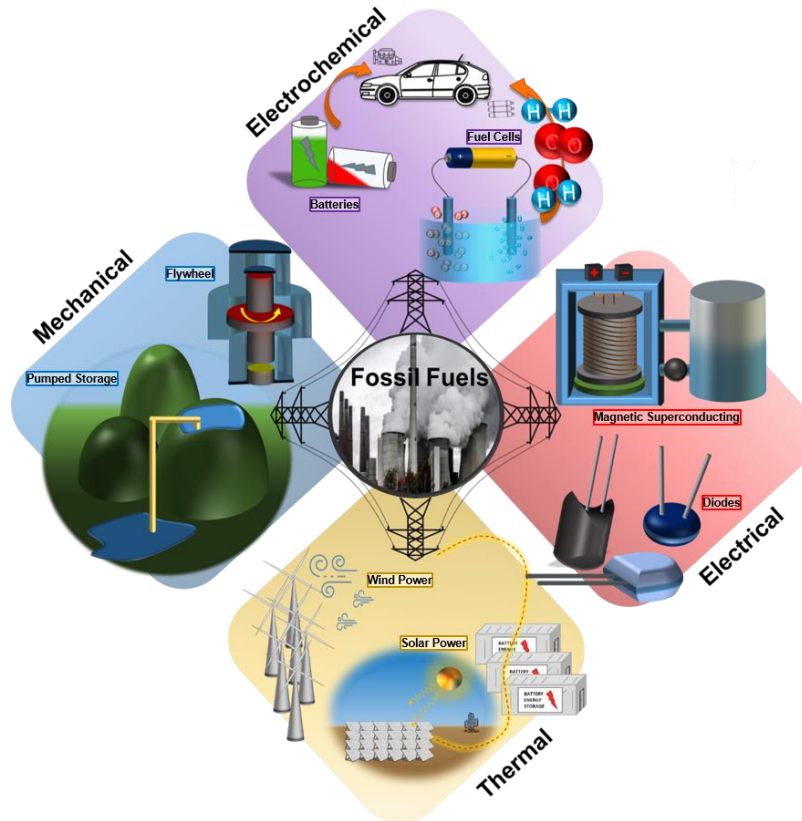


Figure 2-2 Diagram showing energy storage system (ESS) technologies. The diagram is separated into four sections, each illustrating examples of ESSs related to each classification. The ESSs are further labelled.

Mobile as well as stationary applications are the focus of major research within Europe with programs such as 'horizon 2020' making it their purpose to rebuild the ideology behind battery production starting from the ground up whilst maintaining a focus on future sustainably.

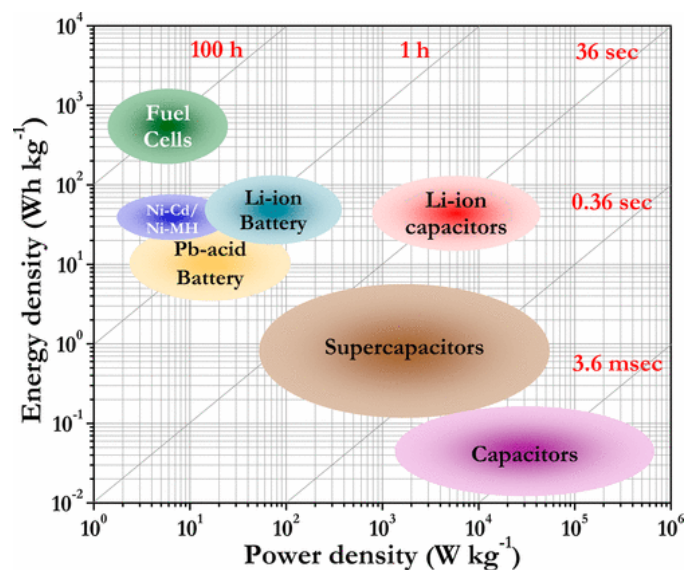


Figure 2-3 Ragone Plot - used for comparing the performance of various energy-storing devices. Typically, this plot helps clarify the difference between batteries and capacitors.^[6]

The Ragone plot in Figure 2-3 shows the relationship between specific energy density and power density of a range of portable ESSs. Where energy density refers to the amount of energy that can be stored in a system, power density refers to the rate at which this energy can be charged or discharged. Batteries tend to have high energy densities and low power densities; they can store a lot of energy and they can release it slowly. On the other hand, capacitors have high power densities and low energy densities; they cannot supply much energy, but they are able to store and release it quickly. For systems such as fuels cells, which are also included in Figure 2-3, the energy delivery can be made infinite as they only need to be provided with a constant supply of reactants.

'Electrochemical energy storage systems' is an umbrella term that is inclusive of all reversible batteries. They can be defined additionally by the scientific term 'secondary' batteries. Secondary batteries can be further divided into an array of different types of battery systems including but not exclusive to lithium-ion, magnesium-sulphur, nickel-cadmium, and lead-acid. Some examples are shown in the timeline in Figure 2-5.

2.2.2 Energy Sources

Geothermal energy is the first existing energy source of our solar system while fossil fuels such as coal, oil, and gas, have been the main energy source for humanity for thousands of years. To this day, fossil fuels still have some of the highest specific energy density making them, to some extent, irreplaceable for certain applications such as in planes (which rely on kerosene, 42.8 MJ kg^{-1}). Rockets on the other hand use liquid hydrogen, (where hydrogen has the highest energy density of all substance as shown in Figure 2-4 of $120\text{-}142 \text{ MJ kg}^{-1}$), as their chosen fuel source due to the low atomic mass and high burning temperatures of $\sim 3300 \text{ }^\circ\text{C}$.

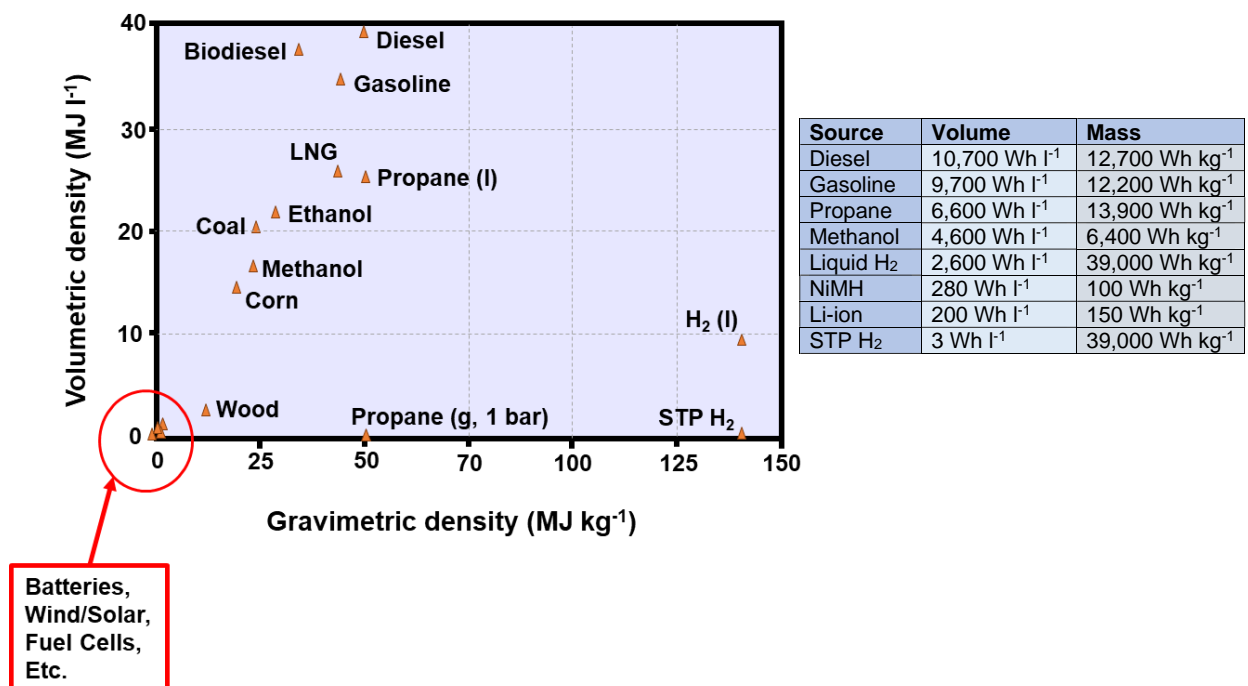


Figure 2-4 Figure to highlight the biggest problem faced by ESSs today - the low energy density of most materials in comparison to fossil fuels and liquid fuels. Table shows some values in watt-hours.

Figure 2-4 compares the energy densities of a range of fuel sources. Fossil fuels perform much better than many of its competitors. Batteries and capacitors in the big picture fall short on this scale. However, the comparison goes beyond just looking at the energy density. Environmental impact, cost, and renewability all play a major role in the selected choice of fuel for different applications.

2.3 The Theory and Subsequent Evolution of the Li-ion Battery

The battery is considered one of the most important discoveries of the 19th century, with the timeline in Figure 2-5 illustrating the development of batteries from the 1800's. Italian physicist Alessandro Volta invented the voltaic pile which is composed of stacked disks of zinc and copper separated by electrolyte-soaked cloth creating a

potential difference and therefore yielding a current. By mid-19th century, many advances had been made in the field of energy storage systems.

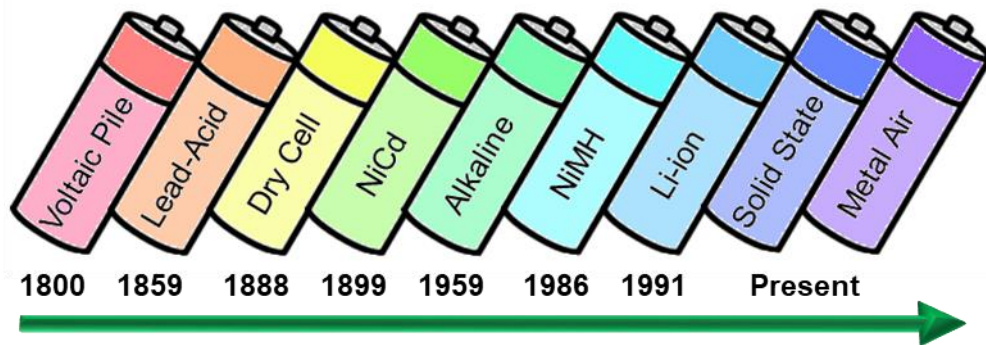


Figure 2-5 Timeline briefly showcasing the development of battery types, giving some examples ranging from the voltaic pile to the more recent solid-state and Na-ion batteries.^[7]

The development of rechargeable batteries began with French physicist Gaston Plante in 1859, who developed the first lead-acid battery, a system which is still in use today more than 150 years later. The anode is made from lead, the cathode of lead oxide, and the electrolyte is an aqueous solution of sulphuric acid. Not long after the development of what we now call 'secondary batteries', there was a large surge in the production of different types of batteries, with nickel-cadmium (NiCad), nickel metal hydride (NiMH), and redox flow cells, being some of the most well-known and commercialised examples.^[8]

As we shift our attention to the creation of the Li-ion battery (and, later, its sister, the Na-ion battery), it is critical to understand why lithium is a viable commercial contender. John B. Goodenough, M. Stanley Whittingham, and Akira Yoshino developed the Li-ion battery, and their contributions to the field of ESSs were recognised with the 2019 Nobel Prize in Chemistry.

Stanley Whittingham developed the first functional lithium battery while John Goodenough significantly boosted the batteries potential by introducing cobalt oxide into the cathode.^[9, 10] Akira Yoshino succeeded in developing a functional and rechargeable Li-ion battery based on Goodenough's lithium-cobalt oxide cathode and an anode composed of petroleum coke (a by-product from the local Japanese oil industries).^[11] From here, the success of Li_xCoO_2 and subsequently LiFePO_4 cathode materials can be traced.^[12, 13]

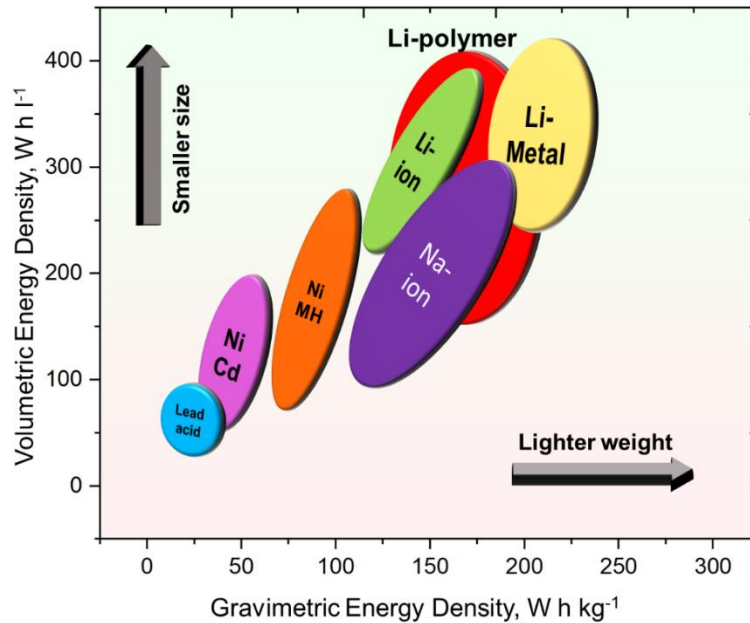


Figure 2-6 Graph illustrating the relationship between gravimetric and volumetric energy densities of a range of batteries. Reimagined from Tarascon.^[14]

The main motivation for research using the Li-ion technology is that it is the lightest electropositive metallic element in the periodic table.^[15] This in turn means that it has a very high specific energy density as opposed to its competitors, as illustrated in the energy density plot in Figure 2-6. Gravimetric energy density refers to the amount of energy stored relative to the mass of the material. Volumetric energy density refers to the amount of energy stored relative to the volume. For example, if a one-litre tank was to be filled with liquid-H₂, then this would not store as much energy compared to other fuel types such as diesel. Whereas if there was a one-kilogram weight limit on fuel storage, then liquid-H₂ would be the best option since it is the lightest of all elements. Similarly, lithium is the lightest metal and for this reason has a similar advantage over its competitors as it has a high specific capacity.

2.4 Fundamental Principles of Electrochemistry

Before looking at the internal mechanism of a Li-ion battery, some constants, fundamental laws, equations, and calculations are briefly discussed below.^[16]

Constants

Faradays constant, F : 96485.3 C mol⁻¹ (Coulombs per mol)

Coulombs constant, k : 8.987 x 10⁹ Nm² C⁻² (Newton square metre per Coulomb)

Ideal gas constant, R : 8.314 J mol⁻¹ K⁻¹ (Joules per mol per Kelvin)

Avogadro's constant, N_A : 6.02 x 10²³ mol⁻¹ (per mole)

Charge of electron, e : 1.602 x 10⁻¹⁹ C (Coulombs)

Standard conditions: temperature T of 278 K (Kelvin), pressure P of 1 bar atm. (atmospheric pressure)

First law of thermodynamics (Law of conservation of energy)

The law of energy conservation was first described by James Prescott Joule who proved that heat and mechanical energy are interchangeable.

'Energy can neither be created nor destroyed, only altered in form'

Batteries store and convert chemical energy into electrical energy. As presented in Figure 2-2, many ESSs require the conversion of one energy source into another for storage.

Ohms Law

In his book *Die galvanische Kette, mathematisch bearbeitet*, Georg Ohm gave his full theory on the electric circuit. He stated that the electromotive force acting in a circuit was a result of the strength of the current compared to the resistance of the internal circuit.

$$V = IR \quad (\text{Eq. 1})$$

V is the voltage (V), I is the current (A), and R is the resistance (Ω).

The direct voltage in a conductor is proportional to the current and inversely proportional to the resistance.

Coulomb's Law (Coulomb's inverse square law)

Coulomb's law describes the magnitude of electrical forces between two point charges. It states that the force is directly proportional to the product of the two charges and is inversely proportional to the squared distance between them.

$$F = k \frac{Q_1 Q_2}{r^2} \quad (\text{Eq. 2})$$

F is the force between two charges (N), k is the Coulomb constant ($\text{Nm}^2 \text{C}^{-2}$), Q_1 and Q_2 are point charges (C), and r is the distance between point charges (m).

Faraday's Law (Law of electrolysis)

The amount of electrical charge that passes through a circuit can be easily described in the equation below.

$$Q = nF \quad (\text{Eq. 3})$$

Q is the charge (C), I is the current (A), and F is the Faraday constant (C mol^{-1}).

Charge transfer

The amount of electrical charge that passes through a circuit per unit time can be easily described in the equation below.

$$Q = It = CV \quad (\text{Eq. 4})$$

Q is the charge (C), I is the current (A), t is the time (h), C is the capacitance (A), and V is the potential difference across the battery (V).

Gibbs Free Energy (GFE) vs. Standard Free Energy (SFE)

When a reaction occurs electrochemically, the underlying principles are based on thermodynamics or kinetics. The system releases energy to do work described as the Gibbs energy.

$$\Delta G = \Delta H - T\Delta S \quad (\text{Eq. 5})$$

$$\Delta G^\circ = -zFE^0 \quad (\text{Eq. 6})$$

ΔG is Gibbs free energy (J), ΔG° is Standard free energy (J), ΔH is the change in enthalpy (J), T is the temperature (K), ΔS is the change in entropy (J K^{-1}), z is the number of electrons involved in the reaction, F is Faraday's constant (C mol^{-1}), E is

the cell potential under non-standard conditions (V) and E° is the standard cell potential (V).

SFE is a thermodynamic potential that described the Gibbs free energy of reactants and products in their standard state (under standard conditions). SFE should not be confused with GFE which is dependent on experimental conditions such as the entropy and enthalpy of a system. The actual temperature and pressure of the system are required to calculate GFE.

The cell voltage can be calculated by rearranging the equation of the standard free energy, ΔG° .

Van't Hoff

Jacobus Henricus van't Hoff was awarded the first Nobel Prize in Chemistry in 1901 for his discovery of chemical dynamics which pioneered chemical equilibria, chemical kinetics and chemical thermodynamics. It was proposed in his book '*Études de Dynamique chimique*'.

$$\frac{d(\ln K_{eq})}{dT} = \frac{\Delta H^\circ}{RT^2} \quad (\text{Eq. 7})$$

T is temperature (K), K_{eq} is the equilibrium constant, H is the standard enthalpy change, and R is the ideal gas constant ($\text{J mol}^{-1} \text{K}^{-1}$).

The Van't Hoff equation above can be combined with Gibbs free energy to produce the Van't Hoff isotherm below.

$$\Delta G = \Delta G^\circ + RT \ln Q \quad (\text{Eq. 8})$$

ΔG is Gibbs free energy (J), ΔG° is Standard free energy (J), T is the temperature (K), R is the ideal gas constant ($\text{J mol}^{-1} \text{K}^{-1}$), and Q is the reaction coefficient.

Nernst equation (graphite anode and LiCoO_2 cathode examples)

The Nernst equation is named after Nobel Prize laureate Walther Nernst and is derived from the work of Van't Hoff.

$$E = E^\circ - \frac{RT}{zF} \ln Q = E^\circ - \frac{RT}{zF} \ln \frac{[\text{Li}^+]_e [\text{C}_6]_s}{[\text{LiC}_6]_s} \quad (\text{Eq. 9})$$

$$E = E^{\circ} - \frac{RT}{zF} \ln Q = E^{\circ} - \frac{RT}{zF} \ln \frac{[LiC_6]_s [CoO_2]_s}{[C_6]_s [LiCoO_2]_s} \quad (\text{Eq. 10})$$

E is the cell potential under non-standard conditions (V), E° is the standard cell potential (V), T is the temperature (K), R is the ideal gas constant ($J \text{ mol}^{-1} \text{ K}^{-1}$), Q is the reaction coefficient, z is the number of electrons involved in the reaction, and F is Faraday's constant ($C \text{ mol}^{-1}$).

The Nernst equation defines the relationship between the ions on either side of the membrane in the batteries. As the potential of a battery is not constant during charge-discharge cycles, the concentration is also changing as the ions are being transported back and forth through the electrolyte. Although all the components in a typical cell are not solid, in a solid-state cell where the concentrations do not change, the ideal battery voltage can be calculated.

Current density

Current density is the amount of current that flows through an area of the electrode.

$$j = \frac{I}{A} \quad (\text{Eq. 11})$$

j is the current density ($A \text{ m}^{-2}$), I is the total current (A), and A is the area of the electrode (m^2).

C-rate

C-rate is the current required to charge or discharge the cell in 1 h.

If a cell has a theoretical specific capacity of 100 Ah kg^{-1} , and is discharged at 1C-rate, then it will discharge the cell at 100 A kg^{-1} in 1 hour.

If the same cell is discharged at a 2C-rate, then the cell will discharge at 200 A kg^{-1} in half the time, so in 30 minutes.

If the same cell is discharged at a 0.5C-rate, then it will discharge the cell at 50 A kg^{-1} , and the discharge process will be twice as long, so it will take 2 hours.

Coulombic efficiency

Coulombic efficiency describes the ratio of charged released during the discharge process, to the charge necessary for charging the battery during a single cycle.

$$CE (\%) = \frac{Q_d}{Q_c} \cdot 100 \quad (\text{Eq. 12})$$

CE is the coulombic efficiency (%), Q_d is the discharge capacity (Ah kg^{-1}), and Q_c is the charge capacity (Ah kg^{-1}).

When CE (%) is lower than 100, this can be associated to an irreversible capacity loss. This is usually a result of side reactions occurring during the charge and discharge processes.

Theoretical specific charge (or capacity)

The theoretical specific charge of a system can be calculated as the amount of charge per gram of reactant based on the molecular weight of the active component of the electrode as well as the number of electrons that are transferable by this material in the electrochemical process. This can be expressed by Faraday's law in the equation below.

$$Q = \frac{zF}{M \cdot 3.6} \quad (\text{Eq. 13})$$

z is the number of electrons transferred during the reaction, M is the molar mass (g), and F is Faraday's constant (C mol^{-1}).

Due to challenges observed in the preparation and internal mechanisms of a battery (discussed in detail in the following sections), this theoretical capacity is seldom reached.

2.5 Working Principles of the Lithium-ion Battery

A battery is a mechanism for electrical energy storage. Chemical energy is converted to electrical energy through chemical reaction processes. In the case of primary batteries, the chemical reaction is irreversible and therefore the batteries are disposable after all the chemical energy has been converted.

The Daniell Cell is a simple example of a galvanic cell shown in Figure 2-7. There are essentially two compartments. The first contains an aqueous solution of ZnSO_4 with a Zn metal electrode. The second contains an aqueous solution of CuSO_4 with a Cu metal electrode. These two compartments are connected by a salt-bridge which is another aqueous solution of KNO_3 .

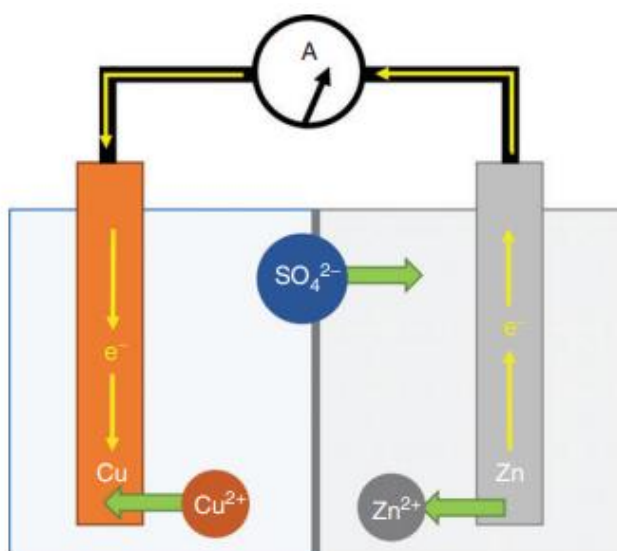
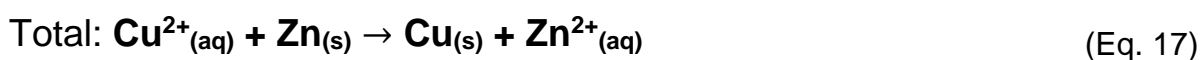


Figure 2-7 Schematic of a Daniell cell which has a Cu-metal cathode and a Zn-metal anode.^[17]

Primary batteries are closed systems that undergo redox reactions by transforming chemical energy from the internal chemical reactions to electrical energy. Once all the reactants have been used up during the discharge, these cells are typically discarded or partially recycled.

Secondary batteries, also termed accumulators, are closed systems which operate under the same principles as a primary battery. However, once the discharge process

in complete, these cells can be recharged by applying an external power to invert the direction of the redox processes. This means that the same cell can be used and recharged multiple times. However due to the complexity of the internal chemistry of a cell, this reusability is not infinite.

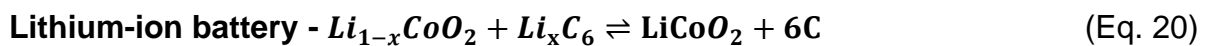
Table 1 The change in electrode processes and polarity across the discharge and charge cycles in batteries. Primary batteries only experience the discharge process while secondary batteries experience the discharge followed by the charge.^[17]

Cell-type		Half Cycle	Polarity	Electrode	Process
Primary	Secondary	Discharge	-	Anode	Oxidation
			+	Cathode	Reduction
Secondary	Secondary	Charge	-	Cathode	Reduction
			+	Anode	Oxidation

The basic equation below represents the charge-discharge processes in variety of commercial secondary cells:



Lead-acid batteries, Eq. 13, are well established, and are known for their presence in most vehicles for SLI (starting, lighting, ignition) services. Nickel-metal hydride batteries, Eq. 14, are an environmentally friendly alternative to Nickel-cadmium batteries making them a good replacement for the AA and AAA batteries typically used for household electronics.



Lithium-ion batteries are of interest to us here. Eq. 15 shows the charge-discharge processes taking place in a commercial Li-ion cell that uses a graphite anode and LiCoO₂ cathode. Each component of the cell can be substituted to use other materials and Figure 2-8 illustrates how a Li-ion battery functions.

The *anode* is often called the *negative electrode* and *cathode* is usually called the *positive electrode*. As shown in Table 1, this is because the polarisation of the electrodes remains negative and positive respectively during the cycling however the terms anode and cathode are reversed during the charging cycle.

The *negative electrode* creates a current by donating electrons that move in an external circuit (electronic conductivity) towards the positive electrode which accepts the electrons during the discharge cycle. Simultaneously, the positively charged Li-ions in solution diffuse through the permeable membrane (ionic conductivity) and combine with electrons to form neutral compounds that sit on the surface of the electrode. This is the spontaneous process of discharging or energy depletion.

When an external current is applied to the *positive electrode*, the freed electrons generate a current. The direction of the current is reversed and forced towards the *negative electrode* where the Li-ions combine with electrons to form neutral species which are then stored in the layers of the graphite. Once the cell is charged it can now be used. This is the process of charging and energy storage.^[18]

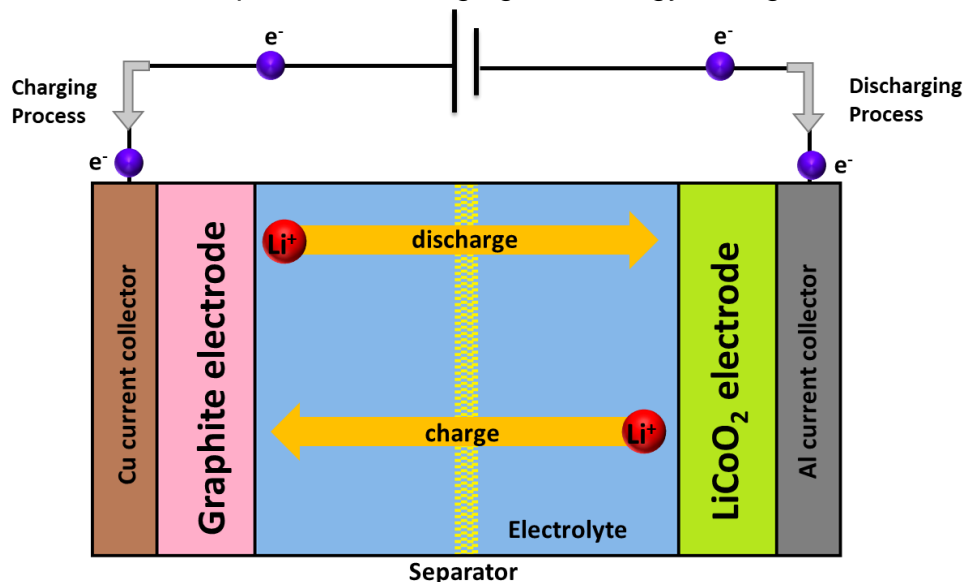
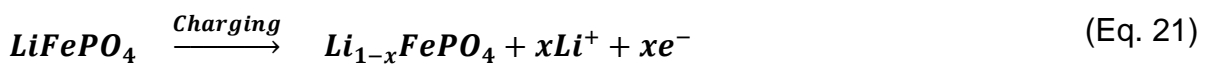
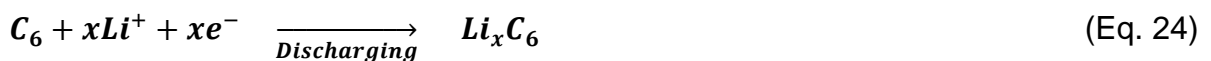


Figure 2-8 Illustration of the charge-discharge mechanism occurring in a Li-ion battery.

Taking LiFePO₄, which is another well-established and commercialised Li-ion battery cathode material, the half reactions for the charging cycles go as followed:

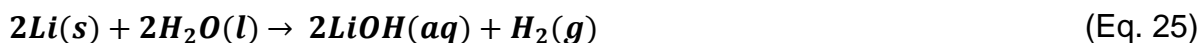


The half reactions for the discharging cycles are shown below:



The *electrolyte* plays an extremely important role in forming a stable and active cell.

This is the medium through which the charged ions are moving and so it is the ionically conductive connection between the electrodes. Most commonly, Li metals salts are dissolved in an aqueous solution and used as the electrolyte. This is because Li-metal reacts vigorously with water in the following reaction:



The standard electrolyte used in Li-ion batteries is 1M lithium hexafluorophosphate (LiPF_6) in ethylene carbonate (EC)/dimethyl carbonate (DMC) (1:1 v/v), otherwise called LP30. This is a polar aprotic electrolyte.

Not only is the electrolyte salt vital, but so are the solvents, because they both have significant contributions and effects on the internal electrochemical behaviour of the cell.

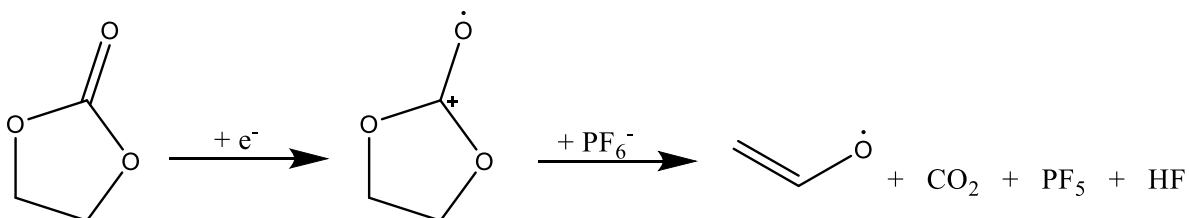


Figure 2-9 The oxidation mechanism of ethylene carbonate (EC) in the presence of LiPF_6 at high potentials.^[19]

LiPF_6 is a low-cost salt where Li^+ cations are balanced by the bulky PF_6^- anions. It is necessary that the electrolyte has a high conductivity, a wide electrochemical stability window (ESW), and contributes to effective SEI formation properties. However, inorganic salt electrolytes are a contributor to safety concerns in Li-ion batteries due to their flammable nature. Specifically, LiPF_6 has a poor thermal stability up to 107 °C and rapidly reacts with moisture to form PF_5 (a powerful Lewis acid), POF_3 (rapidly hydrolysed gas), and HF (toxic and corrosive gas), which initiate transition-metal (TM) dissolution into the electrolyte, destroying the SEI due to the now high acidity of the enclosed environment and as a result reducing the overall electrochemical performance of the cell.^[19] At high temperatures, the oxidation of the organic species such as EC in the presence of PF_6^- contributes to the production of HF as shown in Figure 2-9.^[20] The following Eq. 26-28 represent the high temperature degradation products of LiPF_6 .



It is crucial to use a *separator* between the electrodes to prevent direct contact and cell short-circuiting. As mentioned before, the internal cell should be ionically conductive, while electrical conductivity must occur externally. The separator has an additional purpose which is to be porous enough to allow ions to pass through during cycling. The ions should be capable of moving/diffusing through the membrane in order for the reactions to take place.^[21] Some separators have failure mechanisms that stop the diffusion, and cut-off the cell circuit.

Polyolefin separators are polymer-based microporous membranes. They have a low cost, and high chemical stability. The recommended porosity is usually between 30% to 60%. The separator must be able to hold enough liquid electrolyte while also being able to shut off in case of overheating.^[22]

Polypropylene (PP) and polyethylene (PE) bilayer or trilayer membranes, as shown in Figure 2-10 have a thermal shutdown that is based on the thermal stability of the porous layers. The isotactic PP layer is stable up to ~170 °C while the PE layer is stable up to ~130 °C.^[23] When this temperature is exceeded, the central PE layer melts and prevents further movement of ions. The additional 30 °C to 40 °C safety window is not sufficient enough for the PP layer to withstand any additional heating that may be a result of thermal runaway before the entire separator fails.

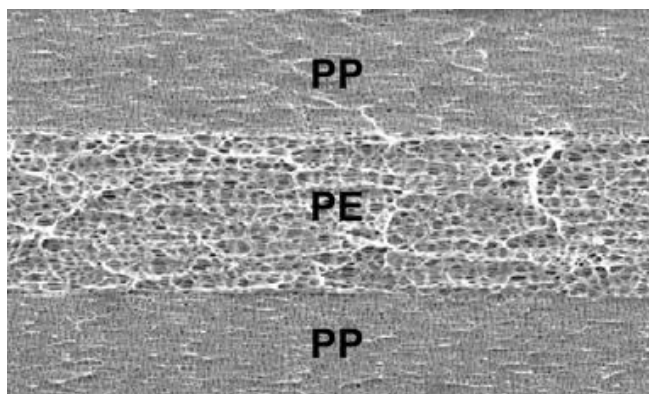


Figure 2-10 SEM image of a PP:PE:PP separator.^[24]

Ideally the separator should provide no resistance to the ion conductivity but complete resistance to the electron conductivity. Glass fibre fabric mats are also widely used as separators in cells due to their highly porous structure that leads to excellent wettability therefore resulting in high electrolyte uptake.^[25] This increases the ionic conductivity and transportation making it a good separator alternative for cell testing.

2.6 Challenges

Dendrites, meaning ‘branches’, a term derived from the Greek ‘dendron’ meaning ‘tree’, is considered to be the ‘holy grail problem’ in Li-ion batteries, and is described as the accumulation of extra Li^+ ions on the surface of the anode as shown in Figure 2-11. Lithium dendrite growth is often the result of the anode being unable to process the Li^+ in time. This makes it necessary to intercalate the ions, so they are absorbed in time to avoid lithium plating.^[21]

In dendrite formation the solid-liquid interfacial energy anisotropy is a key process occurring at the solid-liquid phase boundary that triggers solid-to-liquid transformations such as nucleation in crystal growth.^[26]

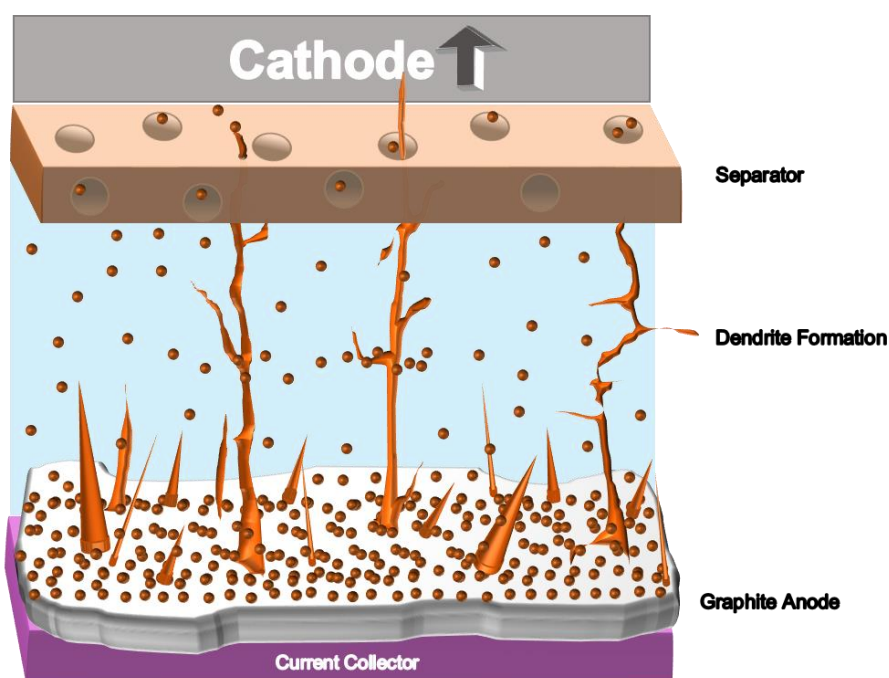


Figure 2-11 Representation of how lithium dendrite formation on the surface of the anode can pierce the separator as it grows towards the cathode.

Dendrite formation is a huge issue in Li-metal and Li-ion batteries alike as the dendrites can pierce the separator thereby reducing battery performance, lifetime and drastically increasing the safety concerns. Dendrites forcing their way through the barrier could result in a direct connection between the electrodes and the electrolyte. The electrolytes are typically liquid and flammable, a combination that has caused lithium-ion battery fires in planes, cars, phones, and laptops.^[27]

The *solid electrolyte interphase* (SEI) is defined as the passive boundary layer formed on the surface of the graphite anode. It is the inevitable product of the unavoidable and irreversible decomposition of the electrode in the presence of an electrolyte

during the first electrochemical cycle forming a passivation layer. This layer is essential in preventing further degradation of the electrode by acting as a protective barrier between the anode and the electrolyte, as illustrated in Figure 2-12. It is essential that a favourable SEI forms which prolongs the lifetime of the battery. Controlling the growth and formation of the SEI is difficult since the processes occur in-situ and are dependent on many factors. Poor SEI formation leads to poor performance.^[28]

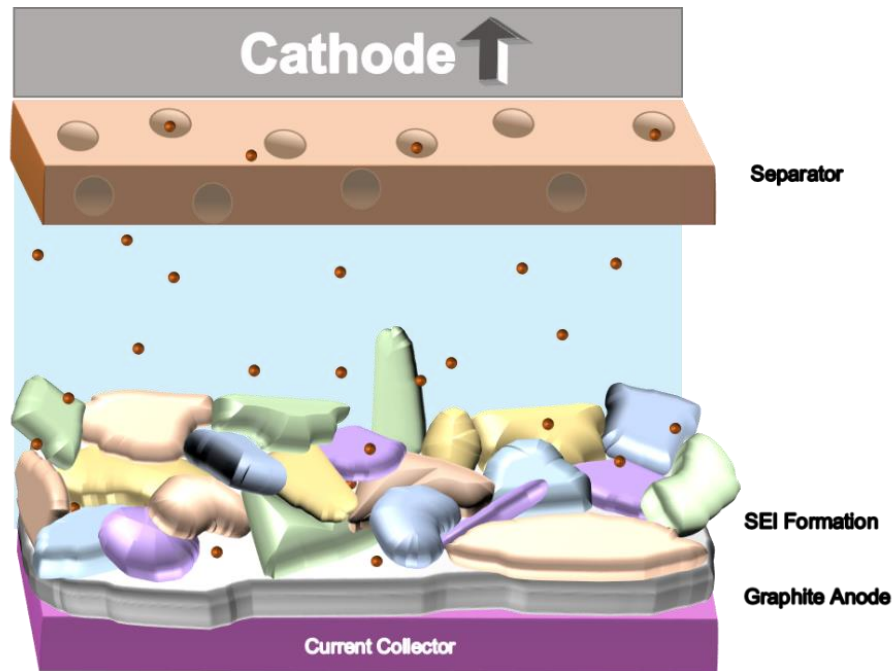


Figure 2-12 Representation of how the SEI might form on the surface of the anode. The coloured shapes are Li-containing by-products.

Thermal Runaway is a chain reaction (Figure 2-13) of hazardous nature and one of the major outcomes when a lithium-ion battery malfunctions and catches fire.

During a battery malfunction the reaction between lithium and the electrolyte solvents used causes the SEI formation of the anode to breakdown in an exothermic reaction and results in a high acidity environment as a result of the reaction products as discussed in section 2.5. Above ~ 100 °C, the electrolyte breaks down further producing volatile gases such as CO_2 or H_2 . When the separator melts, it can either cut off the internal mechanism of the cells by preventing the migration of ions, or if the temperature continues to rise then the complete separator will decompose causing an internal short circuit. At high temperatures above 150 °C the cathode begins to breakdown producing oxygen. Once the temperatures reach above ~ 170 °C, the exothermic reaction can become self-sustaining and the internal pressure due

to the build-up of gases can no longer be contained in the cell. A small spark could then trigger a fire or explosion.

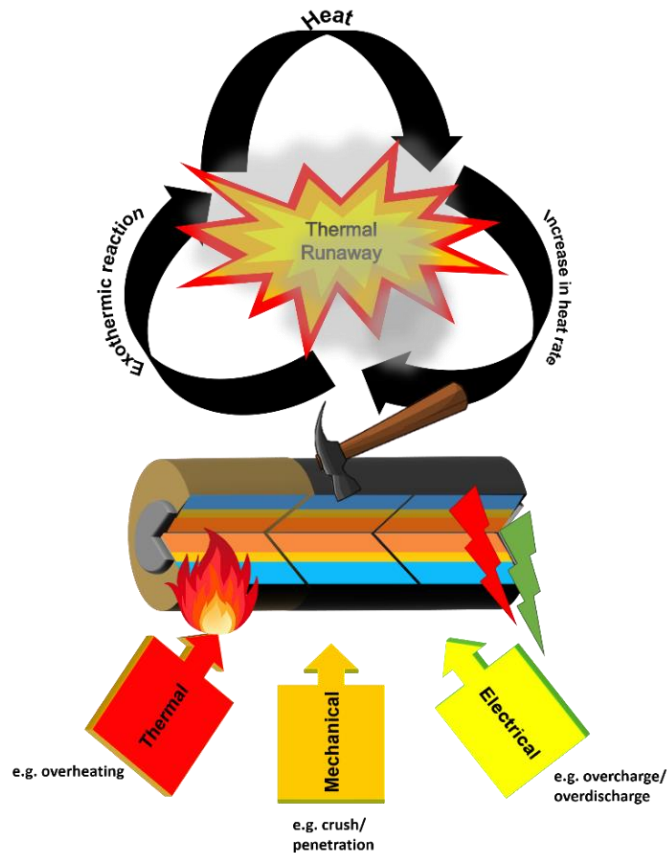


Figure 2-13 A diagram to depict the types of battery malfunctions and how they can cause the thermal runaway process that can occur in a cell.

In February 2022, ‘Felicity Ace’ a large ship loaded with approximately 4000 electric vehicles (EVs) from companies such as Audi, Porsche, and Volkswagen, caught fire on the voyage to the USA from Germany. Although the root of the fire is unconfirmed as of yet, the burning vehicles are enough to suggest they could be the cause of the blaze. Not only is this a safety issue but also an environmental issue as the ship inevitably sank and is being monitored for pollutants as oil, gas, and debris fill the ocean. The diagram shown in Figure 2-13 overviews the key elements that can cause battery failure and how this can trigger a dangerous chain reaction which can result in an explosion.^[27, 29]

Crosstalk Phenomena is a result of parasitic side reactions. As mentioned briefly in section 2.5, TM dissolution is one type of crosstalk. Here the metals in the cathode dissolve in the electrolyte (due to increasing acidity as a result of the parasitic reactions) causing the metals to migrate through the separator and accumulate on the surface of the anode.^[30] This phenomenon was first discovered for the LiMn_2O_4 cathode.^[31] Figure 2-14 below illustrates this phenomenon.

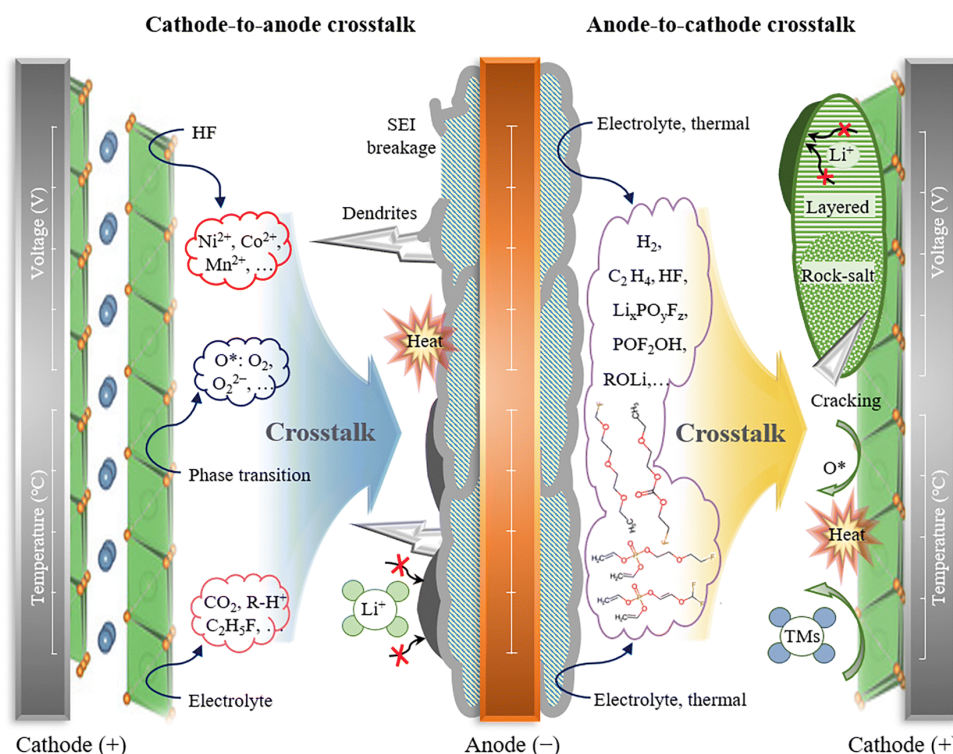


Figure 2-14 Illustration of the cross-talk phenomenon from anode to cathode and vice versa.^[32]

Hydrofluoric (HF) acid attack is known to cause the dissolution of manganese ions and explains the dissolution of Mn^{x+} from the cathode. LiMn₂O₄ is a common example used which contains both Mn^{III} and Mn^{IV}. High potentials, presence of moisture, or a large specific surface area of the active cathode materials can all contribute to Mn dissolution. In the cathode, the Mn³⁺ ions oxidise to Mn⁴⁺, therefore reducing the amount of Mn³⁺ available to undergo the disproportionation reaction between Mn²⁺ and Mn⁴⁺. This is because Mn³⁺ ions are more unstable in solution compared to Mn²⁺, which has a half-filled d-orbital.^[30] The manganese disproportionation reaction is shown below in Eq. 29.



This HF acid attack mechanism and manganese disproportionation does not explain why the concentration of manganese ions in the solution increases at high potentials. Therefore, many additional mechanisms have been proposed in order to explain this phenomenon.^[33]

Other general concerns are mentioned below:

Battery management – Safety features that adhere to the operational restrictions for safety. As previously indicated, some polymer separators provide an automatic shut-off capability. When temperatures rise above 160-170 °C, the passive layer melts and plugs its pores, preventing ion transport. In addition, protective circuits are typically installed into some devices and batteries to prevent overpotential.

Aging – Li-ion batteries degrade quickly, and consumerism is a direct result. As previously discussed, these batteries can suffer from dendrite formation and/or an inadequate SEI layer, reducing the cell's lifetime. When charged to 80% or discharged to 20% (the 80/20 consumer suggestion), they can age more slowly.

Transportation – Pressure effect on batteries when flying. Precautions are taken by airlines when flying with such devices that contain Li-ion batteries. Strict rules on what is allowed on the plane and what can be used during the flight are put into place for safety reasons.

Cost – Costlier than competitor batteries, disadvantageous when looking at large scale consumer items. NiCad/MH batteries are a much cheaper alternative for manufacturers. Lithium is an expensive metal for commercial use and the recyclability of the raw materials is tedious and difficult.

Technology – Cell health is preserved when it is neither fully charged nor discharged. Internal protection circuits must be incorporated for most batteries and devices to prevent overheating, dendrite growth, and/or separator tearing.

Depletion – The depletion of resources extends beyond the internal components of a battery. Direct depletion is associated with battery materials such as the metals employed, such as lithium, manganese, or cobalt. In addition, indirect depletion should be considered, which takes into account the components used to create the cells, such as holders, spacers, and so on.^[34, 35]

Environment – Concerns about the environmental consequences of lithium mining. Water loss, soil contamination, and destruction to aquatic life are only a few of the negative effects of lithium mining on human and animal life.^[36]

2.7 Interest in Na-ion Batteries (NIBs)

Research into using Na-metal as an alternative to Li-metal lies in the cost-effectiveness of the technology. Sodium, being one of the top five most abundant metals in the earth's crust, is more than 1000 times more abundant than lithium, and has somewhat similar physical and chemical properties to lithium. Sodium has a redox potential of -2.71 V while lithium's redox potential is higher as it lies at -3.01 V. Sodium has a gravimetric capacity of 1165 mAh g⁻¹ whereas lithium has more than double the gravimetric capacity of ~3829 mAh g⁻¹. Although the energy density for Na-ion batteries is lower than that of Li-ion batteries there is a place and application for both commercially.^[37]

They are also much safer in retrospect due to the ability to discharge completely to 0 V. This is explained by the fact that sodium does not alloy with lithium (Li_xAl). And it is because of this alloying process that the expensive Cu-foil current collector must be used at the lower potentials (although Cu to Cu⁺ oxidation can occur at 0 V). Because of this additional stability at extreme potentials, the chance of developing dendrites is also much lower compared to Li-cells.^[38] This eliminates the possibility of overheating which is often a result of over-discharging a Li-ion battery. Lithium, beryllium, sodium, magnesium, aluminium, potassium, and calcium are the lightest of all metals in the periodic table according to their atomic weight. Due to the need for light batteries for portable devices, they are well-funded areas of research as Li-metal replacements in energy storage devices. Many electrode materials that have been used in Li-ion batteries have also been tested in sodium-ion batteries with unfavourable results. The cycling performance, cell capacity, and rate capability studies suffer in their performance. This can be explained by taking the ionic radius of each ion into consideration. Na⁺ has an ionic radius of 0.95 Å with is larger than the ionic radius of Li⁺ which is 0.60 Å. This difference in size can affect the SEI formation, the transport properties, and the phase stability of the active electrode materials. Thus, the diffusion mechanisms of inserting and storing sodium within the cathodes are different from those mechanisms within Li-ion batteries. The larger radius of the lower group 1 alkali metals has prospective effects on the energy and power density.

After the development of Li_xCoO₂ as a cathode material by Goodenough, Na_xCoO₂ was reported around the same time to be used as the cathode in sodium-ion

batteries.^[39] The mechanism that takes place during battery operation is shown below in Eq. 30.



However, the rise in Li-ion research meant that research on sodium-ion systems became stagnant since the higher potential and low mass (7 g mol^{-1} compared to 23 g mol^{-1}) of lithium made it more attractive to study. Research on Na-ion systems once again became interesting to academics and industries alike when Stevens and Dahn demonstrated a high reversible capacity of 300 mAh g^{-1} for storage in a Na-ion battery using a hard carbon anode. Even to this day, hard carbons are considered one of the most attractive anode materials for Na-ion batteries.^[40]

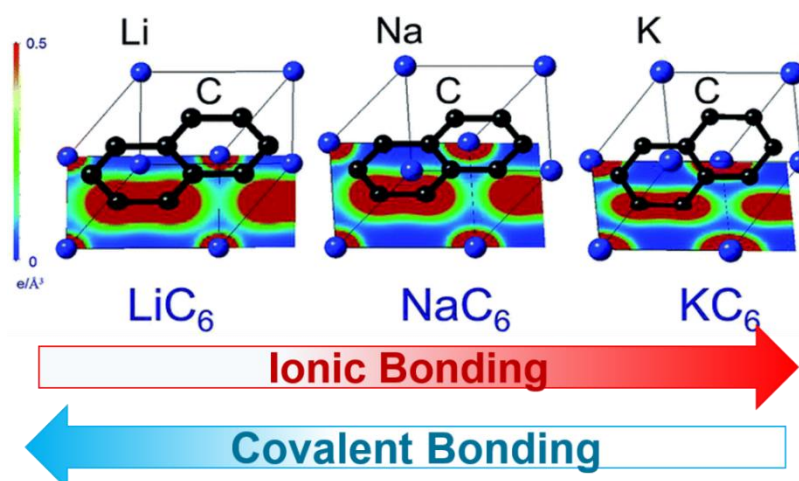


Figure 2-15 Diagram showing the electron density for LiC₆, NaC₆ and KC₆ compositions. Extracted from Moriwake et al.^[41]

Graphite is unable to efficiently accommodate the bulkier Na⁺ ions to form intercalation compounds. The LiC₆, NaC₆ and KC₆ intermediates can be compared through their bonding mechanisms as demonstrated in Figure 2-15. Moriwake reported on the instability of the Na-ion intercalation using detailed first principle calculations describing the chemical bonding between the alkali metal ions and the C₆ graphene layers. Figure 2-15 shows the Li-C bonds have a covalent component that helps to stabilise the Li-ions in the intercalation layers while Na-ions and K-ions observe weaker ionic bonding.^[41]

Currently, many companies have their focus set on commercialising Na-ion technologies, since Na-ion technology to some extent mimics Li-ion technologies (even though the general performance is lower). Figure 2-16 shows how different cells relying on Na-ion technology perform against one another.

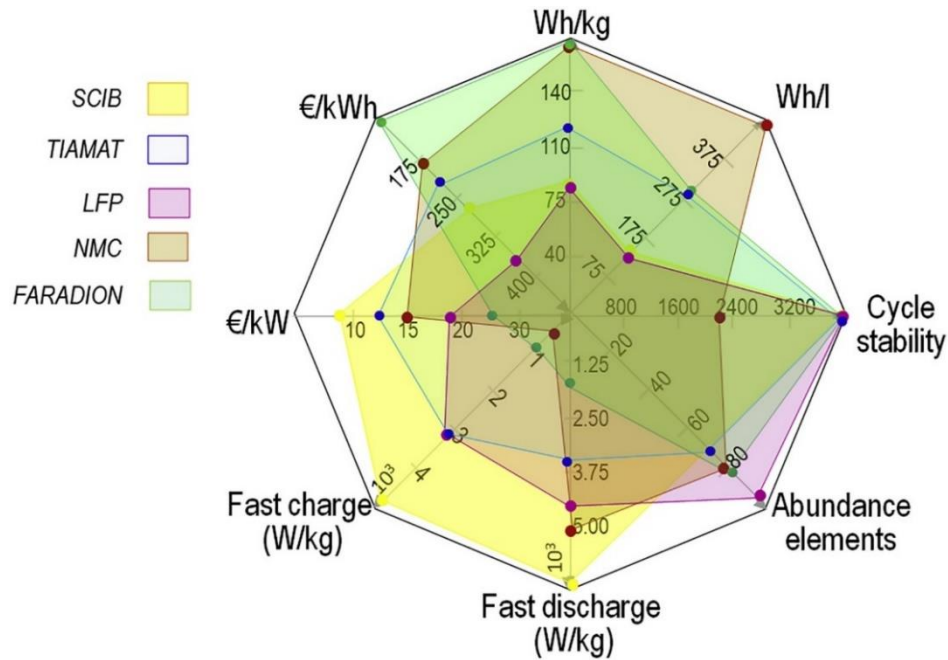


Figure 2-16 Comparison of high power cells relying on Na-ion technologies.^[38]

Iron hexacyanoferrate analogues, also known as Prussian blue (PB) analogues, are promising cathode materials explored for application in Na-ion batteries. This is due to several characteristics: high specific capacity, ionic conductivity, and easy synthesis. Since PB has an open framework, reversible intercalation for ions such as K^+ or Na^+ is possible, as shown in Figure 2-17.^[42]

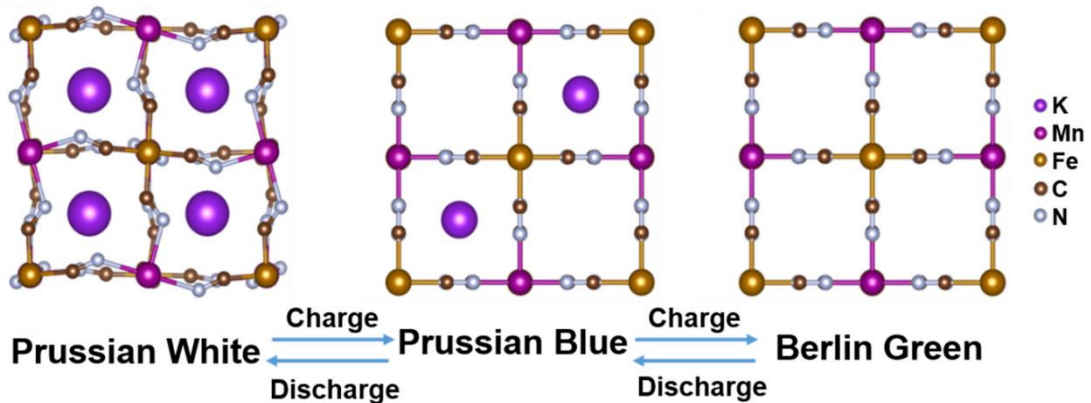


Figure 2-17 Depiction of how the charge-discharge mechanism works for Prussian blue based materials.^[42]

Wang et al synthesised cubic and rhombohedral $Na_{2-x}Fe[Fe(CN)_6]$ and tested them in pouch full cells. They reported the successful cycling performance over 1000 cycles with stable capacities up to 100 mAh g^{-1} as well as the highly reversible structural transformation between cubic, tetrahedral and rhombohedral structures during the sodium intercalation and de-intercalation.^[43] This is just one example from the literature available on the use of PB-based materials in Na-ion batteries.^[44]

2.8 Anode Materials

Recent Advances in Nanotechnology

Nanotechnology is a field of material science that has experienced rapid growth and evolution with the constant development of new and exciting nanomaterials. The principal characteristics of nanoparticles are their size, shape, surface, and internal structure.

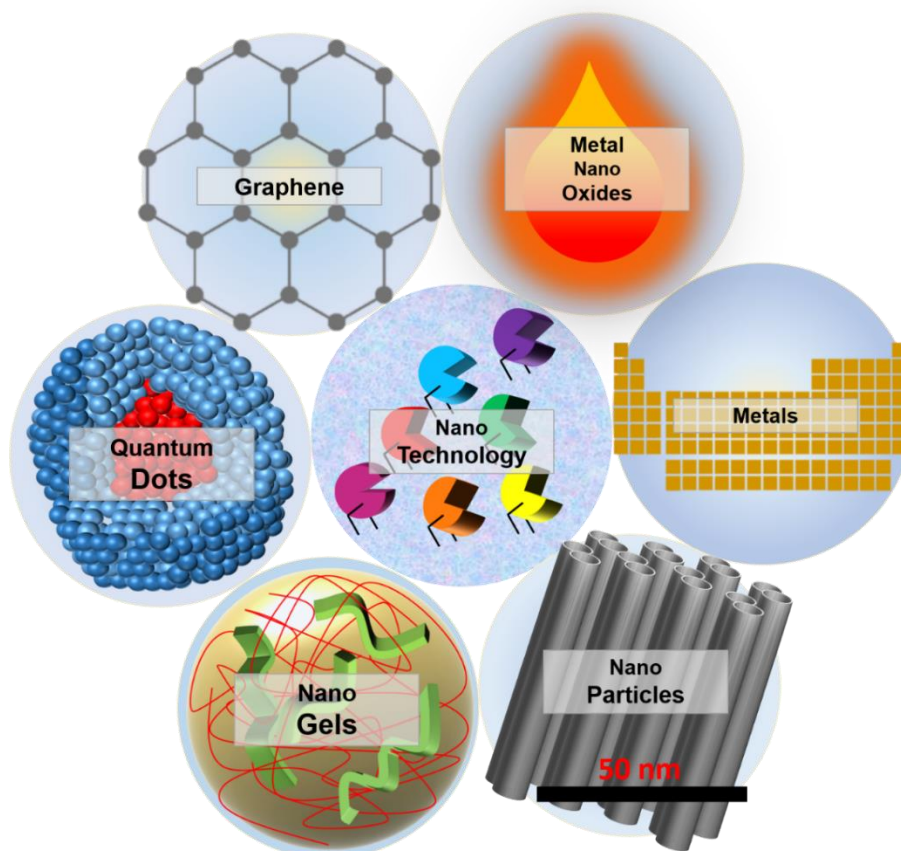


Figure 2-18 Classification of the different types of nanotechnologies.

Nanotechnology is a field of technology that deals with materials on a nanoscale, typically below 100 nm but often includes materials up to 500 nm. They can be divided into many categories, some of them shown in Figure 2-18. Quantum dots are superconducting nanoparticles which are interesting for their unique optical properties.^[45] Nanogels are three-dimensional hydrogel materials formed from polymers used mostly in the field of drug delivery.^[46] Metal supported nanoparticles are also of increasing interest in the field of biomedical sciences. With metals such as silver (Ag), gold (Au), and platinum (Pt) are of major interest due to their photothermal and optical properties.^[47] For the purpose of this thesis (electrochemical applications), the focus from here will remain on graphite/graphene and transition-metal oxides as electrode materials in Li-ion batteries.

2.8.1 Graphite

1994 marks the first commercialised variety of the lithium-ion battery by Sony and Asahi Kasei which was a non-rechargeable lithium-type. This was inspired by the pioneering work of John B. Goodenough in the development of the LiCoO_2 cathode which is arguably one of the most important discoveries in the field of rechargeable batteries.^[9, 12] LiCoO_2 and LiFePO_4 which are both commercially available, contain a key component based on carbon as the anode, which has reinforced the long-term success of lithium-ion batteries.^[9, 13]

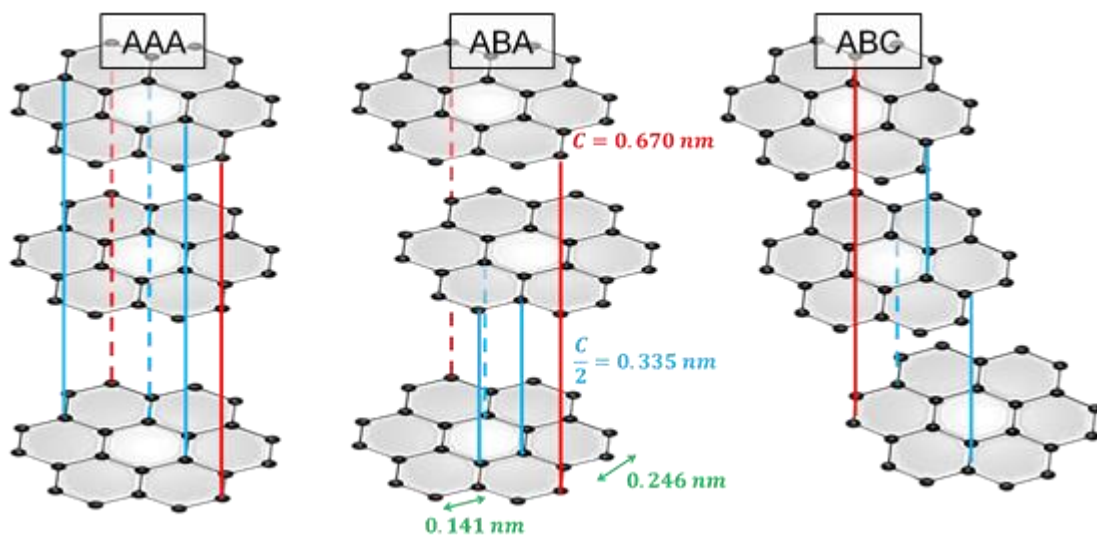


Figure 2-19 The different ways in which graphene layers stack in graphite, this could be in an AAA, ABA, or ABC pattern.

Graphite is a crystalline carbon material consisting of hexagonal stacked graphene sheets. The sp^2 -hybridised carbons are arranged in layers, with layer plane spacing of 0.335 nm. The honeycomb layers are stacked in AAA, ABA and/or ABC arrangements which are shown in Figure 2-19. There is a low conversion energy between each of the three stacking modes, thus all can be present in graphite materials. Intercalation of Li^+ between the graphene sheets has been reported to increase the layer plane spacing by up to 10%. This process is necessary to not only allow the Li^+ to enter but also to remain stored in these layers. A single Li^+ can be hosted by a six-carbon ring forming LiC_6 in the van der Waals region between the layers.^[48]

2.8.2 Soft and Hard Carbons

Slight disorientation of the graphene layers produces 'soft carbon'. Soft carbons have relatively fewer defects and higher crystallinity compared to hard carbons (Figure 2-20). Soft carbons are composed of a mixture of high strain regions with a certain degree of disorder which leads to a higher surface area in addition to low strain regions which are highly ordered which overall give it a high electrical conductivity.^[49] These materials often have little to no microporosity but mesoporous soft carbons with pore diameters between 40-50 nm were prepared by Cao and co-workers for use as the anode material in sodium-ion batteries.^[50] They reported a reversible capacity of 331 mAh g⁻¹ at 30 mA g⁻¹ and capacity retention of 103 mAh g⁻¹ after 3000 cycles at 500 mA g⁻¹ in a Na-ion battery indicating excellent stability and performance and showing the possibilities of such anodes in Na-ion batteries. Soft carbons can be converted to graphite using thermal processes.

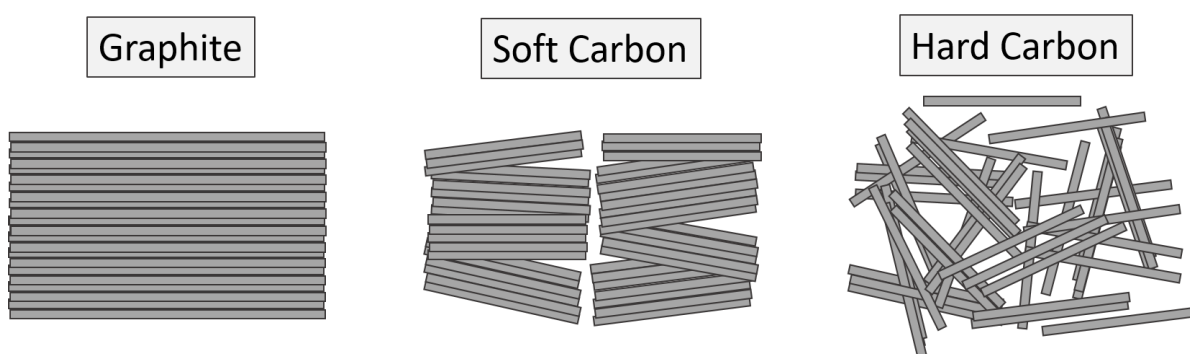


Figure 2-20 A visual representation of the arrangement of graphene in different types of carbons.

Hard carbons, on the other hand, are a form of carbon that cannot be converted to graphite, even when pyrolysed to temperatures above 3000 °C. Hard carbons differ from graphite and soft carbons in physical form as shown in Figure 2-20. Rather than having the neatly stacked layers of graphene or the slightly disordered layers of soft carbon, hard carbons have a highly disordered structure. They are formed during high temperature heat treatment to produce a charcoal rather than a layered structure. They have high micro porosity which makes them ideal for Na-ion battery anode applications.^[51] However, this disordered structure of hard carbons with many defects causes low electrical conductivity which is detrimental to the rate performance of the cell when used in Li-ion cells. Many publications report the facile synthesis and high performance of hard carbon anodes in sodium-ion batteries, and this field of research is continuously growing.^[51, 52] Dou and collaborators wrote a highly informative review on the use of hard carbons in sodium-ion batteries that describes terminology, synthesis, uses, and electrochemical results on the topic.^[53]

2.8.3 Metal Oxides of Cobalt (Co), Iron (Fe), and Manganese (Mn) as Active Electrode Materials

With respect to the negative electrode, carbons or metal oxides are considered the materials of choice. Metal oxides can be classified as having one of the following storage mechanisms i) insertion, ii) alloying, or iii) conversion. The focus here will remain on the latter conversion-type electrodes.^[54, 55]

Because of their high capacities and ease of handling, conversion-type transition metal oxides (TMOs) are by far the most appealing type of conversion material. Over the years, iron, cobalt, manganese, copper, and nickel oxides have garnered a lot of attention. Because of their high specific capacities, abundance, and inexpensive costs, they are being explored as graphite substitutes at the anode of Li-ion batteries.^[54, 56]

2.8.3.1 Cobalt

Cobalt oxides such as the cubic $\text{Co}^{\text{II}}\text{O}$ have advanced redox properties that make them attractive electrode materials. In the anode of a lithium-ion battery, CoO which reacts in the following mechanism $\text{CoO} + 2\text{Li}^+ + 2\text{e}^- \rightleftharpoons \text{Co} + \text{Li}_2\text{O}$ has a high theoretical capacity of 716 mAh g^{-1} . To provide some examples of CoO anodes, CoO nanowire clusters synthesised directly on the surface of the current collector were reported by Cao and colleagues.^[57] These nanowires reported a high capacity of 1516 mAh g^{-1} when measured at 1 C , and a capacity of 1331 mAh g^{-1} at 5 C .

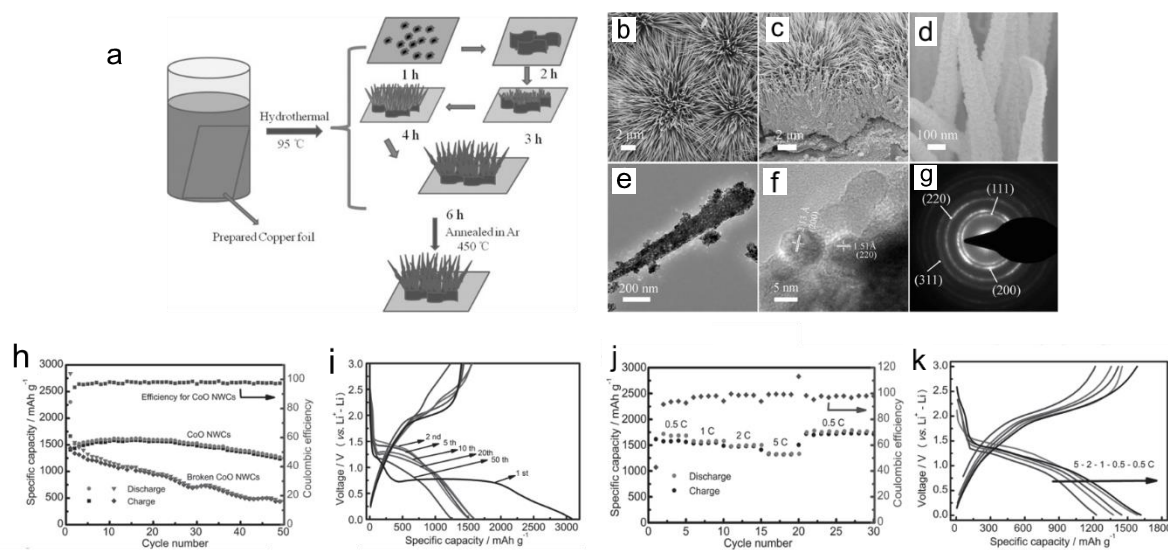


Figure 2-21 a) synthetic procedure b-g) scanning electron microscopy and transmission electron microscopy images and h-k) electrochemical performance of the CoO nanowires prepared by Cao et al.^[57]

Rai and co-workers developed a one-step method of forming spherical 20-30 nm particles of CoO via a urea assisted method.^[58] When cycled as an anode in a lithium-ion cell, a reversible discharge capacity of 855 mAh g⁻¹ was recorded for the 2nd cycle with approximately 66% capacity retention after 23 cycles. Qin et al synthesised nano/microstructures of CoO using hydrothermal methods followed by a subsequent calcination. They obtained an initial discharge capacity of 1370 mAh g⁻¹ and a high reversible capacity of 1148 mAh g⁻¹ after 20 cycles measured at 100 mA g⁻¹.^[59]

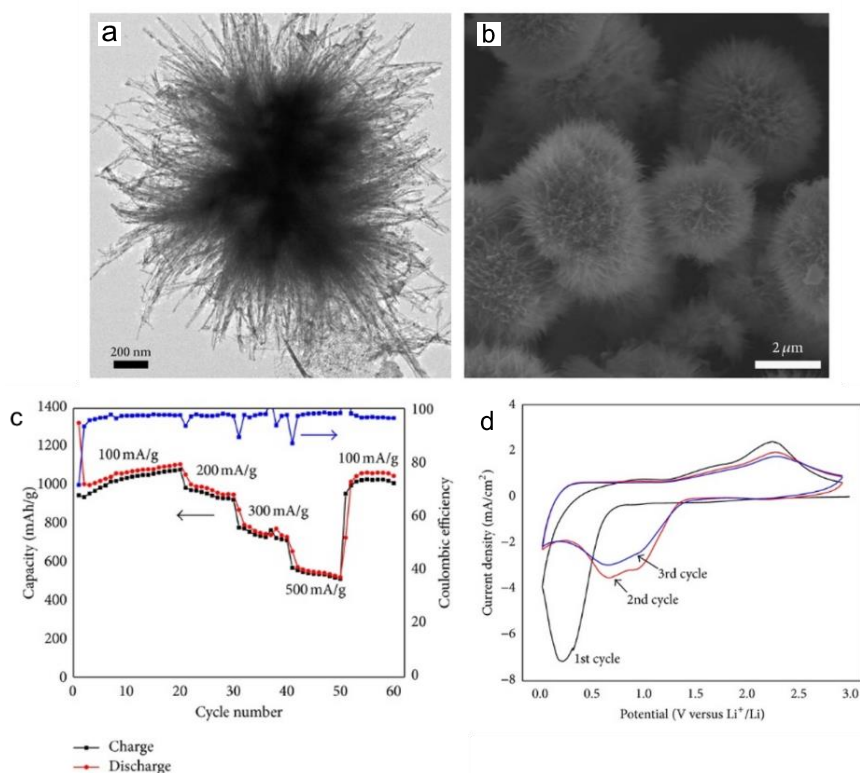


Figure 2-22 a) Transmission Electron Microscopy image of the CoO microstructures; b) field emission scanning electron microscopy image of the CoO microstructures; c) rate capability studies to show lithium storage capability; and d) cyclic voltammetry to show the redox behaviour.^[59]

Co^{II}Co^{III}₂O₄, which has a normal spinel structure is considered to be more attractive due to the higher theoretical capacity of 890 mAh g⁻¹ and the easier preparation methods since the pyrolysis of nearly all cobalt salts in air results in Co₃O₄. Co₃O₄ nanotubes prepared by Lou and colleagues maintained a capacity of 918 mAh g⁻¹ after cycling at 50 mA g⁻¹ for 30 cycles, while Co₃O₄ nanotubes developed by Chen et al maintained a capacity 856.4 mAh g⁻¹ at 0.25 C and 677.2 mAh g⁻¹ at a charging rate of 1 C after 60 cycles. Chen and co-workers developed Co₃O₄ nanowires and compared the performance to the Co₃O₄ nanotubes.^[60]

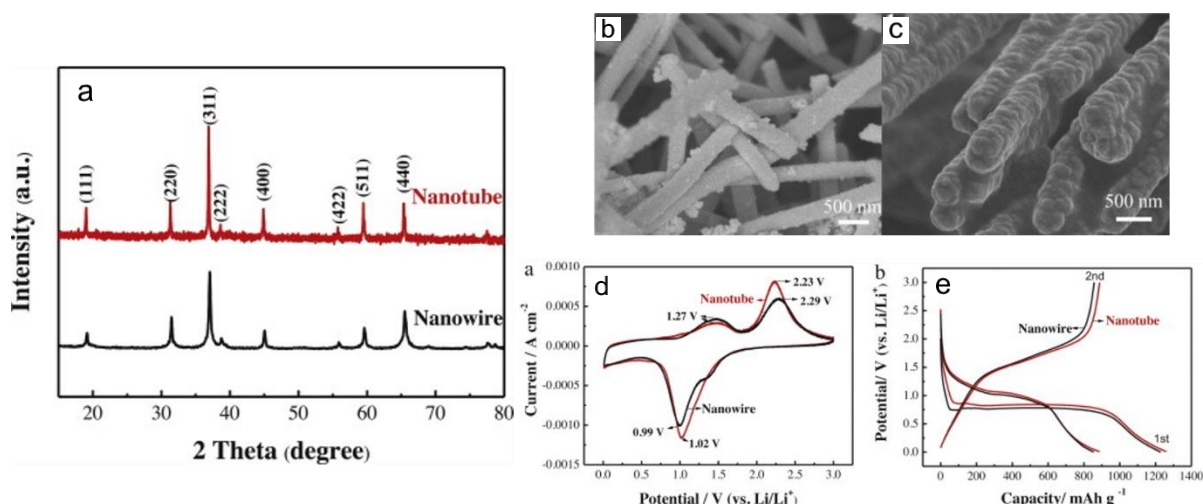


Figure 2-23 a) X-ray powder diffraction patterns of Co_3O_4 nanotubes and nanowires synthesised by Chen et al, b,c) scanning electron microscopy images of nanotubes, and d,e) electrochemical data.^[60]

Due to the ethical and environmental concerns surrounding cobalt mining and refining, research has transitioned to using alternatives such as iron and manganese oxides instead. Although cobalt materials provide a high electrochemical performance, it is paramount to replace cobalt usage with something more sustainable.^[35]

2.8.3.2 Iron

Iron oxides such as $\text{Fe}^{\text{III}}_2\text{O}_3$ and $\text{Fe}^{\text{II/III}}_3\text{O}_4$ are attractive candidates as anode materials. Since iron is one of the most abundant elements in the earth's crust, combined with being cost effective, and avoiding the ethical issues associated with cobalt mining, there is a scope here for the next generation of anode materials. Taking $\alpha\text{-Fe}_2\text{O}_3$ as an example, being cycled in the following conversion mechanism $\alpha\text{-Fe}_2\text{O}_3 + 6\text{Li}^+ + 6\text{e}^- \rightleftharpoons 2\text{Fe} + 3\text{Li}_2\text{O}$ provides a theoretical capacity of 1006 mAh g^{-1} .^[61]

Using a metal organic framework as a template, Cho and co-workers prepared a porous $\alpha\text{-Fe}_2\text{O}_3$ that maintained a capacity of 911 mAh g^{-1} after cycling for 60 cycles at 0.2 C. Increasing the current to 10 C gave a capacity of 424 mAh g^{-1} .^[62] Lou et al reported their hollow $\alpha\text{-Fe}_2\text{O}_3$ structures displayed a competitive performance and high specific capacity owing to the hollow architecture of the oxides that in turn shortened the diffusion pathways for the Li^+ ions.^[63] $\alpha\text{-Fe}_2\text{O}_3$ nanoflakes, synthesised by Reddy and co-workers through hydrothermal methods, were reported to show reversible Li-cycling capacities of 680 mAh g^{-1} with no significant capacity fade after 80 cycles observed.^[64]

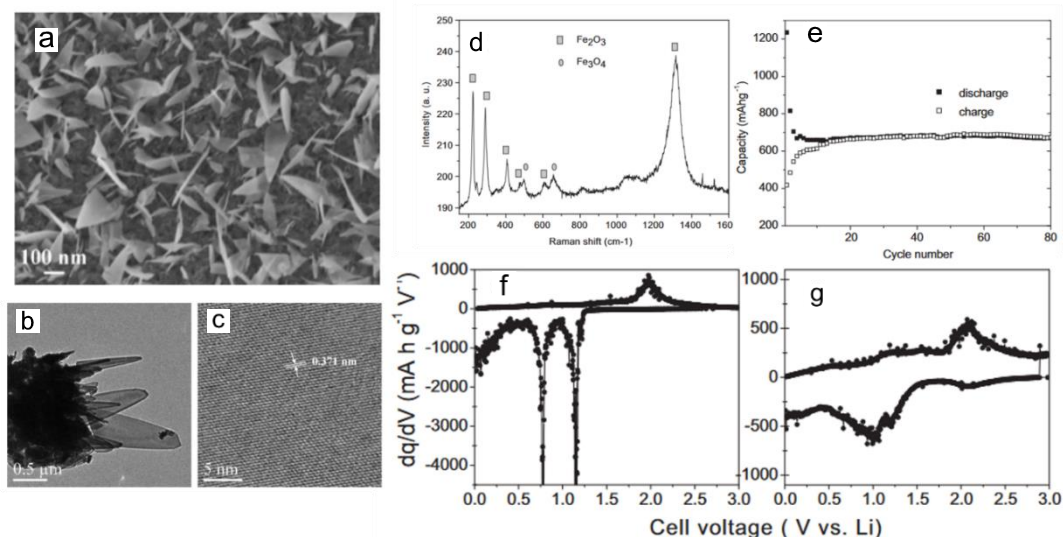


Figure 2-24 a) field emission scanning electron microscopy images of Fe_2O_3 nanoflakes, b,c) transmission electron microscopy images d) raman scattering data of the nanoflakes and the capacity per cycle for 80 cycles e) 1st cycle of the cyclic voltammetry and f,g) show the corresponding differential capacity.^[64]

$\text{Fe}^{\text{II/III}}_3\text{O}_4$ has a high theoretical capacity of 925 mAh g^{-1} and taking into consideration the nanostructure morphology is again key when looking to enhance the electrochemical properties.^[55]

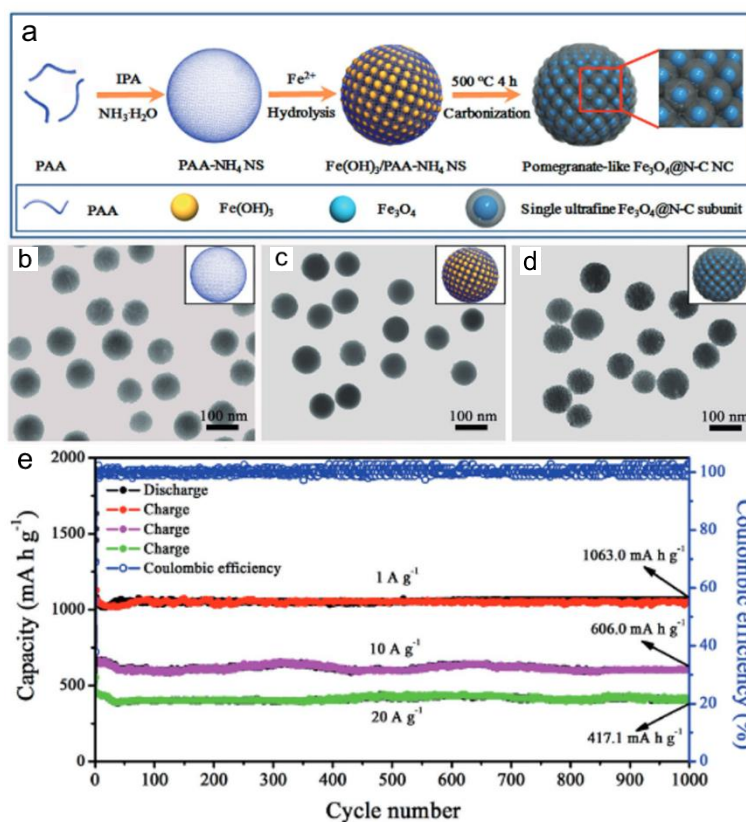


Figure 2-25 a) Schematic representation of the process of creating the Fe_3O_4 @Nitrogen-doped carbon nanoparticles. b, c, and d) Transmission electron microscopy images showing the morphology of each step in the fabrication process. e) The capacity per cycle for 1000 cycles at 1 A g^{-1} , 10 A g^{-1} , and 20 A g^{-1} .^[65]

Fe_3O_4 @Nitrogen-doped carbon nanoparticles (Fe_3O_4 @N-C) were developed in a one-pot synthesis by Liu and colleagues to form nanoclusters of pomegranate-like morphologies of carbon coated ultra-fine nanoparticles that show a high reversible specific capacity of 1204 mAh g^{-1} when cycled at 0.5 A g^{-1} over 100 cycles as the anode in a Li-ion battery. Excellent rate capability properties were observed as the capacities at 1 A g^{-1} , 10 A g^{-1} and 20 A g^{-1} were maintained at 1063 mAh g^{-1} , 606 mAh g^{-1} , and 417 mAh g^{-1} respectively.^[65]

2.8.3.3 Manganese

Manganese oxides such as Mn_3O_4 and MnO_2 have been plentifully researched over the last years owing to their high theoretical capacities and fewer environmental concerns compared to cobalt oxides. Finding methods to induce mechanical strength of Mn_xO_y based electrodes as well as their conductivity are essential to improve performance. It was reported by Abruna and colleagues that a sponge-like Mn_3O_4 , that was investigated as an anode material in a lithium-ion battery was able to maintain a reversible capacity of 800 mAh g^{-1} over 80 charge-discharge cycles with particle sizes of 80 nm .^[66]

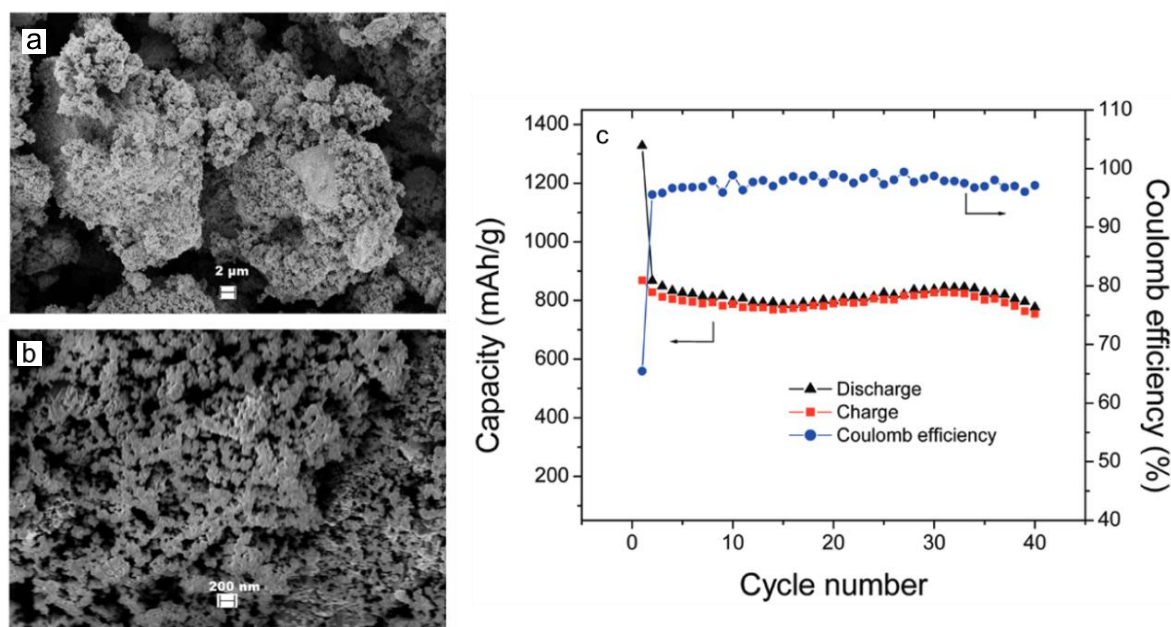


Figure 2-26 a) scanning electron microscopy image at low magnification. b) scanning electron microscopy image at higher magnification. c) charge-discharge capacity and coulombic efficiency measured over 50 cycles.^[66]

Likewise, Fan and Whittingham obtained Mn_3O_4 nanofibers through electrospinning methods with a high initial discharge capacity of 2200 mAh mg^{-1} which was followed by a discharge capacity of 600 mAh g^{-1} for the following 5 cycles.^[67] Wang and

co-workers prepared Mn_3O_4 powders with nanometre sizes that were synthesised via flame spray pyrolysis that delivered a high specific capacity of 1182 mAh g^{-1} when cycled at 200 mA g^{-1} for 110 cycles.^[68] Hashem and co-workers synthesised cryptomelane MnO_2 using lemon peel as a green reducing agent to produce reversible capacities of 160 mAh g^{-1} at 10 mA g^{-1} .^[69]

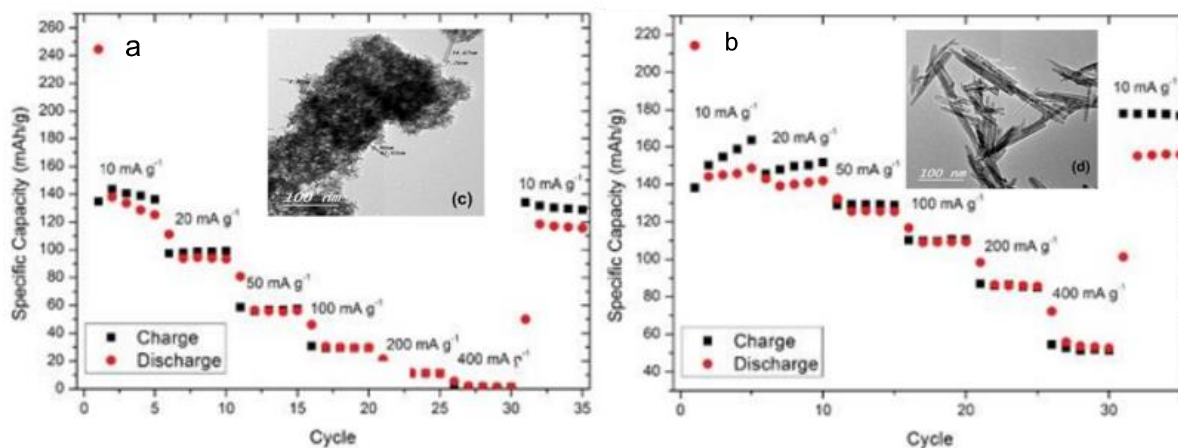


Figure 2-27 Rate capability of lithium half-cells measured using a) lemon juice, and b) using lemon peel.^[69]

These examples show that by selectively choosing processing techniques, different phases and morphologies can greatly influence the performance of the electrode.

2.9 Importance of Lanthanides

Lanthanides are some of the periodic table's least understood and underappreciated elements. They are commonly neglected because their assigned title of "rare earth elements" is frequently construed too literally. Furthermore, because they are heavy metals, they are sometimes disregarded when it comes to portable devices. Despite having fewer oxidation states than the majority of 3d transition metals, 4f lanthanides (shown in Figure 2-28) are critical to the advancement of modern technology.



Figure 2-28 Row of lanthanide elements. Yttrium (Y) is included as it has similar chemical properties as the lanthanides. In terms of size, yttrium would sit between holmium (Ho) and erbium (Er). The location of promethium (Pm) is shown with a green star due to it being a radioactive element.

Along with other metals and alloys, lanthanum has a considerable hydrogen absorption capacity. Lanthanum may absorb hydrogen into its lattice structure when it is exposed to hydrogen gas, resulting in the formation of a solid solution of lanthanum and hydrogen. Hydrogen adsorption or absorption is the term used to describe this process. Due to its distinct electrical structure, which has a $[\text{Xe}] 5d^1 6s^2$ electron shell, lanthanum is able to absorb hydrogen. The hydrogen is absorbed into the lattice structure due to the strong interactions between the lanthanum atoms and the hydrogen molecules made possible by this electron configuration. Because it enables the storage of hydrogen in a solid-state form that is secure and convenient to transport, lanthanum's ability to absorb hydrogen has significant applications in the field of hydrogen storage. In addition, as lanthanum has a great affinity for several contaminants typically present in hydrogen gas, the absorption of hydrogen by lanthanum can also be used in the purification of hydrogen gas streams.

The fact that lanthanide luminescence is the foundation for many different electronic applications is generally well understood. This is caused by either d-f transitions or f-f transitions.^[70]

Luminescent terbium shines green and it is a component of television phosphors. When activated by an electron beam, it can generate green light. When paired with other phosphors that produce red and blue light, this green emission enables the development of a wide spectrum of colours, making it especially useful for colour television screens. Electrons in the 4f shell are elevated to higher energy levels and

enter an excited state when terbium is energized by an electron beam. The energy is released as green light when these electrons reach their ground state. When making television screens, terbium is frequently combined with other rare earth elements like europium and yttrium to produce a variety of colours. A wide spectrum of colours and high-quality images can be created by varying the relative quantities of each phosphor. Terbium's electrical characteristics make it the perfect element for use in television phosphors since they enable the production of high-quality images with a variety of colours.

As a phosphorescent substance that emits a red colour when exposed to ultraviolet (UV) light, europium is utilized in banknotes. Given that it enables the production of distinctive patterns and designs that are only discernible under UV light, this capability is useful for developing security measures that are challenging to copy. Due to its distinct electron structure, which contains a partially filled 4f electron shell, europium is used in banknotes. Europium can release light in reaction to an outside stimulus, such as UV radiation, thanks to its electron structure. A small amount of europium is combined with a solution and then put to the banknote to create a security feature. The europium on the currency emits a characteristic red colour that is challenging to replicate when viewed under UV light. Overall, due to its capacity to emit a distinctive colour under UV light, which offers a highly effective method of preventing counterfeiters and assuring the security of banknotes, europium is a perfect material for use as a security feature in banknotes.

2.9.1 Lanthanides in Energy Storage Devices

Some battery types, particularly nickel-metal hydride (NiMH) batteries, use lanthanides. These batteries are utilised in a wide range of products, such as power tools, portable devices, and hybrid and electric cars. The electrodes of NiMH batteries use lanthanides, such as lanthanum, cerium, and neodymium, as alloying components. These alloys are capable of absorbing and releasing hydrogen ions as the battery is being charged and discharged. The lanthanide-based alloys utilised in these batteries have high energy densities and can deliver large power outputs, making them perfect for use in applications where high energy density and power output are required.

In addition to their use in NiMH batteries, lanthanides are also used in other types of batteries, such as solid oxide fuel cells (SOFCs) and lithium-ion batteries.

Lanthanides can be used as dopants in the electrolyte and cathode materials of SOFCs, helping to improve their performance and stability. In lithium-ion batteries, lanthanides such as lanthanum and cerium are used as additives to help improve the performance and safety of these batteries. Overall, the unique electronic and chemical properties of lanthanides make them useful in a variety of battery technologies, providing high energy density, power output, and improved performance.^[71, 72]

Some examples of publications where lanthanides are incorporated into energy storage devices are given below.

Han, Ciu, and Liu fabricated Ce-doped Mn_3O_4 using hydrothermal synthesis to produce $\text{Mn}_{2.98}\text{Ce}_{0.02}\text{O}_4$ for application as the anode in Li-ion batteries. They reported to have obtained a high capacity of 754 mAh g^{-1} at 100 mA g^{-1} up to 100 cycles. The Ce-doping resulted in larger diffusion channels and created a more stable and robust structure.^[73] Han, Singh, and collaborators doped LiMn_2O_4 with gadolinium using the typical sol-gel method.^[74] Looking at the crystal field of this cathode material, $\text{LiGd}_x\text{Mn}_{2-x}\text{O}_4$, the LiO_4 tetrahedra expanded after doping with gadolinium, meanwhile the MnO_6 octahedra contracted along the z-axis. They theorised that the lithium diffusion takes place through the empty interconnected polyhedra of the spinel framework of this material and that by expanding the tetrahedra, the electrochemical kinetics improved. Nishikawa and colleagues doped gallium nitride with europium to demonstrate a low-voltage red-light emitting diode at room temperature.^[75] The power output over the integrated ${}^5\text{D}_0$ - ${}^7\text{F}_2$ transitions of Eu^{III} was recorded as $1.3 \mu\text{W}$ with a red-light emission at 621 nm. A europium doped CsPbI_2Br perovskite material, prepared by Xiang and co-workers, was tested as an absorber layer on photovoltaic cells and it was demonstrated that the doped perovskite retains 370 hr of thermal stability when exposed to continuous white light while retaining 93% power conversion efficiency (non-doped sample retained 20%).^[76]

The significance of lanthanides can be attributed to a number of their characteristics, including their optical, electronic, and catalytic capabilities, as well as their contributions to the fields of energy (batteries, fuel cells, wind turbines, lighting), and medicine (imaging, radiotherapy, drug development, and disease diagnosis).

2.10 Crystal Field Theory (CFT)

The electronic structure and magnetic properties of transition-metal ions in coordination complexes can be explained using crystal field theory (CFT). The d-orbitals of the core transition metals are affected by the electric field surrounding the ligand atoms. This ligand field then divides the degenerate d-orbitals into two energy levels (one higher and the other lower) as the distance between ligand atom and core metal becomes smaller. The crystal field splitting energy, CFSE (Δ) can be used to show the energy disparity between the two energy levels. The CFSE can be influenced by multiple factors including the size, oxidation state and geometry of the metal ion, and the identity and arrangement of the ligands. For example, larger metal ions would have larger d-orbitals and therefore greater ligand field separation. The Aufbau principle, Hund's rule, and Pauli exclusion principle all have an influence on the occupancy of the d-orbitals in the metal ion. The ligands are considered to be point charges in CFT. It should be noted that this is a simplification. This has however been shown to help predict the electronic structure and characteristics of complexes.

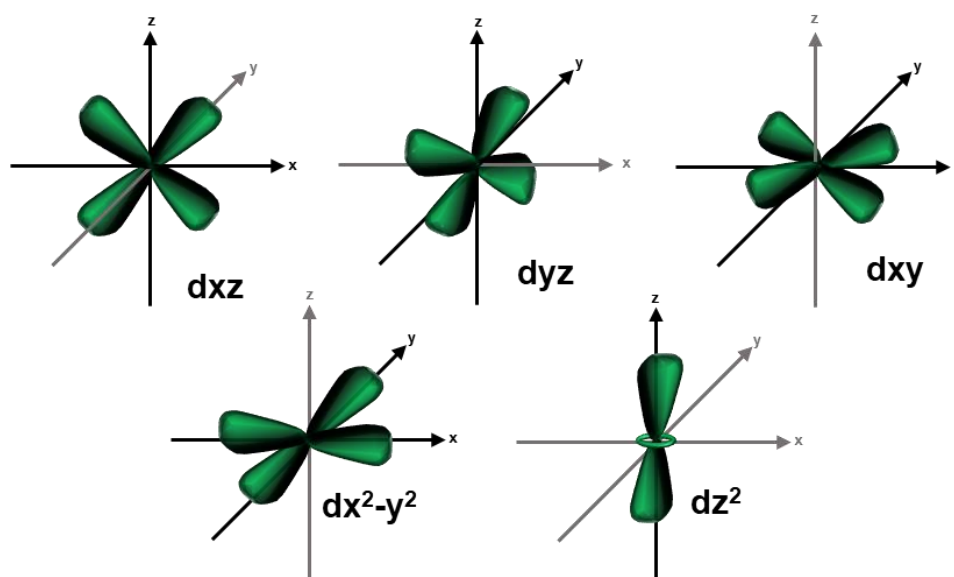


Figure 2-29 Representation of the five d-orbitals in 3d complexes.

Crystal field theory for an octahedral 3d complex – A central metal ion is surrounded by six ligands that are positioned at the vertices of an octahedron. The d-orbitals of the metal ions are influenced by point charges assigned to the ligands, causing the d-orbitals to split into two sets: a set of three higher energy orbitals called e_g orbitals and a set of two lower energy orbitals called t_{2g} orbitals. The t_{2g} orbitals are oriented between these axes, while the e_g orbitals are aligned along the axes that connect the metal ion to the ligands. The energy gap between the t_{2g} and e_g orbitals as a result of

the splitting of the d-orbitals is shown as Δ . For the tetrahedral geometry the t_2 orbitals are higher in energy and the e are lower (Figure 2-30).

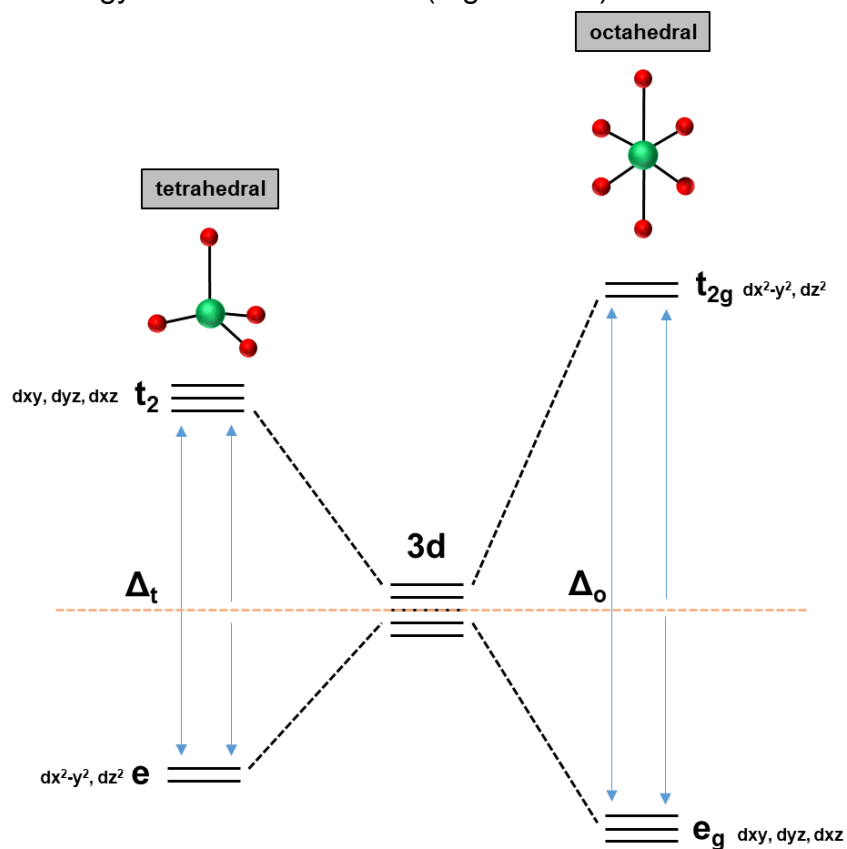


Figure 2-30 Crystal field splitting diagram of the octahedral and tetrahedral coordination environments in a 3d complex.

2.10.1 Jahn-Teller Distortion for Manganese Oxides

When a molecule or complex exhibits electronically degenerate states in its fundamental electronic configuration, the process known as Jahn-Teller distortion occurs, causing a geometric distortion that decreases its symmetry and, consequently, its energy. The distortion results from the connection of these electronic states with the molecule or complex system's vibrational degrees of freedom. Unequally occupied degenerate electronic states are unfavourable and lead to a distortion of the coordination polyhedron. This is illustrated in the case of the Mn^{III} high-spin ion in Figure 2-31.

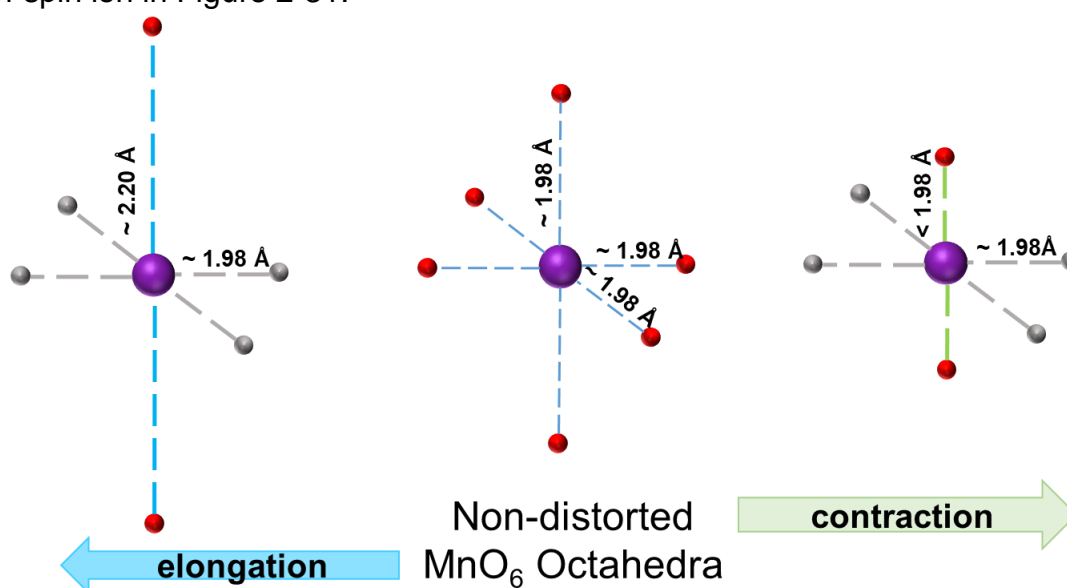


Figure 2-31 Visual representation of the non-distorted MnO_6 octahedra showing the Mn-O bond lengths with Jahn-Teller distortion take place along the z-axis.

Mn-O bond lengths for the non-distorted octahedron are typically 1.96–2.00 Å. For the Jahn-Teller distorted octahedron, two *trans*-related Mn-O bonds are usually elongated to 2.15–2.25 Å, although a compression of these two bonds is sometimes seen. Distortion of the MnO_6 octahedra can also result from structural defects or hydrogen bonding from intercalated water molecules. Furthermore, when channel structures are occupied by heterocations, their charge is balanced by valence-substitution of Mn^{IV} by Mn^{III} , resulting in distortions of the octahedra.

3 Motivation

The chemistry of a battery system directly affects the influencing variables of the system. This explains why it is crucial to concentrate on optimizing battery materials when addressing present issues and creating a battery. To attempt to create better and reproducible active materials, the internal mechanics must be understood. The primary focus of this thesis is on thermally treating 3D metal-based materials for use as the active component of a lithium-ion coin cell's working electrode.

Even if material science and energy storage have made great progress, there is always room for improving and optimizing active materials. Along with the population growth, the demand for better energy storage technologies is rising quickly. As technology has continued to improve since the late 20th Century, the need for electrical energy output has surged on a global scale. In Germany, oil accounts for most of the energy used, followed by natural gas and then a mix of renewable sources. This is an untenable prognosis for the future of transportation in Germany, a nation that is heavily dependent on the auto industry and has a strong economic incentive to keep things that way. Auto-manufactures like BMW and VW are paving the way for an electric vehicle future, but achieving this objective means either optimizing the already existing batteries or developing new competitive materials.^[77]

The Li-ion battery is the current benchmark for batteries. Due to its high load currents, longevity, LiFePO₄ is frequently used as a cathode and is regarded as the most suitable commercial electrode material.

According to literature studies and observing the direction of commercialised products, certain research gaps were identified that motivated this research:

- Lanthanide-induced phase and morphology changes in oxides are relatively unexplored.
- A library of coordination complexes could be used as precursors for electrode materials.

This concept was influenced by the potential of materials that, because of their low toxicity and low cost, are promising as energy storage devices.

4 Clarification of Terms

Terminology

In electrochemistry, numerous terms are used that can be imprecise. Since there is no clear standard for this in the reported literature, it can become misleading when describing various materials, preparations, and subsequent electrochemical operations.

All the cells measured and described in this thesis consist of a half-cell with a counter-electrode made of lithium-metal foil and the working electrode which contains the synthesized active material. In the half-cell electrochemical studies, the 3d-based active materials researched in this thesis serve as the positive electrode in the cell as these cells are comparable to Li-metal batteries, in which the anode will always be the Li-metal. In chapter 8, a Na-ion battery was measured which similarly uses Na-metal foil as the counter-electrode. In a full-cell measurement, the active materials would act as the negative electrode.

A single lithium-ion electrode submerged in a solution of lithium ions makes up a halfcell of a lithium-ion battery. Lithium ions are transferred when the electrode is charged, making the electrode positively charged. Lithium ions are liberated from the electrode during discharge, which makes the electrode negatively charged. In research settings, half-cell lithium-ion batteries are frequently used to assess the performance of novel electrode materials or to investigate the basic electrochemical characteristics of lithium-ion batteries. A Li-metal foil counter-electrode is utilized to provide an endless supply of Li-ions to the cell, unlike a full-cell Li-ion battery. To provide higher energy density and longer cycle life, full-cell lithium-ion batteries having both a cathode (positive electrode) and an anode (negative electrode) are employed in practical applications. Lithium ions can move freely between the electrodes during charging and discharging because the anode and cathode are separated by an electrolyte.

Stripping Model

Lithium stripping refers to the electrochemical process that occurs within lithium-metal batteries. An illustration of the stripping model is shown in Figure 4-1. In rechargeable batteries, the lithium is plated on the negative electrode during the charging process

and stripped off during the discharge process. This stripping can often lead to the formation of dendrites which have been discussed in detail in section 2.6.



The lithium metal is electrochemically oxidised to form lithium ions which migrate across the SEI to the electrolyte and permeate across the separator towards the positive electrode.

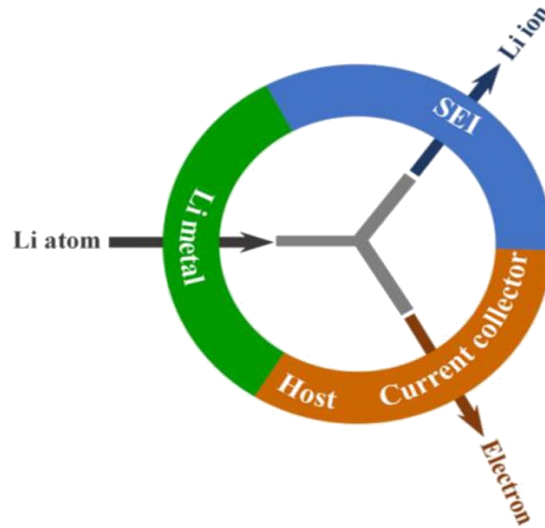


Figure 4-1 Illustration of the stripping model in Li-metal batteries.^[78]

5 Materials, Methods, and Measurements

Material preparation, general methodologies, and measurement specifics will be briefly covered before moving on to the results and discussions in order to provide further insight into the research's processing procedures. Several significant words that are utilized throughout the majority of this thesis are also defined here for clarity.

Table 2 A list of terms and definitions used throughout this thesis taken from the Handbook of Batteries.^[1]

Term	Definition
Active Material	The material in the electrodes of a cell or battery that takes part in the electrochemical reactions of charge or discharge.
Anode	The electrode in an electrochemical cell where oxidation takes place. During discharge, the negative electrode of the cell is the anode. During charge, the situation reverses, and the positive electrode of the cell is the anode.
Battery	One or more electrochemical cells electrically connected in an appropriate series / parallel arrangement to provide the required operating voltage and current levels including, if any, monitors, controls, and other ancillary components (fuses, diodes), case, terminals, and markings.
Capacity	The total number of Ampere-hours (Ah) that can be withdrawn from a fully charged cell or battery under specified conditions of discharge.
Cathode	The electrode in an electrochemical cell where reduction takes place. During discharge, the positive electrode of the cell is the cathode. During charge, the situation reverses, and the negative electrode of the cell is the cathode.
Cation	Ion in the electrolyte carrying a positive charge.
Cell	The basic electrochemical unit providing a source of electrical energy by direct conversion of chemical energy. The cell consists of an assembly of electrodes, separators, electrolyte, container, and terminals.
Charge	The conversion of electrical energy, provided in the form of a current from an external source, into chemical energy within a cell or battery.
Couple	Combination of anode and cathode materials that engage in electrochemical reactions that will produce current at a voltage defined by the reactions.
C-Rate	The discharge or charge current, in Amperes, expressed as a multiple of the rated capacity in ampere-hours.

Current Collector	An inert member of high electrical conductivity used to conduct current from or to an electrode during discharge or charge.
Current Density	The current per unit active area of the surface of an electrode.
Cycle	The discharge and subsequent or preceding charge of a secondary battery such that it is restored to its original conditions.
Density	The ratio of a mass of material to its own volume at a specified temperature.
Diffusion	The movement of species under the influence of a concentration gradient.
Discharge	The conversion of the chemical energy of a cell or battery into electrical energy and withdrawal of the electrical energy into a load.
Electrochemical Cell	A cell in which the electrochemical reactions are caused by supplying electrical energy or which supplies electrical energy as a result of electrochemical reactions: if the first case only is applicable, the cell is an electrolysis cell; if the second case only, the cell is a galvanic cell.
Electrode	The site, area, or location at which electrochemical processes take place.
Electrode Potential	The voltage developed by a single plate either positive or negative against a standard reference electrode typically the standard hydrogen electrode. The algebraic difference in voltage of any two electrodes equals the cell voltage.
Electrolyte	The medium which provides the ion transport mechanism between the positive and negative electrodes of a cell.
Negative Electrode	The electrode acting as an anode when a cell or battery is discharging.
Positive Electrode	The electrode acting as a cathode when a cell or battery is discharging.
Rated Capacity	The number of Ampere-hours a battery can deliver under specific conditions (rate of discharge, end voltage, temperature); usually the manufacturer's rating.
Separator	An ion permeable, electronically nonconductive, spacer or material which prevents electronic contact between electrodes of opposite polarity in the same cell.
Working Electrode	The electrode on which the reaction of interest is occurring.

5.1 Preparation

5.1.1 Complex Synthesis

The experimental section of Chapter 8 discusses the synthesis of the various complexes and the creation of the oxides.

5.1.2 Thermal Treatment

Annealing methods were carried out in air, N₂, or Ar atmospheres. Specific conditions and temperatures for each material are listed in their respective chapter/subchapter and in the experimental section in Chapter 8.

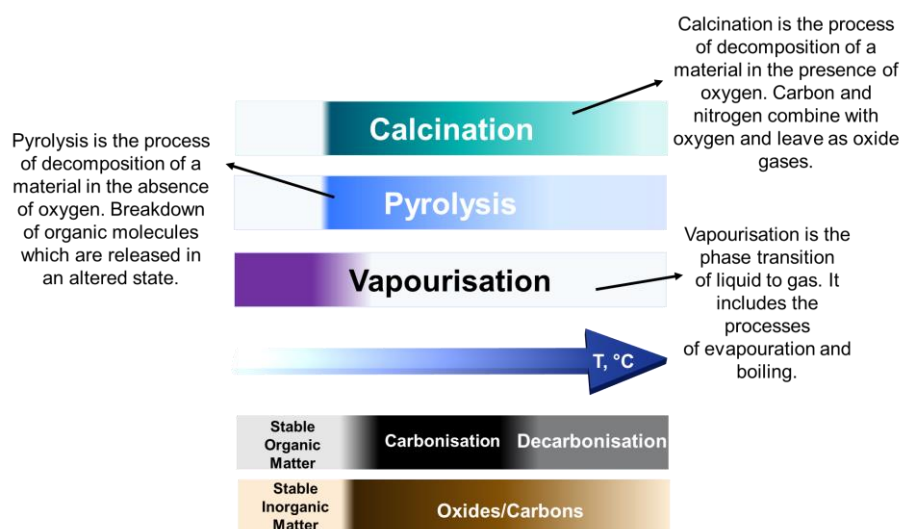


Figure 5-1 The differences between various thermolysis terms explained.

In principle, samples were placed into alumina crucibles and heated to the desired temperature under the desired conditions. Once cooled the samples were stored in a vial and dried under vacuum before transferring to a glove box for storage.

5.1.3 Electrode Preparation

All the working electrodes prepared in this thesis consist of an 80:10:10 mixture of the active compound (80%), a binder (10%), and a conductive agent (10%). The binders used were either a) polyvinylidene fluoride (PVDF) in the presence of N-methylpyrrolidone (NMP) or b) sodium alginate (Na-alg) in H₂O-isopropanol (9:1, w/w). The conductive agent used was highly conductive pyrolytic carbon (Super P).

All samples were ground to homogeneity using a pestle and mortar before forming a slurry for the next step.

5.1.4 Coating on Cu-foil Current Collector

After obtaining the slurry, the paste was coated onto Cu-foil using a doctor blade with a wet electrode thickness of 90 to 150 μm (depending on the sample). The foil was left to dry at room temperature before cutting (12 mm), pressing (7 tons/cm²), and drying further in an oven at 80 °C for 24 h. The dried electrodes were then re-dried under vacuum and placed in an Ar-filled glove box ready for cell assembly. All cells were weighed and the average mass of active material in the cells prepared were attempted to be kept between 1.2 mg and 1.6 mg.

5.1.5 Coin Cell Preparation

All electrochemical data presented in this thesis are a result of measurements in coin cells. All samples were electrochemically tested in half cells against the corresponding metal. The general preparation of the cell was consistent across all samples and is shown in Figure 5-2 below. All cells were prepared in an Ar-filled glovebox.

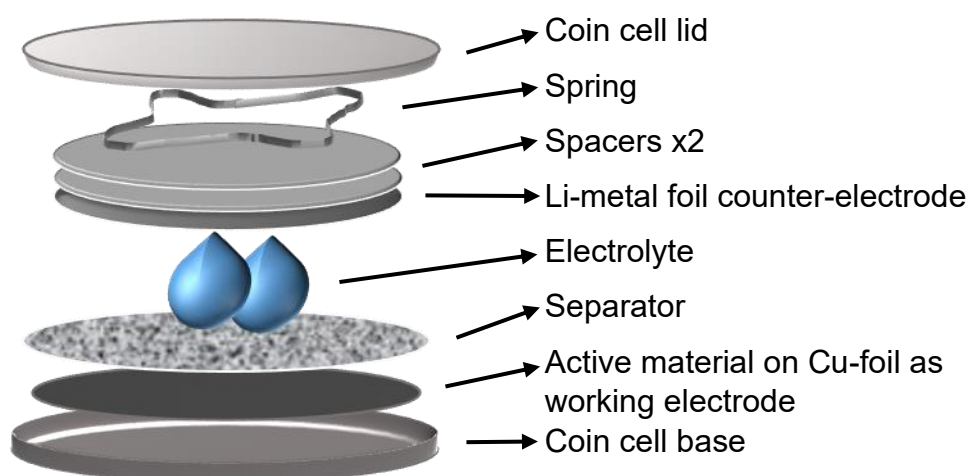


Figure 5-2 General order of coin cell assembly used for cell preparation in this thesis.

In the case of Li-ion coin cells, Li-metal foil was used as the counter-electrode. The Li-metal had a high purity (>99%) and a 12 mm diameter. LP30 which is 1M LiPF₆ in ethylene carbonate/dimethyl carbonate (1:1 w/w) was used as the electrolyte.

For the Na-ion measurement presented in Chapter 6, a thin layer of Na-metal foil was cut and pressed evenly on the surface of the separator and used as the counter-electrode. 1M NaClO₄ in ethylene carbonate/dimethyl carbonate (1:1 w/w) + 5% FEC was used as the electrolyte.

The separator used was either a) a glass microfiber filter from Whatmann with a diameter of 16 mm or b) a PP:PE:PP trilayer polymer separator of diameter 16 mm.

5.2 Measurements

5.2.1 Powder X-ray Diffraction (PXRD)

An essential tool for determining the crystalline structure of materials is powder X-ray diffraction (PXRD) which follows Braggs' Law (Eq. 32).

$$n\lambda = 2d \sin \theta \quad (\text{Eq. 32})$$

n is the number of planes, λ is the wavelength of the incident beam, d is the spacing between the planes and θ is the angle of the incident and reflected beam.

A powdered sample is exposed to an incident X-ray beam of a specific wavelength. Atoms in the crystal lattice scatter or diffract X-rays, creating a characteristic diffraction pattern. The interaction occurs between the X-rays and an electron and the number of electrons around an atom define how strongly the incident X ray beam scatters. The pattern can be utilised to recognise and ascertain crystal symmetry, impurity presence, crystal structure defects, or lattice parameter values.

X-ray diffraction is recorded at various angles while the sample is rotated. According to the Bragg law, the intensity depends on the kind of atom, where it is located within the crystal lattice, and how far apart the crystal planes are from one another. The wavelengths of the X-rays, which are typically between 1 Å and 1.54 Å, are produced by a revolving anode or a cathode ray tube, respectively. This can vary by diffractometer and requirements.

PXRD can also be used in real time or in-situ, however this requires a specialised set up and some modifications. This means that a sample can be monitored whilst its undergoing phase transitions or a chemical reaction, providing insight into the mechanism and kinetics of the occurring transformation. These measurements are typically carried out at synchrotron radiation sources for multiple reasons:

- 1) Strong and highly collimated X-ray beams from synchrotron radiation sources can generate high-quality diffraction data with acceptable signal-to-noise ratios even for weakly scattering materials. This makes it possible to spot tiny changes as materials change in their crystal structure.
- 2) Synchrotron radiation sources make it possible to acquire data quickly, which is crucial for in-situ studies where structural changes may take place quickly. Due to the high photon flux of synchrotron radiation sources, time-resolved data can be collected with quick data acquisition times that can be on the order of milliseconds or less.

- 3) With the tuneable range of X-ray energies that synchrotron radiation sources can provide, it is possible to choose the optimum wavelength to study certain materials and their crystal structures. For research involving materials with intricate crystal structures or those requiring high X-ray energy for penetration, this can be especially helpful.

For X-ray diffraction data, structure model parameters are refined by the Rietveld method. This technique entails modifying several parameters, including atomic location and lattice parameters, to fit a theoretical pattern to an experimental powder pattern. A non-linear least-squares approach is used to minimize the difference between the experimental and calculated patterns in order to fit the data. Since Rietveld analysis considers numerous phases and flaws such as disorder and amorphousness, it has the benefit of allowing complicated structures to be refined.

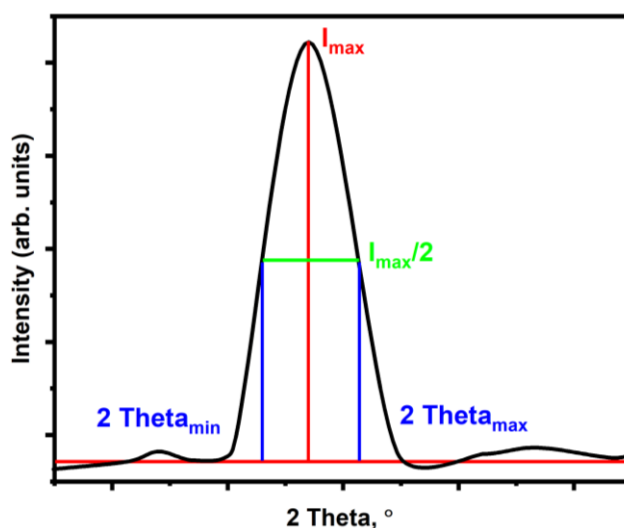


Figure 5-3 Diagram to show how the crystallite size is calculated from a PXRD peak.

The average crystallite size of the measured sample is determined by the Scherrer equation using the measured PXRD and a full width at half maximum (FWHM) fit, as shown in Figure 5-3. R-factors and χ^2 values are used to determine the fit of the data. The R^2 proportion should preferably be more than 97%. When R^2 is less than 97%, the material's anisotropy may be responsible. The crystallite size can easily be determined manually using the Scherrer equation, although Rietveld fitting provides a more precise result.

5.2.2 Scanning Electron Microscopy (SEM)

A concentrated electron beam is used in the analytical technique of Scanning Electron Microscopy (SEM) to scan the sample in a raster pattern. To create an image of the surface morphology of the particles, the electrons that are either scattered or emitted from the sample are detected. A higher magnification than that of an optical

microscope can yield high-resolution images and, depending on the tool and the nature of the material, imaging can even achieve nanoscale resolution. Additionally, the SEM measurements can reveal information about the elemental composition by detecting the secondary and backscattered electrons.

5.2.3 Brunauer-Emmet-Teller (BET) Surface Area Technique

A technique called Brunauer-Emmet-Teller (BET) analysis uses gas adsorption to calculate a material's surface area. It is frequently applied when describing porous materials. The BET technique calculates how much is adsorbed onto the material's surface as a function of gas pressure. The BET equation is then applied to the adsorption isotherm to get the material's surface area.

$$\frac{1}{x\left[\left(\frac{p_0}{p}\right) - 1\right]} = \frac{1}{x_m c} + \frac{c - 1}{x_m c} \left(\frac{p}{p_0}\right) \quad (\text{Eq. 33})$$

Where x is the adsorbed gas quantity, p_0 is the saturation pressure of adsorbate, p is the equilibrium pressure of adsorbate, c is the BET constant $\exp\left(\frac{E_1 - E_L}{RT}\right)$, E_1 is the heat of adsorption for the first layer and E_L is the heat of vaporisation. From x_m the total surface area of the sample material and the specific surface area of the sample can be calculated.^[79]

5.2.4 Infrared Spectroscopy (IR)

By observing the bonds' absorption or transmission of infrared light, infrared spectroscopy (IR), which examines the vibrational modes of substances is a valuable tool. The vibrational modes of the substance in the sample are characterised by the absorption bands in an IR spectrum. The usual range for IR spectroscopy absorption measurements is 400 cm^{-1} to 4000 cm^{-1} .

5.2.5 Raman Spectroscopy

In Raman spectroscopy a sample scatters monochromatic laser radiation inelastically. This means the difference between the energy of the exciting line and the scattered peaks correspond to the frequency of the vibrational modes. Because the symmetry selection rules for Raman spectroscopy differ from those for Infrared, it is possible to identify symmetric vibrations. Raman has a wider spectral range than IR, measuring scattered light between 50 cm^{-1} and 4000 cm^{-1} .

5.2.6 X-ray Absorption Spectroscopy (XAS)

To learn more about an atom's local surroundings, scientists use X-ray absorption spectroscopy (XAS), an element-specific measurement. A sample is exposed to a high frequency X-ray beam, and the energy dependence of the X-ray absorption is determined. X-ray Absorption Near Edge Structure (XANES) and extended X-ray Absorption Fine Structure (EXAFS) are the two useful regions of the XAS.

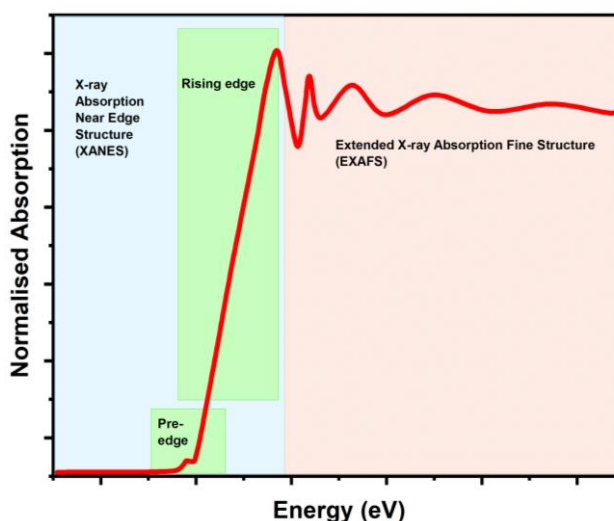


Figure 5-4 X-ray energy absorption spectra showing the pre-edge, XANES, and EXAFS regions.

1. XANES – The X-ray energy is scanned close to the sample's absorption edge. The electron is excited from the core-shell to an excited state at this energy. Here, we can learn about the absorbing atom's local geometric and electrical structure as well as its oxidation state or states (which is often a metal).
2. EXAFS – The X-ray energy is scanned past the sample's absorption edge. Information on the local coordination environment, such as the number and distance of nearby atoms, can be obtained at this point.

Synchrotron radiation facilities offer the high intensity X-ray beam necessary for this kind of investigation. Highly collimated X-rays are created when electrons are accelerated close to the speed of light and then steered by magnetic fields within a ring. Different XAS modes, including transmission, fluorescence, and total electron yield, are available.

5.2.7 Nuclear Magnetic Resonance (NMR)

By detecting the interaction of atomic nuclei with radiofrequency radiation within a magnetic field, it is possible to draw structural conclusions about substances. The magnetic field and atomic nuclei align. The sample receives a radiofrequency pulse that causes the nuclei to spin and produce a signal. The chemical surroundings of the nuclei can be identified by analysis of the frequency and intensity of the signal.

5.2.8 Thermogravimetric/Differential Thermal Analysis (TGA/DTA)

These analytical methods are utilized to investigate the thermally induced changes on heated materials, such as thermogravimetric analysis (TGA) and differential thermal analysis (DTA).

DTA measures the flow of energy into or out of the sample as a function of temperature. TGA measures the change in mass of the sample with temperature. These are usually carried out simultaneously to provide a picture of the overall stability of a substance and to identify its decomposition products.

5.2.9 Vibrating Sample Magnetometer (VSM)

To gauge a sample's magnetic characteristics, a vibrating sample magnetometer (VSM) is utilized. A pick-up coil is placed close to the sample in order to measure its magnetism. The magnetization of the sample changes as the magnetic field is adjusted, and the pick-up coil notices this change. Depending on the magnetic field intensity, the resulting signal is amplified and recorded. The VSM can also be used to investigate how materials' magnetic properties change with temperature. The sample is placed in a temperature-controlled setting, and the magnetization is then measured in relation to temperature. This method, often referred to as temperature-dependent magnetometry, can reveal details about a material's magnetic phase transitions and critical temperatures. A VSM can evaluate hysteresis loops, magnetic anisotropy, magnetic field sweep speeds, magnetic domain imaging, and the characteristics of magnetic nanoparticles.

5.2.10 Galvanostatic Charge-Discharge Cycling (GCD)

A measurement of charge/discharge capacity against voltage at constant currents is called galvanostatic cycling (GC). Specific capacity is expressed in mAh g^{-1} units. The cell is compelled to receive an ongoing current. As the upper and lower ranges of the potential window are reached, a voltage range is selected, and the selected current is driven through the cell to trigger electrochemical processes. This procedure is typically done numerous times to get many cycles. The chronopotentiogram is processed to create a plot of capacity vs. potential, which can be used to investigate the electrochemistry of the cell.

Rate capability tests are carried out on the cells to observe the effect of changing current densities on the overall performance of the cell. The range of current densities are calculated according to the mass of the active material. To have a portable device

with a high-performance battery, the ability to charge faster when required without detrimental effect to the electrode is an essential property. The current applied during cycling is changed to observe if speeding up intercalation/conversion processes causes immense degradation to the electrode.

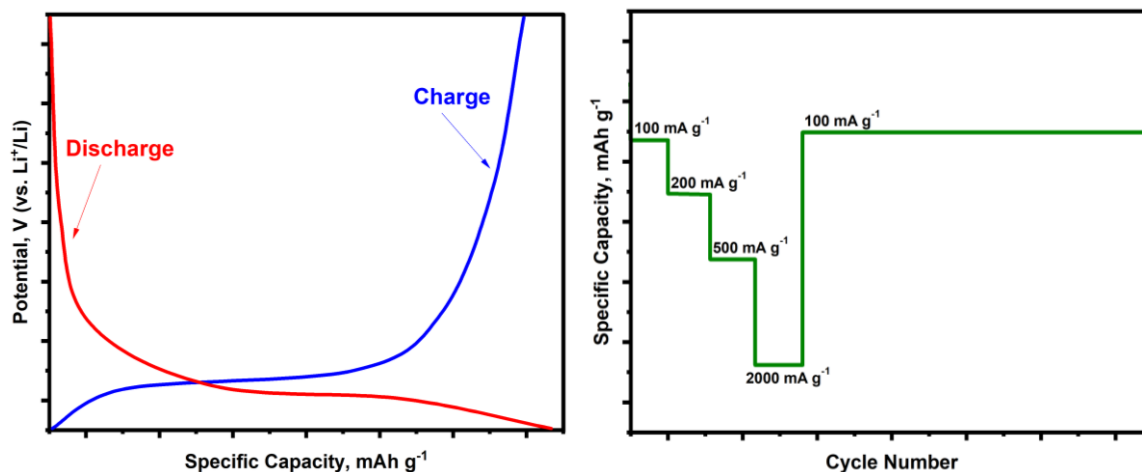


Figure 5-5 Example of a galvanostatic charge-discharge curve for a half-cell (left) and an example of a rate capability plot (right).

High rate-capability without capacity fading is a crucial requirement for future electrodes. Rate capability uses different current densities (mA g^{-1}) to describe the rate of charge-discharge in relation to the capacity.

5.2.11 Cyclic Voltammetry (CV)

When scanning across a voltage window in a range where the electrode and electrolyte are stable, the cyclic voltammetry (CV) method is employed to analyse the change in current. It is possible to observe redox couples that either support or contradict the idea that the substance is reversible. It can offer details on the kinetic or thermodynamic processes, the stability of electrochemistry, and the general functionality of materials.

In a typical solution state experiment, a working electrode (WE), a reference electrode (RE), and a counter-electrode (CE) are immersed in an electrolyte solution. The active substance is cast on the surface of the working electrode or dissolved in the electrolyte. The electrochemical reaction takes place at the WE, while the RE provides a stable voltage to allow for a comparison, and the CE offers a surface for the flow of the charge.

As seen in Figure 5-6, the CV exhibits peaks and troughs that match the electrochemical events taking place. These have shapes that reveal a lot about the kinetics and thermodynamics that are taking place in the experiment. The peak's

location indicates the reaction's potential, and its shape offers data relating to the reaction's pace.

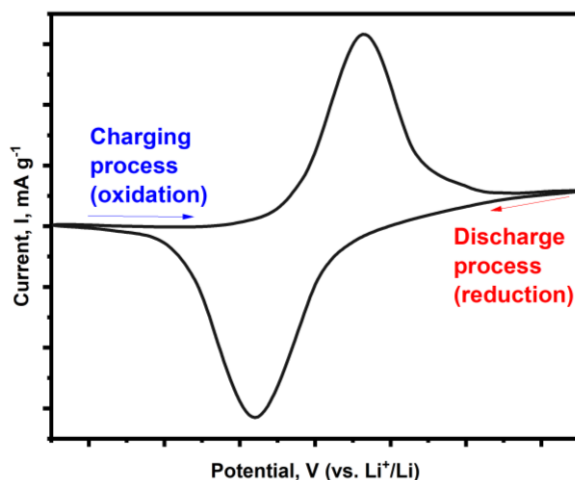


Figure 5-6 Diagram showing a typical sweep using cyclic voltammetry.

The curve's shape demonstrates the impact of altering the measurement's scan rate.

- a) Slow scan rates: Typically, the CV plot has distinct oxidation and reduction peaks which are wide and symmetrical. This is because the electrochemical reactions have time to establish equilibrium at each potential before the potential is changed. Peak currents, according to the Randles-Sevcik equation, are inversely proportional to the square root of the scan rate and depend on the concentration and diffusion coefficient of the species participating in the electrochemical reaction.
- b) Fast scan rates: As the scan rate increases, the CV becomes more distorted and has fewer clear peaks and troughs. This is because the electrochemical reactions are irreversible and are subject to kinetic constraints as a result of the potential changes that do not give them enough time to reach equilibrium.

6 Polymorphism of MnO₂ Nanoparticles Induced by the Addition of Lanthanides

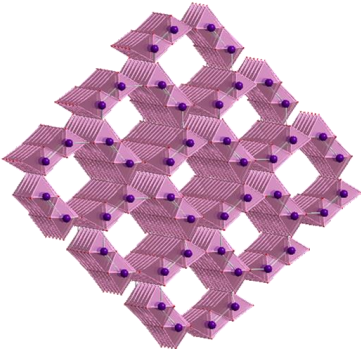
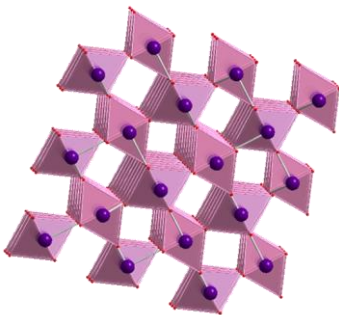
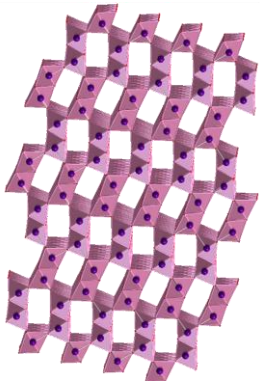
Manganese oxides (Mn_xO_y) exist in over 30 distinct forms, which can be difficult to distinguish. Manganese oxides, due to their heat sensitivity, can shift into additional phases or form mixed phases when subjected to higher temperatures, changing heating rates, or calcination conditions. Manganese oxides can absorb water and generate hydrated forms of their oxides.^[80]

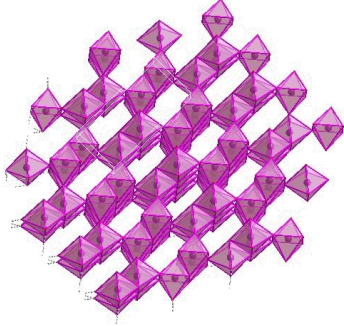
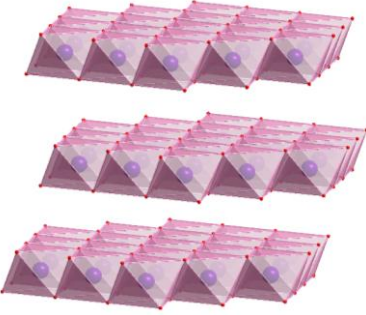
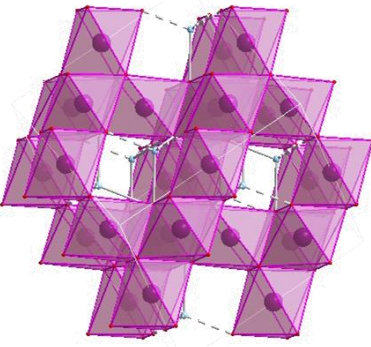
6.1 Manganese Dioxides

Manganese dioxide (MnO₂) is a competitive battery material and one of the most researched active electrode materials due to its high theoretical capacity and low toxicity. Along with the high natural abundance, its powerful reduction potentials, polymorphic crystal structures and tuneable nanomorphology make it suitable as an electrode material.^[81] Pyrolusite β-MnO₂ is the most abundant naturally occurring form, while hollandite α-MnO₂ is the most frequently researched manganese-containing battery cathode material. This is due to its porous structure with channels of 4.6 Å diameter, providing a large area for intercalation.^[82] Nevertheless, it suffers from high capacity loss and degradation during lithiation and delithiation, since the large tunnel structure becomes structurally unstable. However, depending on the type of preparation, other MnO₂ polymorphs can show high capacity, high stability, and minimal degradation leading to increased performance. Manganese dioxide and/or its composite materials are predominantly used as cathode materials in the battery industry and can be classified based on their origin: natural manganese dioxide (NMD), chemical manganese dioxide (CMD), and notably electrolytic manganese dioxide (EMD) in alkaline-manganese dioxide batteries. The manganese dioxide and composites presented here are produced using CMD methods.

In common with α- and β-MnO₂ discussed above, MnO₂-based phases are composed of corner-sharing and/or edge-sharing octahedral MnO₆ subunits as shown previously in Figure 2-31, and described below in Table 3. Mn_xO_y phases containing Mn^{III} can undergo Jahn-Teller distortion of the octahedral geometry about the Mn.

Table 3 Table of MnO₂ Polymorphs: This table provides the mineral name, phase, space group, structure, a brief description on each of the most common polymorphs of MnO₂ that are relevant to this thesis, and their thermal stabilities.

Name (Phase), Space group Axis Model	Crystal Structure	Description of packing, arrangements, and bonds.	Thermal stability under N ₂ ^[83]
Hollandite (α), I4/m Viewed down the c-axis		Hollandite MnO ₂ is a tunnelled structure which is formed of corner- and edge-sharing MnO ₆ octahedra forming 2x2 tunnels across the c-axis. This phase crystallises in the tetragonal space group I4/m with unit cell parameters $a, b = 9.785 \text{ \AA}$ and $c = 2.863 \text{ \AA}$.	Similar thermal behaviour to β -MnO ₂ , converts to Mn ₂ O ₃ above 500 °C
Pyrolusite (β), P4 ₂ /mnm Viewed down the c-axis		Pyrolusite MnO ₂ is composed of corner-sharing MnO ₆ octahedra. The corner-shared octahedral tilt angles are 50°. This 1x1 rutile structure crystallises in the tetragonal space group P4 ₂ /mnm with unit cell parameters $a, b = 4.38 \text{ \AA}$ and $c = 2.85 \text{ \AA}$	Stable up to 500 °C before O ₂ release converts to Mn ₂ O ₃
Ramsdellite (R), Viewed down the a-axis		Ramsdellite MnO ₂ is formed of edge-sharing 2x2 MnO ₆ octahedra connected by corner sharing 2 x 1 MnO ₆ octahedra to form sheet-like structures and crystallises in the orthorhombic space group Pnma with unit cell parameters $a = 9.273 \text{ \AA}$, $b = 2.866 \text{ \AA}$, and $c = 4.533 \text{ \AA}$.	-

<p>γ-MnO₂ C2/m</p> <p>Viewed down the c-axis</p>		<p>Intergrowth MnO₂ has a hybrid structure composed of R-MnO₂ and β-MnO₂. Like other polymorphs of this oxide, it is built of edge and corner shared MnO₆ polyhedra. This hybrid 1x1 and 2x1 structure crystallises in the space group C2/m.</p>	<p>Structure relaxation after 400 °C and converts to β-MnO₂</p>
<p>Birnessite (δ), R$\bar{3}m$</p> <p>Showing the layered structure</p>		<p>Birnessite MnO₂, in contrast to the other polymorphs is a layered structure composed of edge shared MnO₆ octahedra to form 2D flat planes. This multi-layered composition has adaptable interlayer spacing. This MnO₂ crystallises in the monoclinic space group R$\bar{3}m$ with unit cell parameters $a = 5.174 \text{ \AA}$, $b = 2.850 \text{ \AA}$, and $c = 7.336 \text{ \AA}$.</p>	<p>Easily destabilised layers below 200 °C, individual layers thermally stable up to 500 °C</p>
<p>Spinel (λ), Fd$\bar{3}m$</p> <p>Showing the spinel structure</p>		<p>Spinel MnO₂ forms 3D tunnel microstructure with edge and corner shared MnO₆ polyhedra. The octahedral sites are occupied by Mn^{IV}, while corner-sharing MnO₄ tetrahedra contain Mn^{III}. This polymorph crystallises in the cubic space group Fd$\bar{3}m$ with lattice constants equal to 8.03 Å.</p>	<p>Thermally unstable and converts to β-MnO₂ at 250 °C, and subsequently to Mn₂O₃</p>

A study conducted by Hatakeyama et al reported the thermal stability of these phases shown in Table 3 and Figure 6-1.^[83] Another study by Kitchaev et al examined the effects of alkali-metal insertion, protonation, and hydration on the thermodynamics towards formation of different phases of MnO₂.^[84]

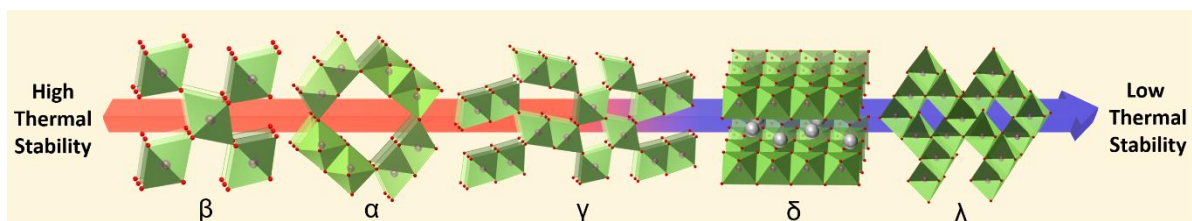


Figure 6-1 Diagram to show the direction of thermal stability of the MnO₂ polymorphs. Adapted from Hatakeyama et al.^[83]

Figure 6-2 shows the α -MnO₂, β -MnO₂, and t-MnO₂ tunnel structures with the size of the tunnels indicated below the picture. The α - and t- structures show how the tunnels

can be occupied by cations. Cations like K^+ or Na^+ are frequently used to stabilize layered formations like birnessite as well as tunnel structures like cryptomelane, hollandite, and todorokite.

Although other phases of MnO_2 exist, the phases mentioned in Table 3 are the most common phases cited in the battery literature and include some of the most readily obtained phases using general MnO_2 preparation methods. These structures can also exist with cations occupying the channel, with some of the Mn^{IV} reducing to Mn^{III} to maintain charge balance.^[85] Examples are shown in Figure 6-2 and Table 4.

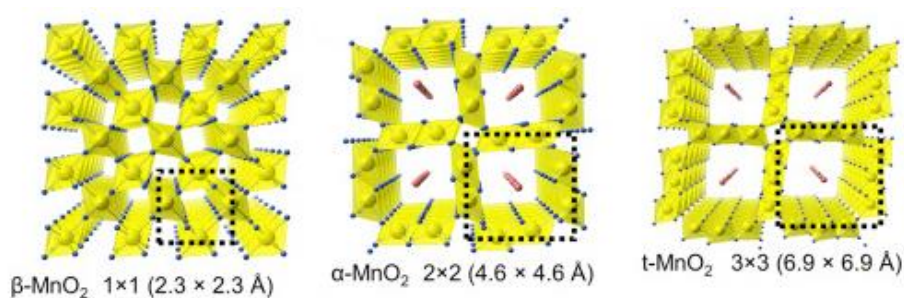


Figure 6-2 α , β , and t channel structures of MnO_2 polymorphs. Each image from left to right shows the perimeter of the tunnels. Extracted from Yuan et.al.^[86]

Figure 6-2 shows how cryptomelane, which is the $\alpha\text{-MnO}_2$ structure, has its channels occupied by K^+ ions. The todorokite structure, which is the 3x3 structure, is stabilised by the presence of cations such as K^+ , Na^+ or Ca^{2+} .

Table 4 Examples of natural Mn_xO_y minerals and their chemical formulae. Extracted from Bernardini et al.^[87]

Mineral	Ideal crystal-chemical formula
Birnessite	$(Na,Ca)(Mn^{IV},Mn^{III})_2O_4 \cdot 1.5H_2O$
Chalcophanite	$(Zn,Fe,Mn^{II})Mn^{IV}_3O_7 \cdot 3H_2O$
Cryptomelane	$(K,Na)(Mn^{IV},Mn^{III})_8O_{16}$
Hausmannite	$Mn^{II}Mn^{III}_2O_4$
Hollandite	$Ba(Mn^{IV}_6,Mn^{III}_2)O_{16}$
Lithiophorite	$LiAl_2(Mn^{IV}_2,Mn^{II})O_6(OH)_6$
Manganite	$\gamma\text{-Mn}^{III}O(OH)$
Manganosite	$Mn^{II}O$
Pyrolusite	$\beta\text{-Mn}^{IV}O_2$
Todorokite	$(Ca,Na,K)(Mn^{IV},Mn^{III})_6O_{12} \cdot nH_2O$

6.2 MnO₂ Nanoparticles (MnO₂-NP)

The materials were created by mechanically grinding 0.5 g of commercially available MnO₂ for 6 hours at 150 rpm in a ball mill. The powder was transferred to a Teflon-lined stainless-steel autoclave with the addition of 10 ml 12M NaOH, followed by hydrothermal treatment at 120 °C. The resulting sample was cooled, washed thoroughly with water and dilute HCl and dried in an oven at 80 °C for 12 hours. Part of the resulting MnO₂-Hydro was taken for analysis before calcining the remainder at 800 °C for 4 hours to form MnO₂-NP. [88, 89] The electrodes were prepared using an 80:10:10 ratio of MnO₂-NP, sodium alginate (Na-Alg), and Super-P, respectively, with LP30 as the electrolyte. Whatmann glass wool fibre was used as the separator, and Li-metal foil was used as the counter-electrode.

The same techniques were used to create lanthanide-containing samples. In the first step (ball milling), lanthanide oxide at a concentration of 5 mol% relative to the MnO₂ was added.

6.2.1 Phase and Morphological Analysis

A diffraction pattern was measured for commercial MnO₂ (Figure 6-3, black line). It shows that it is largely amorphous in nature. There are a few weak and very broad features, and the high baseline below 20°-25° is an additional indication of amorphous character.

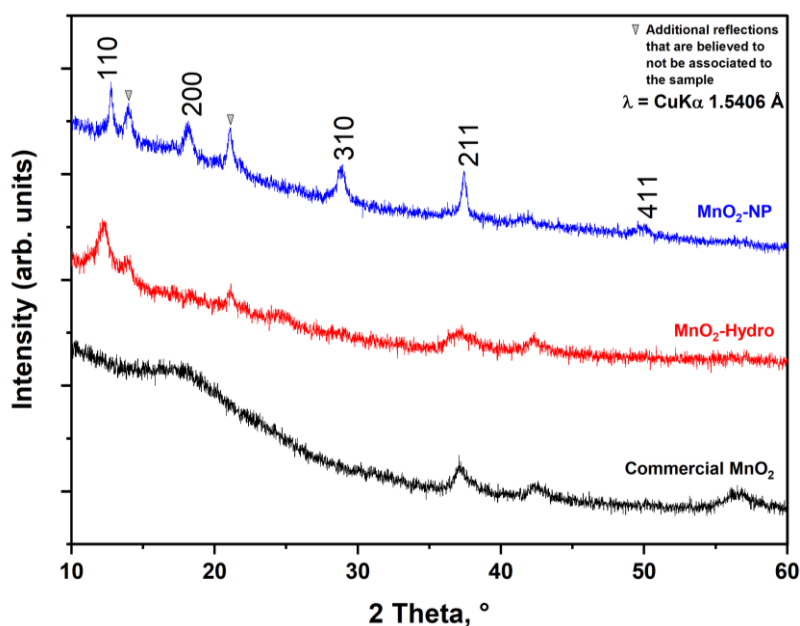


Figure 6-3 XRD patterns of commercial MnO₂ (black), post hydrothermal treatment MnO₂-Hydro (red) and post pyrolysis MnO₂-NP (blue). The hkl indices label the reflections of α -MnO₂.

A diffraction pattern was obtained from the sample after hydrothermal synthesis, labelled MnO₂-Hydro (Figure 6-3, red line). This shows some broad peaks corresponding to reflections from α -MnO₂ between 10° and 25°, indicating the presence of this phase, but with poor crystal quality and/or nanoscale crystallite size.^[90] The diffraction pattern taken after pyrolysis of MnO₂-Hydro to MnO₂-NP (Figure 6-3, blue line), shows that the MnO₂ obtained is now has better crystallinity. There are clear peaks at approximately 13°, 18°, 29°, 38° and 51°, which correspond to hkl indices of 110, 200, 310, 211, and 411 for α -MnO₂. Additional weak peaks at 13.8° and 21.1° labelled with a triangle, are probably the result of instrumental artefacts. Synchrotron in-situ PXRD studies shown below in Figure 6-4 further confirmed that the additional reflections were not related to the sample. They also confirm the phase purity of the α -MnO₂.

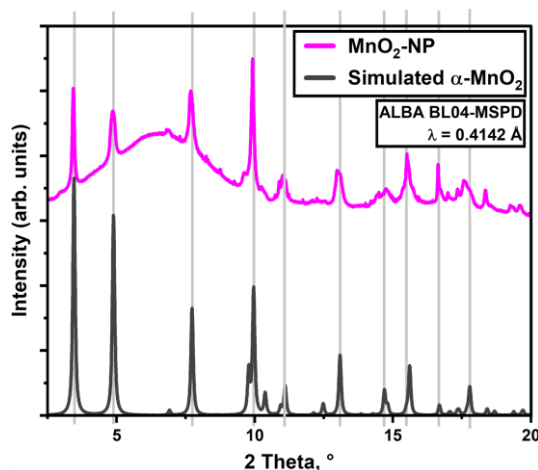


Figure 6-4 MnO₂-NP measured at ALBA beamline BL04, with X-ray wavelength of 0.4142 Å. The pattern shows the synchrotron data of MnO₂-NP compared with the model pattern for α -MnO₂ at the same wavelength. The model used is ICSD 20227.

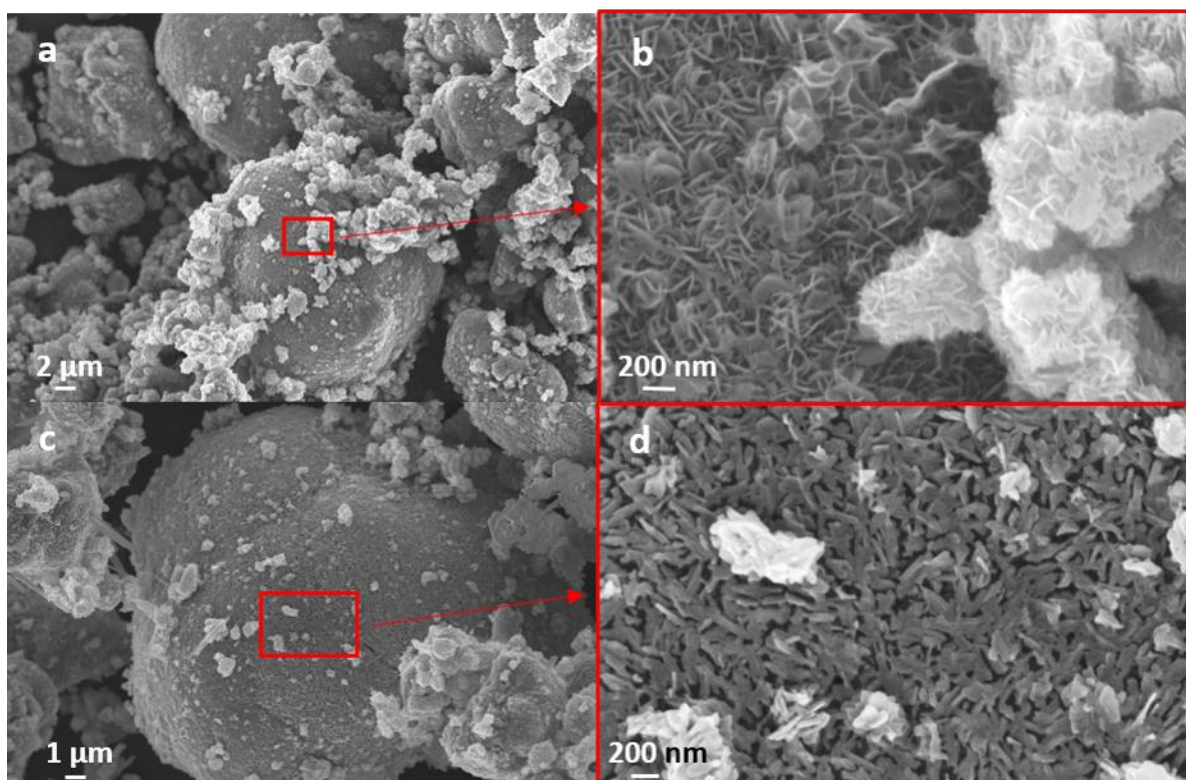


Figure 6-5 SEM images of (a,b) MnO₂-Hydro at scale bars of 2 μm and 200 nm (x10 mag), and (c,d) MnO₂-NP at scale bars of 1 μm and 200 nm (x20 mag).

As shown in the PXRD in Figure 6-3, pyrolysis increases the crystallinity which is confirmed by the presence of sharper reflections. The SEM images of MnO₂-Hydro and MnO₂-NP in Figure 6-5 shows the morphological nature of these materials. MnO₂-Hydro is made up of spherical particles with diameters between 15 and 25 μm, each of which is an agglomerate of nanosheets, as shown in Figure 6-5 a and b. The majority of the sheets are ≤ 300 nm in size. Figure 6-5 c and d show the morphology of the MnO₂-NP, which is now composed of nanorods that are uniformly sized, with lengths between 200 and 300 nm, and are tightly packed. The nanosheets have restructured into nanorods during the pyrolysis at 600 °C while maintaining the bulk spherical particle shape. Such MnO₂ nanorods have been frequently reported as the resulting morphology of α-MnO₂ after calcination.^[89, 91]

6.2.2 Electrochemical Analysis in a Li-ion Coin Cell

MnO₂-NP was analysed electrochemically by cycling in a Li-ion coin cell. From the cyclic voltammetry (CV) curves in Figure 6-6, when the scan rate increases from 0.1 mV s⁻¹ to 15 mV s⁻¹, an increase in resistance is observed for the cell which is shown by the increasing current.

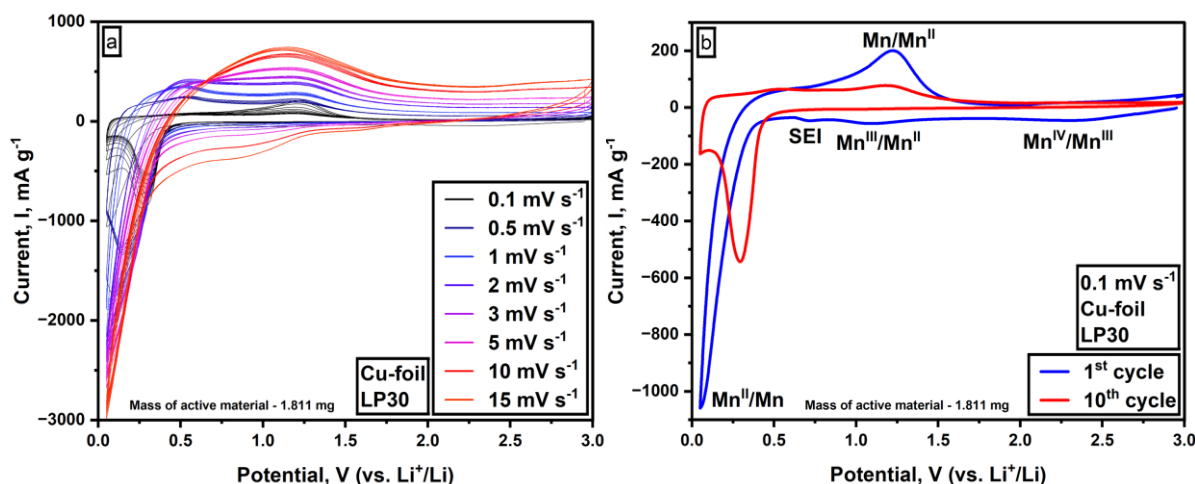
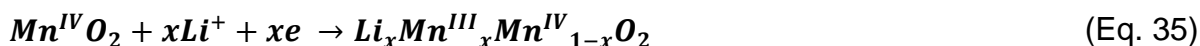


Figure 6-6 a) Cyclic voltammograms of MnO₂-NP collected over eight scan rates: 0.1 mV s⁻¹, 0.5 mV s⁻¹, 1 mV s⁻¹, 2 mV s⁻¹, 3 mV s⁻¹, 5 mV s⁻¹, 10 mV s⁻¹ and 15 mV s⁻¹ b) 1st and 10th cycle measured of MnO₂-NP at 0.1 mV s⁻¹.

At 0.1 mV s⁻¹ there is a well-defined oxidation at 1.23 V and a reduction profile at 0.26 V, which are usual for manganese oxide electrodes. The intercalation process that takes in this cell would follow the following electrochemical pathway:



As shown in Eq. 33 and Eq. 34, the Mn^{IV} is reduced to Mn^{III} as the lithium ion intercalates into the crystal lattice.

Increasing the scan rate to 0.5 mV s⁻¹, results in two different oxidation processes with potentials at 1.23 V and 0.53 V. The scan rates that follow at 1 mV s⁻¹, 2 mV s⁻¹, and 3 mV s⁻¹, all show two oxidation steps which gradually become less discrete. These oxidations are probably a result of step-by-step phase transitions. As a result of the scan rate being increased from 5 mV s⁻¹ to 15 mV s⁻¹ onwards, the kinetic pathway dominates causing the oxidation to shift from the nominal potential. The absence of clear reduction potentials associated with the reduction processes is a result of the kinetic pathway shifting the reduction potentials further to the left at higher scan rates. Likewise, the semi-reversible processes associated with Li⁺ intercalation show the gradual shift of the oxidation peaks to higher potentials due to an increasing over-potential.

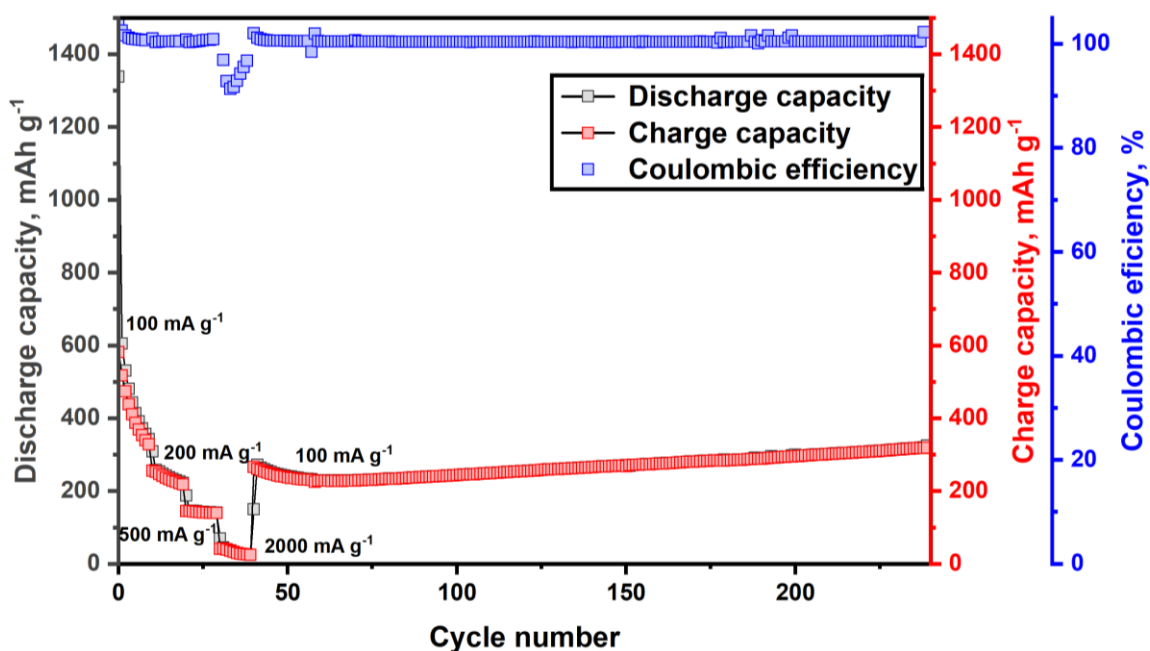


Figure 6-7 Specific discharge capacity, specific charge capacity and coulombic efficiency (CE) vs. cycle number for MnO₂-NP. Rate capability steps of MnO₂-NP measured at 100 mA g⁻¹, 200 mA g⁻¹, 500 mA g⁻¹, and 2000 mA g⁻¹ for 10 cycles each. The rate was then returned to 100 mA g⁻¹ for the remaining 200 cycles.

The rate capability data in Figure 6-7 show that there is a charge/discharge efficiency of >95% for most cycles including the rate capability steps (besides 2000 mA g⁻¹). Some cycles have efficiencies apparently over 100%, which results from incomplete charging.

The specific capacity measured at the first charge density of 100 mA g⁻¹, has a capacity of 1338 mAh g⁻¹ during the initial discharge. This falls to 604 mAh g⁻¹ after the 1st cycle, and by the 10th cycle the capacity reached is 327 mAh g⁻¹. From the 11th to the 20th cycle at a charge density of 200 mA g⁻¹, there is capacity loss from 255 mAh g⁻¹ to 218 mAh g⁻¹ respectively. At 500 mA g⁻¹ the capacity remains relatively consistent between 145 mAh g⁻¹ and 139 mAh g⁻¹ between the 21st and 30th cycles. The capacity loss at 2000 mA g⁻¹ for cycles 31 through 40 ranges between 41 mAh g⁻¹ to 25 mAh g⁻¹ respectively. At cycle 41 the charge density returns to 100 mA g⁻¹ and the capacity measured in 271 mAh g⁻¹. For the remaining 200 cycles, there is a gradual capacity loss to 227 mAh g⁻¹ by the 60th cycle before increasing until it reaches 325 mAh g⁻¹ by the 240th cycle.

α -MnO₂ electrodes have been reported with a reversible capacity of 512 mAh g⁻¹ at a current density of 800 mA g⁻¹ after 300 cycles, and when measured at 200 mA g⁻¹ able to retain a capacity of 618 mAh g⁻¹ after 300 cycles.^[92] MnO₂-NP reaches a capacity of 325 after 240 cycles at 100 mA g⁻¹. The capacity fades slightly before

increasing again during the last 200 cycles, suggesting that the capacity could increase further as the cycle numbers increase during longer-term cycling. The instability observed for the capacity is due to structural or morphological changes occurring at the electrode during cycling since MnO_2 materials are readily polymorphic. MnO_2 -NP coin cells are currently undergoing galvanostatic testing for 1000 cycles per individual scan rate.

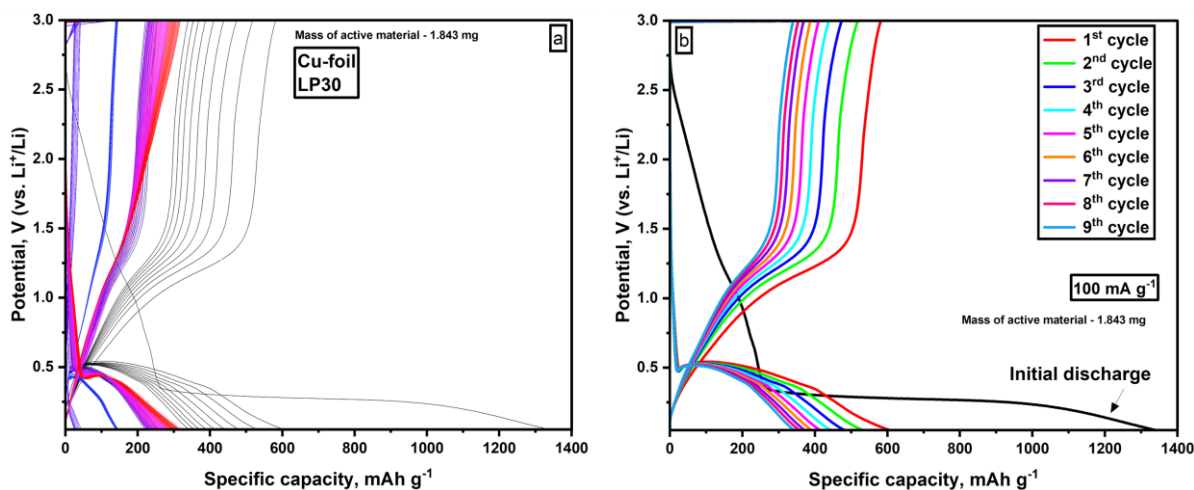


Figure 6-8 a) specific capacity of MnO_2 -NP showing the 240 cycles measured showing the individual current densities at 100 mA g^{-1} , 200 mA g^{-1} , 500 mA g^{-1} , and 2000 mA g^{-1} for 10 cycles each before returning to 100 mA g^{-1} for the remaining 200 cycles. b) a closer look at the first 10 cycles measured at 100 mA g^{-1} .

The discharge profiles for MnO_2 -NP shown in Figure 6-8, display voltage plateaus at the redox potentials of the active material. At lower charge/discharge rates, the plateaus appear to overlap, showing there is partial phase transformation. At higher current densities of 500 mA g^{-1} and 2000 mA g^{-1} , the time during the charge/discharge processes are not long enough to allow complete intercalation/de-intercalation of Li^+ into the MnO_2 -NP active material. Since the charge/discharge states are mostly due to the cell becoming polarised, the plateaus become less distinguishable.

6.3 $\text{MnO}_2 + 5 \text{ mol\% Y}_2\text{O}_3, 5 \text{ mol\% CeO}_2, 5 \text{ mol\% Dy}_2\text{O}_3, \text{ and } 5 \text{ mol\% Yb}_2\text{O}_3$

Ln-containing MnO_2 Nanoparticles

By introducing impurities (or composites) into an oxide material, the changes in phase selection or different morphologies can be explored electrochemically. Dopants are a modification on the grain boundary lattice, keeping the chemistry of the grain boundary the same while changing the physical properties. Alternatively, additives substantially alter the behaviour of the grain boundaries. The former is typically introduced in quantities less than 100 ppm while the latter is usually the introduction of a compound at more than 100 ppm.

Despite being called the rare-earth metals, 4f-elements, termed lanthanides, are found in abundance in the earth's crust. Even the rarest of lanthanides are more abundant than precious metals. Rechargeable nickel metal hydride batteries (NiMH) use a mixture of lanthanide mixed metal hydrides such as lanthanum, cerium, and neodymium. Cell phones such as the iPhone use lanthanum to visually enhance screen colours, together with neodymium and dysprosium without which our phones would not vibrate. Introducing lanthanides into MnO_2 , in quantities larger than doping, makes for an interesting study on the physical properties they are capable of inducing. Although composites using all lanthanides were prepared, only yttrium, cerium, dysprosium, and ytterbium were studied.

Y^{III} is considered an honorary lanthanide. Due to its size its situated between Ho^{III} and Er^{III} .^[93, 94] Ce^{IV} can exhibit both oxidative and reductive properties arising from either the loss of oxygen or through electron transfer.^[95] Due to the large radius associated to the 4f elements, and the quick transfer between Ce^{III} and Ce^{IV} , Dy^{III} has been notably researched for its magnetic properties due to its oblate symmetry and 15/2 ground state.^[96] Yb_2O_3 has been reported to improve electrochemical performance in doping quantities of a LiFePO_4 cathode like that reported by Göktepe.^[97]

Adding these lanthanides into MnO_2 nanoparticles and preparing the samples under a basic hydrothermal synthesis, creates the ability to change their properties by transforming them into additional phases and/or morphologies.^[81, 98, 99] The stacked

PXRD patterns shown in Figure 6-9 provide a brief overview of the effect of the addition of lanthanide oxides on MnO₂-NP.

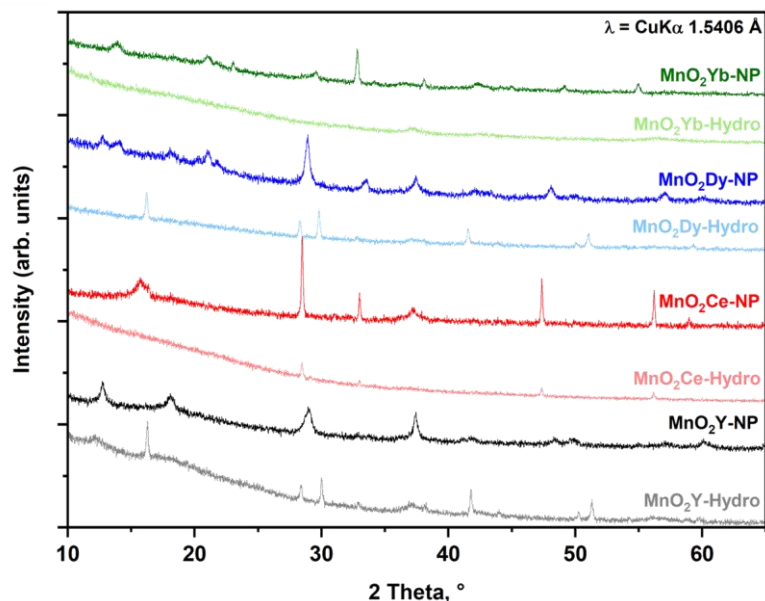


Figure 6-9 Stacked PXRD patterns of 5 mol% of Ln containing samples. MnO₂Ln-Hydro refers to samples after hydrothermal treatment. MnO₂Ln-NP refers to samples after pyrolysis (where Ln = Y, Ce, Dy, or Yb).

Looking at the phases observed for each of the samples prepared, the polymorphism of MnO₂ is dependent on the lanthanides used during synthesis. Figure 6-10 briefly assigns the main phases observed for the pyrolysed materials.

Figure 6-9 and Figure 6-10 shows how the addition of 5 mol% -Y, -Ce, -Dy, and -Yb drastically change the structural form of commercial MnO₂ when calcined. Though the effects of doping electrodes with lanthanides has been abundantly reported for different ESSs, research on the effects of lanthanide addition to intentionally observe their effects on phases and morphologies are less available.^[72, 73] The induced polymorphism is discussed individually for each material in further details over the coming sections. An additional point to note is that MnO₂ polymorphs have their ideal ranges of thermal stability, and it is unusual to have a range of multiple phase combinations present for the same processing conditions.

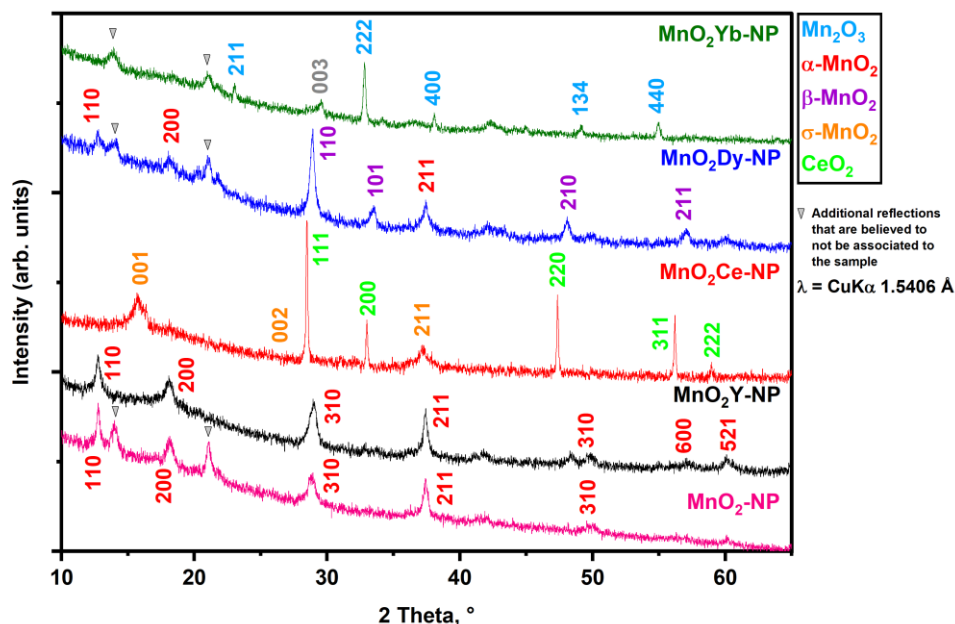


Figure 6-10 Stacked PXRD of pyrolysed MnO_2 materials: MnO_2 -NP, MnO_2 Y-NP, MnO_2 Ce-NP, MnO_2 Dy-NP, and MnO_2 Yb-NP. The hkl indices of polymorph α -phase is labelled in red, β - in purple, σ - in orange, and Mn_2O_3 in blue. Grey triangles show reflections which are a result of instrument error.

Manganese dioxides and their composites can have many different morphologies depending on the preparation methods applied to obtain them. By employing certain procedures, the morphology and purity can be controlled.^[100] Nanorods^[101], nanowires^[102, 103], nanotubes^[98, 104], nanoflowers^[105, 106], nanosheets^[107], nanospheres and nanourchins^[108] are a few examples amongst many other types reported in literature.

Briefly looking at an array of SEM of the compounds, the presence of different phases and phase changes (pre- and post-pyrolysis as seen in the PXRD) correlate to the many morphological changes observed, which are shown in Figure 6-11 below. In-depth analysis of the SEM images with the phase analysis are carried out with each individual material in the forthcoming sections. Furthermore, the Scherrer crystallite size is calculated to account for the average crystallite size in each sample.

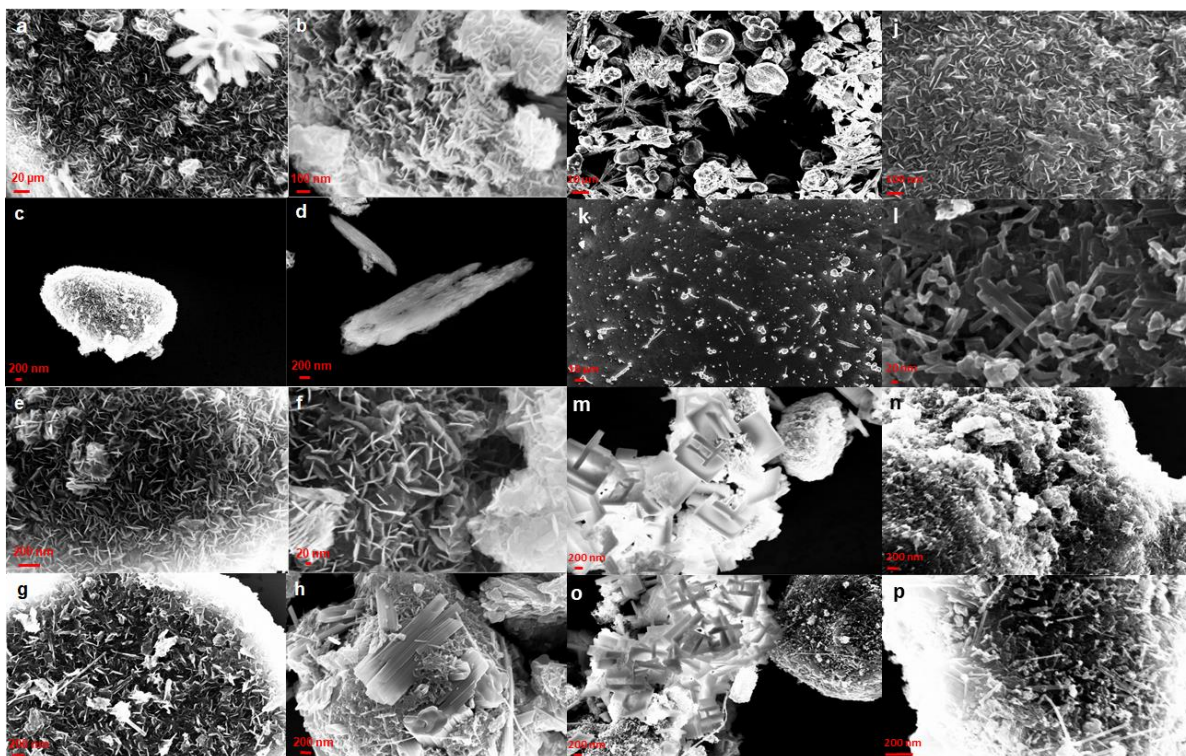


Figure 6-11 SEM images with scale bars a,b) MnO₂Y-Hydro (20 μm, 100 nm) c,d) MnO₂Y-NP (200 nm, 200 nm) e,f) MnO₂Ce-Hydro (200 nm, 20 nm) g,h) MnO₂Ce-NP (200 nm, 200 nm) i,j) MnO₂Dy-Hydro (10 μm, 100 nm) k,l) MnO₂Dy-NP (10 μm, 200 nm) m,n) MnO₂Yb-Hydro (200 nm, 200 nm) o,p) MnO₂Yb-NP (200 nm, 200 nm).

Infrared spectroscopy was carried out on all nanoparticles (the materials collected after hydrothermal synthesis and the materials collected after pyrolysis).^[109] Only the post pyrolysis samples are shown in Figure 6-12.

By observing the infrared spectra of the additive containing samples, we see:

- Broad absorption bands at 3600 cm⁻¹ correlating to the H-O-H stretching collisions and absorption of -OH groups. These are however not seen in Figure 6-12 as they were only present for 'MnO₂Ln-Hydro' samples which are excluded for clarity.
- Adsorbed water on the surface of the oxides is recorded between 1500 cm⁻¹ and 1700 cm⁻¹ as H₂O bending collisions. Again, only seen for 'MnO₂Ln-Hydro' which were excluded for clarity.
- Looking closer at the fingerprint region between ~400 to ~900 cm⁻¹, shows characteristic Mn-O-Mn stretching collisions. All polymorphs of MnO₂ exhibit slight differences in their absorption bands which are presented in Figure 6-12.

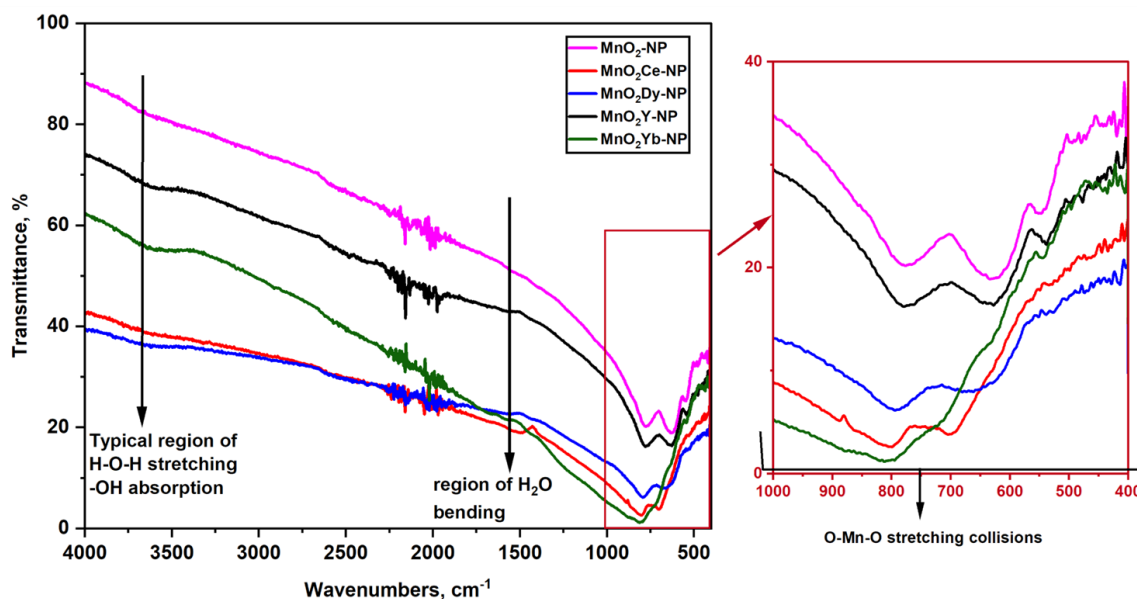


Figure 6-12 Overlapped IR transmission spectra for all 5 mol% Ln samples. Ranges between 400 cm^{-1} to 1000 cm^{-1} represents the MnO_6 octahedral arrangement, 1000 cm^{-1} to 2500 cm^{-1} indicates the Mn-OH interactions and between 3000 cm^{-1} and 4000 cm^{-1} provides information on any constitutional H_2O in MnO_2 . Inset to the right shows the enlarged range between 400 cm^{-1} and 1000 cm^{-1} where characteristic Mn_xO_y bands can be seen.

The characteristic traits that are common for MnO_2 and the possible adsorption of water to make hydrous MnO_2 can be seen in the IR spectrum. Distortion of any MnO_6 octahedra can be explained by the presence of constitutional molecules such as water which can be detected in the FT-IR spectra.^[110] Slight variations in the absorption peaks and positions are related to the variation in crystallographic forms of each polymorph recorded at wavenumbers below 1000 cm^{-1} . Due to the mixed phase nature of these oxides, the IR spectra alone are not informative enough.

The capacity to learn more about the local atomic coordination environments is one of the main benefits of using Raman spectroscopy. When attempting to distinguish between phases in chaotic data, this is helpful. Manganese oxides have been analysed using this method numerous times, and there is a wealth of literature describing the benefits of doing so when attempting to characterize multiple phases.^[111] Raman makes it feasible to distinguish between symmetry changes in the sample, something that is not attainable with IR-only methods.

Due to the variety of phases that can exist in a single sample, studying manganese oxides using conventional techniques like X-ray diffraction is quite difficult. Combining PXRD with IR, Raman, and other techniques confirms the findings because manganese oxides may be “easily” identified in Raman thanks to their characteristic spectra.

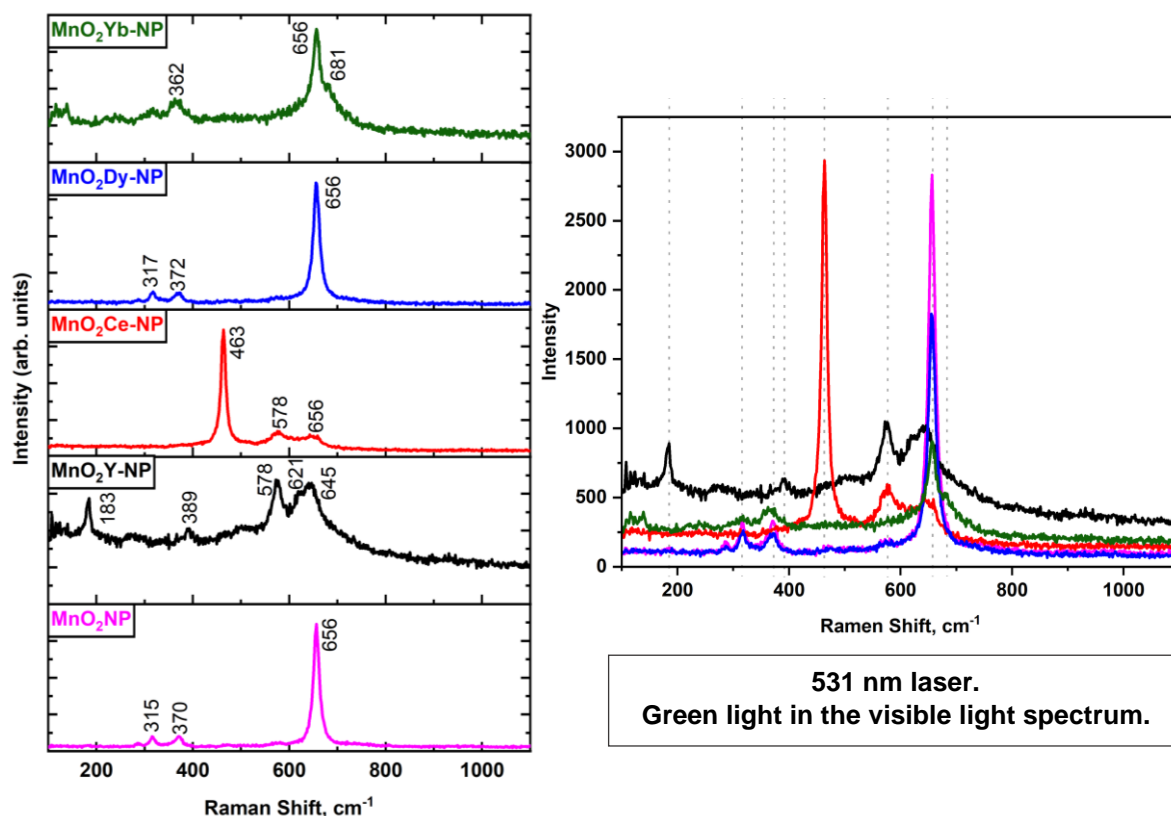


Figure 6-13 Stacked Raman spectra of $\text{MnO}_2\text{-NP}$ and the $\text{MnO}_2\text{Ln-NP}$ composites on the left with assigned wavenumbers. Overlap of the same data on the right. Dotted lines are added for guidance only.

The stacked Raman spectra shown in Figure 6-13 above shows the different characteristic scattering profiles of different phases of MnO_2 .^[87, 111, 112] These phases can be assigned by making literature comparisons. $\text{MnO}_2\text{-NP}$ undergoes scattering with a strong peak at 656 cm^{-1} and two smaller peaks at 315 cm^{-1} and 370 cm^{-1} . This is defined as a $\beta\text{-MnO}_2$ phase. This is further confirmed by the rietveld analysis. $\text{MnO}_2\text{Y-NP}$ has a higher signal to noise ratio; however, characteristic peaks can be easily defined at 645 cm^{-1} , 621 cm^{-1} , 578 cm^{-1} , 389 cm^{-1} and 183 cm^{-1} which correlate to $\alpha\text{-MnO}_2$ as the main phase. $\text{MnO}_2\text{Ce-NP}$ again has a single strong peak at 463 cm^{-1} corresponds to CeO_2 and the two smaller intensity peaks at 578 cm^{-1} and 656 cm^{-1} correspond to $\sigma\text{-MnO}_2$ which matches the XRD patterns obtained. $\text{MnO}_2\text{Dy-NP}$ has reflections like the pristine sample at 656 cm^{-1} , 371 cm^{-1} and 315 cm^{-1} which correlate to $\beta\text{-MnO}_2$. $\text{MnO}_2\text{Yb-NP}$ has a main peak at 656 cm^{-1} , with a small peak shouldering to the right at 681 cm^{-1} . At 362 cm^{-1} there is a broader peak with additional sub structures nearby. These wavenumbers correlate to $\alpha\text{-Mn}_2\text{O}_3$.^[87, 113]

6.3.1 Addition of 5 mol% Y_2O_3 – MnO_2 Y-NP

Although yttrium is not a part of the lanthanide series, it does fall into the rare earth elements category. It has been reported that the addition of yttrium oxide causes mild changes in the performance of lithium-rich cells.^[114]

6.3.1.1 Phase and Morphological Analysis

The diffractogram for MnO_2 Y-Hydro shows two phases present after hydrothermal treatment which are R- MnO_2 and α - MnO_2 . Although R- MnO_2 has sharp peaks suggesting high crystallinity, the baseline shows the amorphousness of α - MnO_2 . After pyrolysis, the oxide crystallises to form MnO_2 Y-NP.

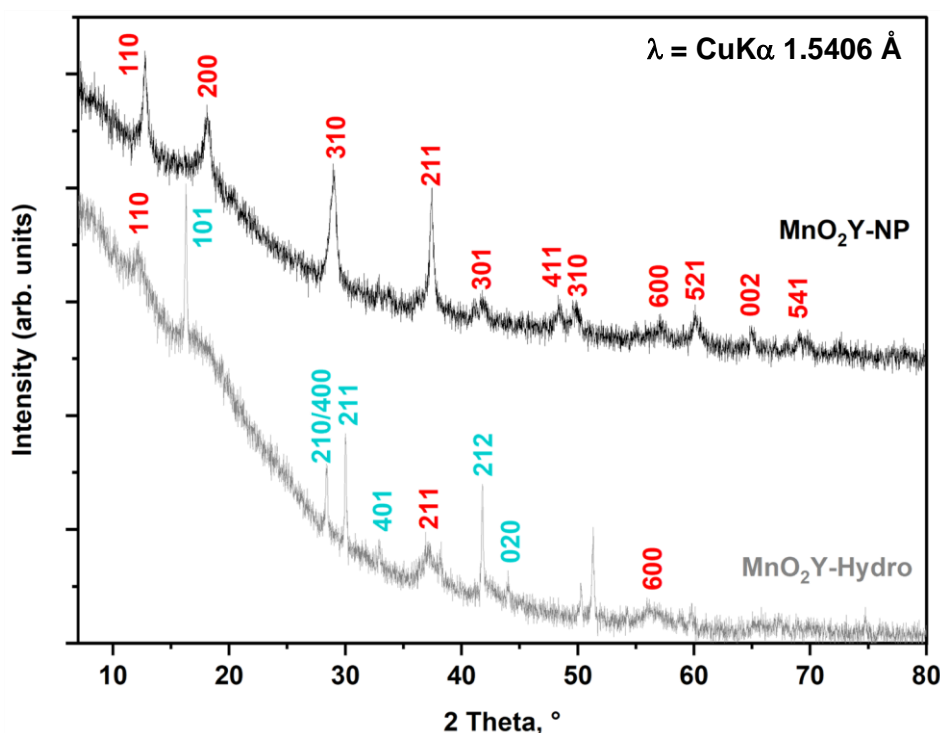


Figure 6-14 Stacked PXRD showing the pattern for the intermediate phases after hydrothermal synthesis MnO_2 Y-Hydro (grey) and the pattern of the final MnO_2 Y-NP after pyrolysis (black). The hkl indices in red indicate indices for α - MnO_2 while the indices represent the presence of R- MnO_2 (turquoise). (α - MnO_2 ICSD 20227, R- MnO_2 ICSD 171866)

MnO_2 Y-Hydro has sharp reflections representing R- MnO_2 (turquoise) which have hkl indices of 111, 210/400, 211, 401, 212 and 020. The broader reflections are from poorly crystalline α - MnO_2 . After pyrolysis to MnO_2 Y-NP, the mixed phases transform to α - MnO_2 . Figure 6-14 assigns the hkl indices for α - MnO_2 as 110, 200, 310, 211, 301, 411, 310, 600, 521 and 541.

The Rietveld analysis shown below in Figure 6-15 confirms the phase assignment for MnO_2 Y-NP to be α - MnO_2 as the major reflections fit the model. By assuming there

was also β - MnO_2 present in the sample, the R_f -factor for α - MnO_2 reduced from 52.9 to 20.11. Because of high baseline activity, not all reflections for α - MnO_2 were visible. However, with a χ^2 of 1.34, the fit agrees with the phase assignment. The analysis carried out in Figure 6-15 was a simple structural analysis which when combined with the Raman spectrum shown in Figure 6-13, confirms there may be some contributions from the β - MnO_2 phase.

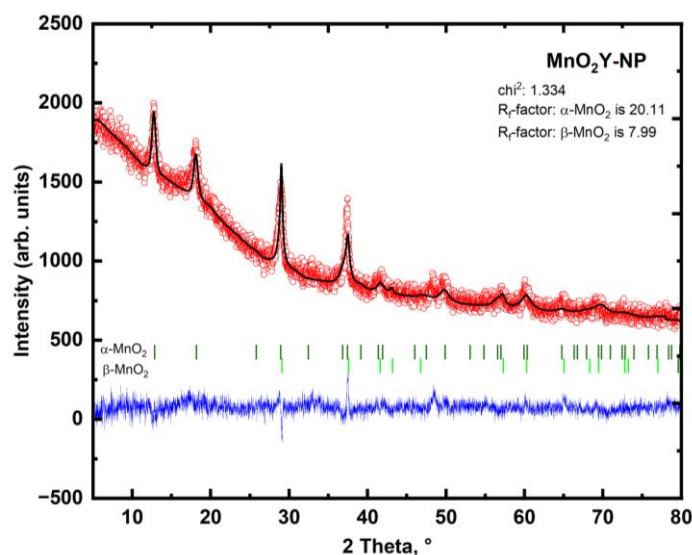


Figure 6-15 Rietveld Analysis of $\text{MnO}_2\text{Y-NP}$ showing the fitting between the experimental diffraction pattern and the model used for the phases α - MnO_2 and β - MnO_2 .

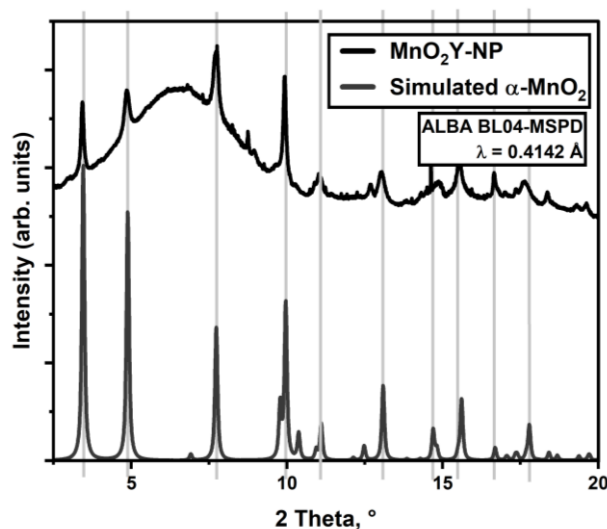


Figure 6-16 $\text{MnO}_2\text{Y-NP}$ measured at ALBA beamline BL04, with X-ray wavelength of 0.4142 Å. The pattern from the synchrotron data of $\text{MnO}_2\text{-NP}$ is compared with the simulated pattern for α - MnO_2 . The model used is **ICSD 20227** (same as for $\text{MnO}_2\text{-NP}$)

The average crystallite size for $\text{MnO}_2\text{Y-NP}$ was calculated for reflections between 10° and 40° . Due to the high baseline activity and broad peaks, significantly large deviations in the FWHM were calculated for the reflections beyond 40° . Figure 6-16 shows the average crystallite size calculated as 10.94 nm.

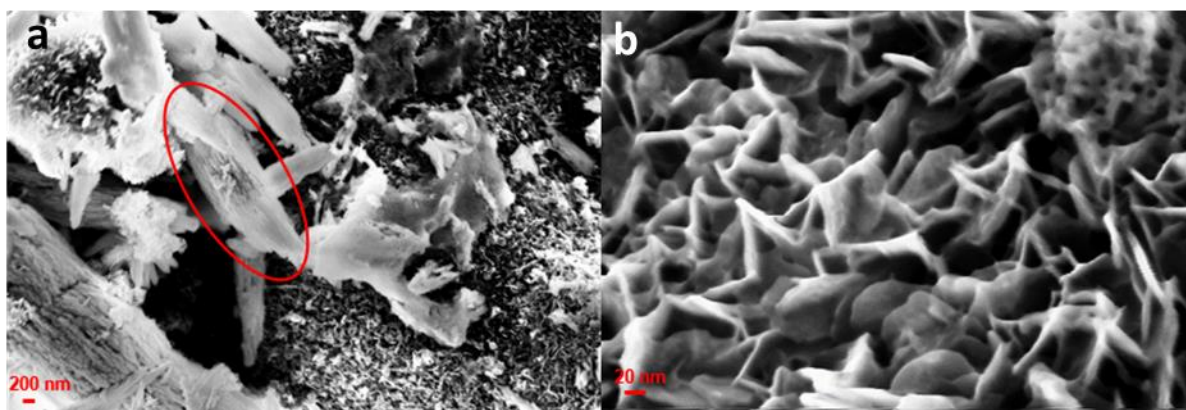


Figure 6-17 SEM analysis of MnO₂Y-NP. The scale bars are a) 200 nm and b) 20 nm (x10 mag). Red circle outlines the fibrous looking morphology that appears alongside the nanosheets in the sample.

The SEM images for MnO₂Y-NP in Figure 6-17, shows two morphologies. The fibrous particles, circled in red, are composed of non-porous, stringy strands of material. Many fibrous MnO₂ nanostructures have been previously reported although they are typically composites containing carbon.^[115] Compared to MnO₂-NP which exclusively consisted of nanorods the presence of fibres is accompanied by spherical particles composed of nanosheets.

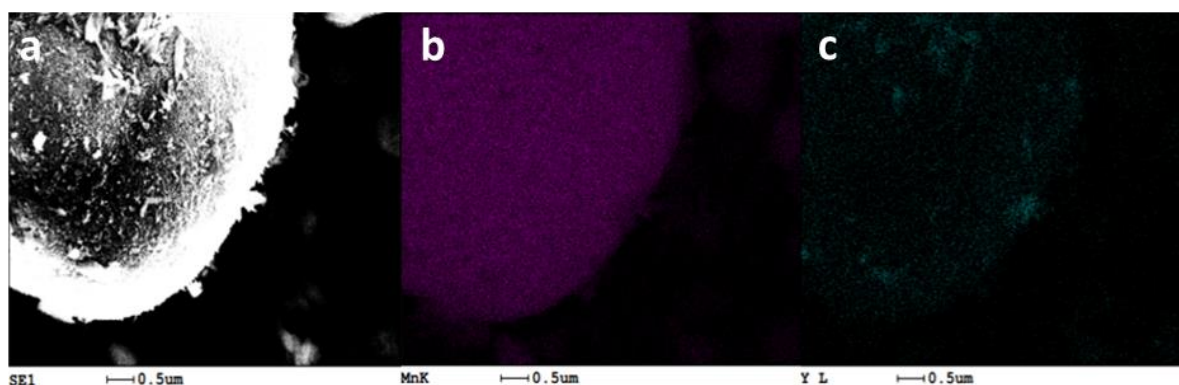


Figure 6-18 Elemental mapping of MnO₂Y-NP at a scale of 0.5 μm. a) shows the SEM image of the particle, b) shows the distribution of manganese across the surface of the particle, and c) shows the distribution of yttrium across the particles.

The elemental distribution of manganese and yttrium can be seen through the EDX mapping shown in Figure 6-18. Manganese (pink) is densely detected on the surface of the particle, while Y (blue) is sparser and appears to accumulate in areas correlating to the location of the fibrous morphology. This could be due to Y^{III} ions replacing the Mn^{III} from the mixed valence Mn^{III/IV}O₂ in the hollandite-type structure causing a phase defect that in turn influences morphological change.

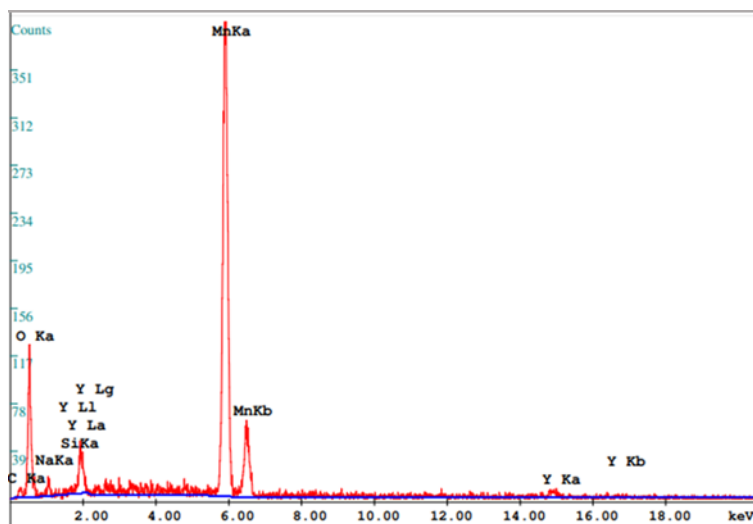


Figure 6-19 Elemental analysis of MnO₂Y-NP showing the detection of Mn, Y, O, and Na.

To quantify the EDX mapping, an elemental analysis was carried out to observe the atomic percentage of metals present on the particle. This is shown in Figure 6-19. Manganese and yttrium atom percentages were calculated at 92.35 % and 7.65 % respectively. Although the percentage of yttrium is higher than expected (as only a 5 mol% of Y₂O₃ was used), yttrium appears in high concentrations on the areas where particles of fibrous morphology are present, therefore clarifying the high atom percentages.

6.3.1.2 Electrochemical Analysis in a Li-ion coin cell

Cyclic voltammetry was measured on an electrode prepared from MnO₂Y-NP and it is shown in Figure 6-20. At 0.1 mV s⁻¹, the oxidation for the first cycle at 1.21 V shifts to 1.16 V for the remaining nine cycles at this scan rate. Likewise, the reduction potential for the first cycle is 0.21 V and shifts to 0.19 V for the duration of the cycles measured at 0.1 mV s⁻¹. Increasing the scan rates to 0.5 mV s⁻¹ and 1 mV s⁻¹ results in two oxidations corresponding to multi-step oxidation processes. These are no distinct reduction potential maxima observed at either scan however the reduction of MnO₂ to Mn₂O₃ via Mn₃O₄ can be predicted and vice versa for the oxidation processes. In-situ PXRD measurements during cycling can confirm this process when synchrotron measurements are possible. The CV profiles scanned beyond 2 mV s⁻¹ show broad oxidation potentials sweeping across the potential with no sharp reduction potentials present.

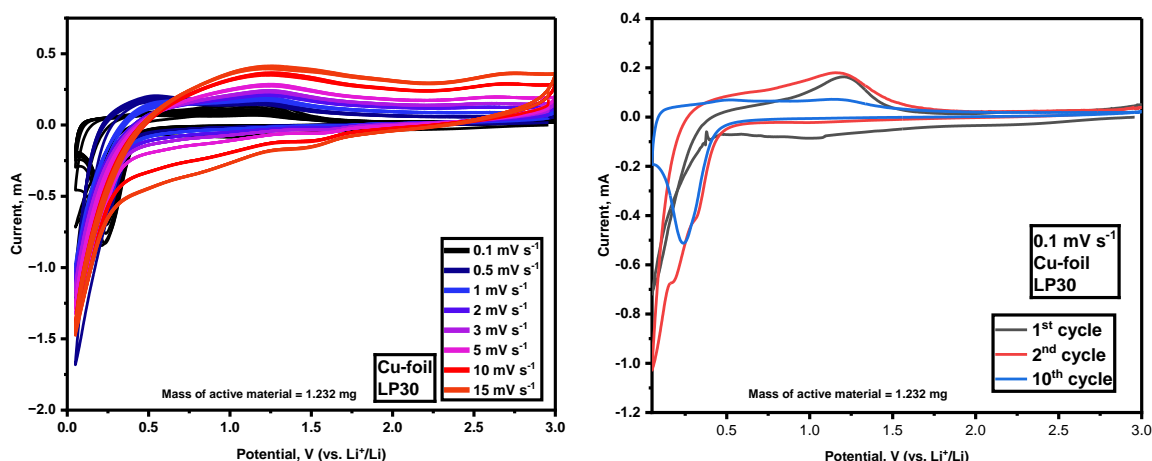


Figure 6-20 Cyclic voltammetry of MnO₂Y-NP collected over eight scan rates: 0.1 mV s⁻¹, 0.5 mV s⁻¹, 1 mV s⁻¹, 2 mV s⁻¹, 3 mV s⁻¹, 5 mV s⁻¹, 10 mV s⁻¹ and 15 mV s⁻¹. Graph to the right shows the first three cycles at 0.1 mV s⁻¹.

240 galvanostatic charge-discharge cycles were measured for MnO₂Y-NP and are shown in Figure 6-21. 10 cycles were measured at each charge density (100 mA g⁻¹, 200 mA g⁻¹, 500 mA g⁻¹ and 2000 mA g⁻¹) before returning to 100 mA g⁻¹ for the remaining 200 cycles. The initial discharge capacity was 1244 mAh g⁻¹. The capacity measured at 100 mA g⁻¹ for the 1st cycle fades to 416 mAh g⁻¹, which is followed by additional capacity loss to 186 mAh g⁻¹ by the 10th cycle. This is a capacity loss of almost 80% from the initial discharge capacity of the cell within the first ten cycles. The coulombic efficiency however remains above 98%.

Further cycling at a rate of 200 mA g⁻¹ shows a capacity fade from 149 mAh g⁻¹ to 123 mAh g⁻¹ after an additional 10 cycles. Cycling at 500 mA g⁻¹ maintains a stable capacity of 78 mAh g⁻¹ throughout the 10 cycles measured while at 2000 mA g⁻¹ the capacity fades from 30 mAh g⁻¹ to 8 mAh g⁻¹. Returning the scan rate to 100 mA g⁻¹ for the 41st cycle, the capacity increases to a reasonable 97 mAh g⁻¹ by the 50th cycle and maintains this stability until the 239th cycle. Compared to reported α -MnO₂ electrode materials and the MnO₂-NP cycled in section 5.1, addition of 5 mol% Y₂O₃ did not increase electrochemical performance of the cell; however, it does stabilise the chemical structure and in turn the capacity. It can be seen in Figure 6-21 that the cell is stable as the capacity from the 40th to the 239th cycle remain at approximately 100 mAh g⁻¹.

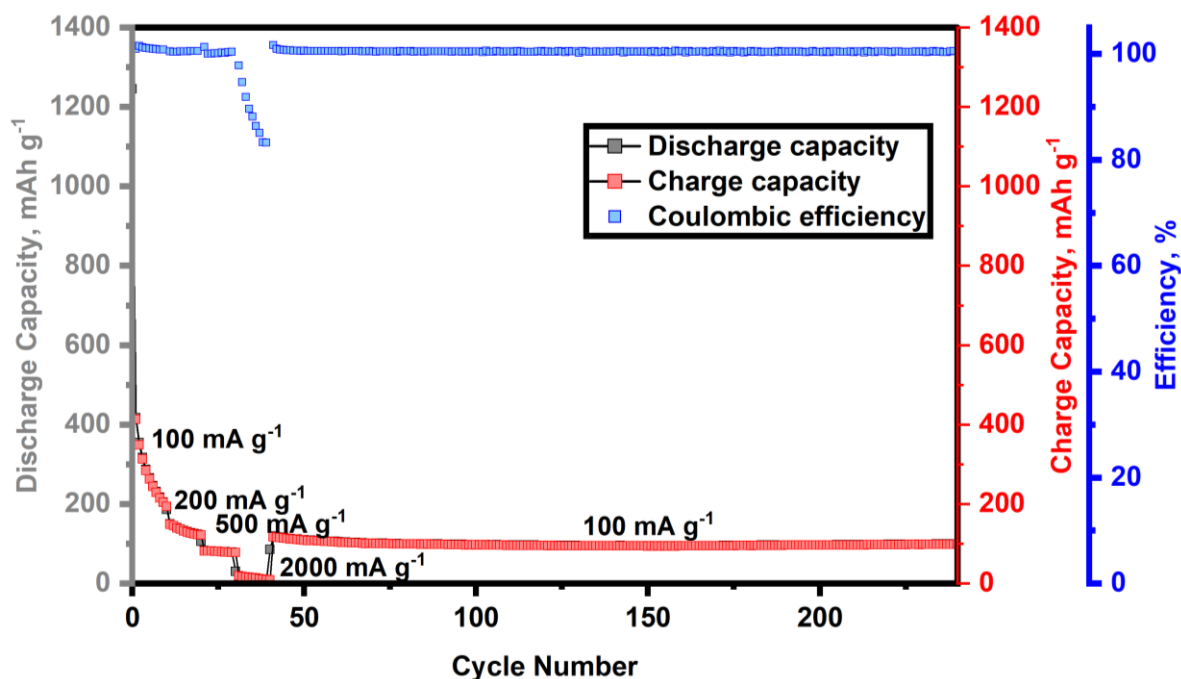


Figure 6-21 Specific discharge capacity, specific charge capacity and Coulombic efficiency (CE) vs. Cycle number for MnO₂Y-NP measured at 100 mA g⁻¹, 200 mA g⁻¹, 500 mA g⁻¹, and 2000 mA g⁻¹ for 10 cycles each. The rate is then returned to 100 mA g⁻¹ for the remaining 200 cycles. The coulombic efficiency per cycle is also show in blue.

5 mol% Y₂O₃-addition showed that the presence of an additive hindered the performance. Assuming the Y^{III} is present in the tunnelled structure of α -MnO₂ in the nanotubes, expansion of the diffusion channels allows for better insertion as well as stabilisation of the structure (which is seen from cycles 40 through 100). The formation of Y-based sub structures on the electrode during cycling such as Y₂O₃ or LiYO₂ can contribute to the low capacities observed after the first cycle. In-situ XAS/EXAFs can monitor the local environment of Mn and Y throughout the measurement.^[93] This would help in understanding the intrinsic effects of the presence of yttrium in the sample.

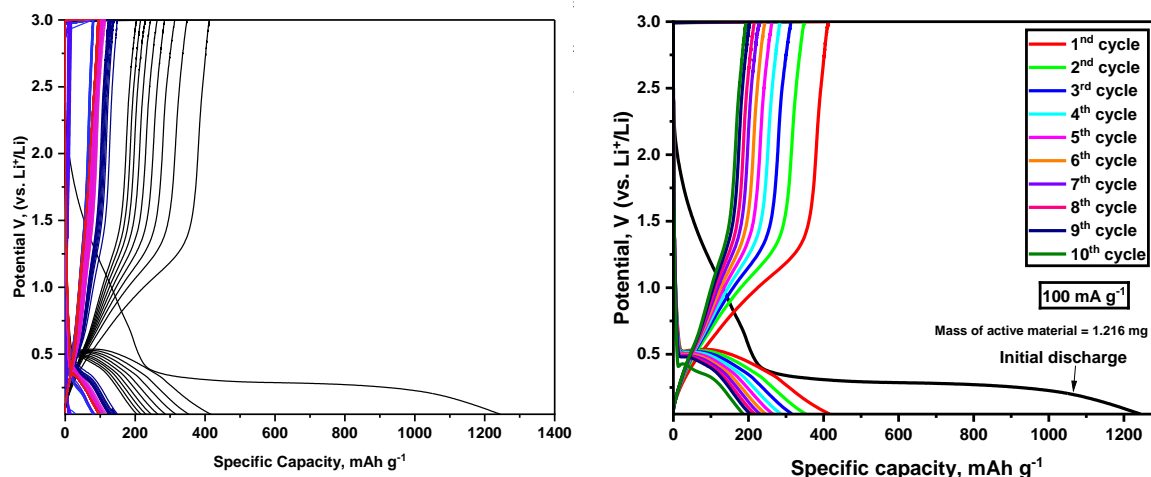


Figure 6-22 Galvanostatic charge-discharge of $\text{MnO}_2\text{Y-NP}$ showing the 240 cycles measured at current densities of 100 mA g^{-1} , 200 mA g^{-1} , 500 mA g^{-1} , and 2000 mA g^{-1} for 10 cycles each before returning to 100 mA g^{-1} for the remaining 200 cycles. Graph to the right shows the first 10 cycles at 100 mA g^{-1} .

This reduction pattern is seen throughout the measurements (although shifting to lower voltages with each current density due to the kinetics at higher charge densities) After the 29th cycle, which is the final cycle at current density 500 mA g^{-1} , there are no redox reactions observed between the 31st and 39th cycle measured at 2000 mA g^{-1} . Returning to 100 mA g^{-1} in the 41st cycles show the return of the two-phase transition observed. Gradually, by the 239th cycle the single plateaus are observed.

6.3.2 Addition of 5 mol% CeO₂ – MnO₂Ce-NP

Being the most abundant of the lanthanides, 5 mol% CeO₂ was introduced to form MnO₂Ce-NP. Cerium oxide nanoparticles have a unique set of properties. They are able to absorb and release oxygen ions, and in the context of lithium-ion batteries, they are able to absorb excess lithium-ions and release them during the charging and discharging processes. This can help to prevent dendrite formation or lithium plating on the electrode surface. Cerium oxide, due to its multivalence, and reports of it stabilising the electrochemistry of Li-ion battery electrodes, was introduced into the nanoparticles in the form of commercially available CeO₂.

6.3.2.1 Phase and Morphological Analysis

Cerium was the only lanthanide added that reduced the manganese to the extent that the diffraction pattern was able to detect the sharp reflections of CeO₂.

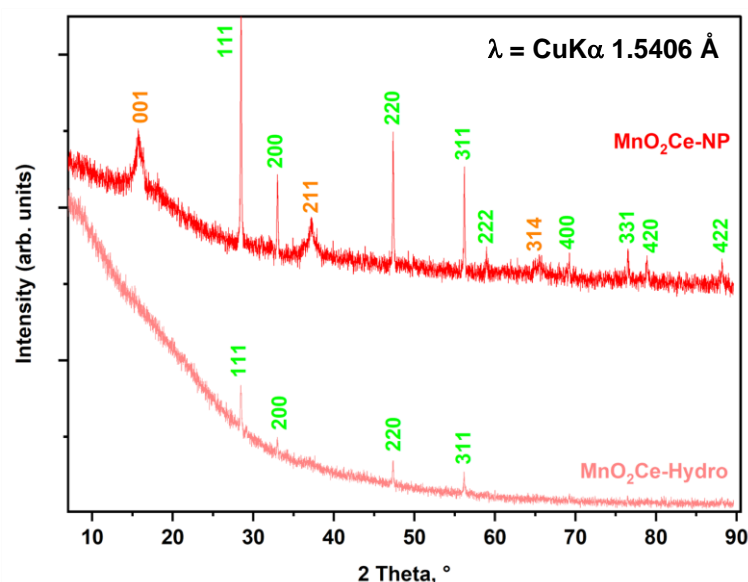


Figure 6-23 Stacked PXRD of MnO₂Ce-Hydro after hydrothermal treatment (red) and MnO₂Ce-NP after pyrolysis (light red) showing the changes caused by the presence of Ce(IV)O₂ on the MnO₂ phase. The hkl indices are shown for CeO₂ (green) and $\delta\text{-MnO}_2$ (orange). (JCPDS no. 34-0394, JCPDS no. 80-1098)

PXRD patterns in Figure 6-23 show that the addition of 5 mol% CeO₂ results in the sharp reflections for CeO₂ becoming apparent in MnO₂Ce-Hydro (light red). For clarification, the hkl indices for CeO₂ are shared in Figure 6-23 in green. There are no reflections visible for MnO₂ or any other manganese oxide compound which suggests they are likely amorphous. The reflections increase in intensity after pyrolysis; 111, 200, 220, 311, 222, 400, 331, 420, and 422 are now visible in the pattern for MnO₂Ce-NP (red). The appearance of broad reflections correlates to the additional phase $\delta\text{-MnO}_2$ denoted by hkl indices 001, 211, and 314 in orange.

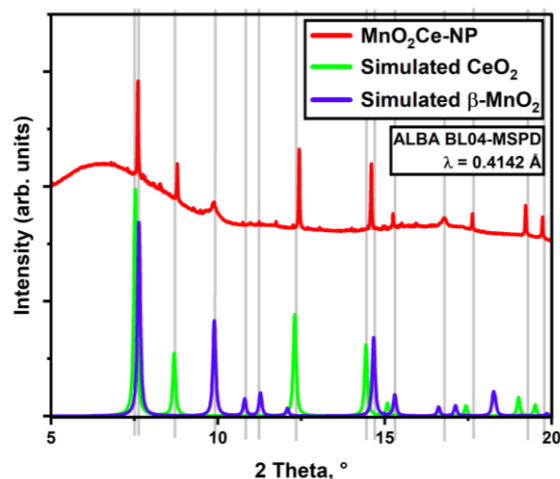


Figure 6-24 MnO₂Ce-NP measured at ALBA beamline BL04, with X-ray wavelength of 0.4142 Å. The pattern on the left is the synchrotron data of MnO₂Ce-NP compared with the simulated pattern for CeO₂ and β-MnO₂ (JCPDS no. 24-0735).

Interestingly, the synchrotron data showed there was also additional contribution of β-MnO₂ in this sample. Individually for each phase, the crystallite size was calculated at 6.75 nm for β-MnO₂ and 40.28 nm for CeO₂. The ex-situ measurements at ALBA were carried out on older samples so the discrepancy in phase is

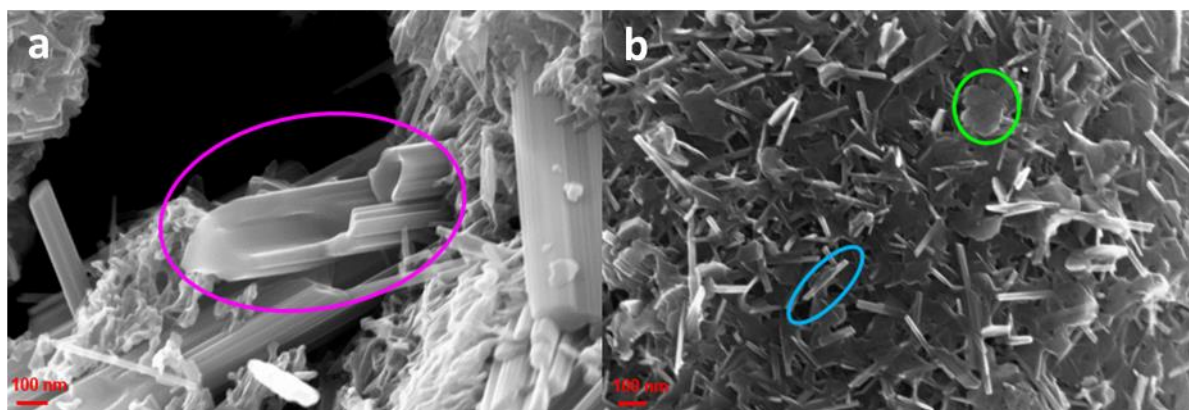


Figure 6-25 SEM of MnO₂Ce-NP after pyrolysis showing the presence of two distinct morphologies which coincides with the presence of two phases. Pink, blue, and green circles showcase the range of morphologies in this sample. a) formation of large hollow tubes and b) presence of nanosheets and nanorods.

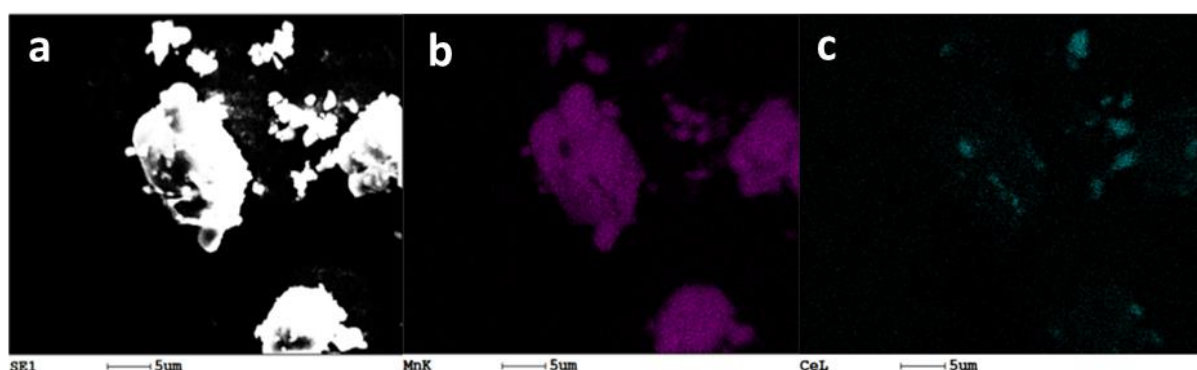


Figure 6-26 EDX analysis of MnO₂Ce-NP showing the distribution of manganese (purple) and cerium (blue) over the surface of the particles.

Looking at the SEM images in Figure 6-25 there are two discrete morphologies visible throughout the bulk material of MnO₂Ce-NP. The morphologies can be defined as **rods**, and what could be considered the pre-formation of **tubes**. Figure 6-25 b shows that there are **sheets** which gradually form into nanorods, a transition that has been reported plentifully before. Heating the sample to higher temperatures and/or for longer time periods of time result in complete conversion of the nanoplatelets to nanorods.^[92] What is arguably more interesting is the tube morphology that is observed. It is readily reported that δ -MnO₂ can deconstruct from its stacked plate structure at high temperatures to form composite compounds with tube structures. Although crystalline δ -MnO₂ was not identified in this sample, the formation of these tube shapes is still unique in this study.

Elemental distribution is shown in Figure 6-26 and it shows the spread of Mn (purple) and Ce (blue) across an area of particles. There is a clear and even distribution across the bulk of the particles however there do remain small areas of high Ce concentration that correspond to areas of visually minimal Mn. Looking at the SEM images in Figure 6-25 a,b for MnO₂Ce-NP, the particles clearly show the mixture of the tube-like structures and the process of nanotube formation within the nanorods. Cerium deposits appear to form amongst the nanoparticles, for example either within or on the surface.

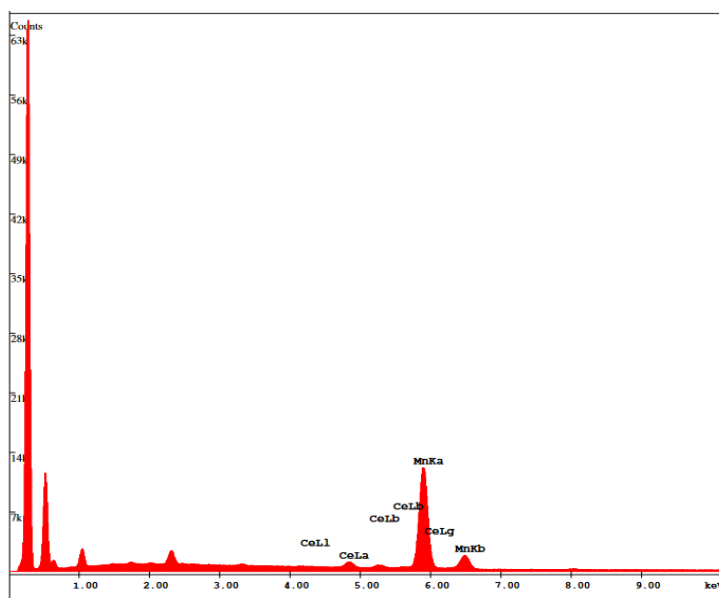


Figure 6-27 EDX elemental analysis of MnO₂Ce-NP showing the detection of manganese and cerium.

Quantifying this mapping, the atomic distribution is given as 92.6% for manganese and 7.4% for cerium. Where there are tubes present, the cerium distribution is

concentrated in those areas. The average Scherrer crystallite size for MnO₂Ce-NP was calculated for reflections between 10° and 90° is 31.6 nm.

6.3.2.2 Electrochemical Analysis in Li-ion Coin Cells

Looking at the general pattern of the CVs plotted for MnO₂Ce-NP in

Figure 6-28, increasing scan rate from 0.1 mV s⁻¹ to 15 mV s⁻¹ follows the same pattern reported previously for MnO₂-NP and MnO₂Y-NP. Reductions at 0.1 mV s⁻¹ have a peak potential of 0.3 V. Cycling at a rate of 0.5 mV s⁻¹, give the peak potentials at 0.15 V.

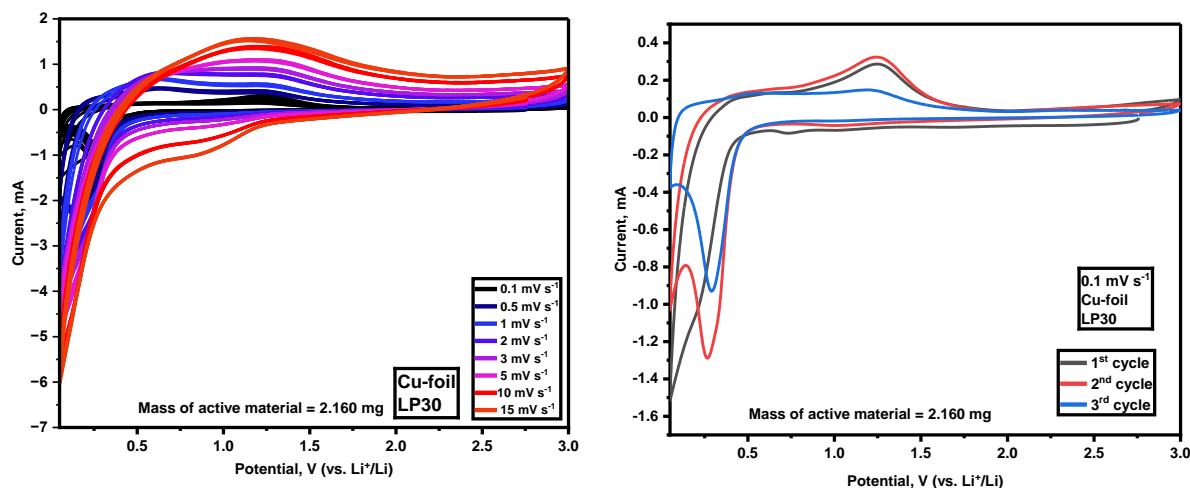


Figure 6-28 Cyclic voltammetry of MnO₂Ce-NP collected over eight scan rates: 0.1 mV s⁻¹, 0.5 mV s⁻¹, 1 mV s⁻¹, 2 mV s⁻¹, 3 mV s⁻¹, 5 mV s⁻¹, 10 mV s⁻¹ and 15 mV s⁻¹. Graph to the right shows the first three cycles at 0.1 mV s⁻¹.

The following scan rates between 1 mV s⁻¹ and 15 mV s⁻¹ show a shift of the reductions to more negative potentials. Oxidation processes are once again similar to those presented for the previous MnO₂ composite materials. The cycling data at 0.1 mV s⁻¹ has the strongest and most defined oxidation process at 1.23 V. Scanning at 0.5 mV s⁻¹ shows the presence of a two-step oxidation process up to 3 mV s⁻¹, and between 5 mV s⁻¹ and 15 mV s⁻¹, the potential of the oxidation at the higher voltages becomes broader due to the ineffective interaction between the electrolyte and electrode.

Rate capability is shown in Figure 6-29 for MnO₂Ce-NP. An initial discharge capacity of 1099 mAh g⁻¹ is recorded. The cell undergoes fast fast capacity degradation between the 1st cycle at 475 mAh g⁻¹ to the 9th cycle at 291 mAh g⁻¹ measured at a current density of 100 mA g⁻¹. During cycling at 200 mA g⁻¹, there is a loss in capacity over the 10 cycles from 227 mAh g⁻¹ to 197 mAh g⁻¹. Cycling at a current density of 500 mA g⁻¹ leads to improved capacity stability with cycle 21 at 139 mAh g⁻¹ and cycle 29 at 132 mAh g⁻¹.

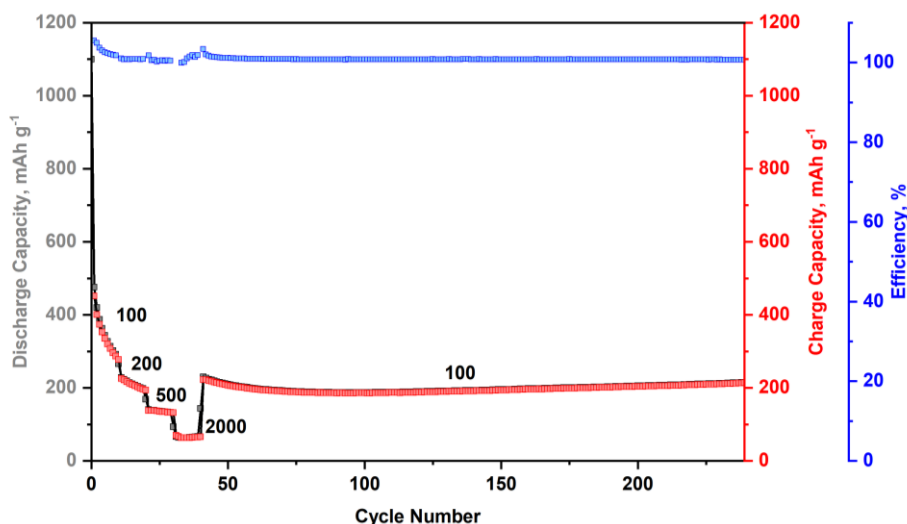


Figure 6-29 Rate capability steps of MnO₂Ce-NP measured at 100 mA g⁻¹, 200 mA g⁻¹, 500 mA g⁻¹, and 2000 mA g⁻¹ for 10 cycles each. The rate is then returned to 100 mA g⁻¹ for the remaining 200 cycles. The coulombic efficiency per cycle is also show in blue.

Finally, at 2000 mA g⁻¹ the capacity remains at approximately 66 mAh g⁻¹ throughout the cycles before going up to 229 mAh g⁻¹ as the current density returns to 100 mA g⁻¹. For the remaining 200 cycles, the capacity drops slightly to 186 mAh g⁻¹ by the 100th cycle but increases up to 240 mAh g⁻¹ by the 239th cycle. This trend of the capacity decreasing before increasing again is an indication of the morphological stabilisation of the electrode during cycling since manganese oxides are readily able to change chemical compositions. The charge-discharge data of MnO₂Ce-NP is shown in Figure 6-30, and it clarifies the effect of current densities on the voltage. As the current densities increase, we tend to notice an increasing overpotential which correlates to low energy efficiency. The initial voltage plateaus are discernible at c.a 0.5 V, although as the current density increases to 200 mA g⁻¹, 500 mA g⁻¹, and 2000 mA g⁻¹, the voltage drops to 0.45 V, 0.35 V, and 0.26 V respectively before stabilising for the remaining cycles at 0.42 V.

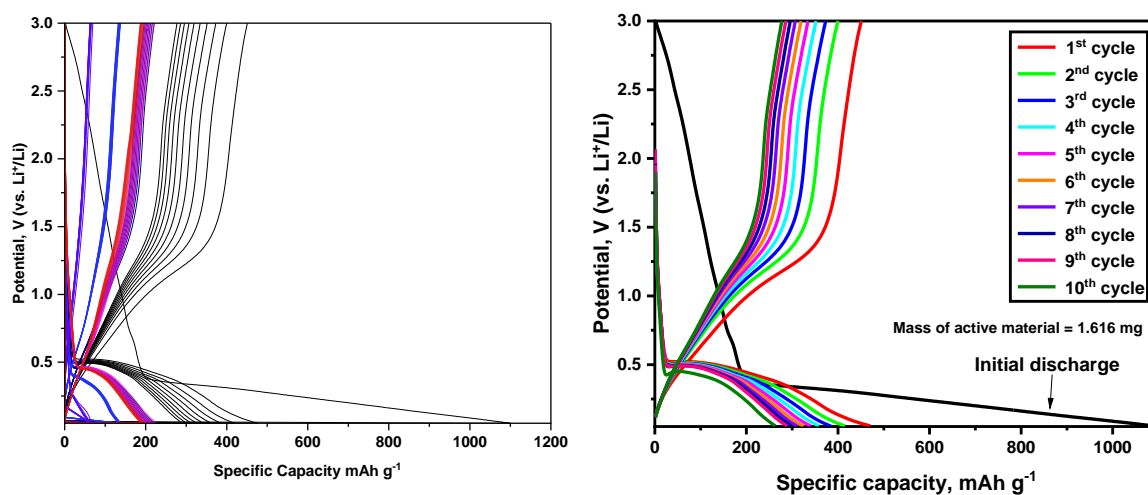


Figure 6-30 Galvanostatic charge-discharge of MnO₂/Ce-NP showing the 240 cycles measured at current densities of 100 mA g⁻¹, 200 mA g⁻¹, 500 mA g⁻¹, and 2000 mA g⁻¹ for 10 cycles each before returning to 100 mA g⁻¹ for the remaining 200 cycles. Graph to the right shows the first 10 cycles at 100 mA g⁻¹.

6.3.3 Addition of 5 mol% Dy₂O₃ – MnO₂Dy-NP

Dysprosium oxide is considered to be a critical raw material. The extraction method combined with the fact that China is the centre for rare-earth metal mining are what make it critical. Dysprosium, alongside terbium and neodymium, are essential in NdFeB permanent magnets. These magnets are well known for their use in energy transition in wind turbines. NdFeB are still the strongest permanent magnets available today, enabling the highest possible conversion of motor torque into energy. Motor technology companies and manufacturers of EV's can reduce costs associated to Li-ion batteries by using NdFeB (containing dysprosium) in the motors since rare-earth elements enable the magnet to function at higher operating temperatures. Dysprosium has also been reported to increase battery performance when used as an additive or dopant for Li-ion battery electrodes. In LiCoO₂, it has been reported that the presence of dysprosium stabilises the Co-O bonds.^[116]

6.3.3.1 Phase and Morphological Analysis

The diffraction patterns of MnO₂Dy-Hydro and MnO₂Dy-NP are shown below in Figure 6-31.

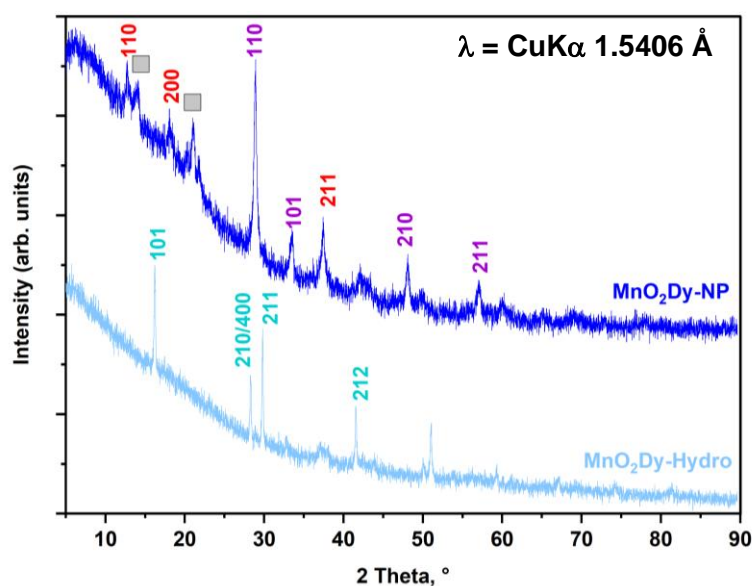


Figure 6-31 Stacked PXRD of MnO₂Dy-Hydro and MnO₂Dy-NP. (JCPDS #024-0735, JCPDS #44-0141)

Addition of 5 mol% Dy₂O₃ results in the formation of a mixed phase sample consisting of α - and β - phases. MnO₂Dy-Hydro consists of majority R-MnO₂ identified with hkl indices of 101, 210/400, 211 and 212 at 16°, 28°, 29°, 41° respectively. After pyrolysis, MnO₂Dy-NP is composed of mixed phase alpha and beta phases denoted

using the hkl indices **110** and **200** at 12.9° and 17.9° for the former phase and **110**, **101**, **210** and **211** for the latter phase.

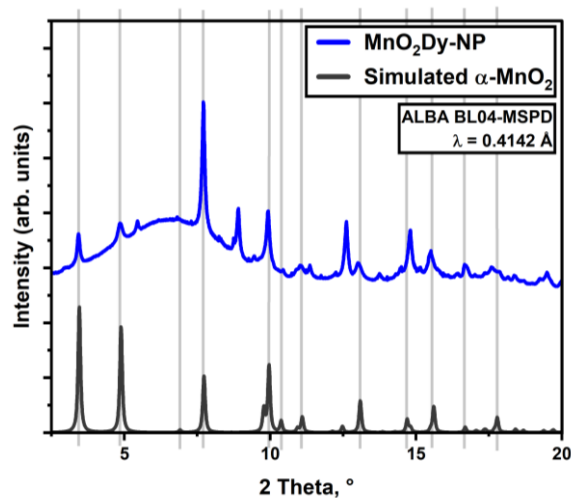


Figure 6-32 MnO₂Dy-NP measured at ALBA beamline BL04, with X-ray wavelength of 0.4142 Å. The pattern on the left is the synchrotron data of MnO₂-NP compared with the simulated pattern for α-MnO₂. There appears to be lesser intense reflections corresponding to β-MnO₂ in this sample.

The average Scherrer crystallite size for MnO₂Dy-NP was calculated for reflections between 10° and 60° is 10.3 nm. A broad range of 2 Theta values were used for the calculations since the quality of the data at higher theta values did not deteriorate and the peak positions were easily discernible unlike for previous compounds.

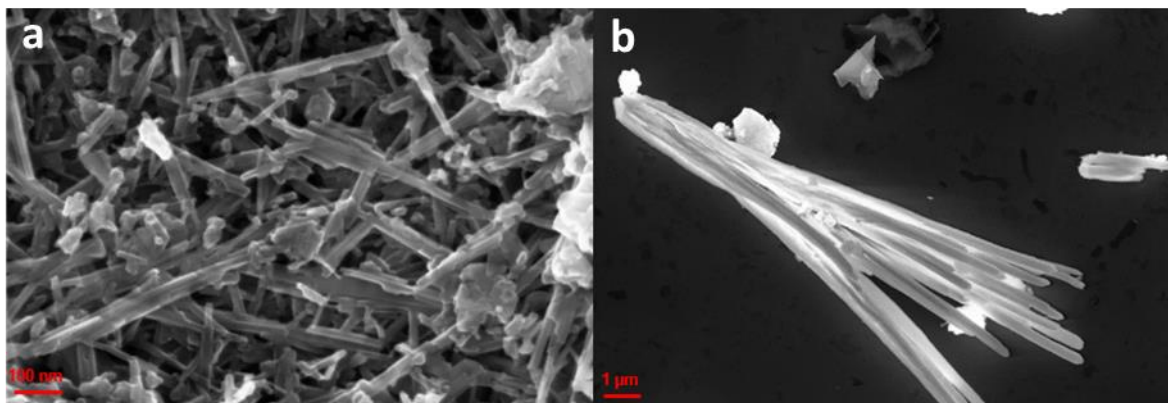


Figure 6-33 SEM images of the two different morphologies observed for MnO₂Dy-NP at scale bars (a) 100 nm and (b) 1 μm.

A further look at the SEM images shows the presence of two morphologies, a rod-like morphology shown in Figure 6-33 a and another fibrous looking branch like morphology shown in Figure 6-33 b. The morphologies are easily identifiable from each other with the nanorods present in spherical particles and averaging lengths of 300 nm, while the fibrous branches are much larger at 10-20 μm and seem to be somewhat combined at one end and flared at the other. The separation of these morphologies across the sample appears to have an even distribution of morphologies, especially when looking at Figure 6-11 k.

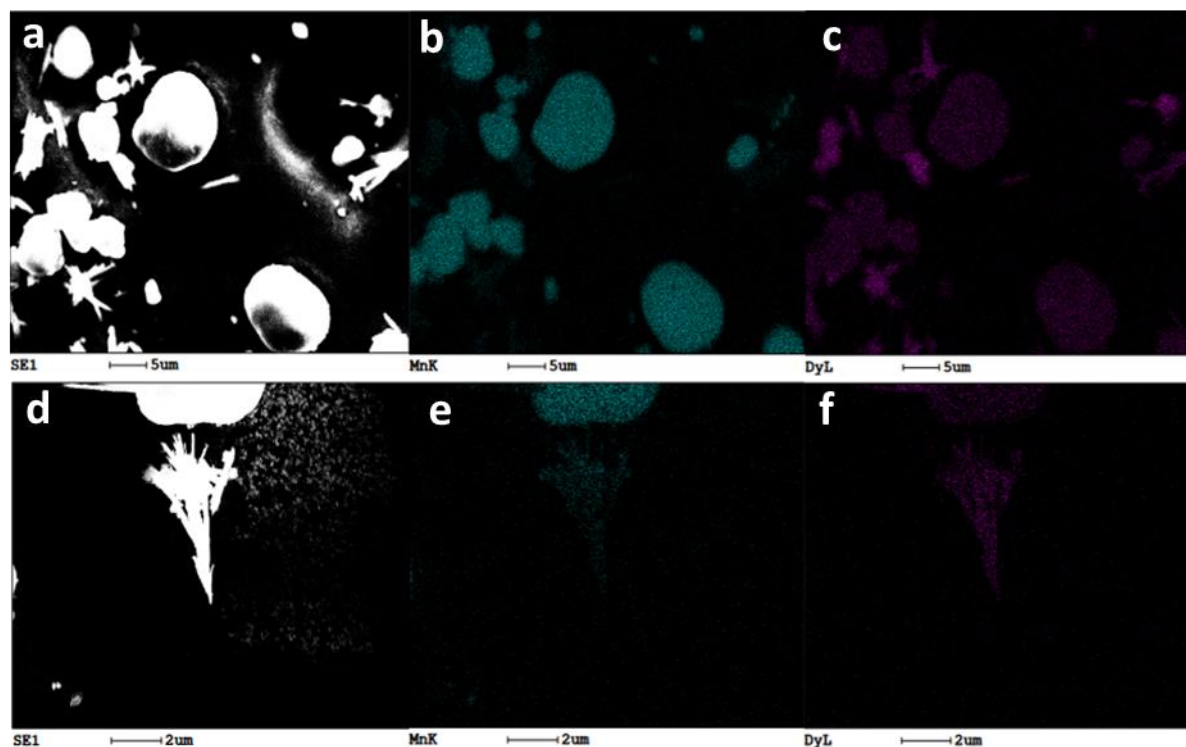


Figure 6-34 (a-c) EDX mapping showing the distribution of Mn (blue) and Dy (purple) over a large area of the sample. (d-f) EDX mapping showing the distribution of Mn and Dy across a small area of the sample showing the difference in distribution of elements in the branch and spherical particles.

Elemental distribution measured through EDX analysis, shows the spread of Mn and Dy over the two different morphologies. The spherical agglomerates of nanorods have a higher presence of Mn over Dy on the surface of the samples which was as expected. However, the branch-like particles observe the opposite trend. The accumulation of Dy across these branches does not completely negate the presence of Mn. The atom percentages were calculated by running an elemental mapping shown in Figure 6-35. The percentage of manganese found on the surface of the particles Figure 6-34 a-c was 89%, compared to Figure 6-34 d-f which was 85%. The percentage of dysprosium found in Figure 6-34 a-c, was 11% and d-f was 15%.

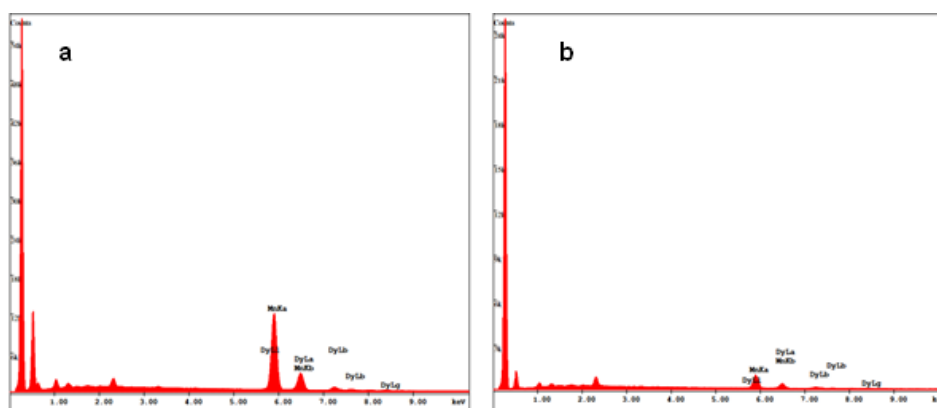


Figure 6-35 EDX elemental analysis of $\text{MnO}_2\text{Dy-NP}$. (a) corresponding to Figure 6-34 a-c (b) corresponding to Figure 6-34 d-f.

The high quantity of Dy detected over these areas are relative to the presence of the two morphologies.

6.3.3.2 Electrochemical Analysis in a Li-ion Coin Cell

Although the CV curves for MnO₂Dy-NP in Figure 6-36 look like those previously shown for MnO₂-NP, MnO₂Y-NP, and MnO₂Ce-NP, a clear difference is the oxidation profiles.

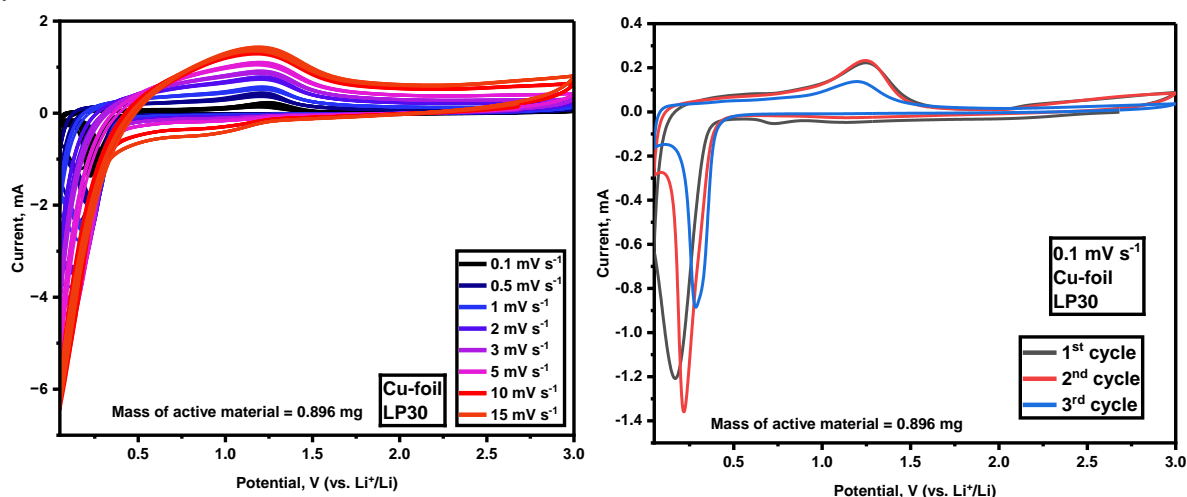


Figure 6-36 Cyclic voltammetry of MnO₂Dy-NP collected over eight scan rates: 0.1 mV s⁻¹, 0.5 mV s⁻¹, 1 mV s⁻¹, 2 mV s⁻¹, 3 mV s⁻¹, 5 mV s⁻¹, 10 mV s⁻¹ and 15 mV s⁻¹. Graph to the right shows the first three cycles at 0.1 mV s⁻¹.

At a scan rate of 0.1 mV s⁻¹ there is an oxidation at 1.18 V. From 0.5 mV s⁻¹ to 2 mV s⁻¹ the oxidation potential remains stable at 1.21 V. From 5 mV s⁻¹ to 15 mV s⁻¹ the oxidations are at 1.18 V. Although the oxidations inevitable become broader during faster scanning, there are no stepwise oxidation processes visible like for the previous compounds. The reduction profile between scan rate 0.1 mV s⁻¹ and 2 mV s⁻¹ show definable maxima at 0.16 V, 0.24 V, 0.20 V, and 0.13 V but as the scan rates increase to 10 mV s⁻¹ and 15 mV s⁻¹ the reductions are not visible. After increasing the scan rate, the effective contribution of the redox reaction was controlled to some extent, owing to poor conductivity, causing the falloff of the capacitance of the MnO₂ material. At the high current density more capacitive contribution is expected.

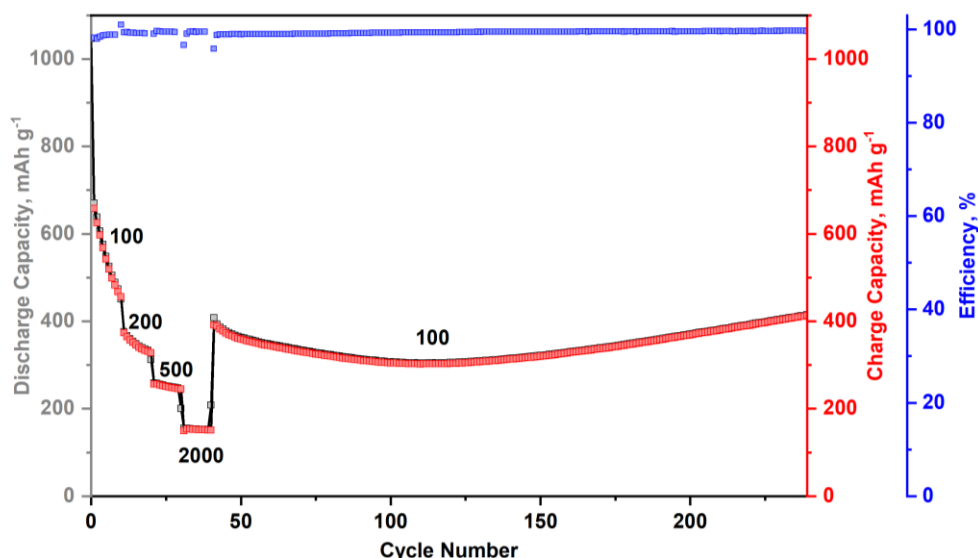


Figure 6-37 Specific discharge capacity, specific charge capacity and Coulombic efficiency (CE) vs. cycle number for MnO₂Dy-NP measured at 100 mA g⁻¹, 200 mA g⁻¹, 500 mA g⁻¹, and 2000 mA g⁻¹ for 10 cycles each. The rate is then returned to 100 mA g⁻¹ for the remaining 200 cycles. The coulombic efficiency per cycle is also show in blue.

The rate capability measurements for MnO₂Dy-NP plotted as cycle number vs capacity in Figure 6-37 show an initial discharge capacity of 1046 mAh g⁻¹ with a high capacity at a current density of 100 mA g⁻¹ of 669 mAh g⁻¹ for the 1st cycle that drops to 472 mAh g⁻¹ by the 9th cycle. During cycling at 200 mA g⁻¹, the capacity drops from 375 mAh g⁻¹ to 323 mAh g⁻¹ by the 19th cycle. At 500 mA g⁻¹, the capacity loss is much less over the 10 cycles ranging from 258 mAh g⁻¹ to 246 mAh g⁻¹. At 2000 mA g⁻¹, the capacity remains relatively stable between 154 mAh g⁻¹ and 151 mAh g⁻¹.

The charge-discharge cycling provides information on voltage loss during each cycle. Figure 6-38 shows the overlap of all cycles as well as the individual charge densities.

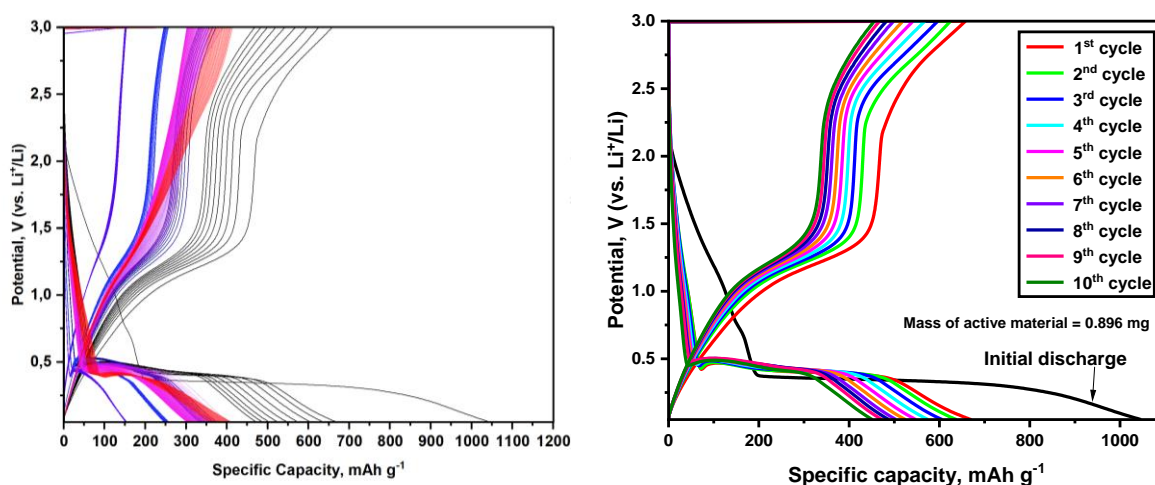


Figure 6-38 Galvanostatic charge-discharge of MnO₂Dy-NP showing the 240 cycles measured at current densities of 100 mA g⁻¹, 200 mA g⁻¹, 500 mA g⁻¹, and 2000 mA g⁻¹ for 10 cycles each before returning to 100 mA g⁻¹ for the remaining 200 cycles. Graph to the right shows the first 10 cycles at 100 mA g⁻¹.

6.3.4 Addition of 5 mol% Yb_2O_3 – $\text{MnO}_2\text{Yb-NP}$

Due to effects of lanthanide contraction, ytterbium has the smallest ionic radius of the lanthanides tested for this chapter. Minute Yb doping in lithium-rich cathode materials has been reported to enhance the cycle stability and improve rate performance.^[117]

6.3.4.1 Phase and Morphological Analysis

$\text{MnO}_2\text{Yb-Hydro}$ is mostly amorphous, consisting of some broad reflections between 35° and 50° .

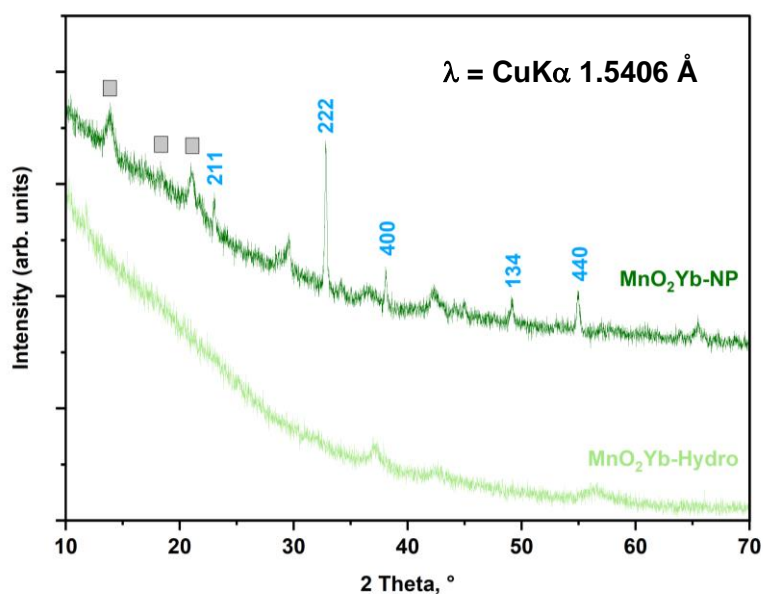


Figure 6-39 Stacked PXRD of $\text{MnO}_2\text{Yb-Hydro}$ and $\text{MnO}_2\text{Yb-NP}$. Blue hkl values represent the phase $\alpha\text{-Mn}_2\text{O}_3$ (JCPDS 089-4836).

For $\text{MnO}_2\text{Yb-NP}$, the hkl indices of 211, 222, 400, 134 and 440 at 23° , 32° , 38° , 49° and 54° respectively represent the presence of $\alpha\text{-Mn}_2\text{O}_3$. These samples were prepared for synchrotron studies (in-situ PXRD) for further analysis.

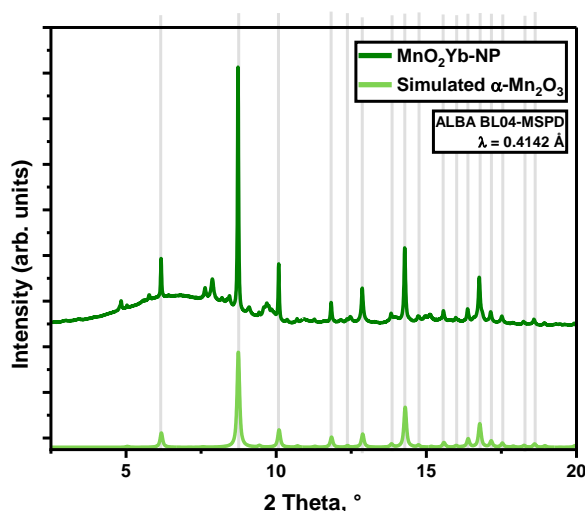


Figure 6-40 $\text{MnO}_2\text{Yb-NP}$ measured at ALBA beamline BL04, with X-ray wavelength of 0.4142 Å. The pattern from the synchrotron data of $\text{MnO}_2\text{-NP}$ is compared with the simulated pattern for $\alpha\text{-Mn}_2\text{O}_3$. The model used was ICSD 9007520. The sample also appears to contain $\alpha\text{-MnO}_2$ with the reflections at $\sim 5^\circ$ and $\sim 8^\circ$ matching ICSD 20227.

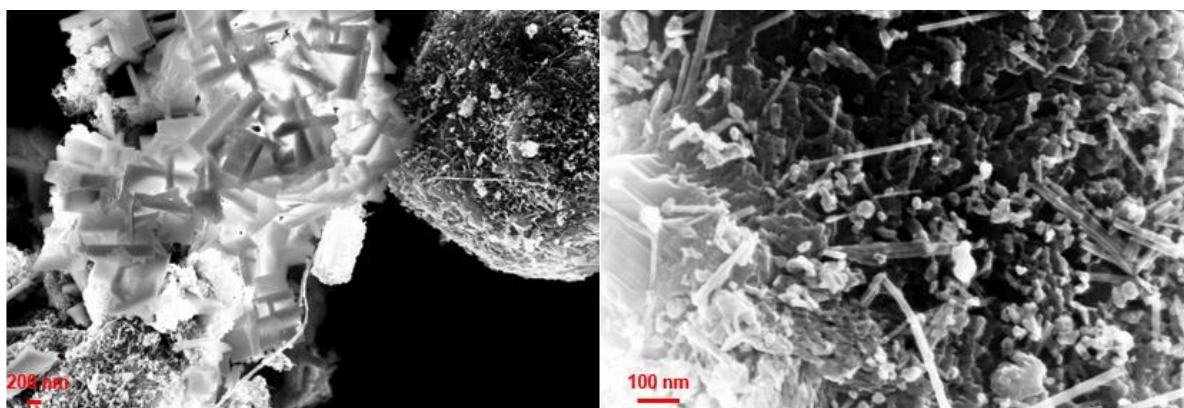


Figure 6-41 SEM images of $\text{MnO}_2\text{Yb-NP}$ showing the different morphologies observed at scale bars of 200 nm and 100 nm.

The SEM images for $\text{MnO}_2\text{Yb-NP}$ showcases yet again just how strongly the different lanthanides effect the morphology of the product. From Figure 6-41, there are both nanowires and brick-like shapes visible in the sample. The nanowires vary in length with majority ranging 100 nm to 300 nm. However, as can be seen in Figure 6-41, there are some extremely long wires scattered throughout the sample that are over 1 μm . Furthermore, the precursor to the nanowires are the nanosheets that are slightly visible in Figure 6-41. The brick-like morphology is unique to this sample with sharp edges. The morphologies are not combined, so to speak they are presented individually in the bulk of the sample rather than combined in the same particles. EDX elemental analysis was carried out to observe the distribution across the particles.

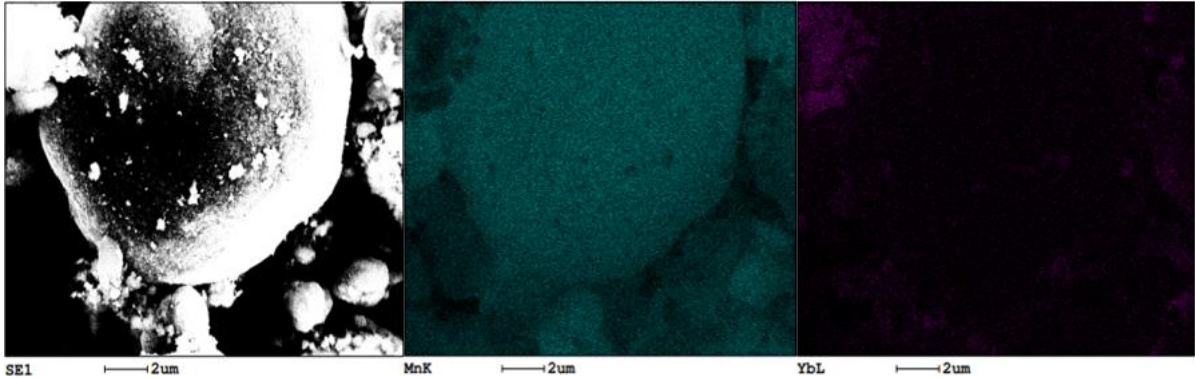


Figure 6-42 Elemental distribution manganese and ytterbium across the surface of a particle of $\text{MnO}_2\text{Yb-NP}$.

Figure 6-42 represents the distribution of manganese (blue) and ytterbium (purple) across an area of the sample. At the top left corner there are some particles associated to the brick morphology. Manganese is clearly the majority phase and the spread of ytterbium across the large spherical particles is very low as expected. However, in the top left corner where there are few particles of the brick morphology, the quantity of ytterbium detected is much larger than manganese. EDX mapping, shown below in Figure 6-43, was calculated to show the atomic percentages of each metal on the surface of the particles.

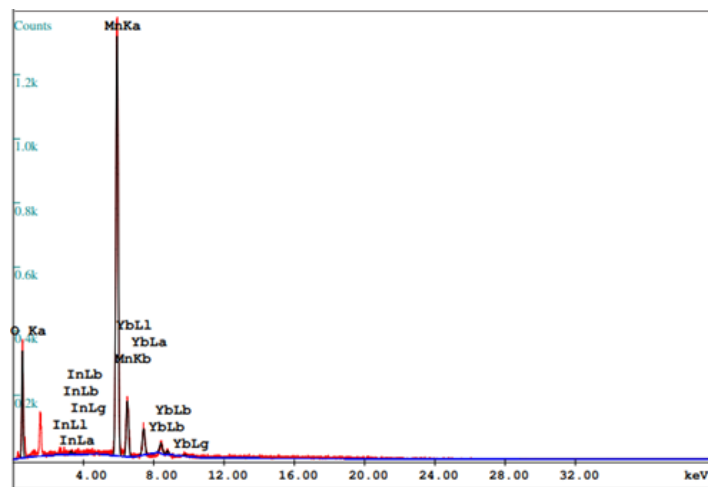


Figure 6-43 EDX Mapping of $\text{MnO}_2\text{Yb-NP}$ showing the detection of manganese and ytterbium across the particle.

Elemental mapping shows the percentage of Mn is 91.60 % and of Yb is 8.40 %. Just like for previously measured samples, this is considered quite high, however according to the preference of Yb accumulation in the different morphologies, this experimentally fits what we see in the SEM.

6.3.4.2 Electrochemical Analysis in a Li-ion Coin Cell

Looking at the CV curves in Figure 6-44, the scan rate at 0.1 mV s^{-1} has two distinct oxidations and reductions. Focusing first on the oxidations at 1.23 V and 0.46 V, they represent the oxidations and are typical profiles seen for MnO_2 batteries. The corresponding reduction profiles at 0.31 V and 0.14 V, which are typically seen for manganese oxide electrodes.

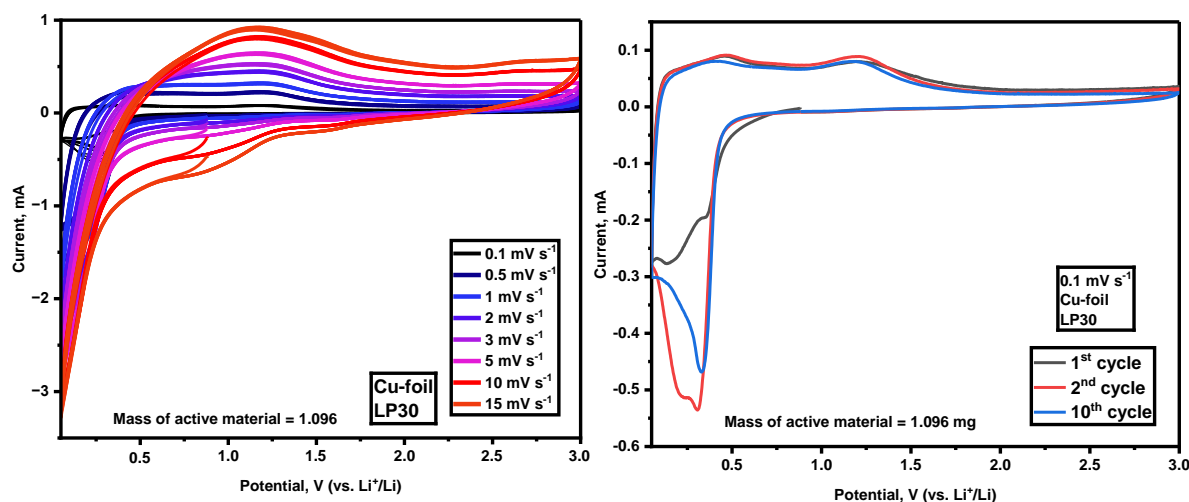


Figure 6-44 Cyclic voltammetry of $\text{MnO}_2\text{Yb-NP}$ collected over eight scan rates: 0.1 mV s^{-1} , 0.5 mV s^{-1} , 1 mV s^{-1} , 2 mV s^{-1} , 3 mV s^{-1} , 5 mV s^{-1} , 10 mV s^{-1} and 15 mV s^{-1} . Graph to the right shows the first three cycles at 0.1 mV s^{-1} .

Increasing the scan rate to 0.5 mV s^{-1} , shows a similar profile with an oxidation at 1.20 V with the second maxima at a lower potential of approximately 0.41 V (although this is more difficult to decipher due to increasing current). The reduction process is visible as a small bump at approximately 0.23 V. As the kinetic processes increase as the scan rates that follow between 1 mV s^{-1} and 15 mV s^{-1} , all show similar oxidation steps which gradually become less distinguishable. The kinetic pathway becomes more dominant due to the faster cycling.

The rate-capability measurements plotted as cycle number vs capacity are shown in Figure 6-45. An initial discharge capacity of 1067 mAh g^{-1} aligns with the other 5 mol% Ln samples measured. The discharge cycles measured at 100 mA g^{-1} , have capacities of 555 mAh g^{-1} at the 1st cycle which drops to 405 mAh g^{-1} by the 10th cycle. At 200 mA g^{-1} , there is capacity loss from 353 mAh g^{-1} to 302 mAh g^{-1} . At 500 mA g^{-1} , 237 mAh g^{-1} to 215 mAh g^{-1} and for 2000 mA g^{-1} between 125 mAh g^{-1} to 120 mAh g^{-1} . Once the current density returns to 100 mA g^{-1} , the capacity at 334 mAh g^{-1} drops to 226 mAh g^{-1} by the 127th cycle before electrode stabilisation causes the capacity to increase again to 265 mAh g^{-1} by the 239th cycle.

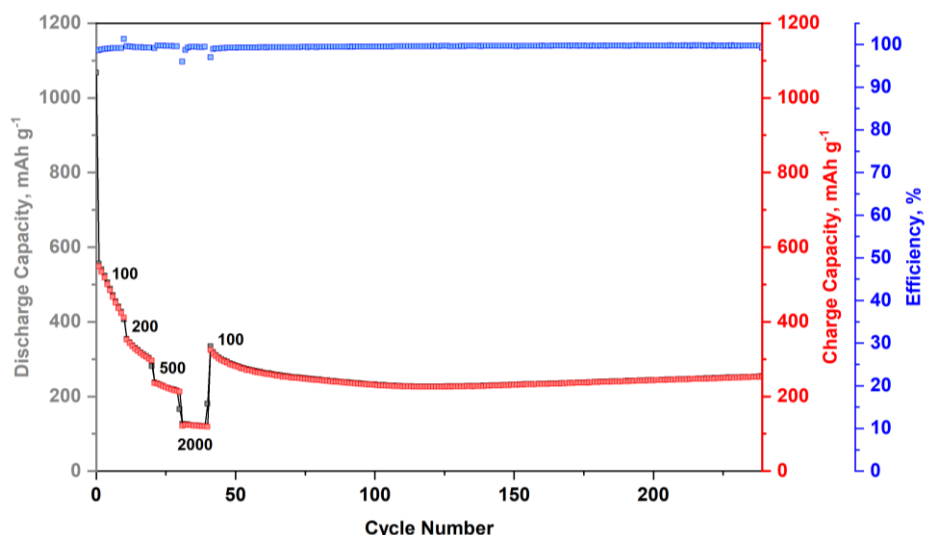


Figure 6-45 Specific discharge capacity, specific charge capacity and Coulombic efficiency (CE) vs. Cycle number for MnO₂Yb-NP measured at 100 mA g⁻¹, 200 mA g⁻¹, 500 mA g⁻¹, and 2000 mA g⁻¹ for 10 cycles each. The rate is then returned to 100 mA g⁻¹ for the remaining 200 cycles. The coulombic efficiency per cycle is also show in the figure in blue.

The voltage profile below in Figure 6-45, shows the voltage plateaus observed at each current density for MnO₂Yb-NP. At 100 mA g⁻¹, 200 mA g⁻¹, and 500 mA g⁻¹ the plateaus steadily remain at around 0.5 V. At 2000 mA g⁻¹ the voltage drops to 0.36 V. The plateau potential returned to 0.5 V until the 75th cycle when it gradually began to drop reaching 0.42 V by the 239th cycle.

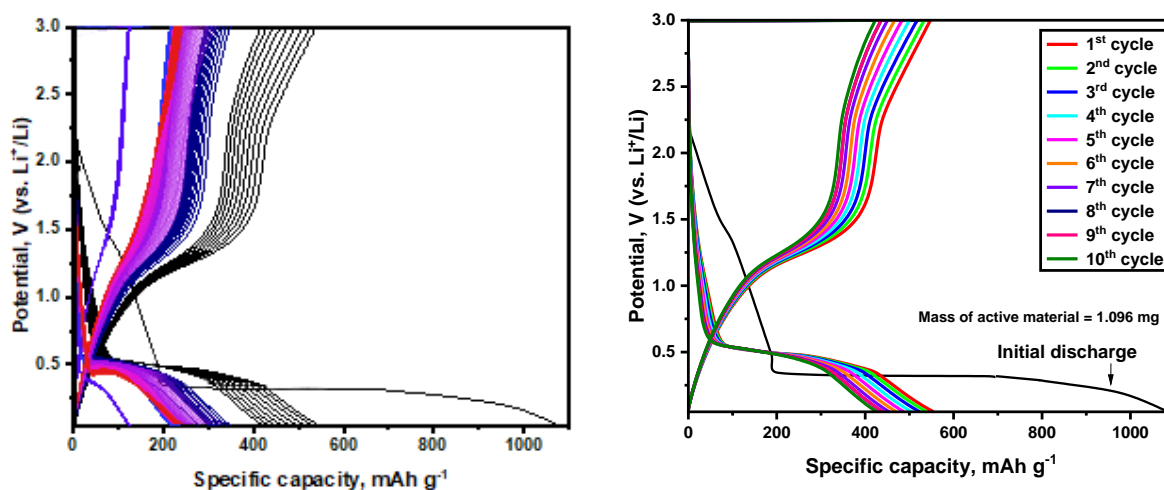


Figure 6-46 Galvanostatic charge-discharge of MnO₂Yb-NP showing the 240 cycles measured at current densities of 100 mA g⁻¹, 200 mA g⁻¹, 500 mA g⁻¹, and 2000 mA g⁻¹ for 10 cycles each before returning to 100 mA g⁻¹ for the remaining 200 cycles. Graph to the right shows the first 10 cycles at 100 mA g⁻¹.

6.4 Summary and Conclusion

Looking at the performance of all five cycled materials, one can make the following conclusions:

- Like the reported literature, the addition of Y_2O_3 resulted in better long-term stability but led to the lowest capacity.
- MnO_2Ce -NP showed the formation of tube-like structures amongst rods and sheets. This was also the only material which partially consisted of its lanthanide oxide. From internal measurements, cerium oxide appears inactive however external measurements are required to confirm this.
- The highest capacity was observed for MnO_2Dy -NP, where the capacity was attributed to the mixture of α - MnO_2 and β - MnO_2 phases. This material was composed of two unique morphologies.
- Additional phase of Mn_2O_3 was identified in the material MnO_2Yb -NP.
- Capacity stability increases at higher rate capabilities which can be seen by looking at the capacity stability after rate capability studies. This rings true for Ce, Dy and Yb containing samples. The maximum capacity after 240 cycles is as follows: MnY (100 mAh g^{-1}) < $MnCe$ (240 mAh g^{-1}) < $MnYb$ (265 mAh g^{-1}) < Mn (325 mAh g^{-1}) < $MnDy$ (412 mAh g^{-1}). The lanthanide oxides were not tested as active materials themselves, but the resultant materials they induced, many of which had polymorphs of Mn_xO_y , were compared to the literature.
- The loading densities were attempted to be kept between 1.2 mg cm^{-2} and 1.6 mg cm^{-2} . It is key to keep loading mass above 1 mg and maintain similar masses for all samples to produce comparable data.

These results would benefit from the following further analysis'; TEM to identify the location of the lanthanide ions within/on the MnO_2 nanoparticles and ex-situ EXAFs measurements to analyse the bond distances and local environments around the Mn and Ln k- and l-edges, respectively.

7 Manganese-based Templated Oxides

There are many reports in the literature utilising complexes such as MOFs and clusters to template porous oxides for a range of applications. [118] The degassing of volatile substituents at elevated temperatures results in the formation of channels that allow the gases to escape. These pores that form increase the surface area of the compound, and with respect to electrode materials, increase the electrode-electrolyte contact providing more area for the conversion reactions to take place.

7.1 Manganese Formate: A Simple Carboxylate-bridged Mn^{II}-MOF

Mn(HCO₂)₂·¹/₃(C₄H₈O₂), referred to as Mn-formate, is a simple and inexpensive MOF synthesised by Dybtev et al. [119] This MOF was previously explored in a pyrolysis optimisation study during my masters studies.

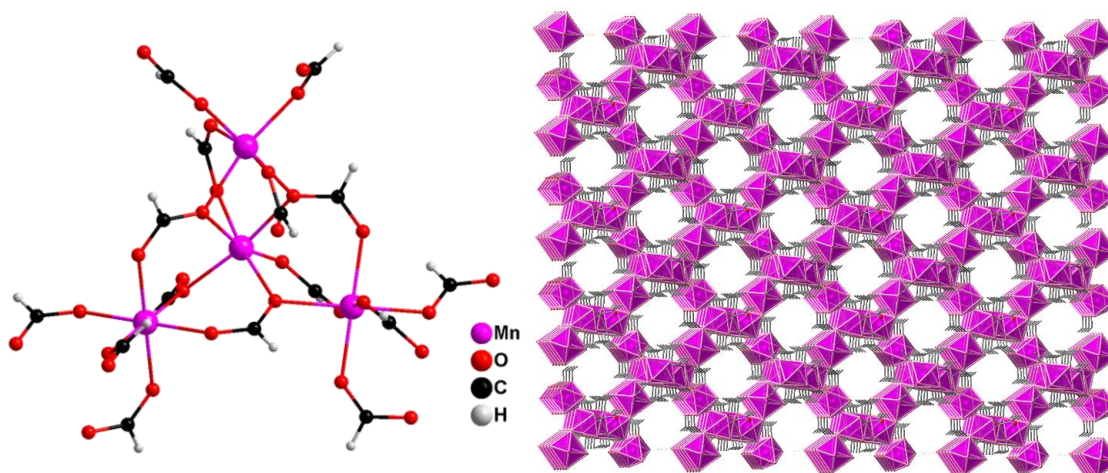


Figure 7-1 The secondary building unit of Mn-formate synthesised as reported by Dybtev et al. The figure shows the asymmetric unit, the symmetry plane, and the packing to showcase the porous nature of the MOF. Each formate anion is bound to three Mn^{II} ions in a syn-syn-anti mode. [119]

Mn-formate was synthesised under solvothermal conditions by combining manganese chloride and formic acid in a solution of dioxane and diethyl ether in a Teflon-line autoclave and placed in the oven for 24 hours at 120 °C. The autoclave was cooled to room temperature to form crystals of Mn-formate, shown in Figure 7-1. Mn-formate has an inverted symmetry and alternating direction of pores which is further illustrated in the crystal packing. The pores are occupied with 1,4-dioxane molecules. MOFs, by nature, are capable of encapsulating guests in their pores, which during solvothermal synthesis is solvent molecules. Pyrolysis of Mn-formate at 400°C under a N₂ atmosphere for results in the oxide MnO:Mn₃O₄ that was characterised further before application in a Li-ion coin cell.

7.1.1 Phase and Morphological Analysis

This process of degassing is the removal of volatile substituents via thermal processes. Here the degassing process eliminated the volatile organic solvent molecules from the MOF cavities. The Thermogravimetric analysis (TGA) measured and shown in Figure 7-2 displays the decomposition of Mn-formate to MnO:Mn₃O₄ where complete MOF to oxide conversion is observed.

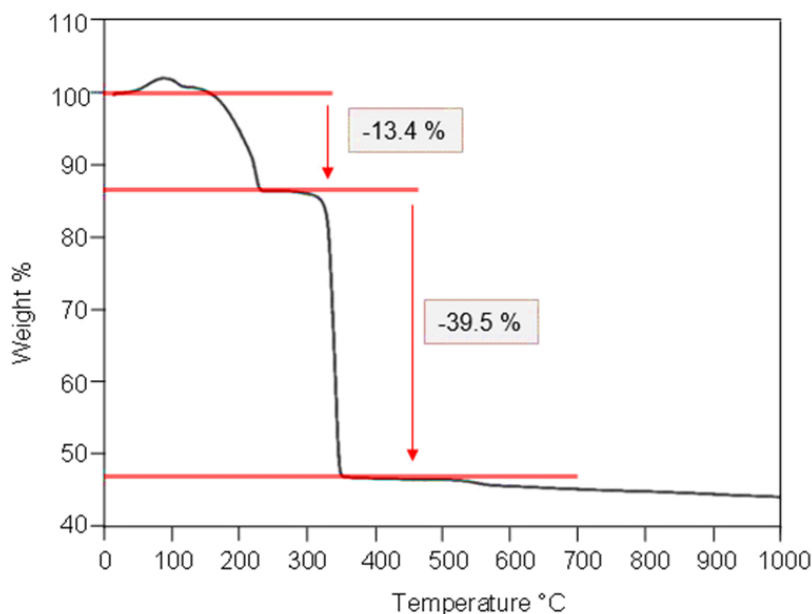


Figure 7-2 TGA analysis of Mn-formate carried out under N₂ at a rate of 5 °C/min from 0 to 1000 °C showing the mass loss that leads to the decomposition of the MOF to the oxide.

A sample of Mn-formate was used for TGA analysis to find the minimum temperature to form the oxide. From this analysis, it was observed that between 150 °C and 220 °C there is an initial mass loss occurring of 13.4% which corresponds to the liberation of dioxane molecules from the MOFs porous structure. Dioxane has a boiling point of 101 °C which further supports solvent evacuation early in the thermal analysis. Following the removal of dioxane (C₄H₈O₂), there is a range of 60 °C from 225 °C to 285 °C where the Mn(HCO₂)₂ MOF structure remains stable.

Continuous heating results in the rapid decomposition of the materials to the resultant oxide with a mass loss of 39.5% from 86.6 % to 47.1 % between 320 and 350 °C. During this process, there is the release of water and carbon dioxide, and the residual weight is attributed to the degradation product which is Mn^{II}O. It should be noted that heating to higher temperatures, using inert gases/air, or increasing the ramping rate, can cause oxidation from Mn^{II}O to Mn^{III}₂O₃, Mn^{II/III}₃O₄ or Mn^{IV}O₂.

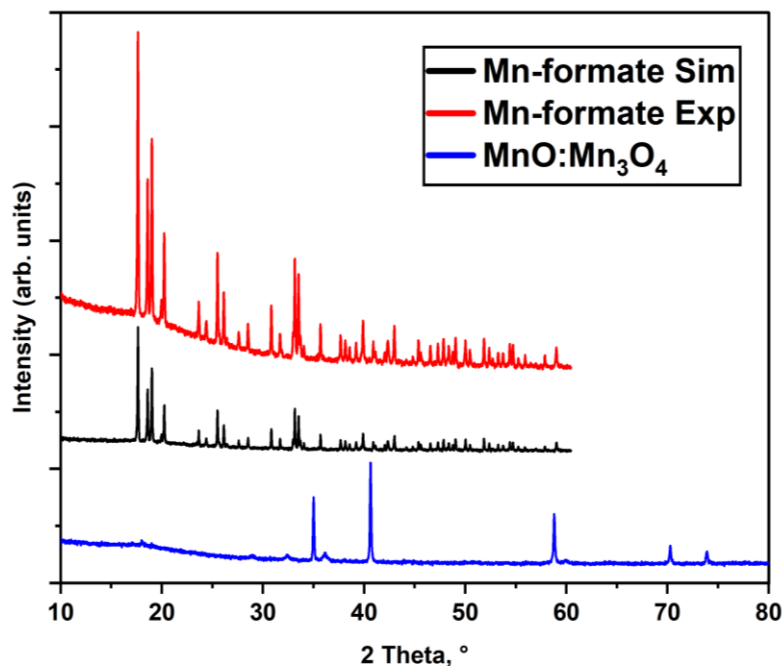


Figure 7-3 Stacked PXRD patterns of the simulated pattern Mn-formate Sim (black), synthesised Mn-formate-Exp (red) and the product of pyrolysis MnO:Mn₃O₄ (blue).

The PXRD pattern for Mn-formate Exp is shown in red in Figure 7-3 and matches the simulated pattern Mn-formate Sim shown in Figure 7-3. This proves the MOF was synthesised in bulk purity. The transition from the complex to the oxide is also shown to be successful by the formation of a combination of the crystalline phases MnO:Mn₃O₄ (blue diffractogram in Figure 7-3). These phases were confirmed by further characterisation through a Rietveld analysis shown below in Figure 7-4.

Rietveld analysis of MnO:Mn₃O₄ clarifies the main phase presented is MnO (refined in the space group Fm-3m). The additional phase is matched to Mn₃O₄, although only as a structural model due to weak reflections. However, the additional peaks fit with all additional reflections.

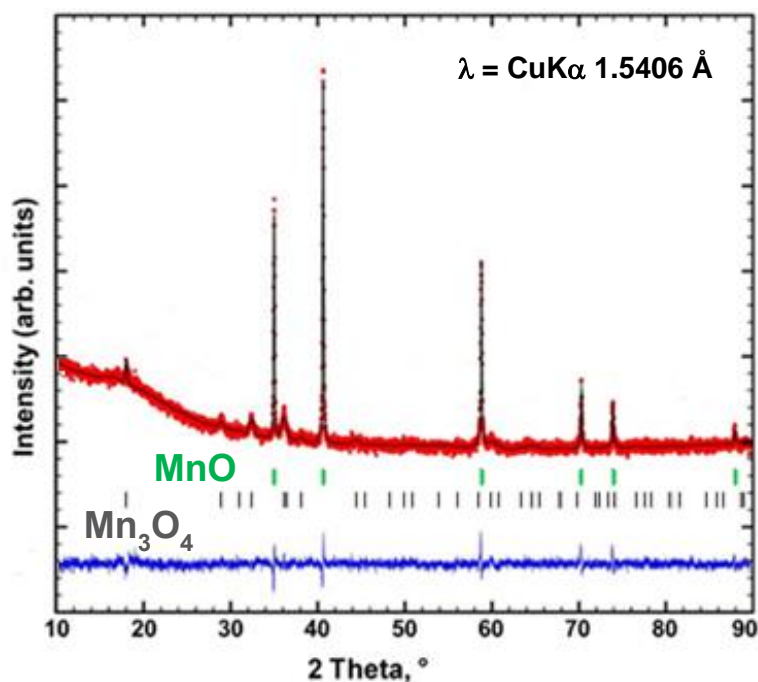


Figure 7-4 Rietveld analysis of MnO:Mn₃O₄ showing data points (red circles), calculated profile (black line), Bragg peak positions for MnO (black vertical lines) and Mn₃O₄ (grey vertical lines), and the difference profile (blue line).

MnO crystallises in the cubic crystal system Fm-3m, where the Mn^{II} is bonded to six equivalent O²⁻ atoms with equivalent bond lengths of 2.22 Å and lattice parameters of 4.45 Å. This forms a mixture of edge- and corner-sharing MnO₆ octahedra. This rock salt structured oxide is made up of non-tilted MnO₆ octahedra. Mn₃O₄ has a spinel structure that crystallises in the tetragonal space group I4₁/amd with lattice parameters a= 5.76 Å and c= 9.47 Å. Mn^{II} is bonded to four O²⁻ atoms to form MnO₄ tetrahedra in the tetrahedral positions of the spinel structure, and Mn^{III} is bonded to six O²⁻ to form MnO₆ octahedra in the octahedral positions of the spinel structure.

SEM images shown in Figure 7-5 show that MnO:Mn₃O₄ formed a sponge-like surface morphology after pyrolysis because of the release of gases such as CO₂, H₂O and dioxane. Pyrolysis of porous compounds can result in this type of morphology which is useful when preparing high surface area electrodes for maximum electrolyte/electrode contact. This type of morphology has been reported many times for manganese oxide materials.

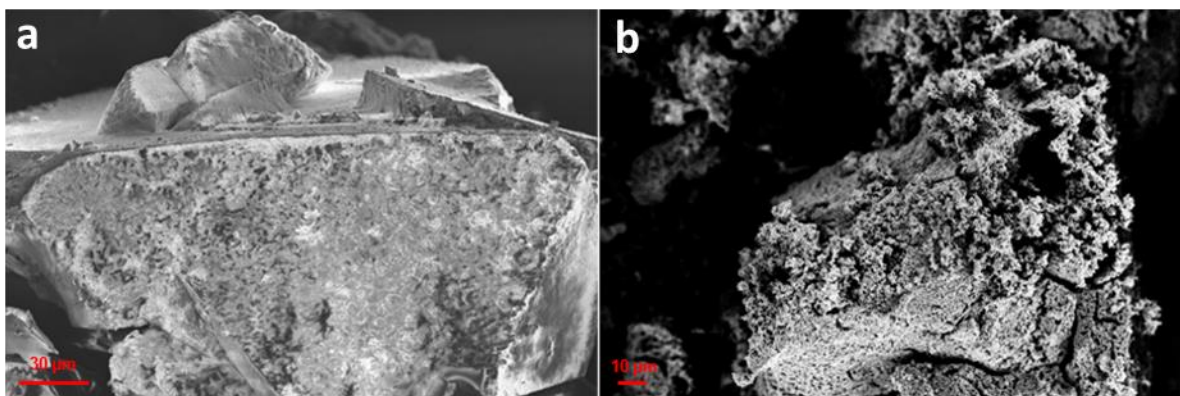


Figure 7-5 SEM images showing the difference in morphology of a) Mn-formate and b) MnO:Mn₃O₄.

Upon magnification on the surface of the oxide in Figure 7-6, there appears to be many defects in the form of smaller adsorbed particles/agglomerates on their surface. This is an indication of a few possibilities; a) a disturbance in the oxide formation causing the uneven surface of the oxides b) the adsorption of an amorphous material on the crystalline surface or c) crystalline material adsorbed on the amorphous oxide surface.

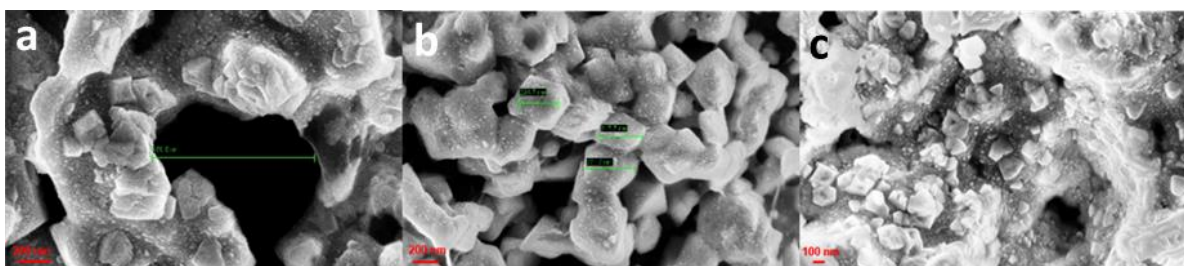


Figure 7-6 a, b, c Magnified SEM images of MnO:Mn₃O₄ at 200 and 100 nm showing the surface morphology of the oxides.

Although uniform pore sizes are not formed for this compound, the spongy morphology seen here has been reported often in literature to result in high surface areas. The irregular pore sizes range from 200 nm to 2 µm. An example is shown in Figure 7-6 where a channel of >900 nm is recorded. Each individual particle is observed to be approximately 200 to 300 nm in diameter. As a result of the varied particle sizes and morphologies, the surface area of this oxide available for electrochemical interaction is considered to be theoretically high, therefore making it a suitable candidate for trial as an electrode material in an energy storage device. Brunauer-Emmett-Teller surface area analysis was carried out at the University of Durham and the results are provided below in Figure 7-7.

The sample was degassed at 200 °C for 16 hours under dynamic high vacuum (10^{-6} mbar) on a Micromeritics 3-Flex gas sorption analyser prior to analysis. The surface area was calculated over the British Standard BET range (P/P₀ 0.05 – 0.3).

Surprisingly, the uptake indicates that the sample was not porous with a negligible BET surface area of $0.7282 \pm 0.0723 \text{ m}^2/\text{g}$. Regardless, $\text{MnO}:\text{Mn}_3\text{O}_4$ samples were still prepared for electrochemical cycling.

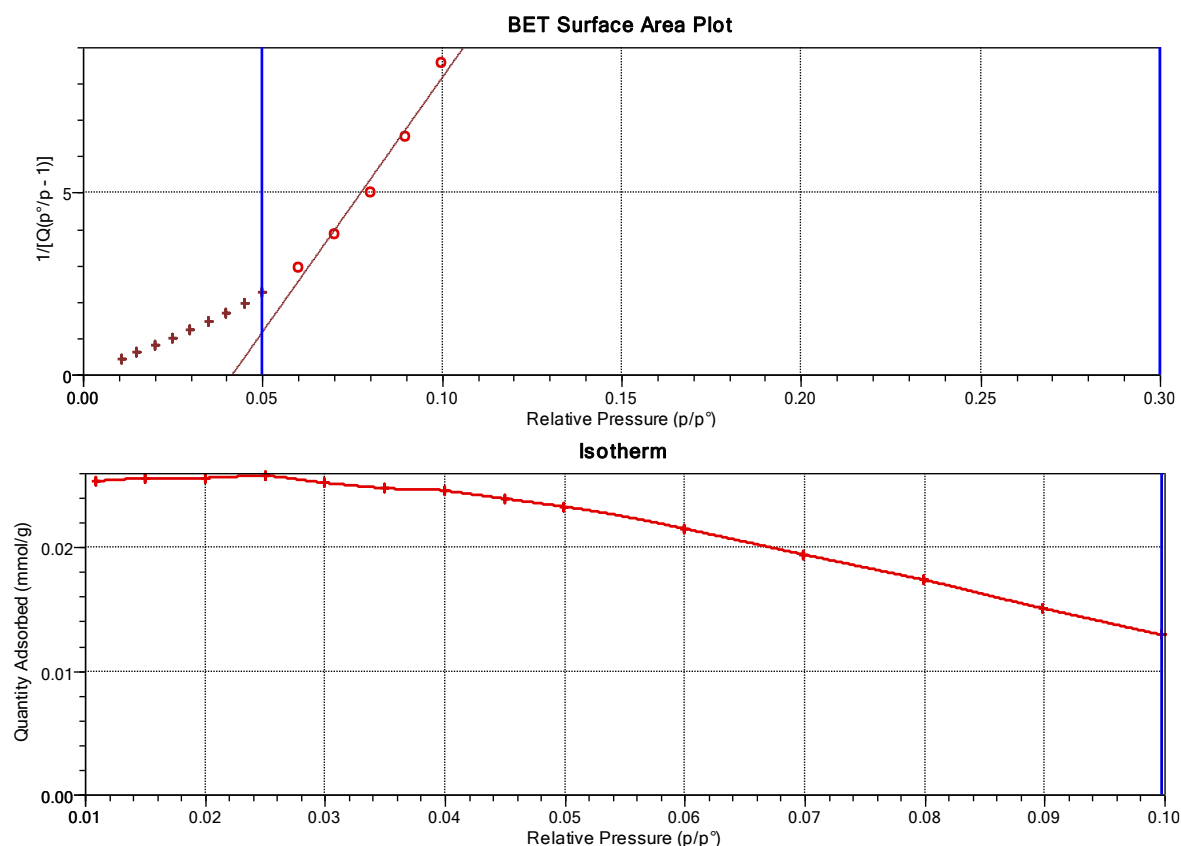


Figure 7-7 BET surface area (top) and isotherm (bottom) plots for $\text{MnO}:\text{Mn}_3\text{O}_4$. These graphs show insignificant uptake of the material and suggests the particles are non-porous.

7.1.2 Electrochemical Analysis in a Li-ion Coin Cell

Typically, MnO is not the most favourable phase for battery electrode applications. Based on the conversion reaction of manganese oxides, research tends to favour the use of MnO_2 which has a high theoretical capacity of 1230 mAh g^{-1} . This is followed by Mn_2O_3 , Mn_3O_4 , and then MnO which have theoretical capacities of 1018 mAh g^{-1} , 936 mAh g^{-1} , and 750 mAh g^{-1} , respectively.

Cyclic voltammetry (CV) and galvanostatic charge/discharge (GCD) cycling are two methods which can be used to filter electrodes that may have a high capacity, stable long-term cycling, and commercial potential from those which are quickly degrading or showing instability in their performance. The cyclic voltammetry data in Figure 7-8 outlines the first 3 cycles of stable redox behaviour associated with this $\text{MnO}:\text{Mn}_3\text{O}_4$ electrode. Measurements were taken from 0.05 V to 3 V vs. Li^+/Li . During the first

discharge cycle, the SEI is formed on the surface of the working electrode as a result of electrolyte decomposition.

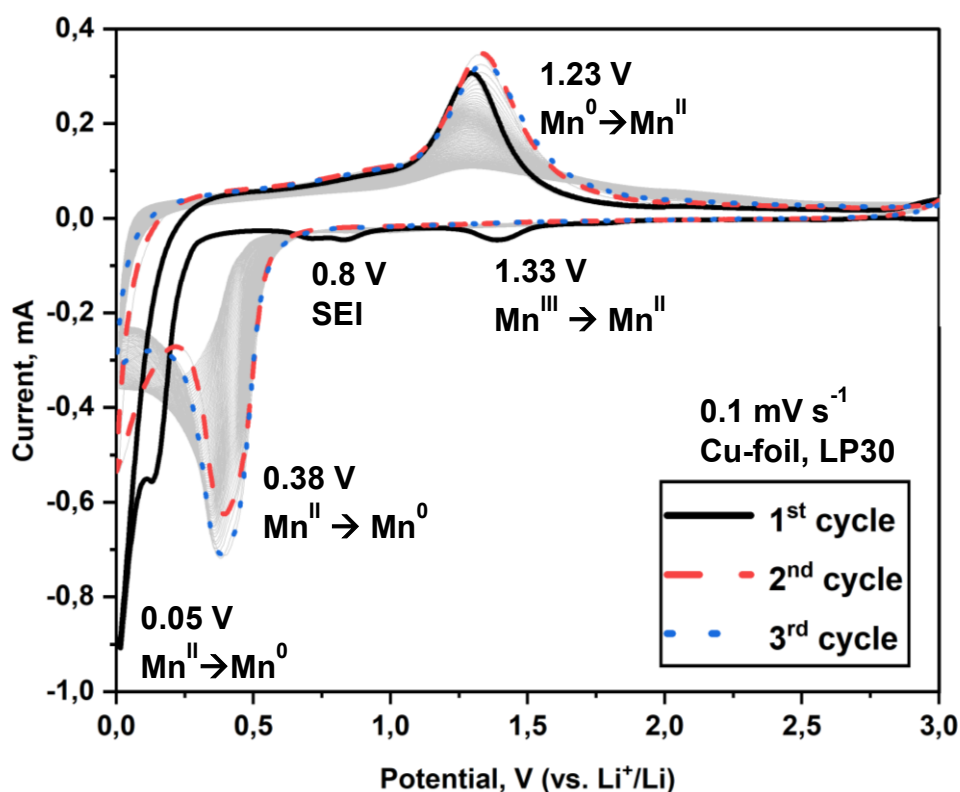


Figure 7-8 Cyclic voltammety measured between 0.05 V and 3 V at 0.1 mV s⁻¹ highlighting the 1st, 2nd, and 3rd cycles shown in black, red, and blue, respectively. The remaining 100 cycles are shown in light grey.

Post SEI formation, from the 2nd cycle onwards characteristic oxidation at the peak potential of 1.23 V and reduction at the peak potential of 0.375 V were recorded. Although the peak positions remained at the same potential, the current steadily decreased as the number of cycles increased pertaining to the amount of reversible chemical reactants remaining in the cell. Fewer electrons are therefore required thus the current (charge per unit time) declines accordingly. This gradual degradation can be further explained by studying the galvanostatic charge-discharge (GCD) data.

Specific capacity was measured for 101 galvanostatic charge-discharge cycles at a current density of 100 mA g⁻¹. Figure 7-9 shows an initial capacity of 1050 mAh g⁻¹. This is followed by a capacity fade during the first discharge cycle to 572 mAh g⁻¹. The capacity fades further to 515 mAh g⁻¹ for the 3rd cycle, and by the 10th cycle falls to 409 mAh g⁻¹.

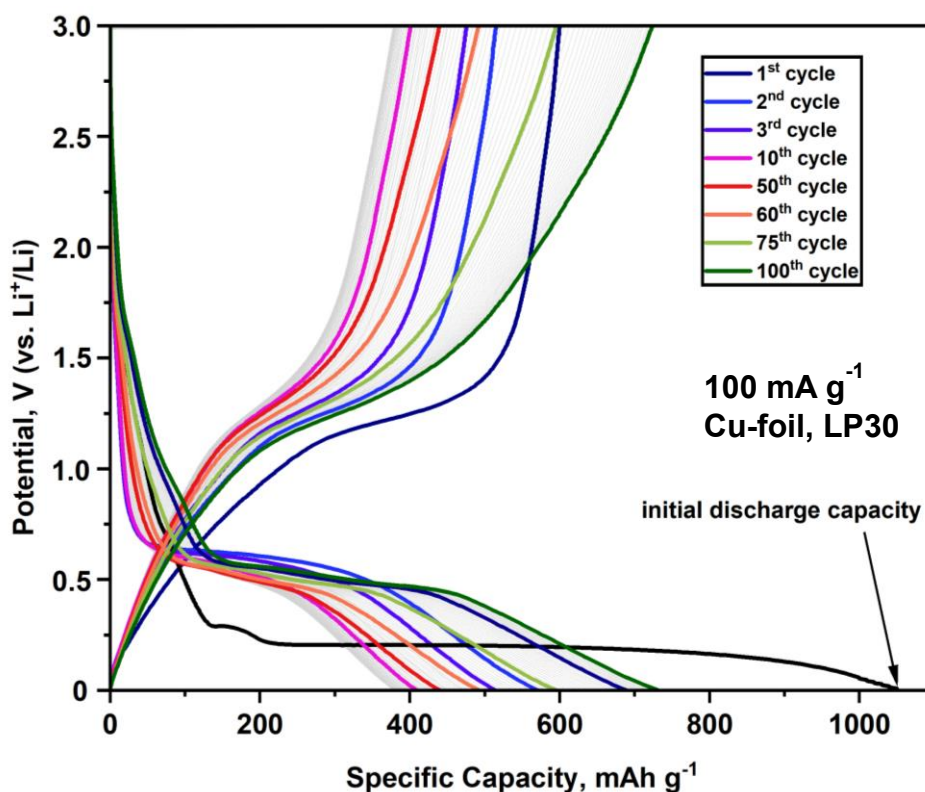


Figure 7-9 Galvanostatic charge-discharge cycling between 0.05 V and 3 V showing both the changes in capacity and the voltage plateau profiles for the 101 cycles measured using MnO:Mn₃O₄ as the active electrode material in a lithium-ion battery. These cycles were measured at a current density of 100 mA g⁻¹.

The capacity gradually continues to fade but by the 50th cycle the capacity increases to 441 mAh g⁻¹. This indicates that the degradation product could have better electrochemical activity. By the 60th cycle, the capacity continues to increase to 493 mAh g⁻¹. The 75th cycle reaches 596 mAh g⁻¹, the 90th cycle reaches 687 mAh g⁻¹ and the final cycle reported has a capacity of 732 mAh g⁻¹. This behaviour of the electrode where the electrode appears to gradually degrade until the structure/morphology stabilises, poses many questions about the nature of the degradation product. If there are new interactions taking place within the cell that are contributing to the increasing capacity, then monitoring this process in-situ would be important to conclude which materials are responsible.

Whilst forcing the electrode to reduce close to 0 V, ex-situ PXRD patterns were collected at 1.0 V, 0.22 V and 0.01 V. The stacked patterns in the Figure 7-10 should show a decrease in intensity as we near the metallic state. However, this is not observed. Instead, there are no drastic changes in the intensity of the patterns unless forced to the metallic nano-domain when held at 0 V.

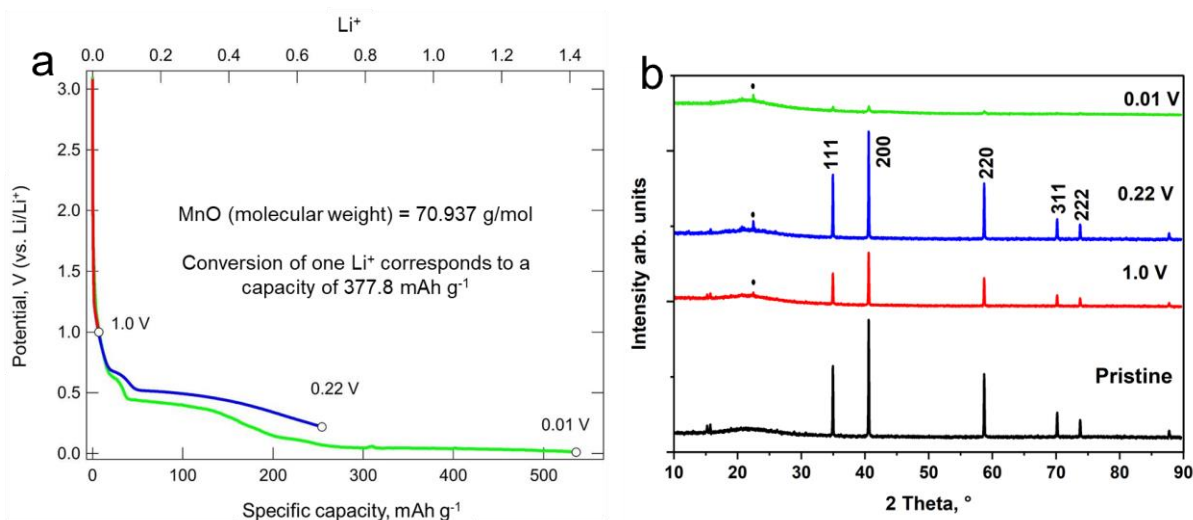


Figure 7-10 The reduction profile to the left shows that as MnO:Mn₃O₄ is reduced in the electrode from 3 V to 0.22 V a capacity is observed with a plateau at ~0.5 V. The inset shows the ex-situ PXRD measured at three voltages where the black pattern is the pristine sample, reducing to 1 V is shown in red, reducing further to 0.22 V is shown in blue and reducing fully to 0.01 V is shown in green. These patterns show there is no reduction of the crystalline Mn^{II} to Mn⁰ observed unless reducing to 0 V. Measured by Dr. Sylvio Indris.

High energy in-situ PXRD synchrotron studies were carried out at ALBA, Barcelona. This investigation is typically used to track the chemical redox reactions that occur during the cycling of the cell. A first glance comparison between the lithiated and delithiated XRD patterns show the transition of certain reflections. The chemical changes are recorded through XRD monitoring. As observed, the MnO remains constant during a full cycle. The lithium is converted to Li₂O. This suggests there is another mechanism involved which is invisible to X-ray diffraction that presents itself in an amorphous state.

A closer look at the first 40 gradual diffraction patterns taken in-situ during a cycle measured at the synchrotron, provides further information on the internal chemical reactions for this electrode. Figure 7-11 briefly shows that there are few changes in the PXRD patterns. The green dots in the pattern represents the reflections for MnO. Other reflections correlate to Cu-foil and lithium and are discussed later in the Rietveld structural refinements.

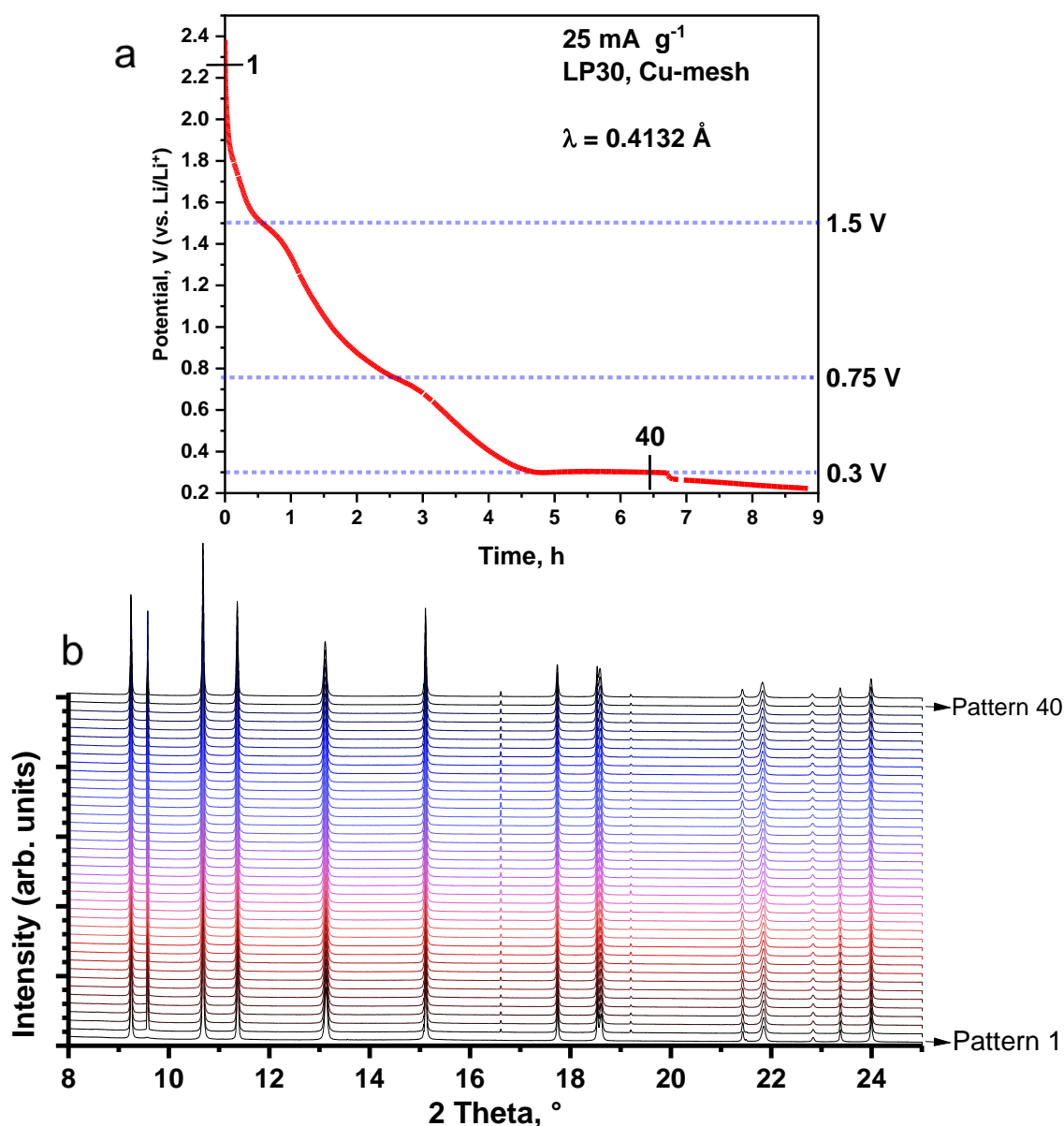


Figure 7-11 (a) The electrochemical discharge data of the cell measured (b) In-situ PXRD measured at ALBA synchrotron during the delithiation cycle. The PXRD shows the first 40 patterns measured. Measured by members of Prof. Helmut Ehrenberg's group at ALBA synchrotron.

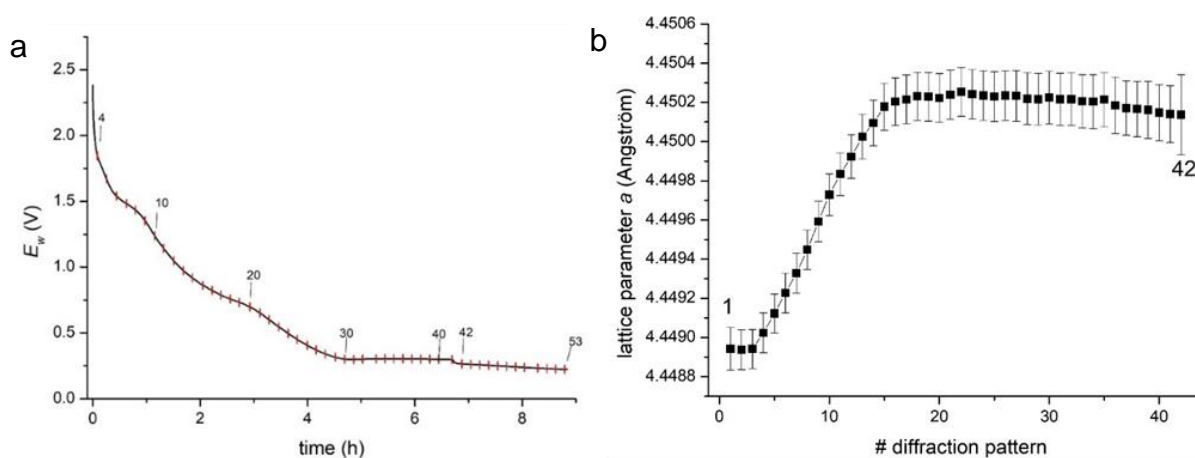


Figure 7-12 (a) electrochemical discharge data of MnO:Mn₃O₄ showing the time taken to discharge the cell while in-situ PXRD patterns were measured. (b) indexed diffraction patterns used to determine the lattice parameters *a* for patterns 1 through 42. Measured by members of Prof. Helmut Ehrenberg's group at ALBA synchrotron.

The data in Figure 7-12 shows the discharge potential between 2.4 V to 0.23 V over an 8 h period. 53 PXRD patterns were taken during this process at regular intervals to monitor the reduction of the electrode material. Rietveld analysis of pattern 1 in Figure 7-13, shows the presence of the MnO crystalline phase in high intensity. As this pattern was taken from the pristine sample before the EC measurement were started, a high intensity of the oxide phases is expected. Further contributions are present from the Cu⁰ foil as well as small contributions from the Li counter-electrode.

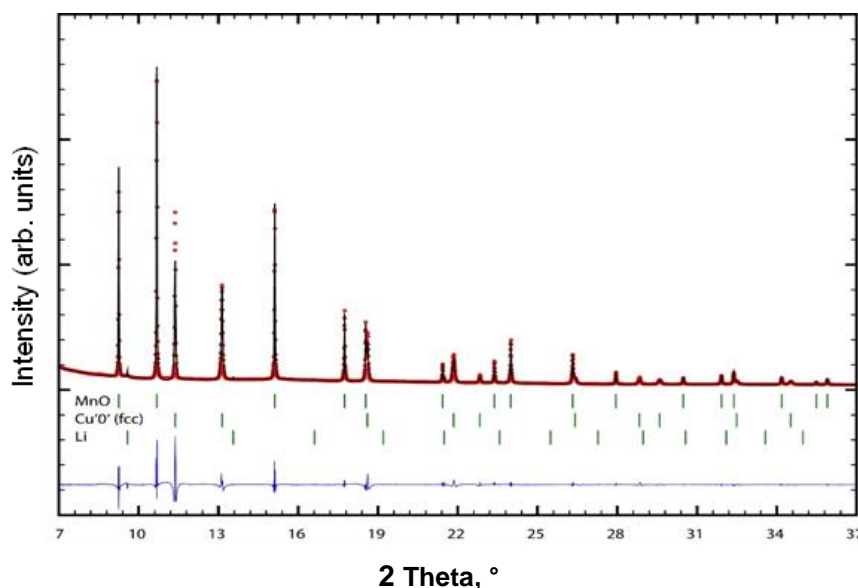


Figure 7-13 Rietveld structural analysis of pattern 1 from the EC data measured at ALBA for MnO:Mn₃O₄ showing the reflections associated to MnO, lithium and Cu-foil. Analysis by Dr. Björn Schwarz.

Rietveld analysis of pattern 40 shows the reflections of MnO are still present, lot of difference in the reflections compared to pattern 1. By looking at the lattice parameters in Figure 7-12, a slight change is observed from 4.4489 Å (pattern 1) to 4.4502 Å (pattern 17) which is merely a difference of 0.0013 Å. As the EC-curve plateaus beyond 30 cycles, there is no significant change in the lattice parameters that can connect with the events of the EC curve.

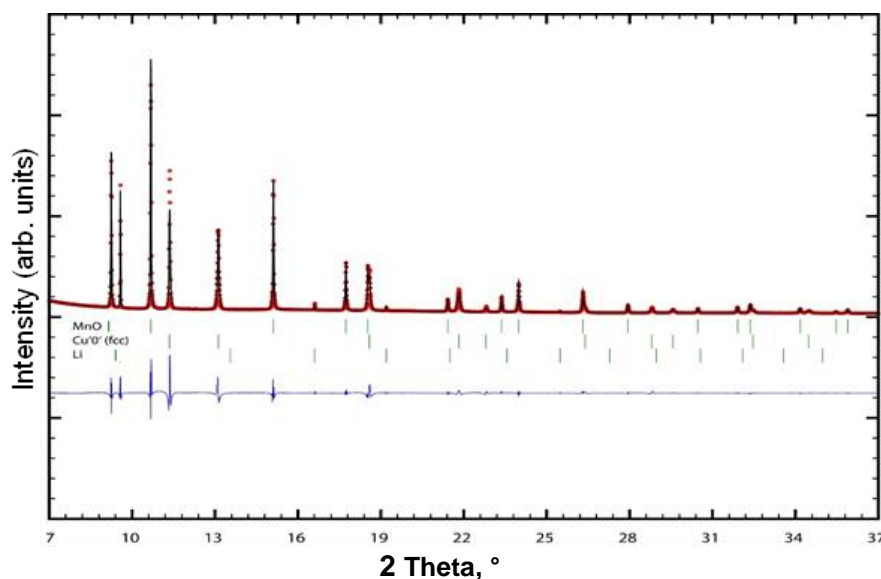


Figure 7-14 Rietveld structural analysis of pattern 40 from the in-situ EC data measured at ALBA for MnO:Mn₃O₄ showing that the reflections for MnO do not change as the cell is delithiated. Analysis by Dr. Björn Schwarz.

What should be seen as a reduction in intensity of the MnO:Mn₃O₄ (which would correlate to a reduction in quantity as Mn^{II} is reduced to Mn⁰), instead shows that no phase changes are occurring. However, reflections for Li to Li⁺ are visible (for example between 9° and 10°) confirming that there is a conversion taking place at the working electrode.

In-situ EXAFs were carried out at DESY Light Source for the MnO:Mn₃O₄ electrode and the resultant data is shown in Figure 7-15. The data shows a shift in binding energy from Mn^{III} to Mn^{II} during the reduction. From here, the hypothesis can be formed that the operando XAS proposes the crystalline MnO phase is an inactive phase during the charge/discharge processes as we see a shift from Mn^{III} to Mn^{II} during cycling. At 1.5 V, absorption at 6558 eV corresponds to the local energy of Mn^{III} from the Mn₂O₃ phase. During the reduction to 0.41 V, a change in binding energy to 6550 eV supports the conversion of Mn^{III} to Mn^{II}. This is a key observation as it confirms the presence and activity of the Mn^{III} oxide. In fact, it is observed that during the discharge, there is an approximate 15 h plateau shown in the V/T graph. This suggests a structural modification due to the applied current and can be assumed to correspond to changes occurring to the amorphous oxide.

The Fourier transform (FT) likewise allows the calculation of bond distances, which further confirm the presence of Mn^{III} (tetrahedral Mn-O 2.05 Å, octahedral Mn-O 1.85 Å) and Mn^{II} (octahedral Mn-O 2.34) at the potential of 1.5 V.

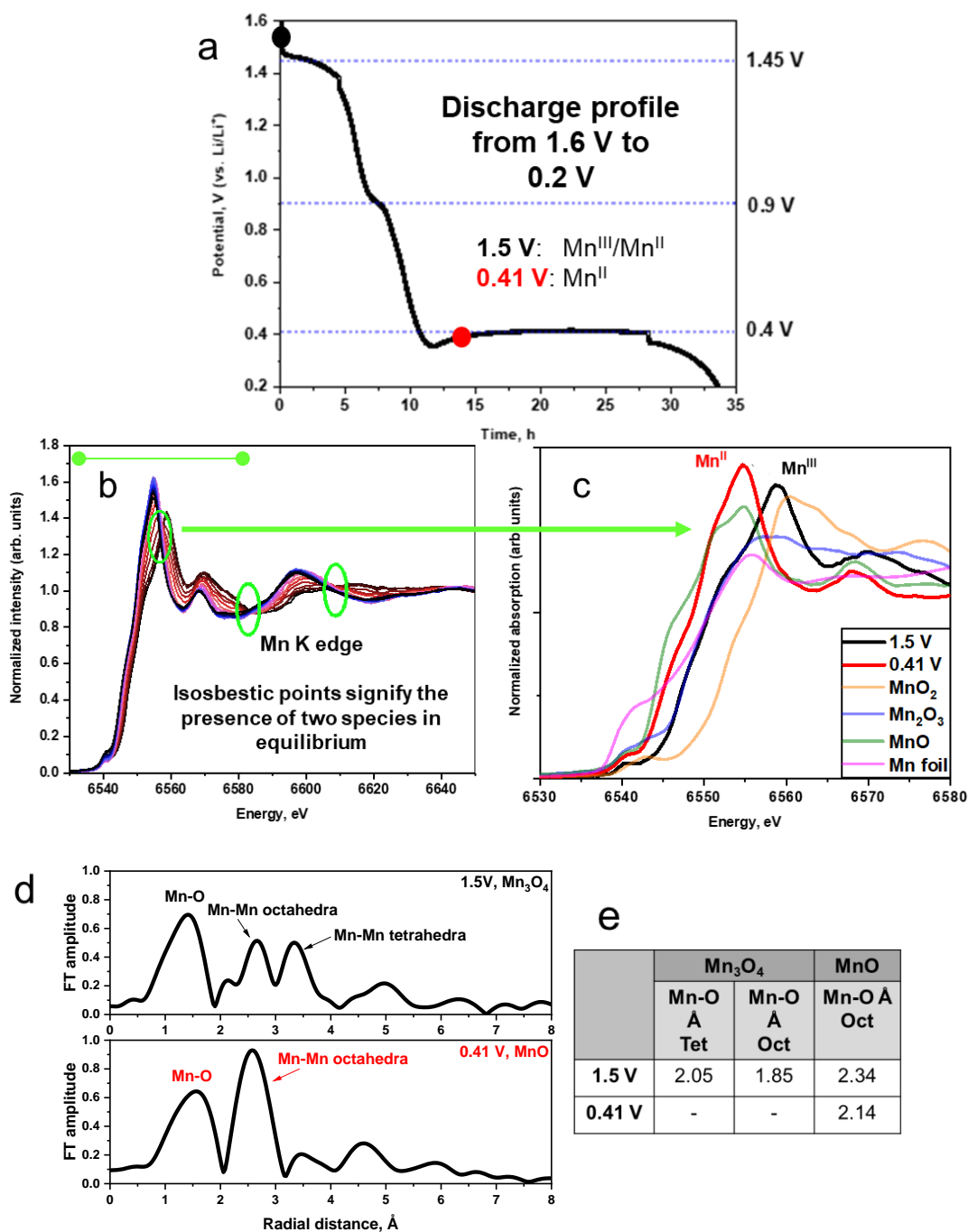


Figure 7-15 (a) electrochemical discharge profile (b) In-situ EXAFS of the local environment around the Mn k-edge in the MnO:Mn₃O₄ electrode material showing the isosbestic points (c) XANES region showing the phase transition during the first discharge process (d) Fourier transform (FT) of the EXAFS and (e) a table to occur the bond distances obtained from the FT. Measured at the DESY light source and analysed with the contributions of Dr. Angelina Sarapulova.

7.1.3 Magnetisation Studies

DC magnetisation measurements were carried out by Dr. Björn Schwarz to support the electrochemical data. Magnetisation allows the intrinsic properties of the material to be determined and thus allows for a qualitative phase analysis of our sample. AC data are not required for the purposes of this analysis.

On an 11.1 mg pristine sample, ZFC and FC measurements were carried out at 500 Oe shown in Figure 7-16. Paramagnetic behaviour was observed from 350 K to 120 K. At 120 K, there is a slight decrease in magnetisation which is a typical occurrence seen for MnO that indicates a paramagnetic to antiferromagnetic transition. This is denoted as T_N (Neel Temperature) and is characteristic for the presence of MnO. Furthermore, at 40 K there is an increase in magnetisation followed by a bifurcation below this temperature indicating a ferro-/ferrimagnetic order below T_C (Curie Temperature) ascribed to the presence of Mn_3O_4 . Below 13 K, there is a marked divergence in the ZFC/FC that could potentially point to a free paramagnetic centre or a defect in the oxide material. The inverse susceptibility plot was used for the Curie-Weiss fit.

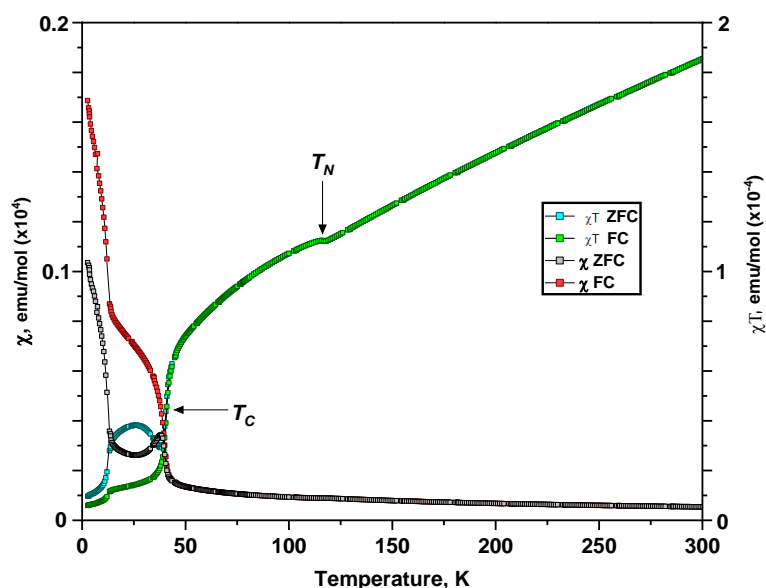


Figure 7-16 χ vs. T and χT vs T graphs of $MnO:Mn_3O_4$ measured from 2K to 300K at 500 Oe. Measured and analysed with contributions from Dr. Björn Schwarz.

Looking at the $1/\chi$ vs T plot, a linear pattern is observed from 0 to 300 K with a small bifurcation at T_c indicating antiferromagnetic behaviour. However, no saturation is reached, even by 300 K.

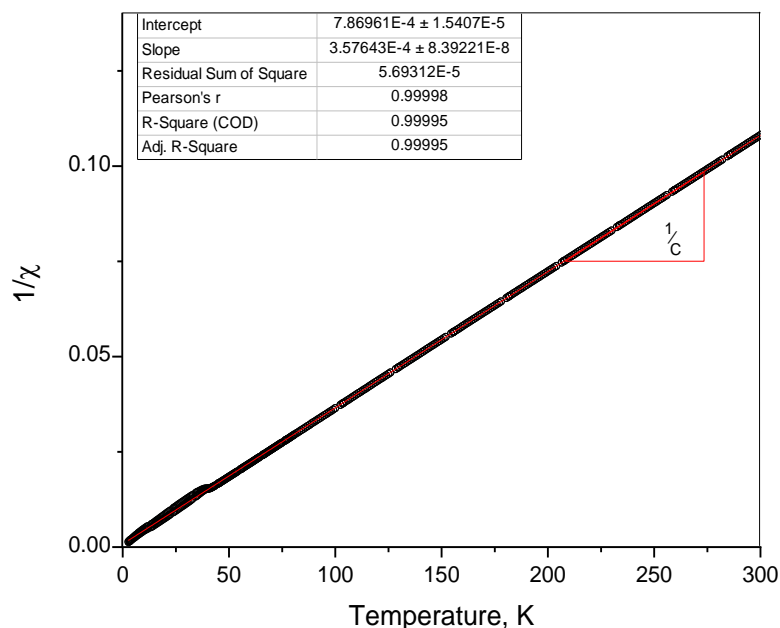


Figure 7-17 $1/\chi$ vs T plot for the inverse susceptibility with additional linear fitting calculating an R^2 value of 99.99%. Analysed with the contributions of Dr. Björn Schwarz.

Assuming that we have pure MnO, an effective paramagnetic moment of $4.68 \mu_B$ per Mn^{II} ion is determined experimentally. However, this is not in agreement with the expected spin only moment of $5.92 \mu_B$ per Mn if the Mn is present as Mn^{II} . If instead we assume that the powder exclusively consists of Mn_3O_4 (or equivalently $MnO_{1.3}$) we obtain an effective moment of $4.87 \mu_B$ that is again not in agreement with theoretical spin only value of $Mn^{2.6+}$ (as $1/3 Mn(II) + 2/3 Mn(III)$) of $5.26 \mu_B$.

Table 5 Different phases of Mn_xO_y and their calculated effective magnetic moments.

	Molar mass (g/mol)	Effective moment per Mn (μ_B)
Mn(II)O	70.9	4.68
Mn(II)	Spin only →	5.92
Mn_3O_4 or $MnO_{1.3}$	75.5	4.87
Mn(2.6) means $1/3 Mn(II) + 2/3 Mn(III)$	Spin only →	5.26
$Mn(III)_2O_3$ or $Mn(III)O_{1.5}$	79.0 ($MnO_{1.5}$)	4.92
Mn(III)	Spin only →	4.9

Supposing the oxide sample consists purely of Mn_2O_3 , we obtain an effective moment of $4.92 \mu_B$ which agrees with the theoretical spin-only value of $4.9 \mu_B$ for Mn^{III} . By taking into consideration the effective magnetic moment μ_B , it is assumed that the majority phase should be considered as Mn_2O_3 with contributions from MnO and Mn_3O_4 . Up to 70000 Oe (7T), no saturation of the magnetisation is reached.

Therefore, from the magnetisation measurements and determination of the effective magnetic moments we make the hypothesis that most of the sample should be considered as Mn_2O_3 since the Mn^{III} ions exhibit the effective magnetic moment of $4.9 \mu_B$. The phase identified as MnO in the PXRD represents the highly crystalline phase with small amounts of Mn_3O_4 detected. It is important to note that only very small amounts of Mn_3O_4 are required to cause ferromagnetic signals at 40 K. Mn_2O_3 appears to have an amorphous structure that prevents it from being detected by PXRD and is considered to make up majority of the sample.^[120]

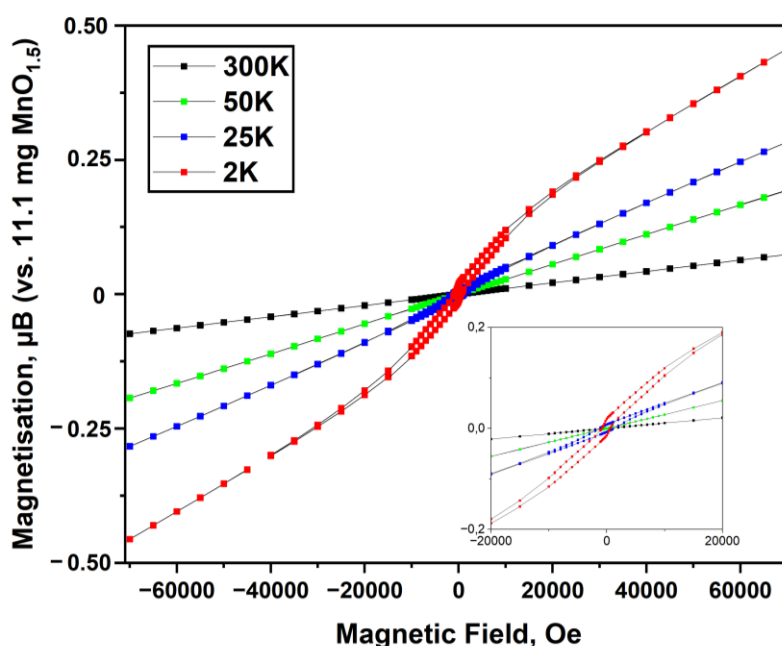


Figure 7-18 Magnetisation showing the open hysteresis at 2 K as well as ferromagnetic ordering above 25K. Measured and analysed with contributions from Dr. Björn Schwarz.

Field scans were performed at 300 K, 50 K, 25 K, and 2 K with a magnetic field $\mu_0 H = 70,000$ Oe (7T). At 2 K and 25 K, a hysteresis is observed. Although MnO is antiferromagnetic, nano oxides of MnO can exhibit ferromagnetic behaviours. Mn_2O_3 which is the additional amorphous phase, exhibits paramagnetic behaviour because of its four unpaired electrons. As can be seen in Figure 7-18, there does not appear to be a saturation of the magnetisation by 70,000 Oe.

7.2 Mn₁₂ Acetate: From an SMM to an Electrode

[Mn₁₂(CH₃COO)₁₆(H₂O)₄O₁₂].2CH₃COOH.4H₂O, from this point onwards referred to as Mn₁₂OAc, was the first molecule identified to have superparamagnetic behaviour below a certain blocking temperature by Sessoli et al.^[121] This dodecanuclear compound shown in Figure 7-19 consists of 4 Mn^{IV} surrounded by 8 Mn^{III} ions with the manganese atoms linked by triply-bridged oxo-atoms and carboxylates linkers from the acetic acid used during the synthesis. Mn₁₂OAc has a S₄ symmetry and the distorted Jahn-Teller octahedra show the oxidation state of manganese must be mixed valence Mn^{III}/Mn^{IV}. This molecule has been studied extensively for its magnetic properties.^[122] Many variations of the complex have since been reported by changing the ligands or the anions, however applications in the field of energy storage systems are sparse.

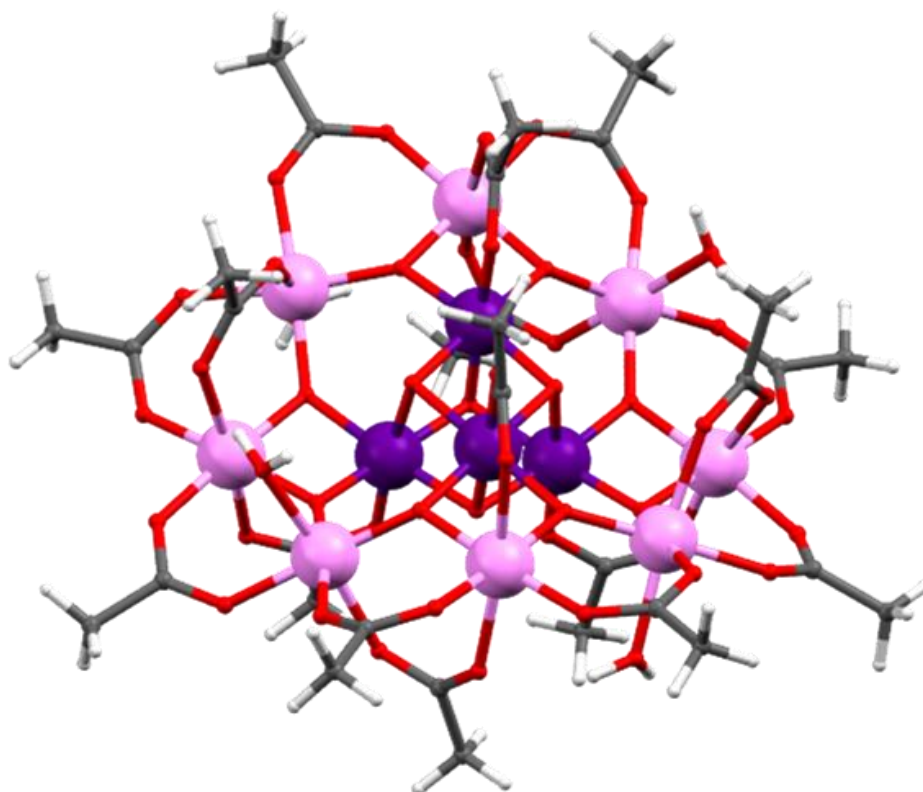


Figure 7-19 The molecular structure of Mn₁₂OAc where the Mn^{IV} ions are shown in purple, Mn^{III} in pink, O²⁻ in red and C in grey.^[123] The repeating unit shows there are no obvious interactions between the neighbouring clusters in the crystal structure.

Mn₁₂OAc is however synthesised in a similar method to many Mn_xO_y nanomaterials that use a manganese salt and potassium permanganate in a low-pH aqueous solution.^[81, 100, 102, 106, 124] Reproduced from the work of T. Lis, who first published this compound in 1980, Mn₁₂OAc was used as a template to form oxides from a high nuclearity, high valence complex.^[125] Mn₁₂OAc was synthesised by adding manganese acetate and KMnO₄ to dilute acetic acid while stirring, before leaving to

crystallise overnight. The crystals of Mn_{12}OAc were collected and dried before calcining in air at $500\text{ }^\circ\text{C}$ for 6 hours at a heating rate of $10\text{ }^\circ\text{C}/\text{min}$. The product of calcination, $\text{Mn}_{12}\text{OAc-}\alpha\text{-MnO}_2$, was collected for further characterisation.

7.2.1 Phase and Morphological Analysis

TGA analysis in Figure 7-20 shows the temperature at which the decomposition to $\text{Mn}_{12}\text{OAc-}\alpha\text{-MnO}_2$ is successful. By heating the sample to $1000\text{ }^\circ\text{C}$, three clear mass loss steps were observed. The first loss correlates to the degassing of solvents such as acetic acid and water with a gradual mass loss of 11.5% between $75\text{ }^\circ\text{C}$ and $211\text{ }^\circ\text{C}$.

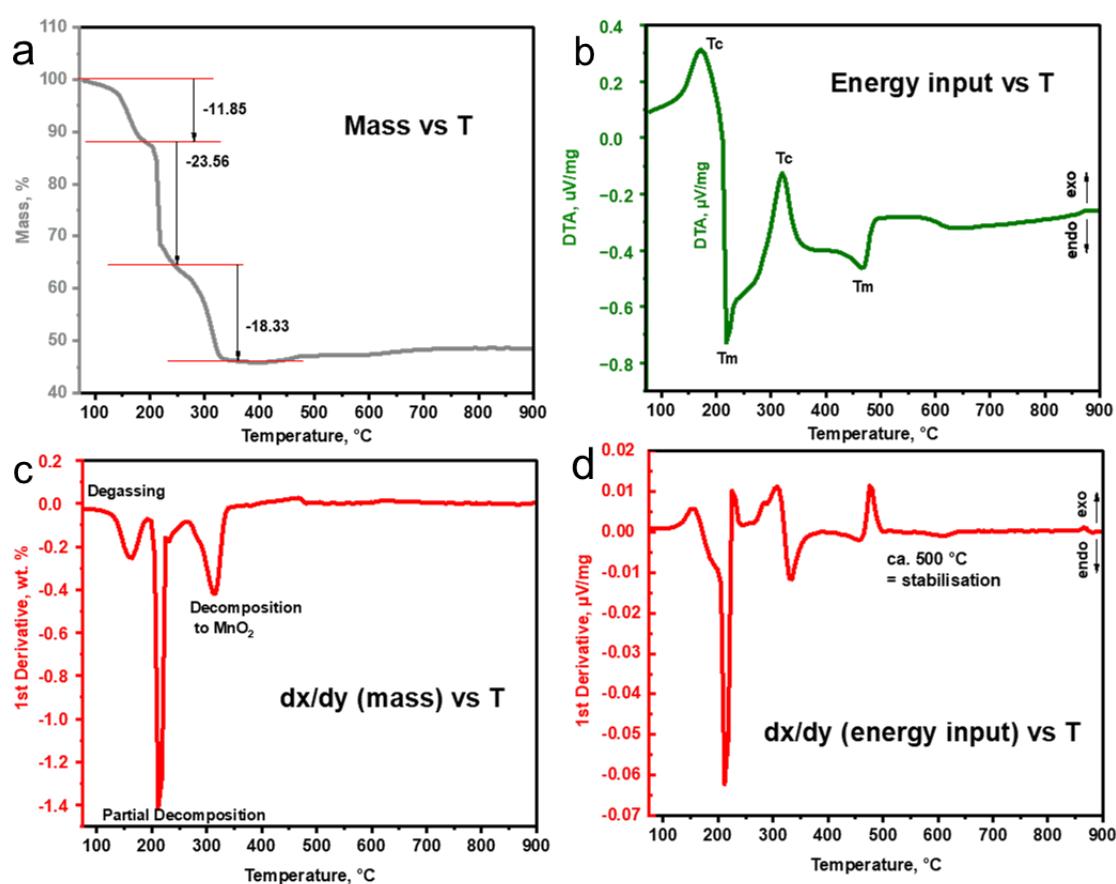


Figure 7-20 Thermal analysis of Mn_{12}OAc from $75\text{ }^\circ\text{C}$ to $900\text{ }^\circ\text{C}$ in air at a rate of $5\text{ K}/\text{min}$. (a) TGA, (b) DTA, (c) TGA 1^{st} derivative and (d) DTA 1^{st} derivative plots are shown.

The second mass loss step corresponds to the formation of $\text{Mn}_{12}(\text{CH}_3\text{OO})_{16}$ via a loss of 23% between $213\text{ }^\circ\text{C}$ and $215\text{ }^\circ\text{C}$. The mass loss step of 18.33% relates to the formation of MnO_2 via a gradually decreasing weight to $336\text{ }^\circ\text{C}$. Further weight changes compensate for phase transitions. The first derivative of the TGA shows the degassing at $162\text{ }^\circ\text{C}$ followed by decomposition at $213\text{ }^\circ\text{C}$ and $314\text{ }^\circ\text{C}$.

The DTA analysis shows a typical glass transition at 173 °C which is followed by endothermic melting at 222 °C that fits with the partial decomposition observed in the TGA. This is followed by crystallisation at 318 °C which aligns to the complete decomposition from complex to oxide. What appears as another endothermic melting at 465 °C can be assigned to the phase changes of the oxide as the temperature increases. DTA analysis supports the TGA observations; melting between 195 °C and 220 °C correlate to the decomposition of Mn_{12}OAc followed by crystallisation shown as the heat input increases in the endothermic direction from 220 °C to 240 °C. This is followed by further crystallisation to 320 °C that corresponds to the formation of MnO_2 . Beyond 320 °C we can assume the higher temperatures are inducing other phases/polymorphs of manganese oxide.

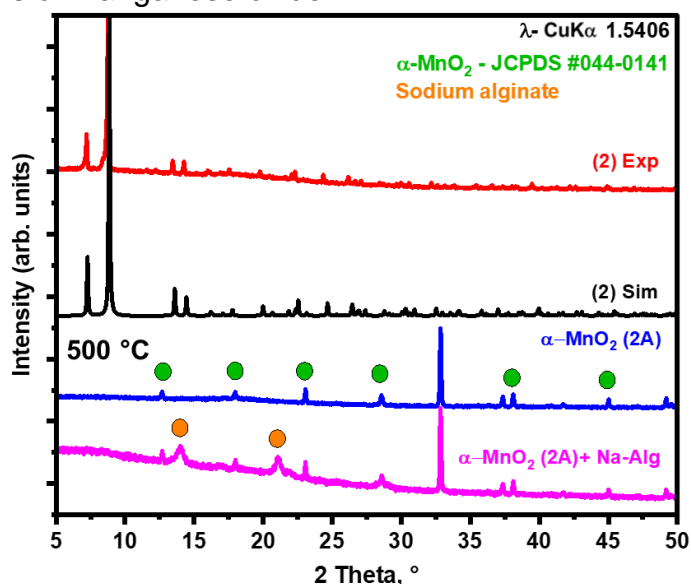


Figure 7-21 Stacked X-ray powder diffractograms of the synthesised Mn_{12}OAc Exp (red) compared to the simulated pattern Mn_{12}OAc Sim (black), Mn_{12}OAc - α - MnO_2 (blue) and Mn_{12}OAc - α - MnO_2 + Na-Alg (pink).

The PXRD reflections shown in Figure 7-21 are in agreement that Mn_{12}OAc was synthesised with bulk purity (red) and the complete conversion to Mn_{12}OAc - α - MnO_2 was successful (blue). In this case, the phase obtained is α - MnO_2 . The oxide was further combined with Na-Alginate and Super P. This is shown in pink in Figure 7-21. The additional broad reflections at 25° and 37° are a result of the binder Na-Alginate (Na-Alg). The risen baseline is a result of the addition of Super-P which is the activated carbon used to increase electrode conductivity. This confirms there is no effect of the additives on the oxide materials while preparing the electrodes.

α -MnO₂, as mentioned previously in chapter 6, consists of a 2x2 tunnel structure composed of edge- and corner- sharing MnO₆ octahedra. This phase crystallises in the tetragonal I4m space group.

Mn₁₂OAc forms large black crystals which can be observed without the need of SEM analysis, shown in Figure 7-22. As synthesised, the crystals form needle-like shapes overnight with lengths up to 0.5 cm. Note: stirring the reaction mixture for longer than 5 minutes during the synthetic procedure results in the formation of a crystalline powder rather than big crystals.



Figure 7-22 Image of Mn₁₂OAc as synthesised showing the large crystals with needle-like morphologies.

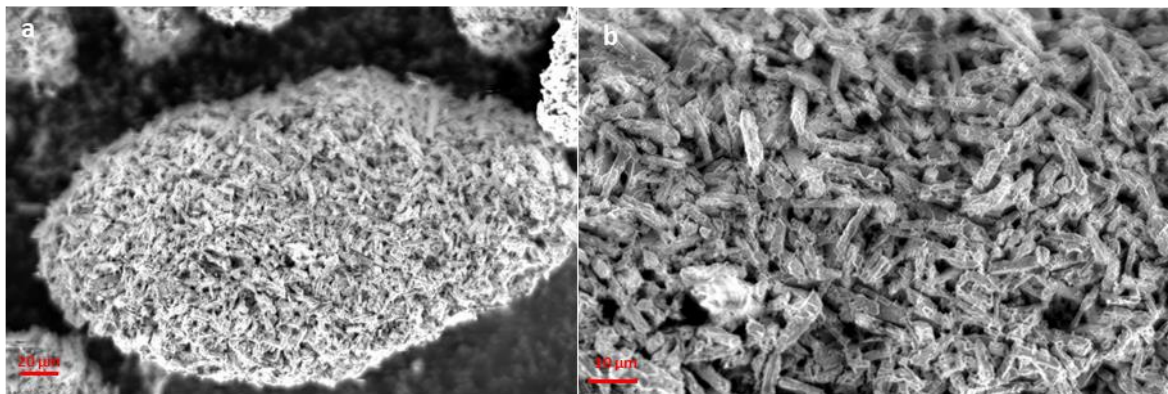


Figure 7-23 SEM images taken of Mn₁₂OAc- α -MnO₂ at scale bars of (a) 20 μ m and (b) 10 μ m (2x mag).

After pyrolysis at 500 °C for 6 h to obtain Mn₁₂OAc- α -MnO₂, the crystallites adopt an intergrown morphology shown in Figure 7-23; the individual particles have rod-like structure which are non-porous. The process of calcination has drastically reduced the particle size to ~10 μ m.

Although the PXRD in Figure 7-21 does not suggest the presence of any impurities related to the KMnO₄ starting material, even a small percentage of unidentified impurities can influence the electrochemical behaviour of the cell by either improving

or reducing the performance. The EDX mapping of the atomic densities shows the distribution of the elements across the surface of an agglomerate of particles.

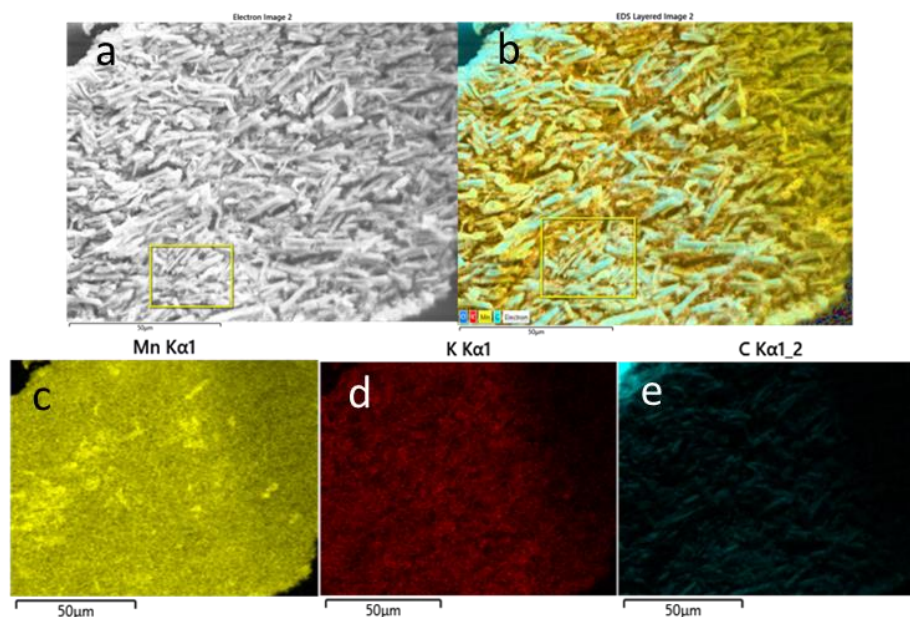


Figure 7-24 EDX mapping of the distribution of Mn, K and C across the surface of a $\text{Mn}_{12}\text{OAc-}\alpha\text{-MnO}_2$ particle. (a) electron microscope image (b) EDX layered image showing the overlapped of key elements (c) distribution of Mn (d) distribution of K and I distribution of C.

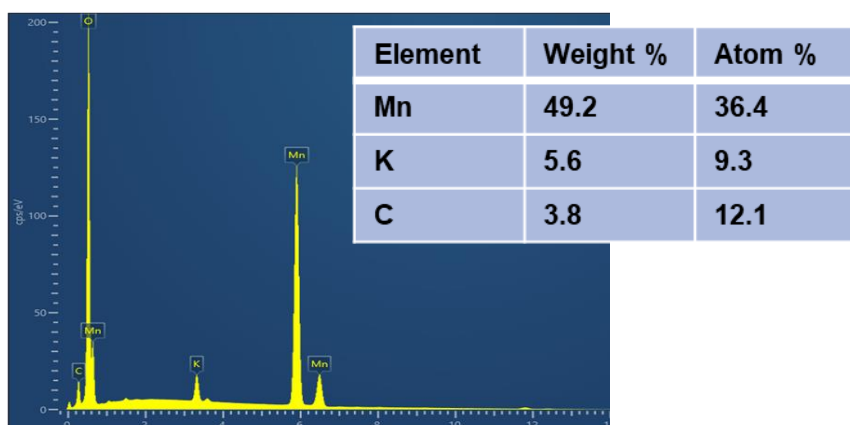


Figure 7-25 Elemental analysis calculated on $\text{Mn}_{12}\text{OAc-}\alpha\text{-MnO}_2$ showing the relative intensities of Mn, O, K and C across the surface of the particle shown in **Figure 7-24**.

Looking at the EDX layered image, the majority of the surface of the sample consists of Mn (yellow), with a sensible quantity of C (blue), and K (red) present. Looking at the PXRD pattern presented earlier in Figure 7-21, the K in the sample does not contribute to any particular crystalline phase such as KMnO_4 or K_2MnO_2 in the bulk material. An EDX analysis was carried out to observe the presence, if any, of remaining K in the $\text{Mn}_{12}\text{OAc-}\alpha\text{-MnO}_2$. The EDX elemental mapping calculated in Figure 7-25 shows the atomic percentages of Mn, K and C are 49.2 %, 5.6%, and 3.8% respectively with the remaining 41.4% coming from oxygen.

7.2.2 Electrochemical Analysis in a Li-ion Coin Cell

Coin cells were prepared with $\text{Mn}_{12}\text{OAc-}\alpha\text{-MnO}_2$ on Cu-foil for CV studies to determine if the internal chemical reactions of the reactants (active material, electrolyte, and counter-electrode) were reversible. The CVs were measured at eight scan rates: 0.1 mV s^{-1} , 0.5 mV s^{-1} , 1 mV s^{-1} , 2 mV s^{-1} , 3 mV s^{-1} , 5 mV s^{-1} , 10 mV s^{-1} , and 15 mV s^{-1} . In, Figure 7-26, the potentials at which the oxidations and reductions occur vary with the changes in scan rate. Increasing the scan rate results in the observation of pseudocapacitance behaviour.

The oxidation peak potential measured at 0.1 mV s^{-1} is at $\sim 1.2 \text{ V}$ and a sharp reduction at 0.25 V . Increasing the scan rate to 0.5 mV s^{-1} , 1 mV s^{-1} and 2 mV s^{-1} shows the oxidation peak potential shift to $\sim 1.5 \text{ V}$. The shape of the CV curves are typical for the pseudocapacitive charge storage mechanism of MnO_2 materials.

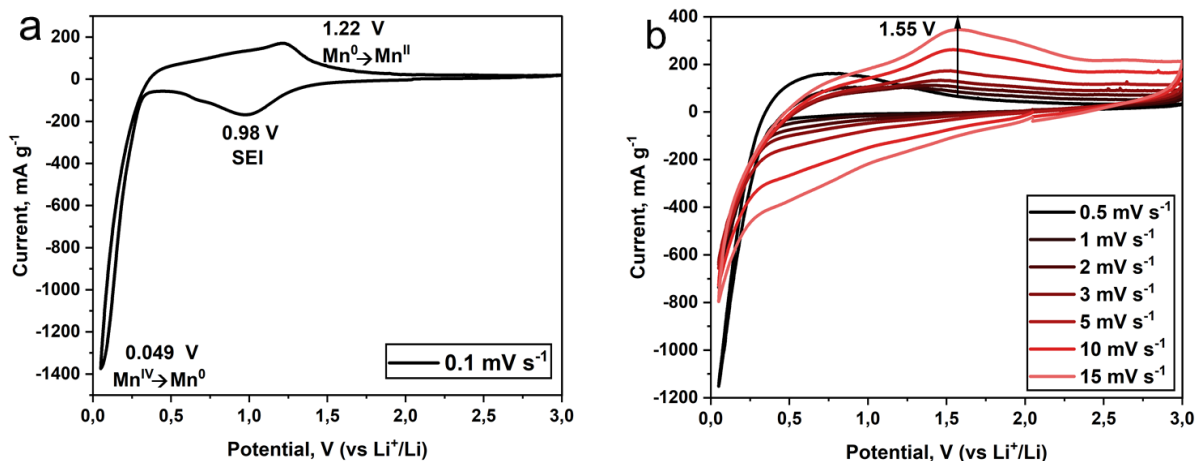


Figure 7-26 Cyclic voltammetry of $\text{Mn}_{12}\text{OAc-}\alpha\text{-MnO}_2$ measured on Cu-foil using multiple scan rates scan rates (a) 0.1 mV s^{-1} (b) 0.5 mV s^{-1} , 1 mV s^{-1} , 2 mV s^{-1} , 3 mV s^{-1} , 5 mV s^{-1} , 10 mV s^{-1} and 15 mV s^{-1} .

Rate capability was measured at current densities of 100 mA g^{-1} , 200 mA g^{-1} , 500 mA g^{-1} and 2000 mA g^{-1} for 10 cycles each before returning to 100 mA g^{-1} for an additional 100 cycles. The coin cell measured had an initial capacity of 1257 mAh g^{-1} . This was followed by capacity loss to 707 mAh g^{-1} in the 1st cycle, and to 616 mAh g^{-1} by the 9th cycle. Increasing the current density to 200 mA g^{-1} , the capacity at the 11th cycle reached 537 mAh g^{-1} which faded to 497 mAh g^{-1} by the 19th cycle. Measurements at 500 mA g^{-1} started at 404 mAh g^{-1} and ended at 376 mAh g^{-1} by the 29th cycle. Finally, increasing the current density to 2000 mA g^{-1} led to capacity fading between 215 mAh g^{-1} and 192 mAh g^{-1} . The current density was returned to 100 mA g^{-1} for the 41st cycle with a capacity of 583 mAh g^{-1} . Figure 7-27 shows degradation between the 80th and 130th cycle where the capacity fluctuates between

453 mAh g⁻¹ and 351 mAh g⁻¹, before stabilising after 130 cycles at a capacity of 368 mAh g⁻¹. Rather than the electrode degrading, it potentially undergoes an in-situ structural change which would explain the capacity fluctuations observed.

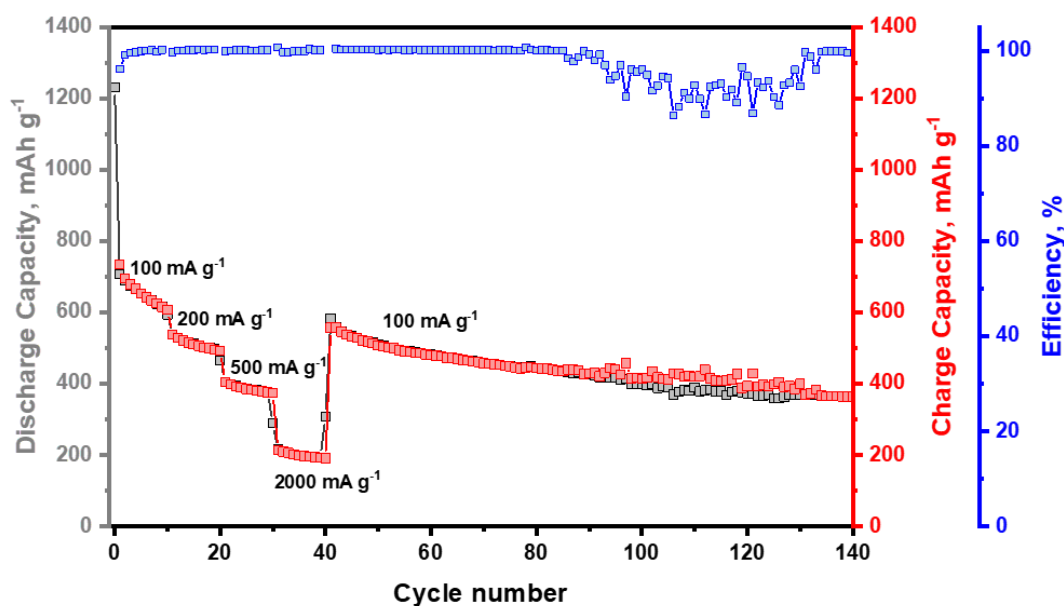


Figure 7-27 Rate capability cycles were measured on Mn₁₂OAc- α -MnO₂ at current densities of 100 mA g⁻¹, 200 mA g⁻¹, 500 mA g⁻¹, and 2000 mA g⁻¹ for 10 cycles each before returning to 100 mA g⁻¹ for the remaining 100 cycles. A region of fluctuating capacity is observed between the 90th and 130th cycle, which stabilises between the 130th and 140th cycle.

The charge-discharge cycles in Figure 7-28 show the voltage changes during the charge/discharge cycling. The voltage plateaus during the charge processes are in favour of a slope at approximately 1.26 V while the discharge processes are comparatively stable at approximately 0.5 V throughout all cycles. The multiple plateaus may correspond to the Mn^{IV}→Mn^{III}→Mn^{II} transitions. However, after the cells are cycled at 2000 mA g⁻¹, the distinctions are less visible.

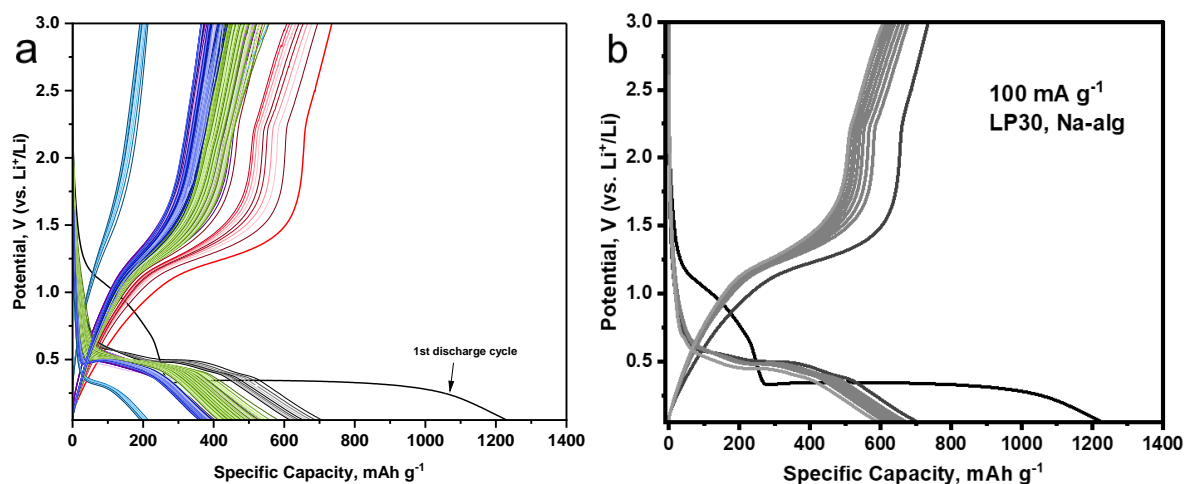


Figure 7-28 (a) Galvanostatic charge-discharge measurements including the rate capability cycles of Mn₁₂OAc- α -MnO₂ at 100 mA g⁻¹, 200 mA g⁻¹, 500 mA g⁻¹, and 2000 mA g⁻¹ for 10 cycles each before returning to 100 mA g⁻¹ for the remaining 100 cycles. (b) Initial discharge curve and first 10 cycles measured at 100 mA g⁻¹.

7.2.3 Magnetisation Studies

Magnetisation studies are useful for oxide materials in order to determine their magnetic behaviour which can in turn provide further information on the phases present in the sample measured. First the pristine sample $\text{Mn}_{12}\text{OAc-}\alpha,\beta\text{-MnO}_2$ was measured for consistency. Mn_{12}OAc , synthesised as described by T. Lis underwent magnetisation studies. The susceptibility was measured from 2 K to 300 K in a magnetic field of 100 Oe.

The ZFC and FC patterns are typically visible for Langevin-type paramagnetism with the localised moments from 300 K to approximately 4 K. Between 4 K and 2 K, a bifurcation indicates the presence of relaxation processes typical for ferromagnetic phases.^[120]

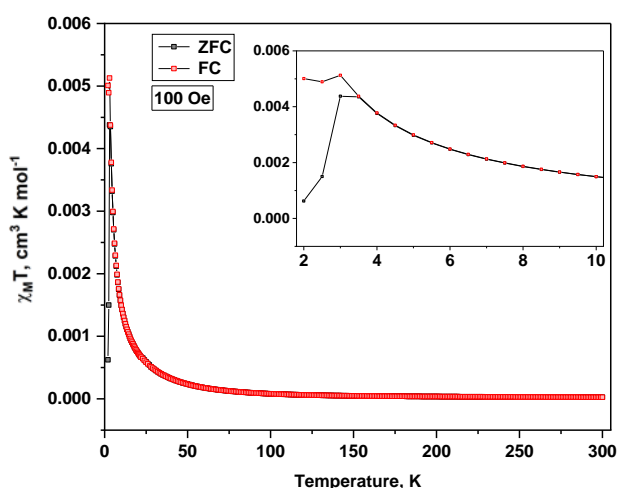


Figure 7-29 χT vs T measured on freshly synthesised Mn_{12}OAc at an applied magnetic field of 100 Oe. Measured by and analysed with the contributions of Dr. Björn Schwarz.

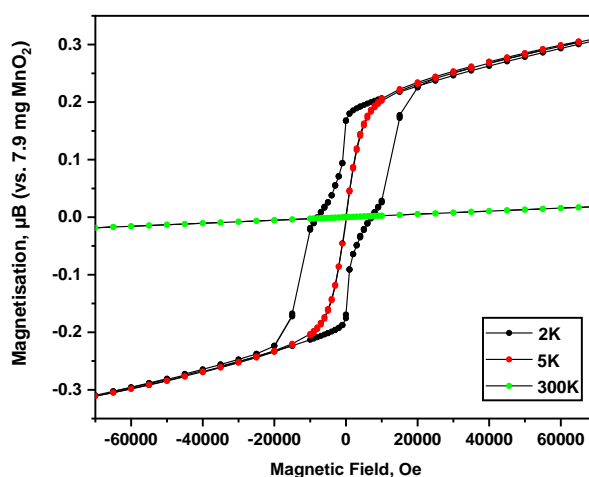


Figure 7-30 Field scans measured on Mn_{12}OAc at 2 K, 5 K and 300 K. Measured by and analysed with the contributions of Dr. Björn Schwarz.

The magnetic field scans show relaxation processes at 2 K represented by the open hysteresis. At 5 K, there is the absence of a hysteresis, although there still appears

to be ferromagnetic ordering. Overall, there is an antiferromagnetic mean field coupling, with ferrimagnetism below 2 K.

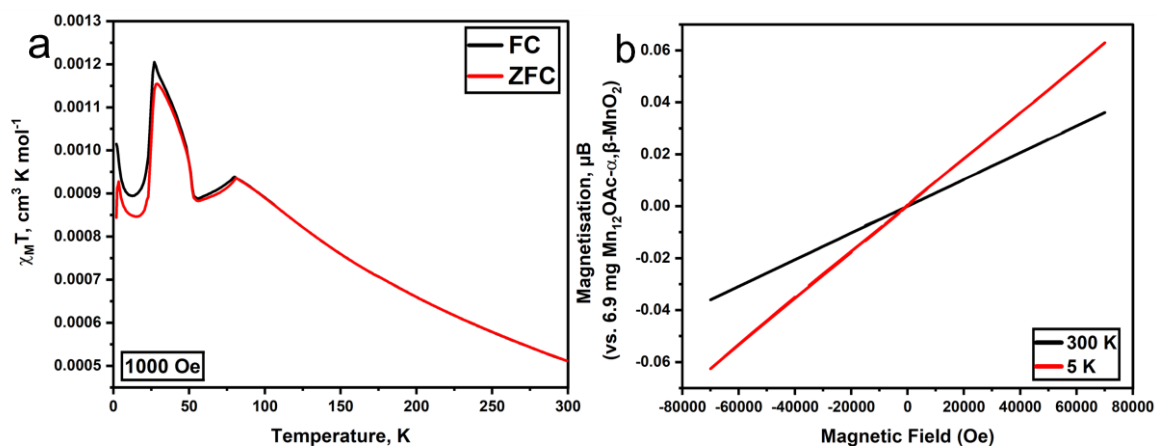


Figure 7-31 (a) χT vs T for ZFC and FC measurements. (b) Magnetic field scans of $\text{Mn}_{12}\text{OAc-}\alpha,\beta\text{-MnO}_2$ at 5 K and 300 K. Measured by and analysed with the contributions of Dr. Björn Schwarz.

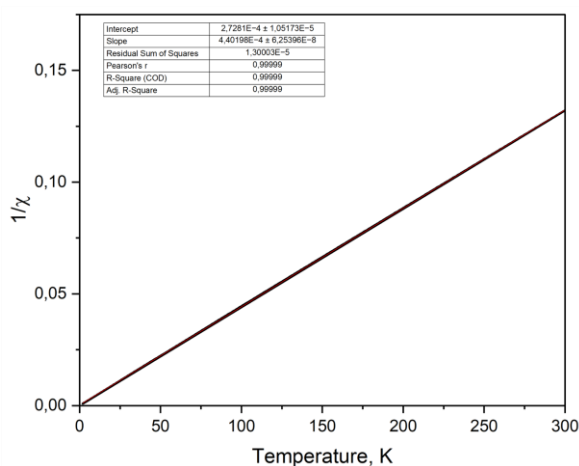


Figure 7-32 $1/\chi$ vs T for $\text{Mn}_{12}\text{OAc-}\alpha,\beta\text{-MnO}_2$. Measured by and analysed with the contributions of Dr. Björn Schwarz.

The ZFC and FC branches for the pyrolysed sample $\text{Mn}_{12}\text{OAc-}\alpha,\beta\text{-MnO}_2$, show a Langevin-type paramagnetism from 300 K to 100 K. Below 100 K there is again a bifurcation indicating the presence of ferromagnetic/ferrimagnetic phases. ZFC means that the sample was cooled without an applied field, thus the magnetisation shows a peak at the transition temp (ferro-/anti-) when the magnetic field scans were carried out at 5 K and 300 K. They show linear dependence of the magnetic moments in the applied field. This suggests the bifurcation features visible under 90 K, are in fact weak effects. The field scans show that there are no open hysteresis loops for $\text{Mn}_{12}\text{OAc-}\alpha,\beta\text{-MnO}_2$ as well as no saturation by 70000 Oe (7T). Below 5 K the oxides were unstable in the applied field and no further magnetisation could be collected. The paramagnetic behaviour observed in Figure 7-31 matches the MnO_2 phases assigned from the crystallographic data and supports those findings.

7.3 Mn₃Ca₃Na₃: Templating from Stacked Sheets

Ako et al reported exciting M₁₈M' complexes that exhibit interesting magnetic behaviours.^[126] Alongside these M₁₈M' complexes, M₃M'₃ complexes were also synthesised with [(Mn^{III}₃Ca^{II}₃(μ₃-Cl)(HL^{Me})₆(H₂O)₆]Cl₂·6.74H₂O reported recently.^[127] By slight experimental modifications, Mn₃Ca₃Na₃ was synthesised by refluxing MnCl₂·4H₂O, CaCl₂, NaN₃, 2,6-bis(hydroxymethyl)-p-cresol and triethylamine in methanol for 3 h before cooling to room temperature and allowing for crystallisation via evaporation over 3 weeks. Mn₃Ca₃Na₃ was pyrolysed under an Ar atmosphere, at a heat rate of 10 °C/min to 400 °C for 4 h before cooling to room temperature to form MnO:Mn₃O₄-400. The pyrolysis was repeated with two additional samples to 600 °C and to 800 °C to form Mn₃O₄-600 and Mn₃O₄-800 respectively.

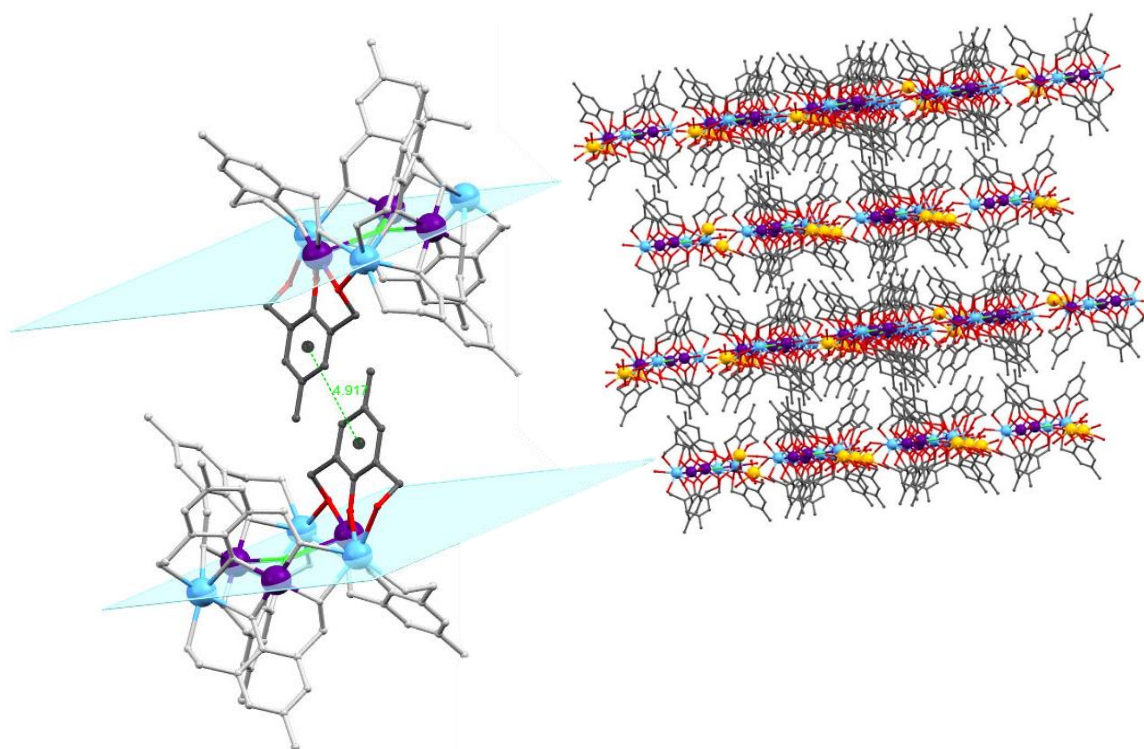


Figure 7-33 The repeating unit of Mn₃Ca₃Na₃ to the right. The centroids between the phenyl rings are calculated as 4.917 Å to the left. Mn^{III} ions are shown in purple, Ca^{II} in blue, O²⁻ in red, C in grey and Na⁺ in yellow. The centroids between the phenyl rings are calculated as 4.917 Å. Solvent molecules and hydrogen atoms are omitted for clarity.

Large clusters that are less supported by a regular 3D-framework can breakdown or form unstable morphologies during calcinations. The reason why the smaller M₃M'₃ clusters appeared to be interesting was because of the proximity of the sp²-hybridised ligands coordinated in the compounds and how they pack in the unit cell. These layers have two 6-membered rings that are slightly displaced from each other though the layers do not appear to have any π-π interactions due to the large distance between

the centroids which measure at 4.917 Å, a value much larger than the sum of the Van der Waals (VDW) radius of carbon which is 3.6 Å.

Pyrolysis was performed under inert conditions with the objective of retaining carbon within the oxide. The presence of a sufficient amount of intrinsic carbon can theoretically support the electrochemistry of the working electrode during cycling, just as the addition of activated carbon aids in the conductivity of electrodes. The clusters were linked through Na⁺ ions to generate neatly stacked sheets for subsequent processing in a version of Ako's Mn₃Ca₃. Sodium azide used in the synthesis also the source of the Na⁺ ions. Because Mn₃Ca₃, synthesised as reported, was thermally unstable during the initial pyrolysis effort, Na⁺ was introduced to help sustain the cluster's stability.

7.3.1 Phase and Morphological Analysis

The diffraction patterns between the synthesised Mn₃Ca₃Na₆ complex and the simulated Mn₃Ca₃Na₆-Sim almost perfectly overlap. There does appear to be additional peaks as well as deviations in intensity which can be accounted for when enlarging the respective 2 Theta regions. Small bumps/weak reflections can be seen in the simulated pattern which match the experimental pattern. CHN elemental analysis was conducted to support the PXRD results (see experimental section).

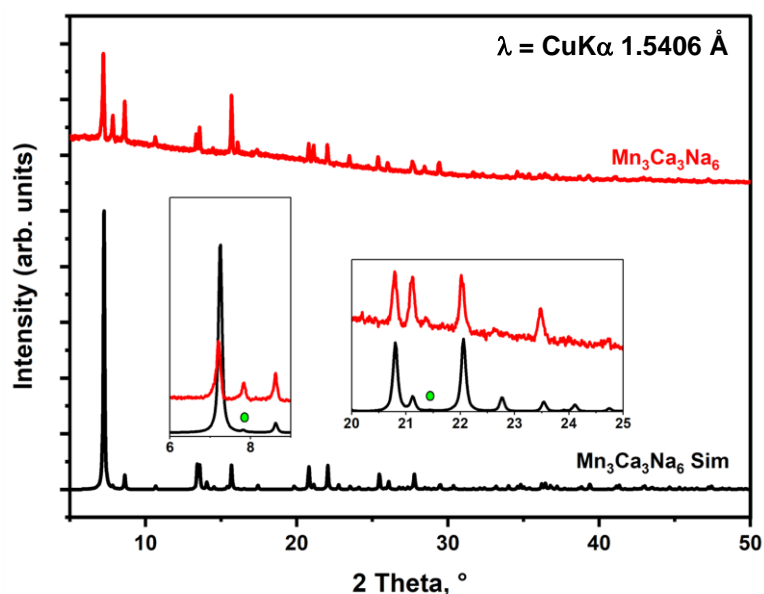


Figure 7-34 Stacked PXRD patterns of the synthesised Mn₃Ca₃Na₃ and simulated Mn₃Ca₃Na₃ Sim. Enlarged inserts on the graph show where the 'additional peaks' are seen as small bumps in the simulated pattern.

Mn₃Ca₃Na₃ was pyrolysed at 400 °C, 600°C and 800°C (all under Ar) to monitor the formation of the most stable phases for electrochemical analysis. The patterns are given below in Figure 7-35.

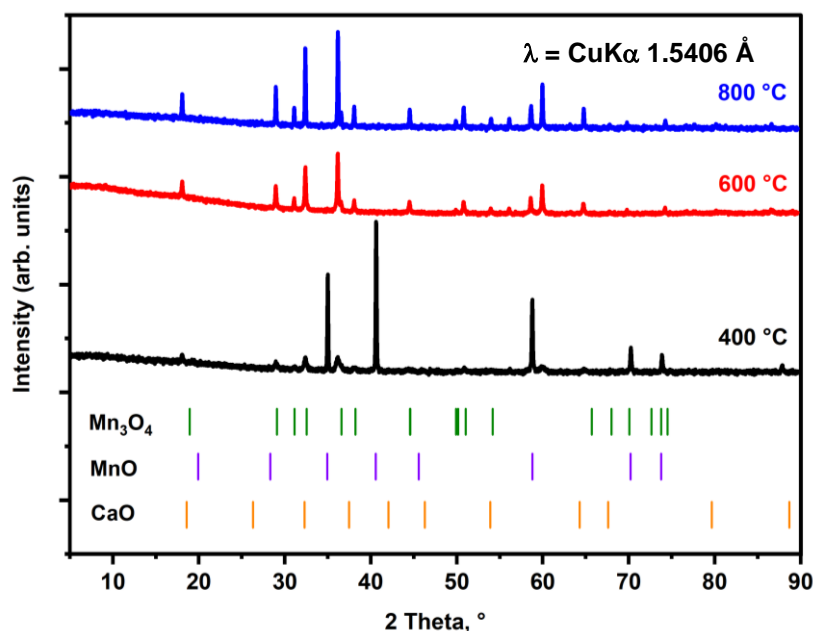


Figure 7-35 Stacked PXRD of the pyrolysis products MnO:Mn₃O₄-400 (black), Mn₃O₄-600 (red), Mn₃O₄-800 (blue), and the simulated phases for Mn₃O₄ (pink), MnO (purple) and CaO (light blue).

There does not appear to be any distinct Ca- or Na- related reflections however that could be due to peak overlapping since CaO has reflections that are close to or overlap Mn_xO_y reflections. The phases presented correlate to MnO and Mn₃O₄. As pyrolysis temperatures increase from 400 °C to 600 °C and then to 800 °C there are noticeable changes in the phases observed. At 400 °C, the sample consists of mixed phase MnO and Mn₃O₄. Increasing the temperature to 600 °C results in the oxidation of the cubic MnO to Mn₃O₄. Increasing the pyrolysis temperature even further to 800 °C does not result in any crystalline phase changes in the PXRD, however the baseline appears to flatten, and the reflection intensities improve.

Upon pyrolysis, these large crystals tend to maintain their bulk shape. Figure 7-36 a-c shows the post-pyrolysis morphologies of MnO:Mn₃O₄-400. The large crystals show a step-like morphology that is the result of templating from layered 2D sheets. The compound also appears to be porous and spongy. Figure 7-36 c shows the morphology at 20x magnification. There are no distinct shapes, and the structure has channels which seem to be composed of agglomerated particles. This sponge-like morphology has been reported plentifully for Mn_xO_y compounds. Mn₃O₄-600 shown in Figure 7-36 d-f, and Mn₃O₄-800 shown in Figure 7-36 g-i, look similar. They both have a sponge-like morphology that at higher magnifications shows distinct non-porous particles. The particle sizes are non-uniform with some ranging 200-400 nm and others ranging 600-900 nm and the particles are polyhedral with no specific shape.

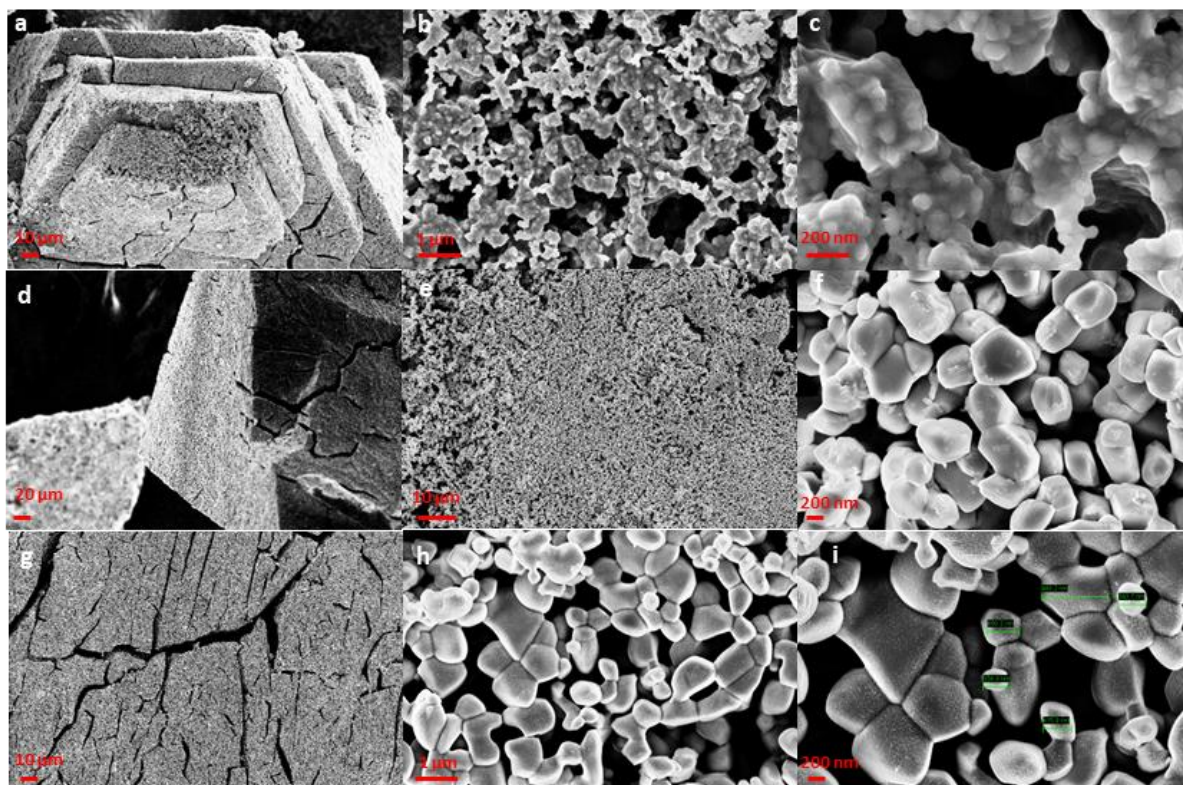


Figure 7-36 SEM images of the post pyrolysis products. a,b,c) MnO:Mn₃O₄-400 pyrolysed at 400 °C d,e,f) Mn₃O₄-600 pyrolysed at 600 °C g,h,i) Mn₃O₄-800 pyrolysed at 800 °C.

7.3.2 Electrochemistry

The electrochemical measurements were carried out on Mn₃O₄-600 because of the reported phase stability obtained. This made it unnecessary to pyrolyse to 800 °C which results in a similar phase and morphology. This allows us to take consideration of the amount of energy being used to process these materials as well as time efficiency during treatment.

In Figure 7-37 the CV shows the redox peaks correlating to the Mn_xO_y active electrode material. According to the CV measured at 0.1 mV s⁻¹, the sole electrochemically active component of this material in a Li-ion coin cell is the Mn₃O₄ and the presence of any impurities based on Ca or Na do not appear to contribute to over potential in the cell nor cause rapid cell degradation.

The 1st cycle shows many substructures as the SEI forms. During the 1st discharge process, these substructures correlate to Li-intercalation into the spinel Mn₃O₄ as well as the non-reversible SEI processes. The characteristic reduction at 0.37 V is typical for Mn^{II} → Mn⁰ and vice versa for the oxidations at 1.23 V. For the remaining cycles measured, the reduction peak potentials shift gradually to 0.24 V while the oxidations remain relatively stable as they shift to 1.28 V during the 2nd cycle and then gradually shifts back to 1.23 V by the 100th cycle.

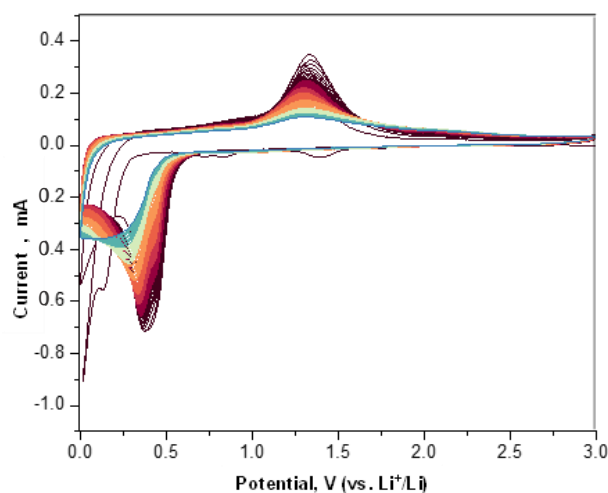


Figure 7-37 Cyclic voltammety of the 100 cycles measured for $\text{Mn}_3\text{O}_4\text{-600}$ at 0.1 mV s^{-1} .

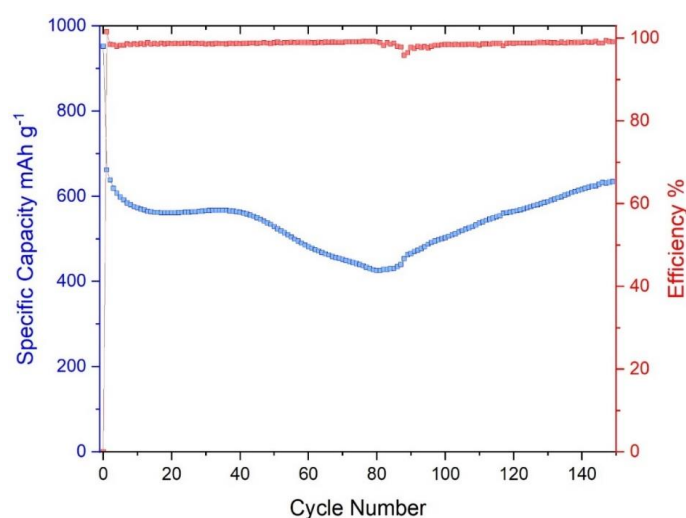


Figure 7-38 Specific capacity of the 150 cycles measured for $\text{Mn}_3\text{O}_4\text{-600}$ at 100 mA g^{-1} .

An initial capacity of 967 mAh g^{-1} is obtained when cycling at 100 mA g^{-1} . Further capacity loss is recorded up to the 10th cycle. There is a window of stability shown by the plateau at 583 mAh g^{-1} between the 10th and 35th cycle. From the 35th cycle to the 81st cycle, there is a gradual reduction in capacity to 451 mAh g^{-1} followed by an increase that continues beyond the 150 cycles shown. It is assumed that the electrode does not degrade but rather modifies its chemical composition to occupy a composition that surpasses the initial 'stable window' observed. With a final capacity of 629 mAh g^{-1} obtained without the capacity stabilising/plateauing, it is fair to predict that the capacity would continue to increase until potentially reaching stability.

7.4 Mn₂₁ Cluster: Azide-rich Complex to Oxide

[Mn^{III}₁₂Mn^{II}₉(μ₄-O)₈-(glycH)₁₂(μ-1,1-N₃)₆(OH₂)₆(N₃)_{1.5}]-Cl₄·ca.7.5H₂O hereby referred to as Mn₂₁ClGlyc was synthetically reproduced from Sanjit et al.^[128] It contains an ‘archaemic structure’ with a central Mn^{II} ion surrounded by 12 slightly disordered Mn^{III} atoms in an isocahedron formation. This is further surrounded by 8 Mn^{II} cations in a cubic arrangement. This complex exhibits a pseudo-MOF structure with a Mn^{II} cation linking each cluster. A kinetic side product of this reaction is NaCl₂. Exchanging the MnCl₂·4H₂O with MnBr₂·4H₂O results in a near-identical complex with substitution of the halide anions to prevent the formation of NaCl. This modification is now referred to as Mn₂₁BrGlyc. All further analysis was continued on Mn₂₁BrGlyc.

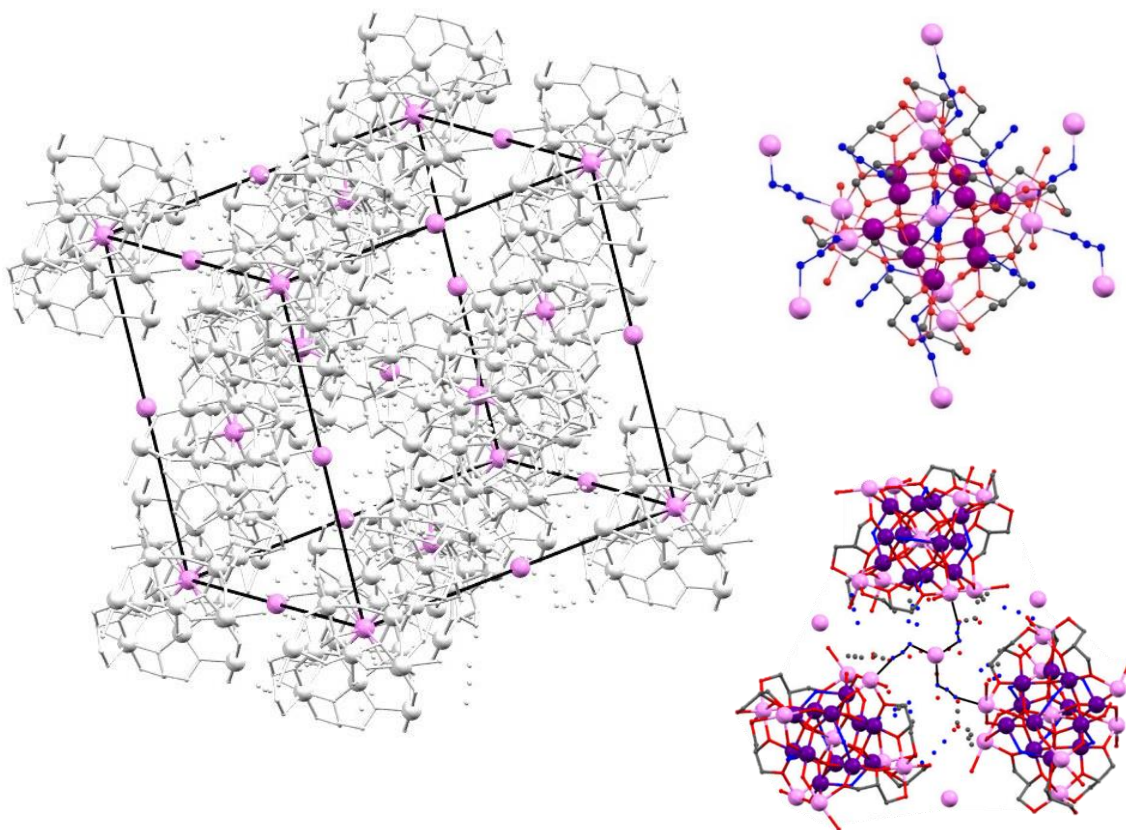


Figure 7-39 Molecular structure of Mn₂₁ClGlyc showing the arrangement of manganese ions to create a 3d-framework.^[128]

Mn₂₁BrGlyc was synthesised by combining MnBr₂·4H₂O and glycerol acetonitrile in one vial. In a second vial NaN₃ was dissolved in methanol. These vials were combined, and 4 drops of triethylamine were added with a glass pipette. The solution was then stirred for 4 h before leaving to crystallise via evaporation over one week. Small black crystals of Mn₂₁BrGlyc were formed that resembled the reported compound. Mn₂₁BrGlyc was then calcined at three temperatures to form MnO-500,

MnO-550, and MnO-600. These compounds were further characterised before application in a Li-ion coin cell.

7.4.1 Phase and Morphological Analysis

There appears to be three gradual, yet clear mass loss steps observed before 400 °C in the TGA. The first loss of 8% between 80°C and 175 °C corresponds to the loss of free waters and MeOH. The second smaller change in weight corresponds to the loss of crystal waters. As the complex contains coordinated N-containing ligands, the final mass loss step correlates to the release of NO_x and N₂ which are the gaseous products from the NaN₃ that was used as a co-ligand.

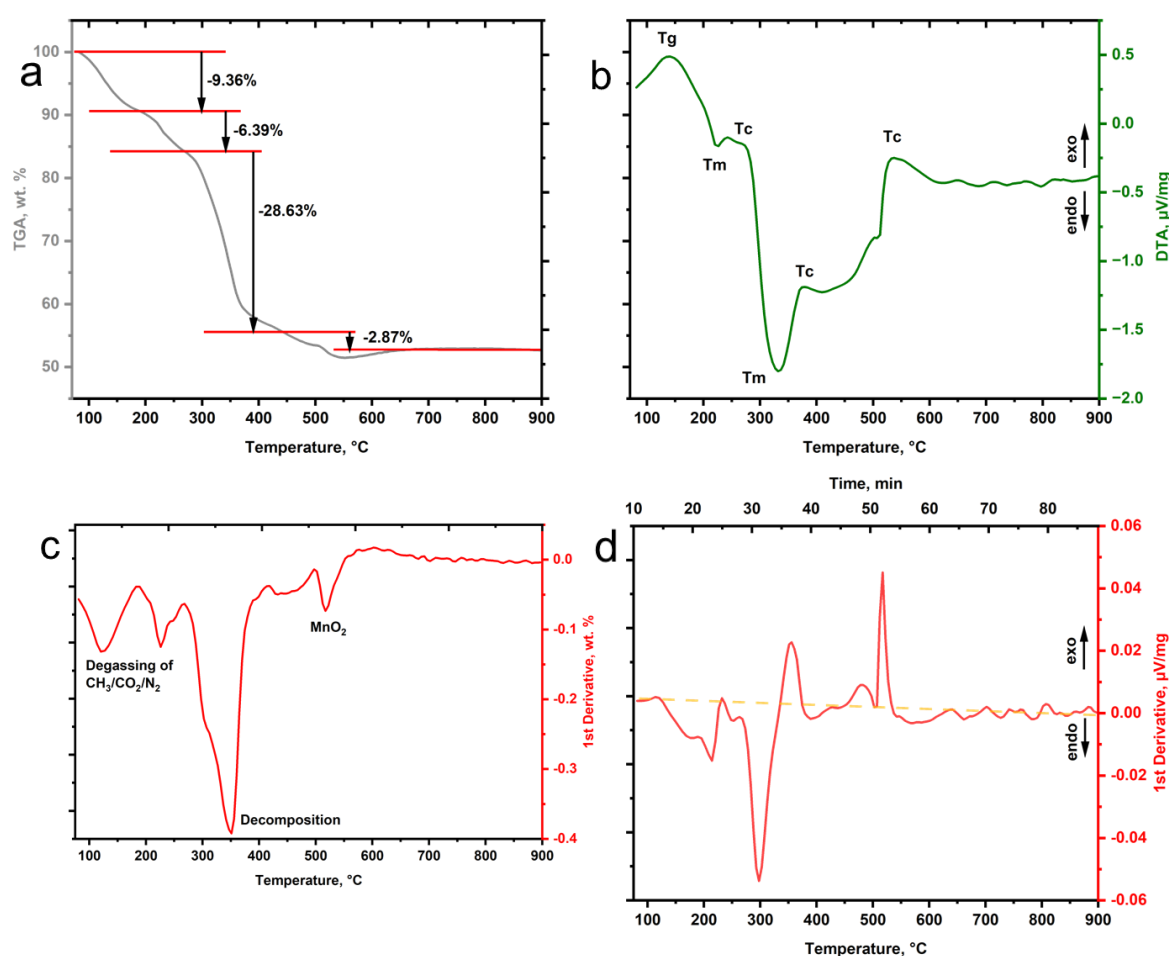


Figure 7-40 (a) TGA and (b) DTA analysis of Mn₂₁BrGlyc. First derivatives of (c) TGA and (d) DTA are provided for clarification of the thermal analysis processes.

And finally, we have the complete decomposition of the complex to the oxide which is yet again a rapid process visualised with the steep drop in weight around 300 °C. As the weight begins to stabilise beyond 500°C, this suggests that would be the ideal temperature for complete oxide formation for electrode applications.

Li-ion cell measurements are previously reported by Nayak et al for this compound however the cells reportedly lasted 3 cycles before degradation. Modification of the

phase and morphology of the material allowed for a more stable oxide material to be developed. The analysis and results are provided and discussed below.

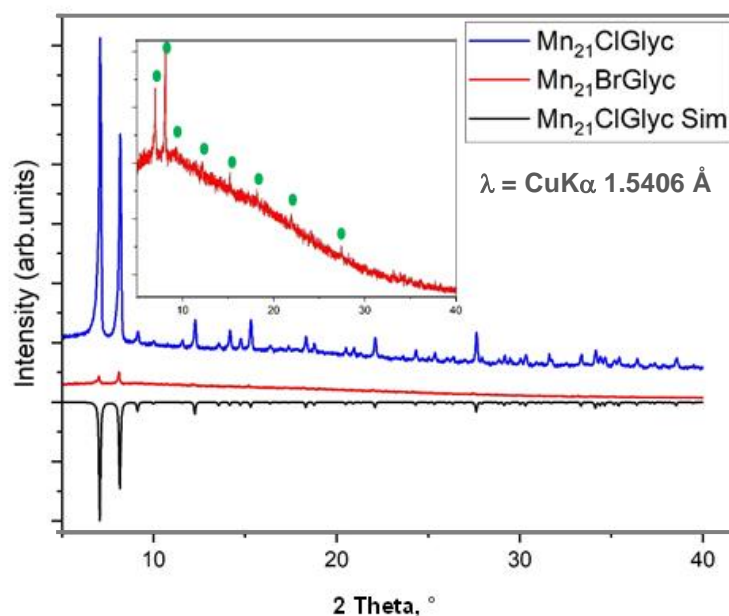


Figure 7-41 Stacked PXRD patterns showing the simulated pattern for $Mn_{21}ClGlyc$ (black), reported $Mn_{21}ClGlyc$ compound (blue) and $Mn_{21}BrGlyc$ analogue (red), with the circles highlighting the major reflections of the complex (green).

Initially, $Mn_{21}ClGlyc$ was reproduced as it was previously reported to have a highly porous, sponge-like structure after pyrolysis under due to the presence of azides as co-ligands in the crystal structure. The fast release of NO_x forced porous channels to develop in the oxide. However, with the presence of Na^+ and Cl^- in solution, the kinetically favourable reaction formed $NaCl$ which can become an impurity in the reaction and hinder the purity of the oxide (black pattern Figure 7-41). Although the crystals of $NaCl$ crystals are large, transparent, and easy to separate from the $Mn_{21}ClGlyc$ crystals which are black and spherical, this became a tedious task. Washing the oxides with water to remove the $NaCl$ reduced the crystallinity of the oxide (red pattern Figure 7-41). $Mn_{21}BrGlyc$ was synthesised as an analogue with a different counter-ion to prevent the formation of $NaCl$ and therefore preventing any impurities that would affect the reproducibility of such materials. Although the PXRD reflections in Figure 7-41 show the analogue $Mn_{21}BrGlyc$ has a lower crystal quality compared to $Mn_{21}ClGlyc$, upon magnification of the diffraction pattern, the corresponding peaks can be seen and confirm that it is the correct compound. Elemental analysis was measured to support the PXRD patterns obtained. This can be found in the experimental section.

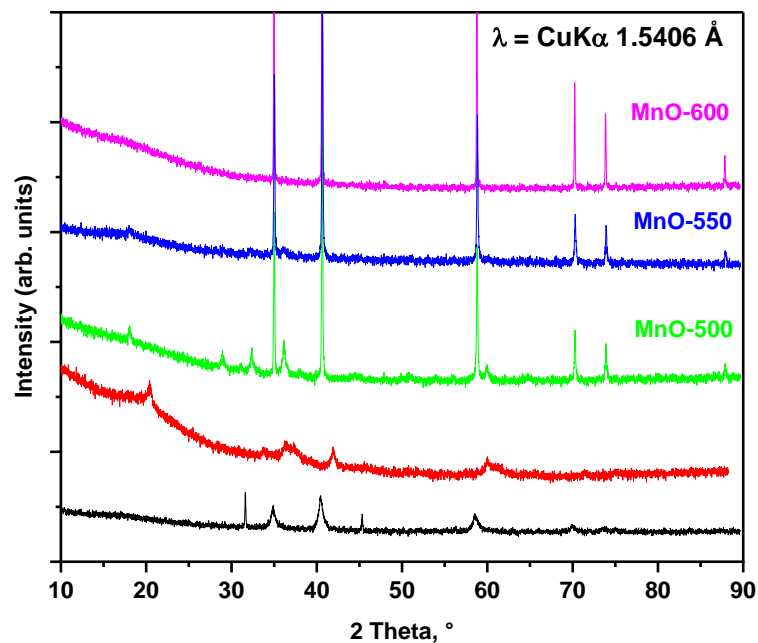


Figure 7-42 Stacked PXRD patterns of the oxides of $\text{Mn}_{21}\text{ClGlyc-MnO}$ (black), $\text{Mn}_{21}\text{ClGlyc-MnO}$ washed with water (red), MnO-500 (green), MnO-550 (blue), and MnO-600 (pink).

Post-pyrolysis PXRD patterns in Figure 7-42 show the increasing purity of the MnO phase as the $\text{Mn}_{21}\text{BrGlyc}$ is pyrolysed to 500, 550 and 600 °C. MnO-500 shows the presence of the main crystalline phase MnO with contributions from Mn_3O_4 at lower intensities. MnO-550 shows the intensity of Mn_3O_4 has reduced, with only trace amounts visible in the diffraction pattern. MnO-600 shows there are no longer any phase impurities, and MnO is the singular crystalline phase present in the sample. Comparing these patterns to the $\text{Mn}_{21}\text{ClGlyc-MnO}$ (black pattern), we see this pattern contains broad peaks of MnO suggesting amorphousness with the sharp crystalline peaks corresponding to NaCl.

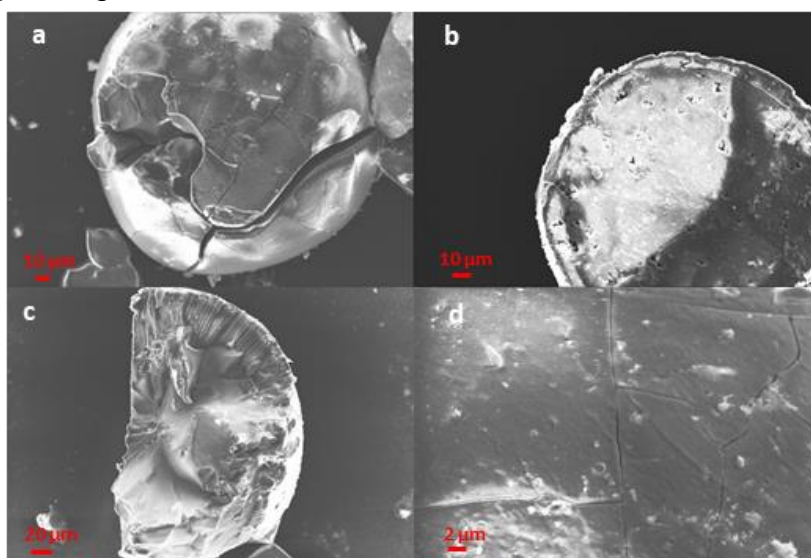


Figure 7-43 SEM images of pristine $\text{Mn}_{21}\text{BrGlyc}$ at a,b) 10 μm, c) 20 μm, and d) 2 μm showing the smooth surface of the crystals.

Mn₂₁BrGlyc has a smooth surface morphology. The spherical crystals are poreless with crystal sizes ranging approximately 250 μm in diameter. The internal morphology of the particles is in accordance with what we see on the surface. This is shown in Figure 7-43.

After pyrolysis to 500 $^{\circ}\text{C}$ under a N₂ atmosphere at a heating rate of 2 $^{\circ}\text{C}/\text{min}$ for 2 hours, the overall morphology of the product MnO-500 changes drastically. Although the appearance of spherical form of the crystals remained, there is a visible change in the surface of the material as we see the development of porous particles shown in Figure 7-44 below.

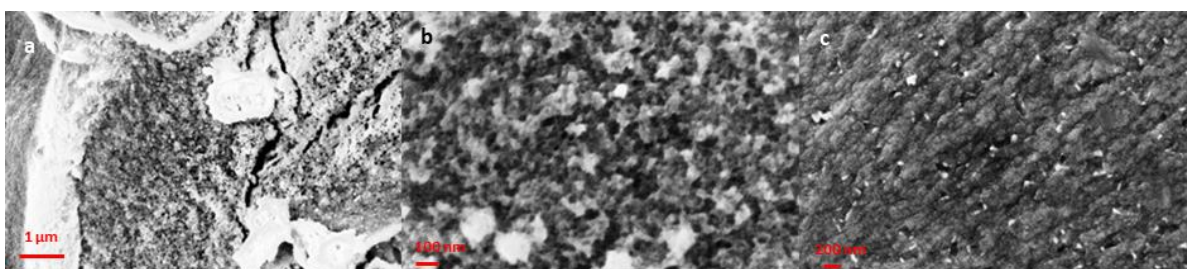


Figure 7-44 SEM images of MnO-500 after pyrolysis under N₂ at 500 $^{\circ}\text{C}$.

Increasing the temperature by 50 $^{\circ}\text{C}$ to form MnO-550, gives a very similar morphology, although the pores appear to be slightly more defined.

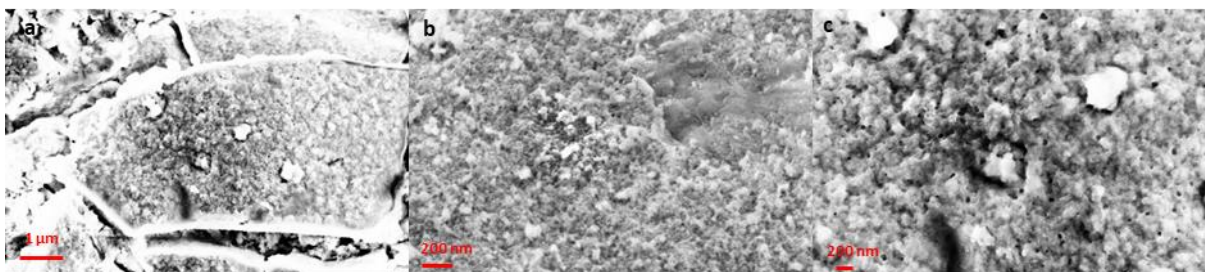


Figure 7-45 SEM images of MnO-550 after pyrolysis under N₂ at 550 $^{\circ}\text{C}$.

Finally, increasing the temperature by a further 50 $^{\circ}\text{C}$ to 600 $^{\circ}\text{C}$, shows the presence of better-defined pores which appear uniform in size and shape and possess a diameter of ~ 50 nm.

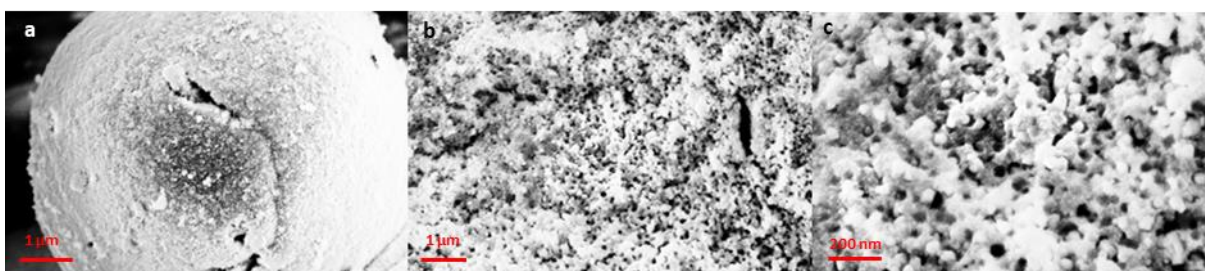


Figure 7-46 SEM images of MnO-600 after pyrolysis under N₂ at 600 $^{\circ}\text{C}$.

Overall, there is not much difference between the morphologies as the nanoporous morphology is visible across all three materials.

Although pyrolysis of this material had been previously carried out, the oxide was reported as being poorly active in a Li-ion battery. Pyrolysis conditions were continuously modified until a uniformly nano-porous oxide was formed with the required phase. Heat rate, gas atmosphere and final temperature were adjusted in an attempt to increase electrochemical activity. This was the primary goal for this material. It was found that pyrolysis under N₂ atmosphere under a low heat rate assisted in achieving uniform porosity while attempts to get the oxide consisting mainly of MnO with trace amounts of Mn₃O₄ impurities was achievable by modifying the temperatures. MnO-600 was studied as the active electrode material in a Li-ion battery due to the more uniform morphology and pure phase obtained.

7.4.2 Electrochemical Analysis

Ten charge/discharge cycles were measured for MnO-600 at a scan rate of 0.1 mV s⁻¹ to observe the basic stability of the electrode. Figure 7-47 shows the development of the redox behaviour through these cycles.

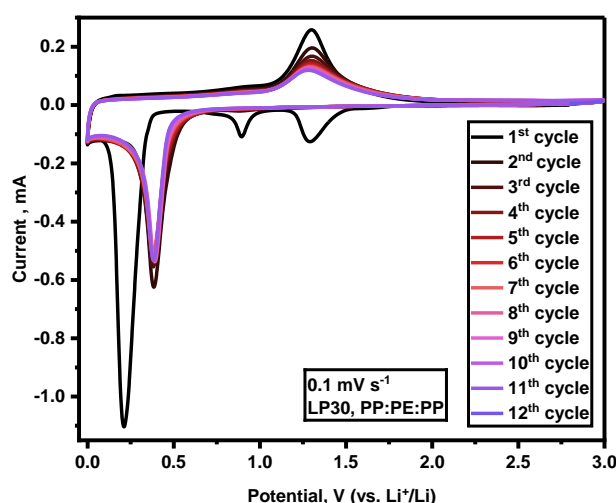


Figure 7-47 CV showing the first 12 cycles of MnO-600 measured at a scan rate of 0.1 mV s⁻¹.

Comparing the CV profile to that which was published by Nayak et al in Figure 7-48, there are two reductions at 1.36 V and 0.7 V assigned to the SEI formation and lithiation during the first cycle that are non-reversible processes, followed by an intense narrow peak at 0.24 V correlating to the Mn^{II} → Mn⁰ conversion. The oxidation at 1.36 V falls within the typical region for Mn_xO_y phase transitions. From the 2nd cycle to the 12th cycle, the oxidation and reduction potentials appear at similar positions with the former at 1.36 V and the latter at 0.4 V. Increasing resistance in the cell is directly proportional to the thickness of the deposited materials. This explains the reduction in current as the cycles continue to measure; the diffusion gradient

decreases and as a result the current is reduced to the diffusion limited region of the peak.

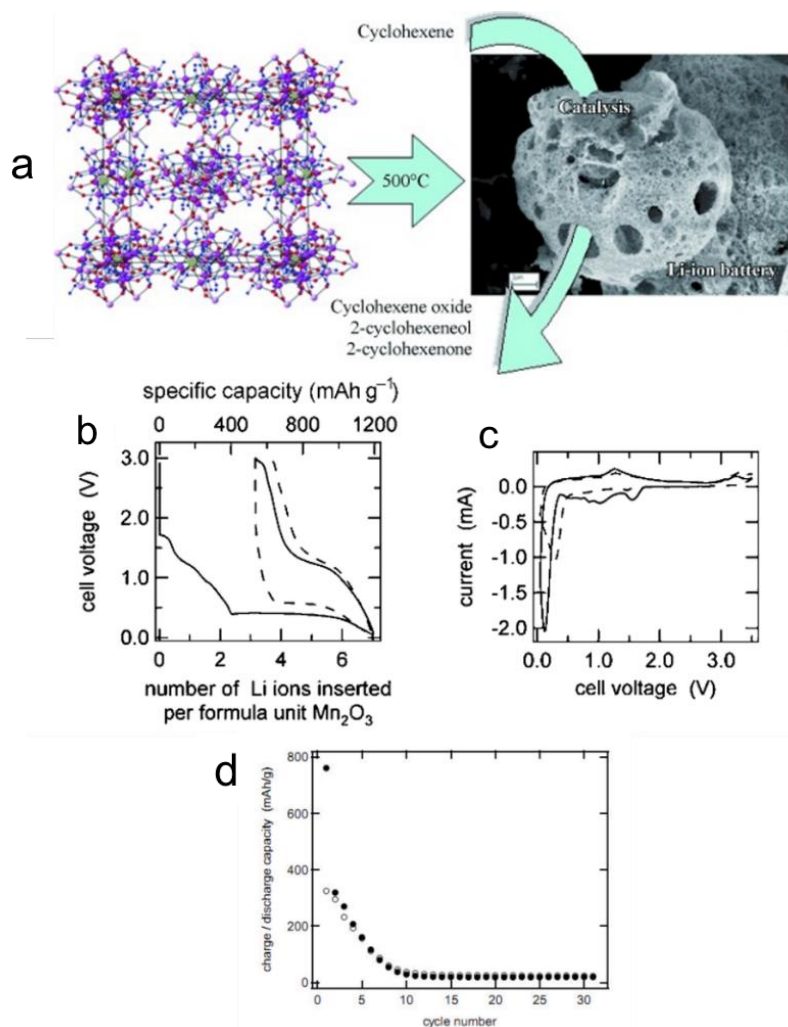


Figure 7-48 (a-c) extracted directly from the publication by Nayak et al.^[129] (d) extracted from the corresponding supplementary information.

Nayak measured 30 cycles of his Mn₂O₃/MnO material as the active material in a Li-ion coin cell. He pyrolysed Mn₂₁CIGlyc to 500 °C in air. However, performance stability in Figure 7-48 d shows the rapid decline of the capacity as cycle number increases. By the 10th cycle, the cell has negligible capacity and was no longer active.

In the 10 galvanostatic cycles measured, an initial capacity of 1310 mAh g⁻¹ is recorded, followed by a capacity of 859 mAh g⁻¹ in 2nd cycle which is a loss of approximately 35%. From the second to the 10th cycle, there is a gradual capacity loss observed up to 713 mAh g⁻¹ which is reasonable as there could still be internal reactions taking place on the electrode surface. The electrode was only measured for 10 cycles to see if this phase/morphology was electrochemically active and stable. The cell itself shows a plateau at 0.4 V just like the reported study from Nayak et al and shown in Figure 7-49 below.

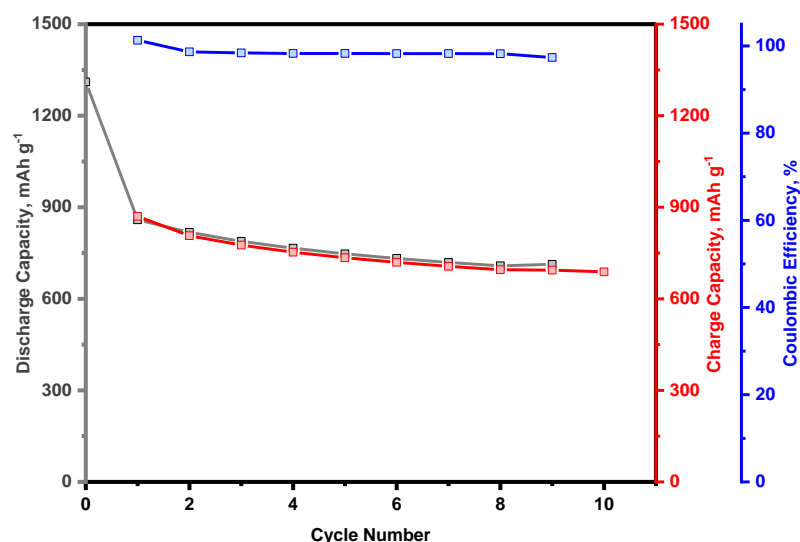


Figure 7-49 Charge-discharge capacity of MnO-600 at a current density of 100 mA g⁻¹.

This is commonly observed for materials which undergo a phase change during cycling. Additionally, looking at the coulombic efficiency, CE of the charge/discharge cycles, shows the efficacy of moving electrons during the cycling process. Capacity loss during the first cycle and therefore low CE%, is expected as there is usually a change in material structure during the first cycle reducing in the intercalation sites and/or the conversion sites. These Li-ions are lost during the formation of the SEI forming stable irreversible complexes on the surface of the electrode. Beyond this, the coulombic efficiency is maintained above 95% for each cycle.

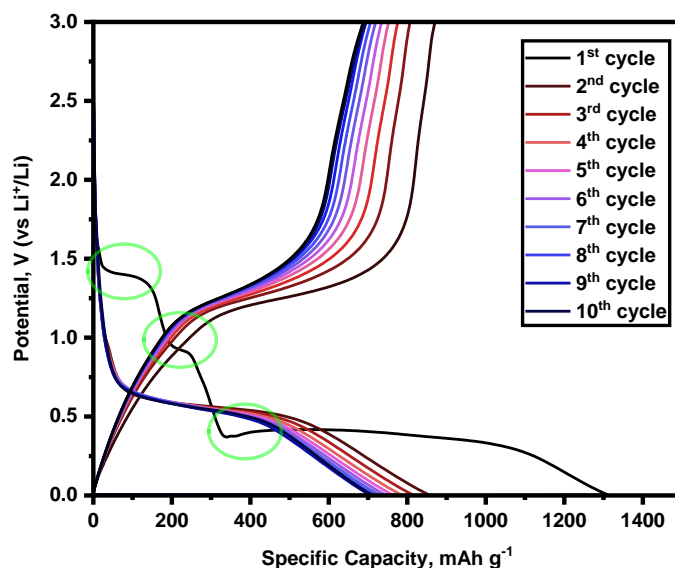


Figure 7-50 Specific capacity for MnO-600 measured at a scan rate of 0.1 mV s⁻¹ for 10 cycles.

Although only 10 cycles were measured, this result is important when considering the types of modifications one should consider, when attempting to improve the performance of a material not only for electrochemical studies but in general for all applications.

7.5 Summary and Conclusion

This chapter focused on giving previously published compounds a new functionality as the active materials in a Li-ion battery. Four compounds were reproduced, each to prove a specific point. Mn-formate, the simplest carboxylate-based MOF, was reproduced from literature and pyrolysed to form a MnO:Mn₃O₄ mixed phase oxide. MnO:Mn₃O₄ proved to create a high performing electrode material with an initial discharge capacity of 1050 mAh g⁻¹ and a capacity of 732 mAh g⁻¹ after 100 cycles cycled at 100 mA g⁻¹. The crystalline phases MnO and Mn₃O₄ were completely inactive during cycling, and it was discovered through the combination of magnetic studies and in-situ EXAFs that there was in fact Mn₂O₃ present in the sample in an undetected amorphous state that provided the capacity observed. This cheap and efficient MOF can be synthesised in bulk quantities, stored for months without experiencing degradation and shows that the simplest of compounds can be treated to create a material that has a high performance in a Li-ion cell.

Mn₁₂OAc was the second compound studied in this chapter. This coordination complex is well known in the field of SMMs and was an attractive compound to study as a battery material due to its mixed valence Mn^{III/IV} oxidation states. The post pyrolysis product Mn₁₂OAc- α -MnO₂ provided a respectable capacity of 368 mAh g⁻¹ at 100 mA g⁻¹ after 140 cycles (including rate capability).

Where Mn-formate and Mn₁₂OAc were synthesised exactly as published, Mn₃Ca₃Na₃ and Mn₂₁BrGlyc were both modifications of previously reported compounds. Mn₃Ca₃Na₃ was pyrolysed to form Mn₃O₄-600 which had an initial discharge capacity of 927 mAh g⁻¹ that reached 629 mAh g⁻¹ after 150 cycles after cycling at 100 mA g⁻¹. The modification to the crystal structure by incorporating a cation, seemed to aid in the stabilisation of the thermal behaviour of the complex. Mn₂₁BrGlyc was pyrolysed to MnO-600 which maintained a capacity of 723 mAh g⁻¹ after 10 cycles measured at 100 mA g⁻¹. By exchanging the anion from Cl⁻ to Br⁻, the NaCl impurity could be avoided, and the formation of a uniformly porous oxide was obtained. In conclusion, this chapter shows that there are many reported compounds in the literature that could and should be reproduced, modified and/or thermally treated to showcase the multifunctionality of a material for diverse applications.

8 Exploring a Di-nuclear Iron^{III} Complex Electrochemically

Two of the most prevalent redox active substances in the crust of the planet are iron and manganese. MnO₂ is an excellent electrode material and semiconductor. Its low price, low toxicity, and ease of preparation make it a highly desirable material for research and development.^[130] However, the manganese road in the South African province of Gqeberha provides 80% of the MnO₂ that is mined. MnO₂ is less intrusive to mine, transport, and store than cobalt, but the dust from the mining has damaged the environment in the Gqeberha region, and the lack of adequate safety measures has resulted in serious health issues for the miners, including cancer and poisoning. Like all forms of extraction, taking resources from the earth can lead to habitat damage, soil degradation, etc. Despite having a more environmentally friendly mining process than cobalt, lithium nevertheless contributes to air and soil pollution. Because of their greater energy density, safety, and sustainability, Na-ion batteries are positioned as the upcoming, promising successor for the industry standard Li-ion. Lithium technologies are typically not directly applicable to sodium batteries, as was previously mentioned in the introduction. This does not imply, however, that lithium technologies cannot be modified to be used in sodium-ion batteries more effectively.

Inspired by the work of Schmitt et al where an Fe-based ‘honeycomb structure’ rich in Na⁺ ions was synthesised, this complex was reproduced and thermally treated. The electrochemical properties of the resulting material were investigated.^[131, 132] Three novel ligands were prepared additionally and characterised as a concept for future work.

8.1 Reproducing K₆Fe₂chnida₂ and Na₆Fe₂chnida₂

8.1.1 Ligand Preparation:

The ligand [(3-carboxy-2-hydroxy-1-naphthyl) methylene]-iminodiacetic acid, termed chnida, that was used by Schmitt et al was prepared using the Mannich reaction. Essentially, 3-hydroxy-2-naphthoic acid was combined with an iminodiacetic acid in the presence of formaldehyde and stirred under acidic conditions to undergo the Mannich reaction shown in Figure 8-1. After 2 hours of stirring, the ligand precipitated out of the solution as a white powder, was collected and dried under vacuum.

The organic pathway in Figure 8-1 shows how chnida was prepared. The Mannich reaction is a way to form carbon-carbon bonds in a two-step reaction. The first step is the nucleophilic addition of formaldehyde on the amine substituent. This is then followed by an in-situ electrophilic substitution reaction between the Schiff base and the aromatic ring.

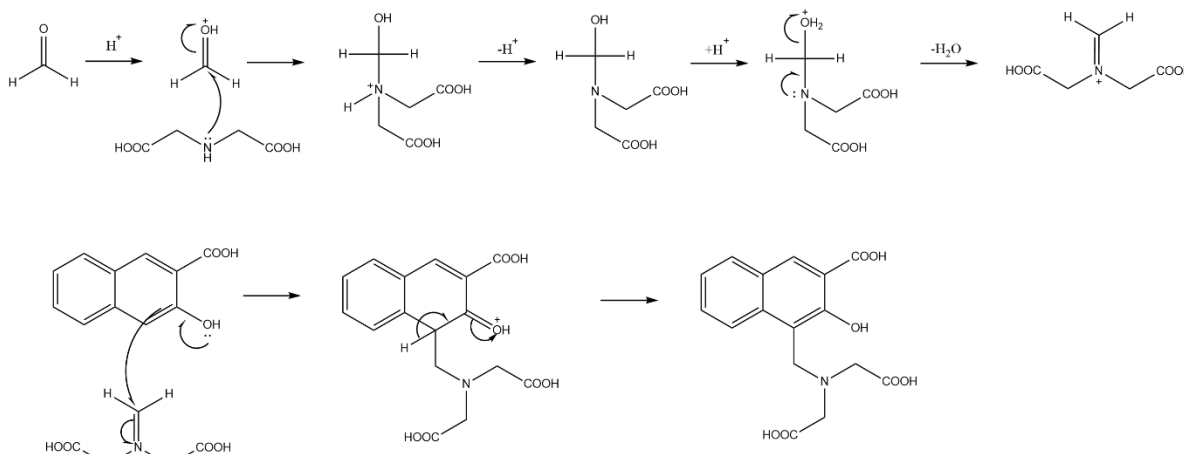


Figure 8-1 Synthetic route for the synthesis of Chnida through the Mannich reaction, using 3-hydroxy-2-naphthoic acid and iminodiacetic acid as the starting materials in an acidic solution.

8.1.2 Synthesis of $K_6Fe_2chnida_2$ and $Na_6Fe_2chnida_2$

K_6 and $Na_6[Fe_2(\mu-O)(\mu-CO_3)-(chnida)_2] \cdot 13.5H_2O$, referred to in short as $K_6Fe_2chnida_2$ and $Na_6Fe_2chnida_2$, were reported by Schmitt who measured not only the magnetic behaviour of the compounds but also processed them using thermal treatment methods to form alkali-iron oxides.^[131] Figure 6-2 shows the complex is arranged in such a way that the polar, carbonate and carboxylate groups form hydrophobic regions within the channels of the structural motif that are parallel to the c-axis. The water bridged potassium ions support the structure to form this 'honeycomb'. The dinuclear iron complex (that is present as Fe^{II}) is penetrating these hydrophilic walls with the $Fe \cdots Fe$ axis parallel to the c-axis and the naphthalene parts of the ligand facing into the channels.

The coordination compounds were synthesised by combining $FeCl_3 \cdot 6H_2O$ with the ligand chnida in methanol. Dropwise, a 2M solution of sodium hydroxide was added to deprotonate the ligand while stirring at room temperature. Ethanol was added to aid in the crystallisation of the complex before leaving the vial to stand for two weeks. The yields for this compound were low, and the complexes were sensitive to solvent loss. Leaving the crystals in solution over a period of two weeks resulted in decomposition while leaving the dry crystals to stand also resulted in decomposition.

This instability of the compounds made it difficult to produce, process and store in bulk.

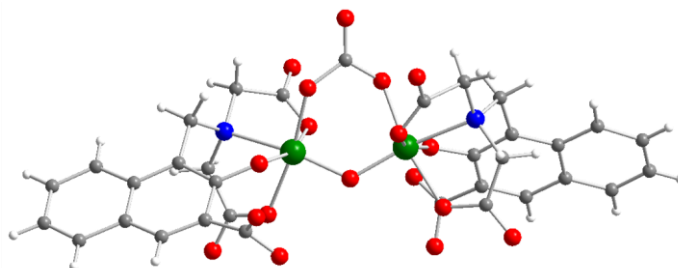


Figure 8-2 Molecular structure of the iron dinuclear complex, $\text{Na}_6\text{Fe}_2\text{chnida}_2$.^[131, 132]

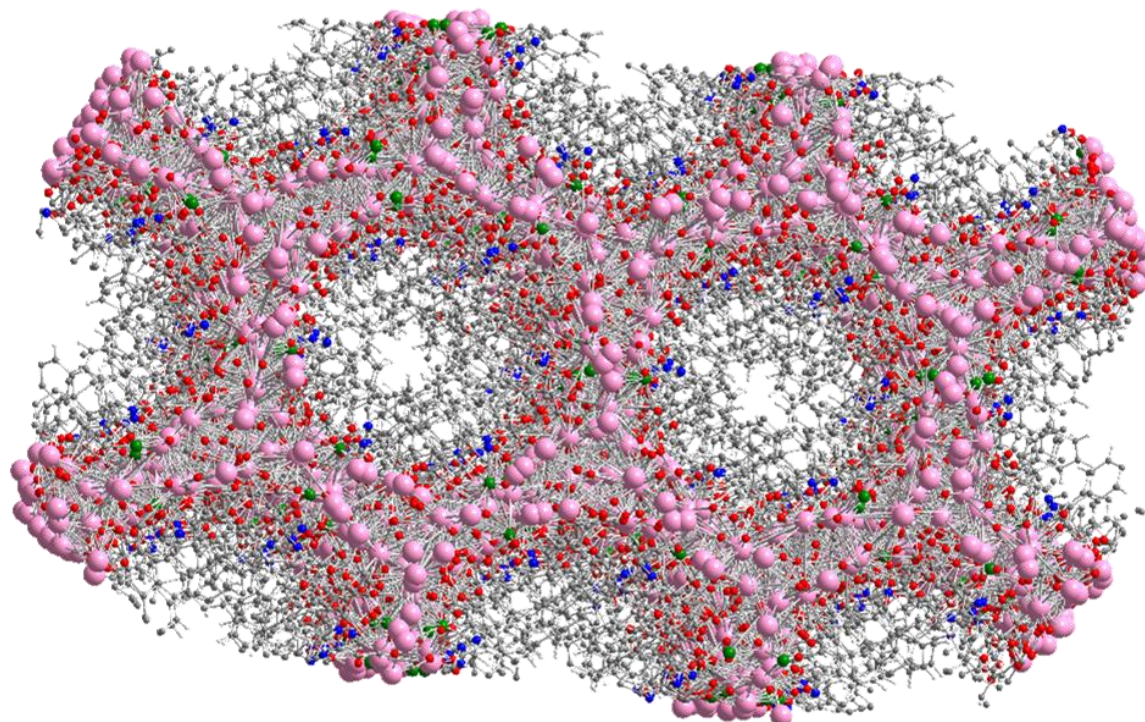


Figure 8-3 Repeating subunit of the dinuclear iron complex of $\text{Na}_6\text{Fe}_2\text{chnida}_2$ showing the separated inorganic and organic areas within the 'honeycomb' structure.^[131, 132]

The large structures are composed of dinuclear iron complexes connected by an alkali-ion network. Although samples containing Li^+ were prepared, the crystals obtained were not measurable and too few to characterise fully. The PXRD shows that $\text{K}_6\text{Fe}_2\text{chnida}_2$ and $\text{Na}_6\text{Fe}_2\text{chnida}_2$ were reproduced successfully. Furthermore, elemental analysis measured for both compounds show they are pure and can be found in the experimental section.

The stacked PXRD patterns shown in Figure 8-4 prove not only the reproducibility of the compounds but also demonstrate that these compounds have a poor long-term stability, shown in the green diffraction pattern which was taken one month after isolation of the $\text{Na}_6\text{Fe}_2\text{chnida}_2$ crystals. The appearance of the peak's change from narrow and sharp which suggest a high crystal quality to broader reflections with a

high baseline showing amorphousness. The presence of the large additional peaks between 20° and 25° represent the degradation products. The most obvious products of decomposition would be iron oxides or alternatively other impurities associated to the solvent loss. Since $\text{Na}_6\text{Fe}_2\text{chnida}_2$ becomes unstable when isolated from the mother solution, it should be calcined immediately to avoid compound decomposition which would affect the reproducibility of the material.

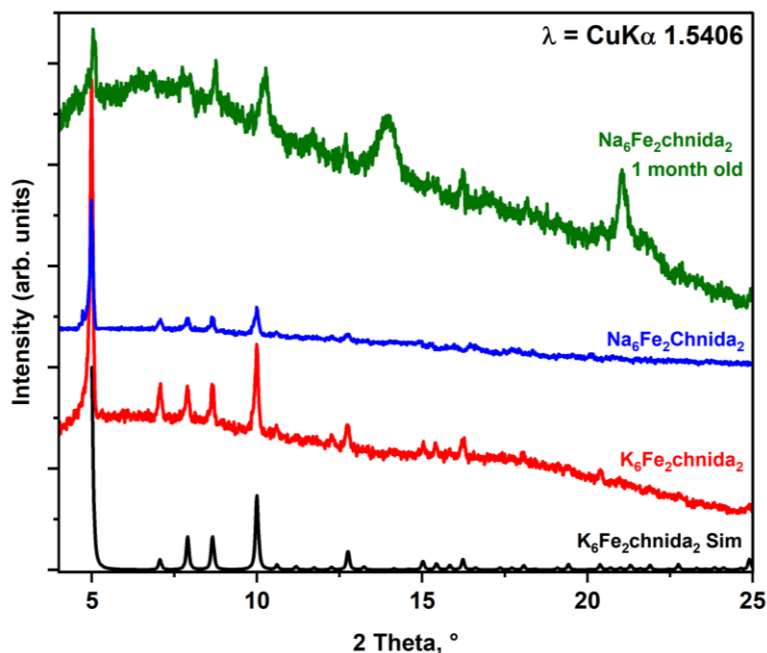


Figure 8-4 Stacked PXRD of simulated $\text{K}_6\text{Fe}_2\text{chnida}_2$ Sim (black), experimental $\text{K}_6\text{Fe}_2\text{chnida}_2$ (red), experimental $\text{Na}_6\text{Fe}_2\text{chnida}_2$ (blue) and the decomposed sample of 1 month old $\text{Na}_6\text{Fe}_2\text{chnida}_2$ (green).

8.1.3 Pyrolysis to the Mixed Phase NaFe_xO_y -500

Pyrolysis of $\text{Na}_6\text{Fe}_2\text{chnida}_2$ at 500°C in air for 6 h resulted in the mixed phase iron oxide NaFe_xO_y -500. Figure 8-5 identifies the phases as Fe_3O_4 (red), Fe_2O_3 (green) and NaCO_3 (blue) using PXRD methods. From the diffraction patterns, we can see broad reflections for Fe_3O_4 . Reflections for Fe_2O_3 are few and weak while the sharpest reflections are observed for NaFeO_2 . Increasing the annealing temperatures would reduce Fe_2O_3 and Fe_3O_4 into FeO . Low yields and stability issues surrounding this complex effectively made it difficult to undertake a systematic study to process different phases using different calcination parameters.

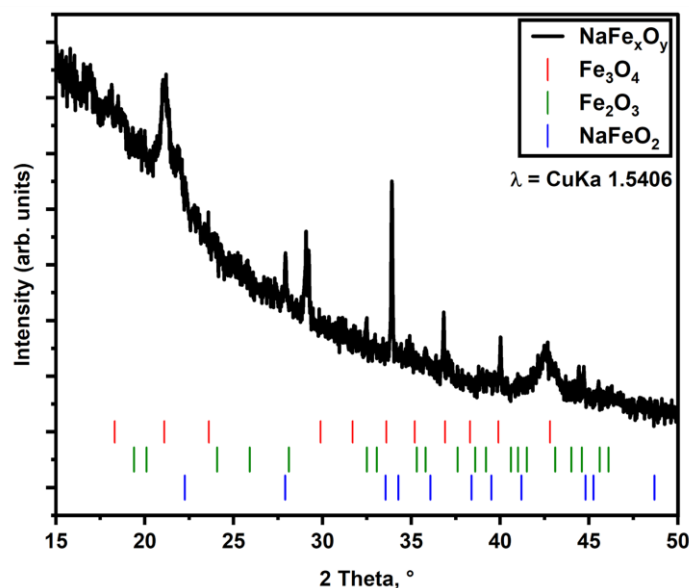


Figure 8-5 The PXRD pattern obtained after pyrolysis to NaFe_xO_y -500 shown in black. The simulated patterns for Fe_3O_4 , Fe_2O_3 , and NaFeO_2 are provided respectively in red, green, and blue for comparison. Reflections related to Na_2CO_3 are not visible. Introduction to Raman spectroscopy given by Dr. Sergei Lebedkin.

Schmitt already reported the formation of alkali-iron oxides through a thermolysis study on these compounds. However, using different furnaces, different parameters, and different lab conditions all play a role in creating reproducible results. Pure phase NaFeO_2 was difficult to obtain as there was always the presence of low crystallinity Fe_3O_4 after pyrolysis which Schmitt did not report. NaFe_xO_y -500 also consists of Fe_2O_3 and although not visible in the PXRD, Na_2CO_3 . NaFe_xO_y -500 was characterised further using SEM and Raman spectroscopy before cycling in a Li-ion and Na-ion coin cell.

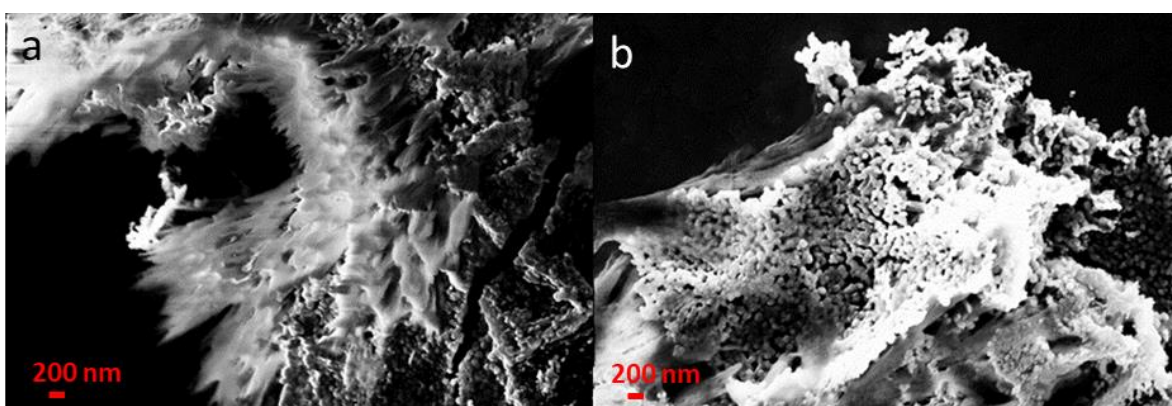


Figure 8-6 SEM images of NaFe_xO_y -500 after pyrolysis at scale bar of 200 nm.

The SEM images collected after pyrolysis in Figure 8-6 show that NaFe_xO_y -500 is made up of a combination of a fibrous-type morphology that corresponds to the Na_2CO_3 in the sample and an additional morphology that looks like nanoparticles for the Fe_xO_y phases. The fibres appear to encase the agglomerated particles, with the fibres on one side and the particles on the other. This makes sense when considering

the morphology of $\text{Na}_6\text{Fe}_2\text{chnid}_2$ which has channels of hydrophobic organic areas surrounded by alkali-rich hydrophilic moieties. However, higher quality electron microscopy images would be required to confirm this combined with elemental mapping to show the distribution of the different elements.

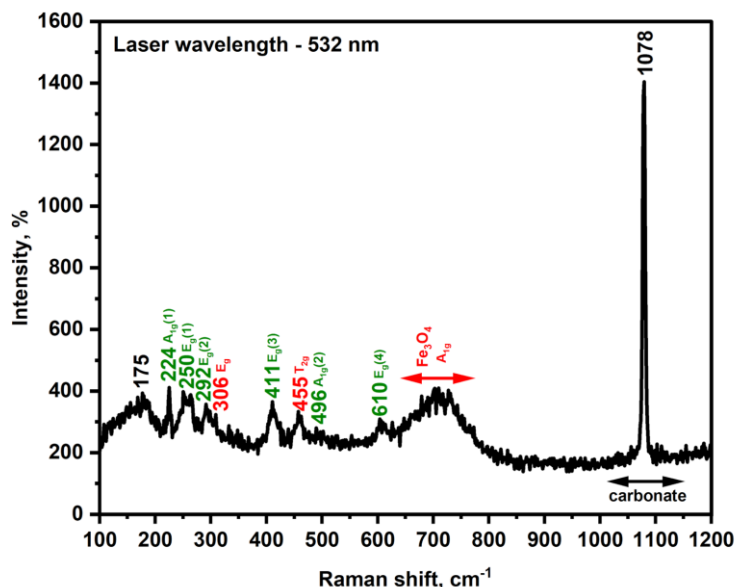


Figure 8-7 Raman spectra of $\text{NaFe}_x\text{O}_y\text{-500}$ showing the characteristic shifts associated to the presence of carbonates, Fe_2O_3 and Fe_3O_4 . The wavelength of the laser used was 532 nm. ^[133]

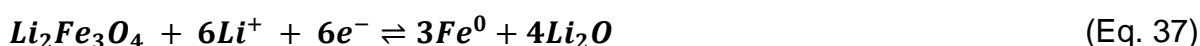
The Raman spectra shown in Figure 8-7 further clarifies the presence of different phases in the sample. Raman active phases are non-centrosymmetric. The strong peak at 1078 cm^{-1} correlates to the presence of carbonates. Peaks at 306 cm^{-1} , 455 cm^{-1} and the broad range across 650 cm^{-1} to 750 cm^{-1} correspond to Fe_3O_4 . Like that seen in the PXRD, the broad peaks suggest the amorphousness of this phase. Likewise, the carbonate peak is strong and sharp matching the crystallinity seen in the PXRD. This is due to the amorphous phases having distorted bond angles and so the long-range order is lost, neighbour interactions are affected, and this causes a shift in the vibrational frequency. The presence of such distortions causes the broader bands. The spectrum for Fe_3O_4 is generally weaker than Fe_2O_3 , which has defining peaks at 225 cm^{-1} , 250 cm^{-1} , 292 cm^{-1} , 411 cm^{-1} , 496 cm^{-1} , and 610 cm^{-1} .

8.1.4 Electrochemical Analysis in a Li-ion Coin Cell

The CV curves shown in Figure 8-8 follow the patterns reported previously for Fe_3O_4 active materials. The 1st cycle measured at 0.1 mV s^{-1} shown in, shows a broad reduction at 0.74 V with a shoulder at 1.18 V . The shoulder which has probably overlapped with the stronger peak at 0.74 V is the intercalation of lithium into the spinel Fe_3O_4 structure.



This sharp cathodic peak at 0.74 V is typical for the conversion reaction of Fe^{II} to Fe^0 that forms Li_2O . This process is shown in the reaction below which shows the electrochemical behaviour of Fe_3O_4 :



This is followed by four oxidations at 0.55 V , 1.13 V , 1.51 V and 1.80 V . The anodic peaks at 0.55 V and 1.13 V are related to irreversible reactions that disappear in the following cycles. The oxidations at 1.5 V and 1.8 V are associated to the oxidation of Fe^0 to Fe^{II} (FeO) and Fe^{III} (Fe_2O_3) respectively in the reversible multi-step reaction.

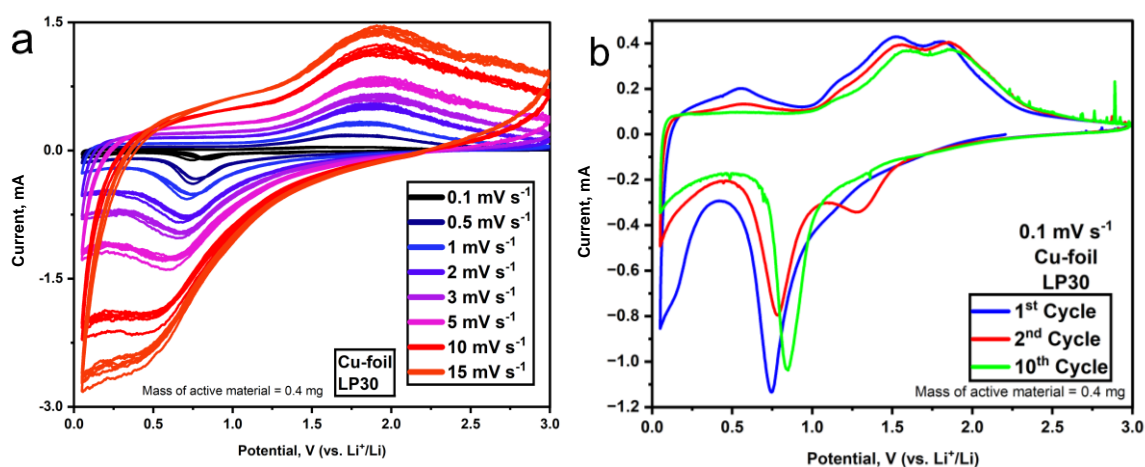


Figure 8-8 Current vs. Voltage (CV) diagram for $\text{NaFe}_x\text{O}_y-500$ in a Li-ion coin cell at multiple scan rates: 0.1 mV s^{-1} , 0.5 mV s^{-1} , 1 mV s^{-1} , 2 mV s^{-1} , 3 mV s^{-1} , 5 mV s^{-1} , 10 mV s^{-1} , and 15 mV s^{-1} .

From the 2nd cycle onwards all additional peaks besides the single reduction at 0.83 V and the oxidations at 1.59 V and 1.87 V disappear. As the scan rate increases, the broader peaks with larger hysteresis' are observed. There seems to be regions of instability during cycling which is shown by the fluctuating points observed at potentials above 1.5 V in the anodic region and the potentials below 0.75 V in the cathodic region.

Observing the first 140 cycles, which includes the rate capability measurements at current densities of 100 mA g^{-1} , 200 mA g^{-1} , 500 mA g^{-1} , and 2000 mA g^{-1} , the initial

capacity is 616 mAh g^{-1} , followed by what appears to initially be the slow degradation of the cell through the different current densities and even during the long-range cycling from cycle 41 to 140. Between 40 and 55, the cell maintains a certain level of stability before the capacity begins to drop with each additional cycle measured. At the 140th cycle, the capacity totals 128 mAh g^{-1} . The cell was left to cycle for a further 100 cycles to see how long the degradation process may take.

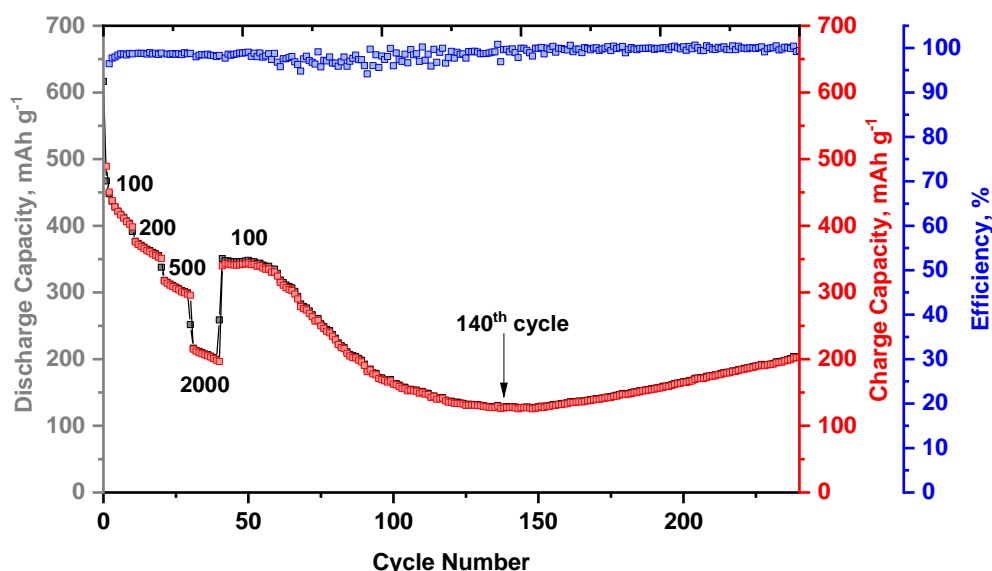


Figure 8-9 Rate capability of $\text{NaFe}_x\text{O}_y\text{-500}$ showing cycle number vs capacity for the first 40 cycles measured at current densities of 100 mA g^{-1} , 200 mA g^{-1} , 500 mA g^{-1} , and 2000 mA g^{-1} , before returning back to 100 mA g^{-1} for long term cycling of over 200 additional cycles.

From the 140th cycle onwards, the capacity gradually increases up to the 240th cycle where the capacity is 203 mAh g^{-1} . $\text{NaFe}_x\text{O}_y\text{-500}$ undergoes phase/structural changes. What becomes clear is that there is restorative behaviour at the electrode and longer cycling times would allow the full capacity and potential stability of the electrode to be observed.

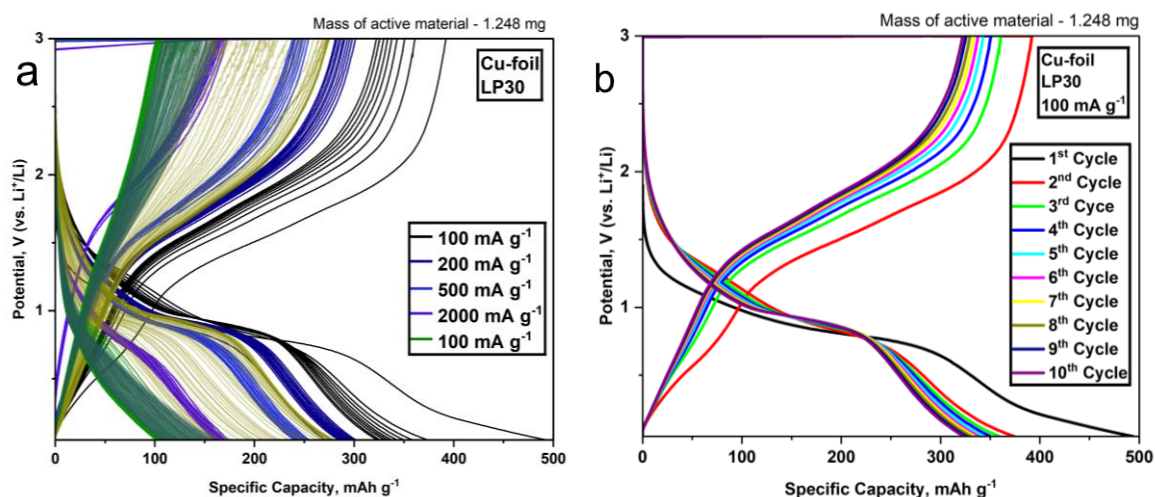


Figure 8-10 Galvanostatic charge/discharge measurements of $\text{NaFe}_x\text{O}_y\text{-500}$ used as the active electrode material in a Li-ion cell. 10 cycles were measured at each current density of 100 mA g^{-1} , 200

mA g^{-1} , 500 mA g^{-1} , and 2000 mA g^{-1} , before returning to 100 mA g^{-1} for the remaining 200 cycles measured.

The plateaus in the GCD show the phase transitions occurring during cycling which correlate to the dQ/dV plot below in Figure 8-10. During the initial galvanostatic discharge, there is a plateau at 0.77 V which correlates to a peak in the dQ/dV plot.

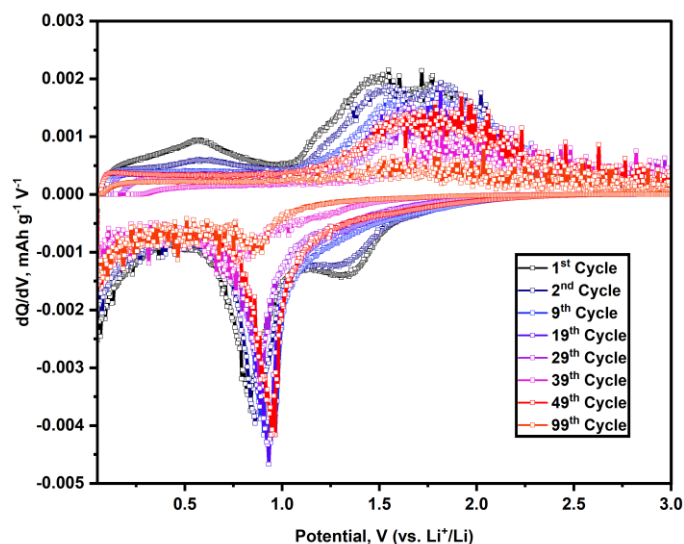


Figure 8-11 'Differential Capacity' dQ/dV vs. V plot for NaFe_xO_y -500.

From hereon, the plateaus favour a sloped profile. During the 1st cycle, there is only one charge plateau observed in the GCD, which correlates to two oxidations at 1.51 V and 1.80 V in the dQ/dV that agree to the gradual oxidation of Fe^0 , to Fe^{II} , and then to Fe^{III} . There are two reduction processes measured at 1.3 V and 0.83 V . The reduction at 1.34 V is due to the initial intercalation mechanisms.

8.1.5 Electrochemical analysis in a Na-ion Coin Cell

The CV curves shown in Figure 8-12 for the Na-ion cell are like that seen for the Li-ion cell. The 1st cycle measured at 0.1 mV s⁻¹ shown in Figure 8-12, shows three reduction steps followed by three oxidations. The reduction potentials at corresponds to the intercalation of sodium into the spinel Fe₃O₄ structure shown in the equation below:



This cathodic peak at 0.37 V is the conversion reaction of Fe^{II} to Fe⁰ that forms Na₂O. This process is shown in the reaction below which shows the electrochemical behaviour of Fe₃O₄:



Additional reductions/substructures correspond to the SEI formation. The oxidations are recorded at 0.7 V and 1.12 V. These anodic peaks are associated to the oxidation of Fe⁰ to Fe^{II} (FeO) and Fe^{III} (Fe₂O₃) respectively in the reversible multi-step reaction.

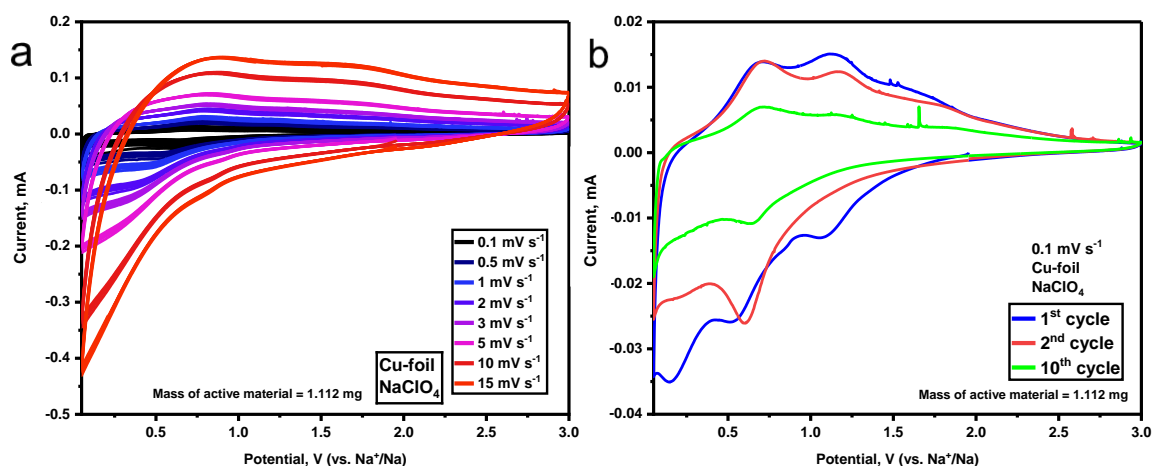


Figure 8-12 Cyclic voltammetry measured for NaFe_xO_y-500 in a Na-ion coin cell at multiple scan rates: 0.1 mV s⁻¹, 0.5 mV s⁻¹, 1 mV s⁻¹, 2 mV s⁻¹, 3 mV s⁻¹, 5 mV s⁻¹, 10 mV s⁻¹, and 15 mV s⁻¹.

The 2nd cycle through to the 10th cycle at a sweep rate of 0.1 mV s⁻¹ only shows single reduction potentials and this cathodic peak gradually becomes less visible over the additional sweep rates. Likewise, the anodic peak positions remain at the same potentials but gradually become broader and less definable as the sweep rates increase.

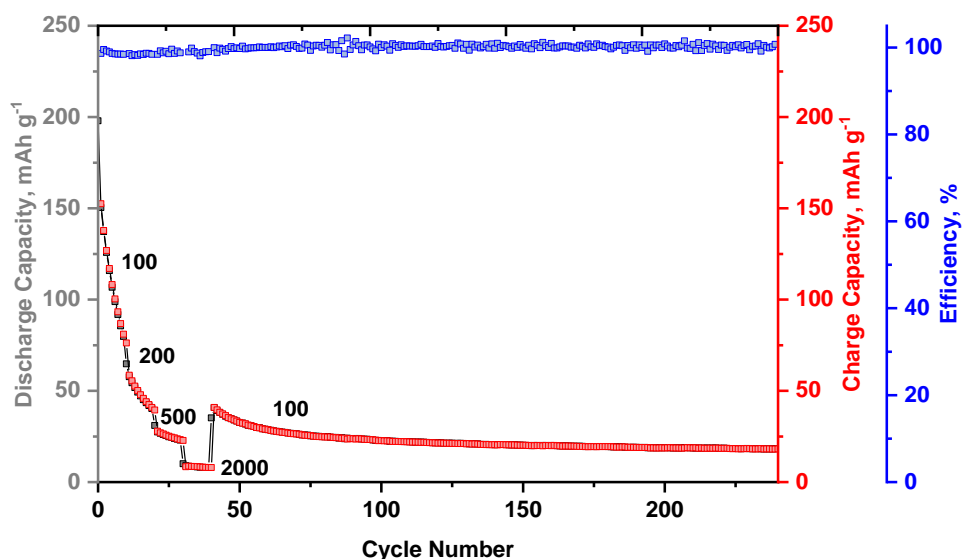


Figure 8-13 Rate capability of $\text{NaFe}_x\text{O}_y\text{-500}$ showing cycle number vs capacity for the first 40 cycles measured at current densities of 100 mA g^{-1} , 200 mA g^{-1} , 500 mA g^{-1} , and 2000 mA g^{-1} , before returning to 100 mA g^{-1} for the long term cycling over 200 additional cycles.

Rate capability cycling of $\text{NaFe}_x\text{O}_y\text{-500}$ records an initial discharge capacity of 197 mAh g^{-1} at 100 mA g^{-1} which undergoes drastic capacity fade by the 10th cycle to 76 mAh g^{-1} . Increasing the current density to 200 mA g^{-1} , the capacity fades from 58 mAh g^{-1} to 39 mAh g^{-1} between the 11th and 20th cycles. At 500 mA g^{-1} , the capacity fades from 27 mAh g^{-1} to 22 mAh g^{-1} . At 2000 mA g^{-1} , there is an average capacity of 8 mAh g^{-1} . Returning the current density to 100 mA g^{-1} , the capacity increases to 40 mAh g^{-1} before gradually fading over the following 200 cycles to 18 mAh g^{-1} .

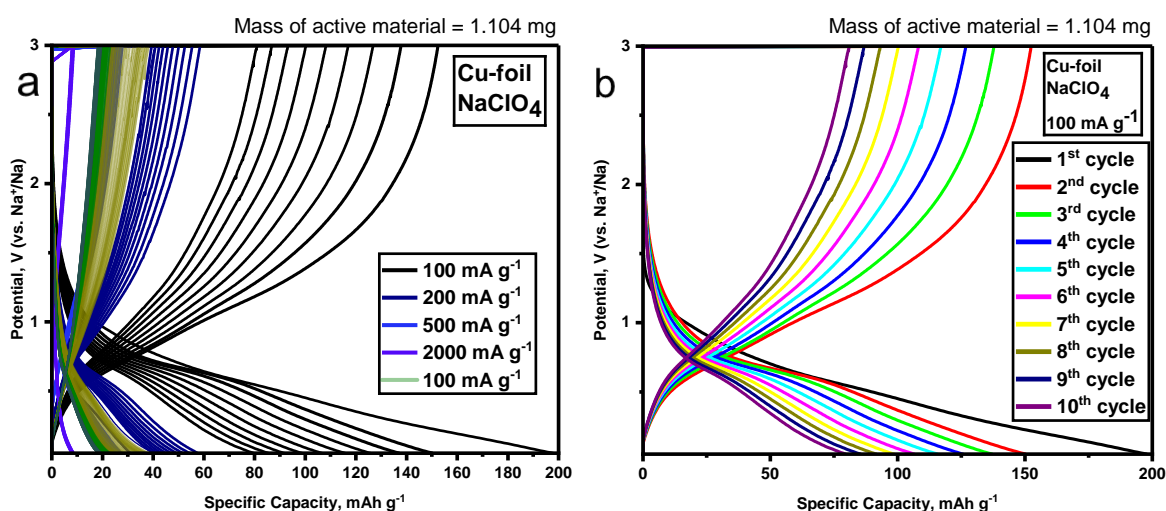


Figure 8-14 Galvanostatic charge-discharge of a Na-ion cell using $\text{NaFe}_x\text{O}_y\text{-500}$ as the active electrode material. 10 cycles were measured at each current density of 100 mA g^{-1} , 200 mA g^{-1} , 500 mA g^{-1} , and 2000 mA g^{-1} , before returning to 100 mA g^{-1} for the long-term cycling over 200 additional cycles.

The plateaus in the GCD show the phase transitions occurring during cycling which correlate to the dQ/dV plot in Figure 8-15. During the initial galvanostatic discharge,

the plateau at 0.71 V corresponds to reduction to Fe^0 . All cycles favour plateaus with a sloped profile which make using the dQ/dV plot even more vital.

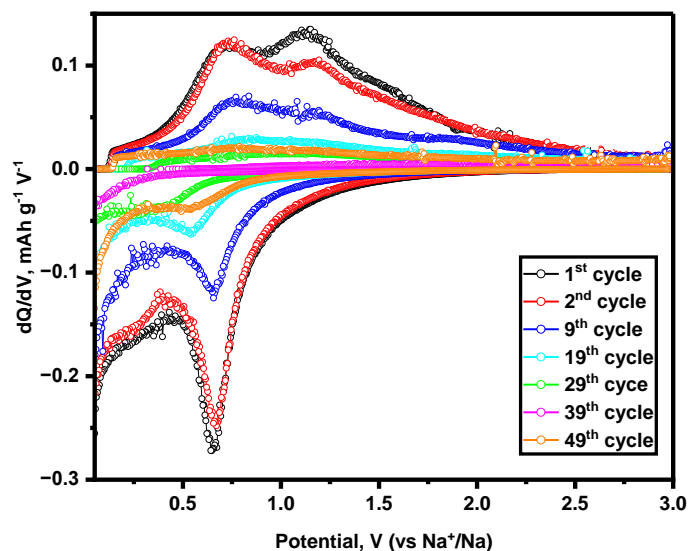


Figure 8-15 dQ/dV for NaFe_xO_y -500 processed from the galvanostatic cycling.

During the 1st cycle, there is only one discharge plateau observed in the GCD, which correlates to two oxidations at 0.75 V and 1.21 V in the dQ/dV that agree to the gradual oxidation of Fe^0 , to Fe^{II} , and then to Fe^{III} . This profile is consistent across all cycles measured showing the reversibility of the redox profiles. Unlike the Li-ion cell measured, the cycling profiles obtained for the Na-ion cells are much smoother with little to no fluctuating data points suggesting that even though the Li-ion cell observed higher capacities (whilst also seemingly undergoing in-situ electrode modifications), the presence of sodium within the active material could be the cause of destabilisation of the electrode.

8.2 Characterisation of Additional Ligands

Ligands:

- [(3-Carboxy-2-hydroxy-1-naphthyl) methylene]-N-(2-acetamido) iminodiacetic acid (chnaida)
- [(3-Carboxy-2-hydroxy-1-naphthyl) methylene]-tris(hydroxymethyl) amino methane (chntoham)
- [(3-Carboxy-7-methoxy-2-hydroxy-1-naphthyl) methylene]-iminodiacetic acid (omechnida)

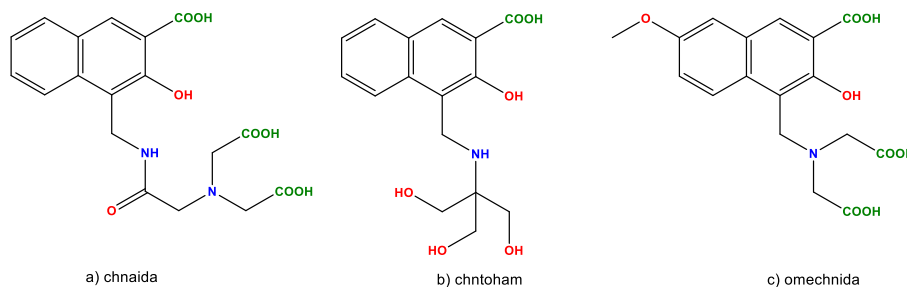


Figure 8-16 The additional ligands synthesised: (a) chnaida, (b) chntoham, and (c) omechnida.

These ligands are all a variation of chnida, with chnaida using N-(2-acetamido) iminodiacetic acid and chntoham using the readily available buffer tris-hydroxymethylamine. Chnaida and chntoham are novel and previously unreported/unpublished ligands. Likewise, omechnida is similar to the reported chnida but with a methoxy- substituent on the naphthoic acid. It is also a possibility to extend the π -system further, to increase the carbon saturation of the resultant ligand and therefore the compounds once crystallised. Although these ligands all bear a resemblance to the already published chnida, there remains the serendipity of large honeycomb coordination during crystallisation which is believed to be tuned by both the flexible amine and the π -system of the ligand.

This project is open to many variations and when considering future studies, a comprehensive set of ligands could be prepared by exploring an extension of the carbon system either by expanding the π -systems of the ligand or adding additional functional groups. The modifications of the ligand chnida were prepared and characterised by NMR, IR, and EA.

Overlap of Infrared Spectra (IR)

The overlap of the infrared spectra shows the presence of the main functional groups expected for each ligand. IR analysis of the ligands show the presence of amines, amides, and carboxylate groups for ligand characterisation and confirmation of the formation of the Mannich ligands. Combined with the NMR data and CHN elemental analysis (EA) provided in the experimental section, the bulk purity of the ligands is confirmed.

Chnida, shown in green, has sharp peaks attaining to the C-H stretching modes at 3010 cm^{-1} for the sp^2 C-H and at 2990 cm^{-1} for the sp^3 C-H of the phenyl ring. Medium peaks are visible for the C=O stretch at 1650 cm^{-1} and 1720 cm^{-1} , the O-H bend at 1380 cm^{-1} and the C-N wag at 1230 cm^{-1} . Tertiary amines do not show any peaks in the IR due to the absence of an N-H bond. However, C-N stretches can be used to confirm at least the presence of a C-N bond.

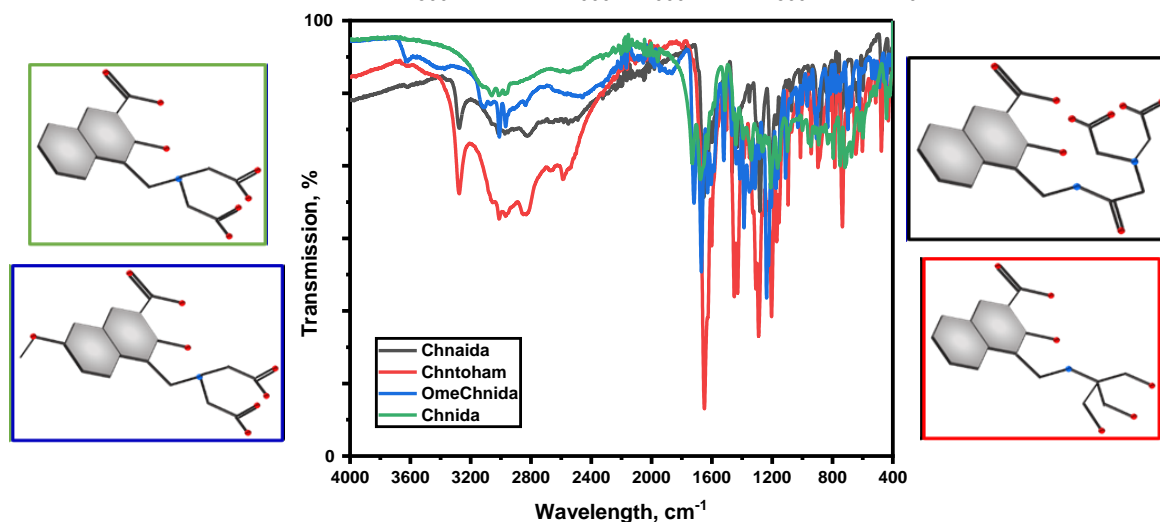


Figure 8-17 Overlap of the infrared spectra of **chnida**, **omechnida**, **chnaida**, and **chntoham**.

Omechnida, shown in blue, is very similar to the pattern of **chnida** besides the low strength presence of the C-O-CH₃ stretching vibration at 2800 cm^{-1} . This is accompanied by sharper peaks for the C-H stretches for sp^2 C-H at 3010 cm^{-1} and sp^3 C-H at 2950 cm^{-1} , sharper C=O stretches at 1750 cm^{-1} and 1680 cm^{-1} , sharper O-H bending at 1360 cm^{-1} and stronger C-N wagging at 1250 cm^{-1} .

Chnaida, shown in black, has a similar general profile to the spectra of **chnida** and **omechnida**. The broad O-H stretch for COOH is between 2250 cm^{-1} and 3250 cm^{-1} as well as the three C=O stretches assigned between 1600 cm^{-1} and 1700 cm^{-1} . The 2° amine stretch at 3300 cm^{-1} correlates to the Mannich addition of the amino substituent.

Chntoham, shown in red, gives a stronger transmission of all peaks. The similar O-H stretching, and the C-N wagging are seen as like **chntoham**. The N-H stretch is present at the same wavenumber, likewise, is the O-H bend and C-N bend. As the ligands are in general extremely similar with the presence of the C-N, C-O, N-H and C=O stretching/bending suggesting the successful amine/amide addition, NMR was carried out to further confirm the successful ligand formation and purity. NMR and EA data can be found in chapter 9.

8.3 Summary and Conclusions

To summarise, a large alkali-iron coordination complex which has separated organic and inorganic layers, was reproduced to apply as the active electrode material in both a Li-ion and Na-ion battery. As discussed in the literature, many compounds that observe high performance in Li-ion batteries often cannot be transferred directly into a Na-ion battery due to the difference in the ionic radius of the alkali metals effecting their storage properties. Although a capacity of only 18 mAh g⁻¹ was obtained after cycling NaFe_xO_y-500 in a Na-ion coin cell, the stability of the performance leaves room for modifications. In a Li-ion cell, a capacity of 203 mAh g⁻¹ was obtained after cycling. Pyrolysing these oxides to higher temperatures as well as using different gas atmospheres could result in an improvement of the crystallinity and/or the performance.

Additional ligands were prepared to showcase the potential to synthesise a broader range of alkali-rich complexes to aim to form sodium-iron oxides for Na-ion battery applications.

9 Complete Experimental

All chemicals were purchased from Sigma Aldrich, Alfa Aesar, TCI, abcr or bldpharm.

Chapter 4

MnO₂-NP: This material was prepared by mechanically grinding commercial 0.5 g MnO₂ using a ball mill at 150 rpm for 6 hours. The powder was transferred to a Teflon-lined steel autoclave with the addition of 10 ml 12M NaOH and followed by hydrothermal synthesis at 120 °C. The sample was cooled, washed thoroughly with water and dilute HCl and dried in the oven at 80°C for 12 hours to form MnO₂-Hydro. This was calcined at 600 °C for 4 hours.

MnO₂Y-NP: Prepared like MnO₂-NP but with the addition of 5 mol% Y₂O₃ to the MnO₂ before ball milling.

MnO₂Ce-NP: Same as MnO₂Y-NP but with the addition of 5 mol% CeO₂.

MnO₂Dy-NP: Same as MnO₂Y-NP but with the addition of 5 mol% Dy₂O₃.

MnO₂Yb-NP: Same as MnO₂Y-NP but with the addition of 5 mol% Yb₂O₃.

Chapter 5

Mn-formate:

Synthesised as reported by Dybsteven et al.: In a beaker 198 mg of MnCl₂·4H₂O, 151 µL of formic acid, 8 ml of diethyl formamide, and 4 ml of dioxane were combined and sonicated until the dissolution of all solids. The solution was then transferred to a Teflon-lined stainless-steel autoclave to undergo solvothermal synthesis at 120 °C for 24 h. The sample was cooled at a rate of 2 °C/min. Pale pink crystals of Mn-formate formed during cooling and were collected for characterisation and further analysis.

EA Mn(HCO₂)₂·0.33(C₄H₈O₂)·1.2(H₂O): Theoretical: C 20.3 H 33.6. Experimental: C 20.3 H 33.4.

Mn-formate was pyrolysed at 400 °C under a nitrogen atmosphere at a rate of 10 °C/min to form MnO:Mn₃O₄. It was held at this temperature for 10 minutes before cooling to room temperature for further characterisation and analysis.

Mn₁₂OAc:

Synthesised exactly as reported by Lis. T.: Mn(CH₃COO)₂.4H₂O (4 g) was added to 60% CH₃COOH (40 ml) in a beaker and stirred at room temperature until dissolved. KMnO₄ (1g) was dissolved in ~20ml water and added dropwise to the beaker. Once all the permanganate had been added, the solution was stirred for an additional 5 minutes before removing the magnetic stirrer and leaving to crystallise. Overnight, large crystals of red/black needles formed. They were filtered for further analysis.

EA C₃₆H₇₂Mn₁₂O₅₆: Theoretical: C 21.0 H 3.5 O 43.5. Experimental: C 21.2 H 3.1 O 43.6.

Mn₁₂OAc was calcined at in air at 500 °C for 6 hours at a heating rate of 10 °C/min. The product of calcination, Mn₁₂OAc- α -MnO₂, was collected for further characterisation.

Mn₃Ca₃Na₃:

Modified from the synthesis reported by Ako et al. This complex crystallises in the same space group with similar unit cell parameters. The charge is not quite balanced, but this compound was ultimately pyrolysed to form an oxide. 100 mg MnCl₂.4H₂O, 2 μ l Et₃N, 140 mg 2,6-bis(hydroxymethyl)-4-methylphenol, and 30 mg NaN₃ were combined to form a slurry in a mixture of MeCN and MeOH and stirred for 2 h at room temperature. CaCl₂ was added gradually, and the solution was refluxed for 3 h to afford a clear brown solution. The solution was cooled to room temperature before covering with parafilm and leaving to crystallise over a period of 3 weeks.

EA C₅₄H₉₀Ca₃ClMn₃Na₃O₃₀: Theoretical: C 41.5 H 5.8 O 30.7. Experimental: C 41.4 H 5.6 O 31.2.

Mn₃Ca₃Na₃ was pyrolysed under an Ar atmosphere, at a heat rate of 10 °C/min to 400 °C for 4 h before cooling to room temperature to form MnO:Mn₃O₄-400. The pyrolysis was repeated with two additional samples to 600 °C and to 800 °C to form Mn₃O₄-600 and Mn₃O₄-800 respectively.

Mn₂₁BrGlyc:

Modified from the synthesis reported by S. Nayak.^[128] This molecular compound is the analogue of the chloride containing structure reported by Nayak. MnBr₂.4H₂O, glycerol, TEA, NaN₃, MeOH were combined and stirred at room temperature for 4 h

before leaving to crystallise via evaporation for 1 week. The complex was pyrolysed to 400 °C at a rate of 2°C/min for 1 hour to produce the uniformly porous oxide.

EA C₃₆H₁₀₂Br₄Mn₂₂N₃₆O₅₉: Theoretical: C 12.3 H 2.9 N 14.3 O 26.8. Experimental: C 12.5 H 2.7 N 14.1 O 26.6.

Mn₂₁BrGlyc was calcined at four temperatures, 500, 550 and 600 to give MnO-500, MnO-550, and MnO-600. MnO-600 was studied electrochemically.

Chapter 6

Chnida (333 g/mol)

Chemicals: iminodiacetic acid, H₂O, 30%-NaOH solution, 3-hydroxy-2-naphthoic acid, acetic acid, 40%-formaldehyde, EtOH.

Reproduced as reported by the literature from W. Schmitt. Iminodiacetic acid (732 mg, 0.005 mol) was added to H₂O (25 ml) with 30%-NaOH, to neutralise to pH 6.5. The solution was then acidified by addition of 3-hydroxy-2-naphthoic acid (1090 mg, 0.005 mol) in acetic acid (80 ml). The solution was left to stir for 20 minutes at room temperature before adding 40%-formaldehyde solution (537 mg, 1.34 ml, 0.072 mol) dropwise. 30 minutes after the addition of the aldehyde, a pale-yellow precipitate began to form. The reaction mixture was left to stir for a further 2 hours at room temperature and then left overnight. The cream product was washed with H₂O (150 ml) followed by EtOH (150 ml). Yield 503 mg (with respect to 3-hydroxy-2-naphthoic acid)

IR (cm⁻¹): 3125 (m,br), 3058 (m,br), 3008 (w), 2520 (m,br), 1651 (s), 1625 (sh), 1596 (sh), 1512 (m), 1466 (s), 1430 (m), 1349 (w), 1283 (s), 1214, (m) 1198 (sh), 1170 (sh), 1145 (m), 1136 (sh), 1093 (w), 1070 (m), 1010 (w), 954 (m), 900 (m), 876 (m), 842 (w), 830 (w), 787 (m), 766 (m), 745 (m,br), 730 (m), 471 (s).

NMR: NMR(500MHz, DMSO): δ(ppm) = 3.30 (s, 4H, CH₂), 4.10 (s, 4H, CH₂), 7.14 (m, 1H, 5-CH naphthalene), 7.33 (m, 1H, 6-CH, naphthalene), 7.79 (m, 1H, 4-CH, naphthalene), 8.07 (m, 1H, 7-CH, naphthalene), 8.52 (m, 1H, 3-CH, naphthalene), 12.17 (br, 1H, OH).

EA: Theoretical, C 57.66 H 4.54 N 4.2 O 33.6. Experimental, C 57.9 H 4.4 N 4.1 O 33.6

NaFechnida:

Chemicals: chnida, $\text{FeCl}_3 \cdot 6\text{H}_2\text{O}$, MeOH, EtOH, 2M-NaOH/2M-KOH.

This complex was synthesised as reported by W. Schmitt.^[132] In a beaker, $\text{FeCl}_3 \cdot 6\text{H}_2\text{O}$ (135 mg, 0.5 mmol) and the synthesised ligand Chnida (75 mg, 0.22 mmol) were suspended in methanol (30 ml) and stirred at room temperature for 20 minutes to form a slurry. Dropwise, 2M-NaOH (2 ml) was added until a clear red solution was obtained.

Additional ligandsOmechnida (363 g/mol)

Chemicals: Iminodiacetic acid, H_2O , 30%-NaOH solution, 3-hydroxy-7-methoxy-2-naphthoic acid, acetic acid, 40%-formaldehyde, EtOH.

The ligand omechnida was synthesised by adding iminodiacetic acid (732 mg, 0.005 mol) to H_2O (25 ml) with 30%-NaOH added slowly to neutralise to pH 6.5. The solution was then acidified by addition of 7-hydroxy-6-methoxy-2-naphthoic acid (1090 mg, 0.005 mol) in acetic acid (80 ml). The solution was left to stir for 20 minutes at room temperature before adding 40%-formaldehyde solution (537 mg, 1.34 ml, 0.072 mol) dropwise. 30 minutes after the addition of the aldehyde, a pale-yellow precipitate began to form. The reaction mixture was left to stir for a further 2 hours at room temperature and then left overnight. The cream product of omechnida was washed with H_2O (150 ml) followed by EtOH (150 ml). Yield 503 mg (with respect to 3-hydroxy-2-naphthoic acid).

IR (cm^{-1}): 3110 (m,br), 3063 (m,br), 3006 (s), 2966 (m,br), 2833 (w,br), 2462 (m,br), 1706 (s), 1675 (s), 1627 (m), 1601 (sh), 1576 (sh), 1520 (s), 1464 (m), 1433 (sh), 1412 (sh), 1386 (s), 1343 (sh), 1312 (m), 1278 (s), 1235 (s), 1227 (sh), 1205 (sh), 1175 (sh), 1171 (sh), 1136 (sh), 1106 (s), 1093 (m), 1024 (m), 1003 (w), 968 (w), 908 (m), 830 (m), 842 (w), 830 (w), 701 (m), 671 (sh), 619 (m).

NMR: NMR(500MHz, DMSO): δ (ppm) = 3.29 (s, 4H, CH_2), 3.82 (s, 3H, O- CH_3), 4.13 (s, 4H, CH_2), 7.03 (m, 1H, 6-CH naphthalene), 7.35 (m, 1H, 4-CH naphthalene), 8.03 (m, 1H, 7-CH, naphthalene), 8.40 (m, 1H, 3-CH, naphthalene), 8.52 (m, 1H, 3-CH, naphthalene), 12.44 (br, 1H, OH).

EA: Theoretical, C 56.04 H 4.98 N 3.84 O 35.13. Experimental, C 56.2 H 4.7 N 3.9 O 35.2.

Chnaida (366 g/mol)

Chemicals: N-(2-acetamido) iminodiacetic acid, H₂O, 30%-NaOH, 3-hydroxy-2-naphthoic acid, acetic acid, 40%-formaldehyde, EtOH.

N-(2-acetamido) iminodiacetic acid (1045 mg, 0.055 mol) was added to H₂O (25 ml) with 30%-NaOH, to neutralise to pH 6.5. The solution was then acidified by addition of 3-hydroxy-2-naphthoic acid (940 mg, 0.05 mol) in acetic acid (80 ml). The solution was left to stir for 20 minutes at room temperature before adding 40%-formaldehyde solution (537 mg, 1.34 ml, 0.072 mol) dropwise. 30 minutes after the addition of the aldehyde, a pale-yellow precipitate began to form. The reaction mixture was left to stir for a further 2 hours at room temperature. The pale-yellow product was washed with H₂O (150 ml) and then with EtOH (150 ml). Yield 731 mg (with respect to 3-hydroxy-2-naphthoic acid).

IR (cm⁻¹): 3273 (s), 3018 (m,br), 3006 (s), 2830 (m,br), 2554 (m,br), 1662 (m), 1623 (sh), 1592 (sh), 1511 (m), 1464 (sh), 1429 (sh), 1347 (w), 1274 (s), 1218 (m), 1200 (sh), 1175 (sh), 1144 (sh), 1136 (sh), 1072 (m), 955 (m), 895 (m), 873 (m), 830 (w), 787 (m), 770 (w), 748 (m), 722 (sh), 638 (b), 600 (w), 472 (m).

NMR: NMR(500MHz, DMSO): δ (ppm) = 3.36 (s, 4H, CH₂), 4.83 (s, 4H, CH₂), 7.24 (m, 1H, 5-CH naphthalene), 7.35 (m, 1H, 6-CH naphthalene), 7.77 (m, 1H, 4-CH, naphthalene), 8.13 (m, 1H, 7-CH, naphthalene), 8.44 (m, 1H, 3-CH, naphthalene), 8.55 (s, 1H, NH), 11.08 (br, 1H, OH).

EA: Theoretical, C 55.38 H 4.65 N 7.18 O 32.79. Experimental, C 55.4 H 4.5 N 7.3 O 32.8.

Chntoam (318 g/mol)

Chemicals: tris(hydroxymethyl)amino methane, H₂O, 30%-NaOH, 3-hydroxy-2-naphthoic acid, acetic acid, 40%-formaldehyde, EtOH.

Tris(hydroxymethyl)amino methane (666 mg, 0.055 mol) was added to H₂O (25 ml). This formed a basic solution which was slowly acidified by addition of 3-hydroxy-2-naphthoic acid (940 mg, 0.05 mol) in acetic acid (80 ml). The solution was left to stir for 20 minutes at room temperature before adding 40%-formaldehyde solution (537 mg, 1.34 ml 0.072 mol) dropwise until the reaction mixture turned yellow. 30 minutes after the addition of the aldehyde, a pale-yellow precipitate began to form. The reaction mixture was left to stir at room temperature overnight. The yellow product

was washed with H₂O (150 ml) followed by EtOH (150 ml). Yield 587 mg (with respect to 3-hydroxy-2-naphthoic acid).

IR (cm⁻¹): 3227 (s), 3018 (m,br), 3011 (m,br), 2966 (m,br), 2837 (m,br), 2659 (m,br) 2579 (m) 1644 (s), 1601 (sh), 1498 (w), 1446 (m), 1429 (s), 1312 (sh), 1287 (m), 1200 (s), 1218 (m), 1200 (sh), 1171 (sh), 1153 (sh), 1093 (sh), 1067 (w), 1016 (m), 938 (m), 886 (b), 787 (m), 736 (s), 640 (b), 597 (w), 541 (w), 512 (w), 472 (m), 429 (m).

NMR: NMR(500MHz, DMSO): δ (ppm) = 3.39 (s, 6H, CH₂), 4.20 (s, 4H, CH₂), 4.94 (s, 3H, CH₂-OH), 6.36 (s, 1H, NH), 7.16 (m, 1H, 5-CH naphthalene), 7.31 (m, 1H, 6-CH, naphthalene), 7.78 (m, 1H, 4-CH, naphthalene), 8.11 (m, 1H, 7-CH, naphthalene), 8.46 (m, 1H, 3-CH, naphthalene), 8.46 (s, 1H, NH), 12.52 (br, 1H, OH).

EA: Theoretical, C 58.24 H 6.19 N 4.53 O 31.04. Experimental, C 59.8 H 6.5 N 5.1 O 29.6.

10 Bibliography

- [1] D. Linden, T. Reddy, *Handbook of Batteries*, McGraw-hill, **2002**.
- [2] K. Oldham, J. Myland, A. Bond, *Electrochemical Science and Technology: Fundamentals and Applications*, Wiley, **2011**.
- [3] J. M. Tarascon, P. Simon, *Electrochemical Energy Storage*, Wiley, **2015**.
- [4] H. Wang, S. Hamanaka, T. Yokoyama, H. Yoshikawa, K. Awaga, *Chemistry – An Asian Journal* **2011**, 6, 1074-1079.
- [5] U. S. E. P. Agency, United States government, **2023**.
- [6] V. Aravindan, J. Gnanaraj, Y.-S. Lee, S. Madhavi, *Chemical Reviews* **2014**, 114, 11619-11635.
- [7] L. Panasonic Energy Co., **2023**.
- [8] F. Schipper, D. Aurbach, *Russ. J. Electrochem.* **2016**, 52, 1095-1121.
- [9] K. Mizushima, P. C. Jones, P. J. Wiseman, J. B. Goodenough, *Mater. Res. Bull.* **1980**, 15, 783-789.
- [10] M. S. Whittingham, *Science* **1976**, 192, 1126-1127.
- [11] X. Zhao, Y. Wu, Y. Wang, H. Wu, Y. Yang, Z. Wang, L. Dai, Y. Shang, A. Cao, *Nano Research* **2020**, 13, 1044-1052.
- [12] J. B. Goodenough, *Nature Electronics* **2018**, 1, 204-204.
- [13] A. K. Padhi, K. S. Nanjundaswamy, J. B. Goodenough, *Journal of The Electrochemical Society* **1997**, 144, 1188.
- [14] C. E. L. Foss, **2014**; J. M. Tarascon, M. Armand, *Nature* **2001**, 414, 359-367.
- [15] J.-M. Tarascon, *Nature Chemistry* **2010**, 2, 510-510.
- [16] C. Liao, in *Batteries*, IOP Publishing, **2021**, pp. 1-1-1-24.
- [17] F. Nobili, R. Marassi, in *Encyclopedia of Electrochemistry*, **2020**, pp. 1-36.
- [18] B. Dunn, H. Kamath, J.-M. Tarascon, *Science* **2011**, 334, 928-935.
- [19] S. Solchenbach, M. Metzger, M. Egawa, H. Beyer, H. A. Gasteiger, *Journal of The Electrochemical Society* **2018**, 165, A3022.
- [20] J. Y. Han, S. Jung, in *Batteries*, Vol. 8, **2022**.
- [21] S. Klein, J. M. Wrogoemann, S. van Wickeren, P. Harte, P. Bärmann, B. Heidrich, J. Hesper, K. Borzutzki, S. Nowak, M. Börner, M. Winter, J. Kasnatscheew, T. Placke, *Advanced Energy Materials* **2022**, 12, 2102599.
- [22] D. V. Horváth, R. Tian, C. Gabbett, V. Nicolosi, J. N. Coleman, *Journal of The Electrochemical Society* **2022**, 169, 030503.
- [23] X. Gao, W. Sheng, Y. Wang, Y. Lin, Y. Luo, B.-G. Li, *J. Appl. Polym. Sci.* **2015**, 132.
- [24] P. Arora, Z. Zhang, *Chemical reviews* **2004**, 104 10, 4419-4462.
- [25] J. Zhu, M. Yanilmaz, K. Fu, C. Chen, Y. Lu, Y. Ge, D. Kim, X. Zhang, *J. Membr. Sci.* **2016**, 504, 89-96.
- [26] Y. Zhao, K. Liu, H. Hou, L.-Q. Chen, *Materials & Design* **2022**, 216, 110555.
- [27] Y. Chen, Y. Kang, Y. Zhao, L. Wang, J. Liu, Y. Li, Z. Liang, X. He, X. Li, N. Tavajohi, B. Li, *Journal of Energy Chemistry* **2021**, 59, 83-99; X. Feng, M. Ouyang, X. Liu, L. Lu, Y. Xia, X. He, *Energy Storage Materials* **2018**, 10, 246-267.
- [28] S. J. An, J. Li, C. Daniel, D. Mohanty, S. Nagpure, D. L. Wood, *Carbon* **2016**, 105, 52-76.
- [29] Y. Kang, Z. Liang, Y. Zhao, H. Xu, K. Qian, X. He, T. Li, J. Li, *Science China Materials* **2020**, 63, 1683-1692; H. Maleki, G. Deng, A. Anani, J. Howard, *Journal of the Electrochemical Society* **1999**, 146, 3224-3229.
- [30] S. G. Yoon, K. H. Lee, M. Kim, *Appl. Phys. Lett.* **2022**, 121.
- [31] J. C. Hunter, *Journal of Solid State Chemistry* **1981**, 39, 142-147; R. J. Gummow, A. de Kock, M. M. Thackeray, *Solid State Ionics* **1994**, 69, 59-67.
- [32] Y. Song, L. Wang, L. Sheng, D. Ren, H. Liang, Y. Li, A. Wang, H. Zhang, H. Xu, X. He, *Energy & Environmental Science* **2023**, 16, 1943-1963.
- [33] T. Liu, A. Dai, J. Lu, Y. Yuan, Y. Xiao, L. Yu, M. Li, J. Gim, L. Ma, J. Liu, C. Zhan, L. Li, J. Zheng, Y. Ren, T. Wu, R. Shahbazian-Yassar, J. Wen, F. Pan, K. Amine, *Nature Communications* **2019**, 10, 4721; D. Tang, Y. Sun, Z. Yang, L. Ben, L. Gu, X. Huang, *Chemistry of Materials* **2014**, 26, 3535-3543; G. Zhou, X. Sun, Q.-H. Li, X. Wang, J.-N. Zhang, W. Yang, X. Yu, R. Xiao, H. Li, *The Journal of Physical Chemistry Letters* **2020**, 11, 3051-3057; T. Aoshima, K. Okahara, C. Kiyohara, K. Shizuka, *Journal of Power Sources* **2001**, 97-98, 377-380; N.-S. Choi, J.-T. Yeon, Y.-W. Lee, J.-G. Han, K. T. Lee, S.-S. Kim, *Solid State Ionics* **2012**, 219, 41-48.

- [34] L. Oliveira, M. Messagie, S. Rangaraju, J. Sanfeliix, M. Hernandez Rivas, J. Van Mierlo, *Journal of Cleaner Production* **2015**, *108*, 354-362.
- [35] J. F. Peters, M. Weil, in *Resources*, Vol. 5, **2016**.
- [36] W. Mroziak, M. A. Rajaeifar, O. Heidrich, P. Christensen, *Energy & Environmental Science* **2021**, *14*, 6099-6121.
- [37] M. D. Slater, D. Kim, E. Lee, C. S. Johnson, *Adv. Funct. Mater.* **2013**, *23*, 947-958.
- [38] J.-M. Tarascon, *Joule* **2020**, *4*, 1616-1620.
- [39] C. Fouassier, G. Matejka, J.-M. Reau, P. Hagenmuller, *Journal of Solid State Chemistry* **1973**, *6*, 532-537.
- [40] D. A. Stevens, J. R. Dahn, *Journal of The Electrochemical Society* **2000**, *147*, 1271.
- [41] H. Moriwake, A. Kuwabara, C. A. J. Fisher, Y. Ikuhara, *RSC Advances* **2017**, *7*, 36550-36554.
- [42] X. Chen, Y. Xia, X. Fang, K. Zhang, Y. Xiong, Z. Jian, *Journal of Materials Science* **2022**, *57*, 14015-14025.
- [43] W. Wang, Y. Gang, Z. Hu, Z. Yan, W. Li, Y. Li, Q.-F. Gu, Z. Wang, S.-L. Chou, H.-K. Liu, S.-X. Dou, *Nature Communications* **2020**, *11*, 980.
- [44] S. Gourang Patnaik, I. Escher, G. A. Ferrero, P. Adelhelm, *Batteries & Supercaps* **2022**, *5*, e202200043; Y. Yang, J. Zhou, L. Wang, Z. Jiao, M. Xiao, Q.-a. Huang, M. Liu, Q. Shao, X. Sun, J. Zhang, *Nano Energy* **2022**, *99*, 107424; J. Peng, W. Zhang, Q. Liu, J. Wang, S. Chou, H. Liu, S. Dou, *Advanced Materials* **2022**, *34*, 2108384.
- [45] M. A. Cotta, *ACS Applied Nano Materials* **2020**, *3*, 4920-4924.
- [46] M. Karg, A. Pich, T. Hellweg, T. Hoare, L. A. Lyon, J. J. Crassous, D. Suzuki, R. A. Gumerov, S. Schneider, I. I. Potemkin, W. Richtering, *Langmuir* **2019**, *35*, 6231-6255.
- [47] A. A. Yaqoob, H. Ahmad, T. Parveen, A. Ahmad, M. Oves, I. M. I. Ismail, H. A. Qari, K. Umar, M. N. Mohamad Ibrahim, *Frontiers in Chemistry* **2020**, *8*.
- [48] J. Asenbauer, T. Eisenmann, M. Kuenzel, A. Kazzazi, Z. Chen, D. Bresser, *Sustainable Energy & Fuels* **2020**, *4*, 5387-5416.
- [49] Z. Jian, C. Bommier, L. Luo, Z. Li, W. Wang, C. Wang, P. A. Greaney, X. Ji, *Chemistry of Materials* **2017**, *29*, 2314-2320.
- [50] B. Cao, H. Liu, B. Xu, Y. Lei, X. Chen, H. Song, *Journal of Materials Chemistry A* **2016**, *4*, 6472-6478.
- [51] L.-F. Zhao, Z. Hu, W.-H. Lai, Y. Tao, J. Peng, Z.-C. Miao, Y.-X. Wang, S.-L. Chou, H.-K. Liu, S.-X. Dou, *Advanced Energy Materials* **2021**, *11*, 2002704.
- [52] N. Sun, H. Liu, B. Xu, *Journal of Materials Chemistry A* **2015**, *3*, 20560-20566; I. El Moctar, Q. Ni, Y. Bai, F. Wu, C. Wu, *Functional Materials Letters* **2018**, *11*, 1830003.
- [53] X. Dou, I. Hasa, D. Saurel, C. Vaalma, L. Wu, D. Buchholz, D. Bresser, S. Komaba, S. Passerini, *Mater. Today* **2019**, *23*, 87-104.
- [54] M. V. Reddy, G. V. Subba Rao, B. V. R. Chowdari, *Chemical Reviews* **2013**, *113*, 5364-5457.
- [55] S. Fang, D. Bresser, S. Passerini, *Advanced Energy Materials* **2020**, *10*, 1902485.
- [56] J. Du, Q. Li, J. Chai, L. Jiang, Q. Zhang, N. Han, W. Zhang, B. Tang, *Dalton Transactions* **2022**, *51*, 9584-9590.
- [57] K. Cao, L. Jiao, Y. Liu, H. Liu, Y. Wang, H. Yuan, *Adv. Funct. Mater.* **2015**, *25*, 1082-1089.
- [58] A. K. Rai, L. T. Anh, J. Gim, J. Kim, *Ceram. Int.* **2013**, *39*, 9325-9330.
- [59] D. Qin, P. Yan, G. Li, Y. Wang, Y. An, J. Xing, *Journal of Nanomaterials* **2014**, *2014*, 489862.
- [60] M. Chen, X. Xia, J. Yin, Q. Chen, *Electrochimica Acta* **2015**, *160*, 15-21.
- [61] P. Poizot, S. Laruelle, S. Grugeon, L. Dupont, J. M. Tarascon, *Nature* **2000**, *407*, 496-499.
- [62] X. Xu, R. Cao, S. Jeong, J. Cho, *Nano Lett.* **2012**, *12*, 4988-4991.
- [63] L. Zhang, H. B. Wu, S. Madhavi, H. H. Hng, X. W. Lou, *Journal of the American Chemical Society* **2012**, *134*, 17388-17391.
- [64] M. V. Reddy, T. Yu, C. H. Sow, Z. X. Shen, C. T. Lim, G. V. Subba Rao, B. V. R. Chowdari, *Adv. Funct. Mater.* **2007**, *17*, 2792-2799.
- [65] B. Liu, Q. Zhang, Z. Jin, L. Zhang, L. Li, Z. Gao, C. Wang, H. Xie, Z. Su, *Advanced Energy Materials* **2018**, *8*, 1702347.
- [66] J. Gao, M. A. Lowe, H. D. Abruña, *Chemistry of Materials* **2011**, *23*, 3223-3227.
- [67] Q. Fan, M. S. Whittingham, *Electrochem. Solid-State Lett.* **2007**, *10*, A48.
- [68] H. Wang, J. Zhao, D. Xie, H. Huang, P. Rao, J. Mao, *Frontiers in Chemistry* **2022**, *10*.
- [69] A. M. Hashem, H. Abuzeid, M. Kaus, S. Indris, H. Ehrenberg, A. Mauger, C. M. Julien, *Electrochimica acta* **2018**, *262*, 74-81.
- [70] J.-C. G. Bünzli, *Eur. J. Inorg. Chem.* **2017**, *2017*, 5058-5063.

- [71] J. F. C. B. Ramalho, A. N. Carneiro Neto, L. D. Carlos, P. S. André, R. A. S. Ferreira, in *Handbook on the Physics and Chemistry of Rare Earths*, Vol. 61 (Eds.: J.-C. G. Bünzli, V. K. Pecharsky), Elsevier, **2022**, pp. 31-128.
- [72] S. Singh, P. Singh, M. Viviani, S. Presto, *Int. J. Hydrogen Energy* **2018**, *43*, 19242-19249; S. Hui, A. Petric, *J. Eur. Ceram. Soc.* **2002**, *22*, 1673-1681.
- [73] X. Han, Y. Cui, H. Liu, *J. Alloys Compd.* **2020**, *814*, 152348.
- [74] S. C. Han, S. P. Singh, Y.-h. Hwang, E. G. Bae, B. K. Park, K.-S. Sohn, M. Pyo, *Journal of The Electrochemical Society* **2012**, *159*, A1867.
- [75] A. Nishikawa, T. Kawasaki, N. Furukawa, Y. Terai, Y. Fujiwara, *Applied Physics Express* **2009**, *2*, 071004; B. Mitchell, V. Dierolf, T. Gregorkiewicz, Y. Fujiwara, *J. Appl. Phys.* **2018**, *123*.
- [76] W. Xiang, Z. Wang, D. J. Kubicki, W. Tress, J. Luo, D. Prochowicz, S. Akin, L. Emsley, J. Zhou, G. Dietler, M. Grätzel, A. Hagfeldt, *Joule* **2019**, *3*, 205-214.
- [77] J. W. Benjamin Wehrmann, *Clean Energy Wire* (sourced from AGEb), **2021**.
- [78] F.-N. Jiang, S.-J. Yang, H. Liu, X.-B. Cheng, L. Liu, R. Xiang, Q. Zhang, S. Kaskel, J.-Q. Huang, *SusMat* **2021**, *1*, 506-536.
- [79] F. Salvador, C. Sánchez-Jiménez, M. J. Sánchez-Montero, A. Salvador, in *Stud. Surf. Sci. Catal.*, Vol. 144 (Eds.: F. Rodriguez-Reinoso, B. McEnaney, J. Rouquerol, K. Unger), Elsevier, **2002**, pp. 379-386.
- [80] T. Hatakeyama, H. Li, N. L. Okamoto, K. Shimokawa, T. Kawaguchi, H. Tanimura, S. Imashuku, M. Fichtner, T. Ichitsubo, *Chemistry of Materials* **2021**, *33*, 6983-6996.
- [81] S. Sivakumar, L. Nelson Prabu, *Materials Today: Proceedings* **2021**, *47*, 52-55.
- [82] K. You, Y. Yuan, X. Liao, W. Song, X. He, H. Jin, S. Wang, in *Crystals*, Vol. 12, **2022**.
- [83] T. Hatakeyama, N. L. Okamoto, T. Ichitsubo, *Journal of Solid State Chemistry* **2022**, *305*, 122683.
- [84] D. A. Kitchaev, S. T. Dacek, W. Sun, G. Ceder, *Journal of the American Chemical Society* **2017**, *139*, 2672-2681.
- [85] L. M. Housel, L. Wang, A. Abraham, J. Huang, G. D. Renderos, C. D. Quilty, A. B. Brady, A. C. Marschilok, K. J. Takeuchi, E. S. Takeuchi, *Accounts of Chemical Research* **2018**, *51*, 575-582.
- [86] Y. Yuan, C. Liu, B. W. Byles, W. Yao, B. Song, M. Cheng, Z. Huang, K. Amine, E. Pomerantseva, R. Shahbazian-Yassar, J. Lu, *Joule* **2019**, *3*, 471-484.
- [87] S. Bernardini, F. Bellatreccia, A. Casanova Municchia, G. Della Ventura, A. Sodo, *Journal of Raman Spectroscopy* **2019**, *50*, 873-888.
- [88] T. Lis, B. Jeżowska-Trzebiatowska, *Acta Crystallographica Section B* **1977**, *33*, 2112-2116.
- [89] D. Su, H.-J. Ahn, G. Wang, *Journal of Materials Chemistry A* **2013**, *1*, 4845-4850.
- [90] T. Ungár, *Scripta Mater.* **2004**, *51*, 777-781.
- [91] D. Su, H.-J. Ahn, G. Wang, *NPG Asia Materials* **2013**, *5*, e70-e70; R. T. Rasheed, H. Mansoor, R. R. Al-Shaikhly, T. A. Abdullah, A. D. Salman, T. Juzsakova, **2020**.
- [92] L. Li, C. Nan, J. Lu, Q. Peng, Y. Li, *Chem. Commun.* **2012**, *48*, 6945-6947.
- [93] Q. Yang, J. Lin, F. Li, J. Zhang, E. Zurek, G. Yang, *Physical Review Materials* **2021**, *5*, 044802; N. Li, R. An, Y. Su, F. Wu, L. Bao, L. Chen, Y. Zheng, H. Shou, S. Chen, *J. Mater. Chem. A* **2013**, *1*.
- [94] Y. Tian, X. Kang, L. Liu, C. Xu, T. Qu, *Journal of Rare Earths - J RARE EARTH* **2008**, *26*, 279-283.
- [95] C. Xu, X. Qu, *NPG Asia Materials* **2014**, *6*, e90-e90.
- [96] J. D. Rinehart, J. R. Long, *Chemical Science* **2011**, *2*, 2078-2085.
- [97] H. Göktepe, *Res. Chem. Intermed.* **2013**, *39*, 2979-2987.
- [98] J. Luo, H. Zhu, H. Fan, J. Liang, H. Shi, G. Rao, J. Li, Z. Du, Z. Shen, *The Journal of Physical Chemistry C* **2008**, *112*, 12594-12598.
- [99] J. M. d. O. Cremonuzzi, D. Y. Tiba, S. H. Domingues, *SN Applied Sciences* **2020**, *2*, 1689.
- [100] S. Dawadi, A. Gupta, M. Khatri, B. Budhathoki, G. Lamichhane, N. Parajuli, *Bull. Mater. Sci.* **2020**, *43*, 277.
- [101] M. Sugantha, P. Ramakrishnan, A. Hermann, C. Warm Singh, D. Ginley, *Int. J. Hydrogen Energy* **2003**, *28*, 597-600.
- [102] M. Wei, Y. Konishi, H. Zhou, H. Sugihara, H. Arakawa, *Nanotechnology* **2005**, *16*, 245.
- [103] W. Li, R. Zeng, Z. Sun, D. Tian, S. Dou, *Scientific Reports* **2014**, *4*, 6641; W. Li, X. Cui, R. Zeng, G. Du, Z. Sun, R. Zheng, S. P. Ringer, S. X. Dou, *Scientific Reports* **2015**, *5*, 8987.
- [104] H. Begum, M. S. Ahmed, S. Jeon, *RSC Advances* **2016**, *6*, 50572-50580.
- [105] H. Zhang, G. Cao, Z. Wang, Y. Yang, Z. Shi, Z. Gu, *Nano Lett.* **2008**, *8*, 2664-2668; C. Lin, H. Zhang, X. Zhang, Y. Liu, Y. Zhang, *ACS Appl Mater Interfaces* **2023**.

- [106] S. Khamsanga, R. Pornprasertsuk, T. Yonezawa, A. A. Mohamad, S. Kheawhom, *Scientific Reports* **2019**, *9*, 8441.
- [107] W. Zhai, C. Wang, P. Yu, Y. Wang, L. Mao, *Anal. Chem.* **2014**, *86*, 12206-12213.
- [108] A. Hashem, A. Abdel-Ghany, R. El-Tawil, A. Bhaskar, B. Hunzinger, H. Ehrenberg, A. Mauger, C. Julien, *Ionics* **2016**, *22*, 2263-2271.
- [109] A. Yuan, X. Wang, Y. Wang, J. Hu, *Electrochimica Acta* **2009**, *54*, 1021-1026.
- [110] M. V. Ananth, S. Pethkar, K. Dakshinamurthi, *Journal of Power Sources* **1998**, *75*, 278-282.
- [111] J. E. Post, D. A. McKeown, P. J. Heaney, **2020**, *105*, 1175-1190.
- [112] T. Gao, H. Fjellvåg, P. Norby, *Anal. Chim. Acta* **2009**, *648*, 235-239.
- [113] D. Nayak, S. Ghosh, V. Adyam, *Mater. Chem. Phys.* **2018**, *217*, 82-89.
- [114] H. Ronduda, M. Zybert, A. Szczęśna, T. Trzeciak, A. Ostrowski, P. Wieciński, W. Wiecezorek, W. Raróg-Pilecka, M. Marcinek, *Solid State Ionics* **2020**, *355*, 115426.
- [115] M. I. Domínguez, P. Navarro, F. Romero-Sarria, D. Frías, S. A. Cruz, J. J. Delgado, M. A. Centeno, M. Montes, J. A. Odriozola, *J Nanosci Nanotechnol* **2009**, *9*, 3837-3842.
- [116] S. Hao, Y. Li, S. Liu, S. Wang, Y. Xiong, X. Ren, G. Cao, J. Zheng, J. Pan, *Journal of Alloys and Compounds* **2022**, *927*, 166843; T. Junne, N. Wulff, C. Breyer, T. Naegler, *Energy* **2020**, *211*, 118532.
- [117] L. Bao, Z. Yang, L. Chen, Y. Su, Y. Lu, W. Li, F. Yuan, J. Dong, Y. Fang, Z. Ji, C. Shi, W. Feng, *ChemSusChem* **2019**, *12*, 2294-2301.
- [118] W. Zhang, X. Jiang, Y. Zhao, A. Carné-Sánchez, V. Malgras, J. Kim, J. H. Kim, S. Wang, J. Liu, J.-S. Jiang, Y. Yamauchi, M. Hu, *Chemical Science* **2017**, *8*, 3538-3546; Y.-F. Wang, Y. Liang, Y.-F. Wu, J. Yang, X. Zhang, D. Cai, X. Peng, M. Kurmoo, M.-H. Zeng, *Angew. Chem. Int. Ed.* **2020**, *59*, 13232-13237; P. A. Kobielska, R. Telford, J. Rowlandson, M. Tian, Z. Shahin, A. Demessence, V. P. Ting, S. Nayak, *ACS Applied Materials & Interfaces* **2018**, *10*, 25967-25971.
- [119] D. N. Dybtsev, H. Chun, S. H. Yoon, D. Kim, K. Kim, *Journal of the American Chemical Society* **2004**, *126*, 32-33.
- [120] X. Sun, E. Feng, Y. Su, K. Nemkovski, O. Petravic, T. Brückel, *Journal of Physics: Conference Series* **2017**, *862*, 012027.
- [121] R. Sessoli, D. Gatteschi, A. Caneschi, M. A. Novak, *Nature* **1993**, *365*, 141-143.
- [122] K. M. Mertes, Y. Suzuki, M. P. Sarachik, Y. Myasoedov, H. Shtrikman, E. Zeldov, E. M. Rumberger, D. N. Hendrickson, G. Christou, *Solid State Commun.* **2003**, *127*, 131-139; M. Tombers, J. Meyer, J. Meyer, A. Lawicki, V. Zamudio-Bayer, K. Hirsch, J. T. Lau, B. von Issendorff, A. Terasaki, T. A. Schlathöler, R. A. Hoekstra, S. Schmidt, A. K. Powell, E. Kessler, M. H. Prosenc, C. van Wüllen, G. Niedner-Schatteburg, *Chemistry – A European Journal* **2022**, *28*, e202102592.
- [123] A. Cornia, A. C. Fabretti, R. Sessoli, L. Sorace, D. Gatteschi, A. L. Barra, C. Daiguebonne, T. Roisnel, *Acta Crystallogr C* **2002**, *58*, m371-373.
- [124] H.-E. Wang, D. Qian, *Mater. Chem. Phys.* **2008**, *109*, 399-403; Z. H. Raheem, A. M. A. Al Sammarraie, *AIP Conference Proceedings* **2020**, *2213*, 020187.
- [125] T. Lis, *Acta Crystallographica Section B* **1980**, *36*, 2042-2046.
- [126] A. M. Ako, B. Burger, Y. Lan, V. Mereacre, R. Clérac, G. Buth, S. Gómez-Coca, E. Ruiz, C. E. Anson, A. K. Powell, *Inorganic Chemistry* **2013**, *52*, 5764-5774.
- [127] A. M. Ako, C. E. Anson, R. Clérac, A. J. Fitzpatrick, H. Müller-Bunz, A. B. Carter, G. G. Morgan, A. K. Powell, *Polyhedron* **2021**, *206*, 115325.
- [128] S. Nayak, Y. Lan, R. Clérac, C. E. Anson, A. K. Powell, *Chem Commun (Camb)* **2008**, 5698-5700.
- [129] S. Nayak, S. Malik, S. Indris, J. Reedijk, A. K. Powell, *Chemistry – A European Journal* **2010**, *16*, 1158-1162.
- [130] J. E. Post, *Proceedings of the National Academy of Sciences* **1999**, *96*, 3447-3454.
- [131] W. Schmitt, J. P. Hill, S. Malik, C. A. Volkert, I. Ichinose, C. E. Anson, A. K. Powell, *Angew. Chem. Int. Ed.* **2005**, *44*, 7048-7053.
- [132] W. Schmitt, J. P. Hill, M. P. Juanico, A. Caneschi, F. Costantino, C. E. Anson, A. K. Powell, *Angew. Chem. Int. Ed.* **2005**, *44*, 4187-4192.
- [133] M. Testa-Anta, M. A. Ramos-Docampo, M. Comesaña-Hermo, B. Rivas-Murias, V. Salgueiriño, *Nanoscale Advances* **2019**, *1*, 2086-2103.

11 Table of Figures

Figure 2-1 Lifecycle of Li-ion batteries. ^[5]	2
Figure 2-2 Diagram showing energy storage system (ESS) technologies. The diagram is separated into four sections, each illustrating examples of ESSs related to each classification. The ESSs are further labelled.	4
Figure 2-3 Ragone Plot - used for comparing the performance of various energy-storing devices. Typically, this plot helps clarify the difference between batteries and capacitors. ^[6]	4
Figure 2-4 Figure to highlight the biggest problem faced by ESSs today - the low energy density of most materials in comparison to fossil fuels and liquid fuels. Table shows some values in watt-hours.....	6
Figure 2-5 Timeline briefly showcasing the development of battery types, giving some examples ranging from the voltaic pile to the more recent solid-state and Na-ion batteries. ^[7]	7
Figure 2-6 Graph illustrating the relationship between gravimetric and volumetric energy densities of a range of batteries. Reimagined from Tarascon. ^[14]	8
Figure 2-7 Schematic of a Daniell cell which has a Cu-metal cathode and a Zn-metal anode. ^[17]	14
Figure 2-8 Illustration of the charge-discharge mechanism occurring in a Li-ion battery.	16
Figure 2-9 The oxidation mechanism of ethylene carbonate (EC) in the presence of LiPF ₆ at high potentials. ^[19]	17
Figure 2-10 SEM image of a PP:PE:PP separator. ^[24]	18
Figure 2-11 Representation of how lithium dendrite formation on the surface of the anode can pierce the separator as it grows towards the cathode.....	19
Figure 2-12 Representation of how the SEI might form on the surface of the anode. The coloured shapes are Li-containing by-products.....	20
Figure 2-13 A diagram to depict the types of battery malfunctions and how they can cause the thermal runaway process that can occur in a cell.	21
Figure 2-14 Illustration of the cross-talk phenomenon from anode to cathode and vice versa. ^[32]	22
Figure 2-15 Diagram showing the electron density for LiC ₆ , NaC ₆ and KC ₆ compositions. Extracted from Moriwake et al. ^[41]	25
Figure 2-16 Comparison of high power cells relying on Na-ion technologies. ^[38]	26
Figure 2-17 Depiction of how the charge-discharge mechanism works for Prussian blue based materials. ^[42]	26
Figure 2-18 Classification of the different types of nanotechnologies.....	27
Figure 2-19 The different ways in which graphene layers stack in graphite, this could be in an AAA, ABA, or ABC pattern.	28
Figure 2-20 A visual representation of the arrangement of graphene in different types of carbons.	29
Figure 2-21 a) synthetic procedure b-g) scanning electron microscopy and transmission electron microscopy images and h-k) electrochemical performance of the CoO nanowires prepared by Cao et al. ^[57]	30
Figure 2-22 a) Transmission Electron Microscopy image of the CoO microstructures; b) field emission scanning electron microscopy image of the CoO	

microstructures; c) rate capability studies to show lithium storage capability; and d) cyclic voltammetry to show the redox behaviour. ^[59]	31
Figure 2-23 a) X-ray powder diffraction patterns of Co ₃ O ₄ nanotubes and nanowires synthesised by Chen et al, b,c) scanning electron microscopy images of nanotubes, and d,e) electrochemical data. ^[60]	32
Figure 2-24 a) field emission scanning electron microscopy images of Fe ₂ O ₃ nanoflakes, b,c) transmission electron microscopy images d) raman scattering data of the nanoflakes and the capacity per cycle for 80 cycles e) 1 st cycle of the cyclic voltammetry and f,g) show the corresponding differential capacity. ^[64]	33
Figure 2-25 a) Schematic representation of the process of creating the Fe ₃ O ₄ @Nitrogen-doped carbon nanoparticles. b, c, and d) Transmission electron microscopy images showing the morphology of each step in the fabrication process. e) The capacity per cycle for 1000 cycles at 1 A g ⁻¹ , 10 A g ⁻¹ , and 20 A g ⁻¹ . ^[65]	33
Figure 2-26 a) scanning electron microscopy image at low magnification. b) scanning electron microscopy image at higher magnification. c) charge-discharge capacity and coulombic efficiency measured over 50 cycles. ^[66]	34
Figure 2-27 Rate capability of lithium half-cells measured using a) lemon juice, and b) using lemon peel. ^[69]	35
Figure 2-28 Row of lanthanide elements. Yttrium (Y) is included as it has similar chemical properties as the lanthanides. In terms of size, yttrium would sit between holmium (Ho) and erbium (Er). The location of promethium (Pm) is shown with a green star due to it being a radioactive element.....	36
Figure 2-29 Representation of the five d-orbitals in 3d complexes.	39
Figure 2-30 Crystal field splitting diagram of the octahedral and tetrahedral coordination environments in a 3d complex.	40
Figure 2-31 Visual representation of the non-distorted MnO ₆ octahedra showing the Mn-O bond lengths with Jahn-Teller distortion take place along the z-axis.....	41
Figure 4-1 Illustration of the stripping model in Li-metal batteries. ^[78]	44
Figure 5-1 The differences between various thermolysis terms explained.	47
Figure 5-2 General order of coin cell assembly used for cell preparation in this thesis.....	48
Figure 5-3 Diagram to show how the crystallite size is calculated from a PXRD peak.	50
Figure 5-4 X-ray energy absorption spectra showing the pre-edge, XANES, and EXAFS regions.....	52
Figure 5-5 Example of a galvanostatic charge-discharge curve for a half-cell (left) and an example of a rate capability plot (right).....	54
Figure 5-6 Diagram showing a typical sweep using cyclic voltammetry.	55
Figure 6-1 Diagram to show the direction of thermal stability of the MnO ₂ polymorphs. Adapted from Hatakeyama et al. ^[83]	58
Figure 6-2 α , β , and t channel structures of MnO ₂ polymorphs. Each image from left to right shows the perimeter of the tunnels. Extracted from Yuan et.al. ^[86]	59
Figure 6-3 PXRD patterns of commercial MnO ₂ (black), post hydrothermal treatment MnO ₂ -Hydro (red) and post pyrolysis MnO ₂ -NP (blue). The hkl indices label the reflections of α -MnO ₂	60
Figure 6-4 MnO ₂ -NP measured at ALBA beamline BL04, with X-ray wavelength of 0.4142 Å. The pattern shows the synchrotron data of MnO ₂ -NP compared with the	

- model pattern for α -MnO₂ at the same wavelength. The model used is ICSD 20227.61
- Figure 6-5** SEM images of a,b) MnO₂-Hydro at scale bars of 2 μ m and 200 nm (x10 mag), and c,d) MnO₂-NP at scale bars of 1 μ m and 200 nm (x20 mag).62
- Figure 6-6** a) Cyclic voltammograms of MnO₂-NP collected over eight scan rates: 0.1 mV s⁻¹, 0.5 mV s⁻¹, 1 mV s⁻¹, 2 mV s⁻¹, 3 mV s⁻¹, 5 mV s⁻¹, 10 mV s⁻¹ and 15 mV s⁻¹ b) 1st and 10th cycle measured of MnO₂-NP at 0.1 mV s⁻¹.63
- Figure 6-7** Specific discharge capacity, specific charge capacity and coulombic efficiency (CE) vs. cycle number for MnO₂-NP. Rate capability steps of MnO₂-NP measured at 100 mA g⁻¹, 200 mA g⁻¹, 500 mA g⁻¹, and 2000 mA g⁻¹ for 10 cycles each. The rate was then returned to 100 mA g⁻¹ for the remaining 200 cycles.64
- Figure 6-8** a) specific capacity of MnO₂-NP showing the 240 cycles measured showing the individual current densities at 100 mA g⁻¹, 200 mA g⁻¹, 500 mA g⁻¹, and 2000 mA g⁻¹ for 10 cycles each before returning to 100 mA g⁻¹ for the remaining 200 cycles. b) a closer look at the first 10 cycles measured at 100 mA g⁻¹.65
- Figure 6-9** Stacked PXRD patterns of 5 mol% of Ln containing samples. MnO₂Ln-Hydro refers to samples after hydrothermal treatment. MnO₂Ln-NP refers to samples after pyrolysis (where Ln = Y, Ce, Dy, or Yb).67
- Figure 6-10** Stacked PXRD of pyrolysed MnO₂ materials: MnO₂-NP, MnO₂Y-NP, MnO₂Ce-NP, MnO₂Dy-NP, and MnO₂Yb-NP. The hkl indices of polymorph α -phase is labelled in red, β - in purple, σ - in orange, and Mn₂O₃ in blue. Grey triangles show reflections which are a result of instrument error.68
- Figure 6-11** SEM images with scale bars a,b) MnO₂Y-Hydro (20 μ m, 100 nm) c,d) MnO₂Y-NP (200 nm, 200 nm) e,f) MnO₂Ce-Hydro (200 nm, 20 nm) g,h) MnO₂Ce-NP (200 nm, 200 nm) i,j) MnO₂Dy-Hydro (10 μ m, 100 nm) k,l) MnO₂Dy-NP (10 μ m, 200 nm) m,n) MnO₂Yb-Hydro (200 nm, 200 nm) o,p) MnO₂Yb-NP (200 nm, 200 nm).69
- Figure 6-12** Overlapped IR transmission spectra for all 5 mol% Ln samples. Ranges between 400 cm⁻¹ to 1000 cm⁻¹ represents the MnO₆ octahedral arrangement, 1000 cm⁻¹ to 2500 cm⁻¹ indicates the Mn-OH interactions and between 3000 cm⁻¹ and 4000 cm⁻¹ provides information on any constitutional H₂O in MnO₂. Inset to the right shows the enlarged range between 400 cm⁻¹ and 1000 cm⁻¹ where characteristic Mn_xO_y bands can be seen.70
- Figure 6-13** Stacked Raman spectra of MnO₂-NP and the MnO₂Ln-NP composites on the left with assigned wavenumbers. Overlap of the same data on the right. Dotted lines are added for guidance only.71
- Figure 6-14** Stacked PXRD showing the pattern for the intermediate phases after hydrothermal synthesis MnO₂Y-Hydro (grey) and the pattern of the final MnO₂Y-NP after pyrolysis (black). The hkl indices in red indicate indices for α -MnO₂ while the indices represent the presence of R-MnO₂ (turquoise). (α -MnO₂ ICSD 20227, R-MnO₂ ICSD 171866).72
- Figure 6-15** Rietveld Analysis of MnO₂Y-NP showing the fitting between the experimental diffraction pattern and the model used for the phases α -MnO₂ and β -MnO₂.73
- Figure 6-16** MnO₂Y-NP measured at ALBA beamline BL04, with X-ray wavelength of 0.4142 Å. The pattern from the synchrotron data of MnO₂-NP is compared with

the simulated pattern for α -MnO ₂ . The model used is ICSD 20227 (same as for MnO ₂ -NP).....	73
Figure 6-17 SEM analysis of MnO ₂ Y-NP. The scale bars are a) 200 nm and b) 20 nm (x10 mag). Red circle outlines the fibrous looking morphology that appears alongside the nanosheets in the sample.	74
Figure 6-18 Elemental mapping of MnO ₂ Y-NP at a scale of 0.5 μ m. a) shows the SEM image of the particle, b) shows the distribution of manganese across the surface of the particle, and c) shows the distribution of yttrium across the particles.	74
Figure 6-19 Elemental analysis of MnO ₂ Y-NP showing the detection of Mn, Y, O, and Na.....	75
Figure 6-20 Cyclic voltammetry of MnO ₂ Y-NP collected over eight scan rates: 0.1 mV s ⁻¹ , 0.5 mV s ⁻¹ , 1 mV s ⁻¹ , 2 mV s ⁻¹ , 3 mV s ⁻¹ , 5 mV s ⁻¹ , 10 mV s ⁻¹ and 15 mV s ⁻¹ . Graph to the right shows the first three cycles at 0.1 mV s ⁻¹	76
Figure 6-21 Specific discharge capacity, specific charge capacity and Coulombic efficiency (CE) vs. Cycle number for MnO ₂ Y-NP measured at 100 mA g ⁻¹ , 200 mA g ⁻¹ , 500 mA g ⁻¹ , and 2000 mA g ⁻¹ for 10 cycles each. The rate is then returned to 100 mA g ⁻¹ for the remaining 200 cycles. The coulombic efficiency per cycle is also show in blue.	77
Figure 6-22 Galvanostatic charge-discharge of MnO ₂ Y-NP showing the 240 cycles measured at current densities of 100 mA g ⁻¹ , 200 mA g ⁻¹ , 500 mA g ⁻¹ , and 2000 mA g ⁻¹ for 10 cycles each before returning to 100 mA g ⁻¹ for the remaining 200 cycles. Graph to the right shows the first 10 cycles at 100 mA g ⁻¹	78
Figure 6-23 Stacked PXRD of MnO ₂ Ce-Hydro after hydrothermal treatment (red) and MnO ₂ Ce-NP after pyrolysis (light red) showing the changes caused by the presence of Ce(IV)O ₂ on the MnO ₂ phase. The hkl indices are shown for CeO ₂ (green) and σ -MnO ₂ (orange). (JCPDS no. 34-0394, JCPDS no. 24-0735).....	79
Figure 6-24 MnO ₂ Ce-NP measured at ALBA beamline BL04, with X-ray wavelength of 0.4142 Å. The pattern on the left is the synchrotron data of MnO ₂ Ce-NP compared with the simulated pattern for CeO ₂ and β -MnO ₂	80
Figure 6-25 SEM of MnO ₂ Ce-NP after pyrolysis showing the presence of two distinct morphologies which coincides with the presence of two phases. Pink, blue, and green circles showcase the range of morphologies in this sample. a) formation of large hollow tubes and b) presence of nanosheets and nanorods.	80
Figure 6-26 EDX analysis of MnO ₂ Ce-NP showing the distribution of manganese (purple) and cerium (blue) over the surface of the particles.	80
Figure 6-27 EDX elemental analysis of MnO ₂ Ce-NP showing the detection of manganese and cerium.	81
Figure 6-28 Cyclic voltammetry of MnO ₂ Ce-NP collected over eight scan rates: 0.1 mV s ⁻¹ , 0.5 mV s ⁻¹ , 1 mV s ⁻¹ , 2 mV s ⁻¹ , 3 mV s ⁻¹ , 5 mV s ⁻¹ , 10 mV s ⁻¹ and 15 mV s ⁻¹ . Graph to the right shows the first three cycles at 0.1 mV s ⁻¹	83
Figure 6-29 Rate capability steps of MnO ₂ Ce-NP measured at 100 mA g ⁻¹ , 200 mA g ⁻¹ , 500 mA g ⁻¹ , and 2000 mA g ⁻¹ for 10 cycles each. The rate is then returned to 100 mA g ⁻¹ for the remaining 200 cycles. The coulombic efficiency per cycle is also show in blue.	84
Figure 6-30 Galvanostatic charge-discharge of MnO ₂ Ce-NP showing the 240 cycles measured at current densities of 100 mA g ⁻¹ , 200 mA g ⁻¹ , 500 mA g ⁻¹ , and	

2000 mA g ⁻¹ for 10 cycles each before returning to 100 mA g ⁻¹ for the remaining 200 cycles. Graph to the right shows the first 10 cycles at 100 mA g ⁻¹	85
Figure 6-31 Stacked PXRD of MnO ₂ Dy-Hydro and MnO ₂ Dy-NP. (JCPDS #024-0735, JCPDS #44-0141)	86
Figure 6-32 MnO ₂ Dy-NP measured at ALBA beamline BL04, with X-ray wavelength of 0.4142 Å. The pattern on the left is the synchrotron data of MnO ₂ -NP compared with the simulated pattern for α-MnO ₂ . There appears to be lesser intense reflections corresponding to β-MnO ₂ in this sample.	87
Figure 6-33 SEM images of the two different morphologies observed for MnO ₂ Dy-NP at scale bars (a) 100 nm and (b) 1 μm.	87
Figure 6-34 (a-c) EDX mapping showing the distribution of Mn (blue) and Dy (purple) over a large area of the sample. (d-f) EDX mapping showing the distribution of Mn and Dy across a small area of the sample showing the difference in distribution of elements in the branch and spherical particles.	88
Figure 6-35 EDX elemental analysis of MnO ₂ Dy-NP. (a) corresponding to Figure 6-34 a-c (b) corresponding to Figure 6-34 d-f.....	88
Figure 6-36 Cyclic voltammetry of MnO ₂ Dy-NP collected over eight scan rates: 0.1 mV s ⁻¹ , 0.5 mV s ⁻¹ , 1 mV s ⁻¹ , 2 mV s ⁻¹ , 3 mV s ⁻¹ , 5 mV s ⁻¹ , 10 mV s ⁻¹ and 15 mV s ⁻¹ . Graph to the right shows the first three cycles at 0.1 mV s ⁻¹	89
Figure 6-37 Specific discharge capacity, specific charge capacity and Coulombic efficiency (CE) vs. cycle number for MnO ₂ Dy-NP measured at 100 mA g ⁻¹ , 200 mA g ⁻¹ , 500 mA g ⁻¹ , and 2000 mA g ⁻¹ for 10 cycles each. The rate is then returned to 100 mA g ⁻¹ for the remaining 200 cycles. The coulombic efficiency per cycle is also show in blue.	90
Figure 6-38 Galvanostatic charge-discharge of MnO ₂ Dy-NP showing the 240 cycles measured at current densities of 100 mA g ⁻¹ , 200 mA g ⁻¹ , 500 mA g ⁻¹ , and 2000 mA g ⁻¹ for 10 cycles each before returning to 100 mA g ⁻¹ for the remaining 200 cycles. Graph to the right shows the first 10 cycles at 100 mA g ⁻¹	90
Figure 6-39 Stacked PXRD of MnO ₂ Yb-Hydro and MnO ₂ Yb-NP. Blue hkl values represent the phase α-Mn ₂ O ₃ (JCPDS 089-4836).	91
Figure 6-40 MnO ₂ Yb-NP measured at ALBA beamline BL04, with X-ray wavelength of 0.4142 Å. The pattern from the synchrotron data of MnO ₂ -NP is compared with the simulated pattern for α-Mn ₂ O ₃ . The model used was ICSD 9007520. The sample also appears to contain α-MnO ₂ with the reflections at ~5° and ~8° matching ICSD 20227.....	92
Figure 6-41 SEM images of MnO ₂ Yb-NP showing the different morphologies observed at scale bars of 200 nm and 100 nm.....	92
Figure 6-42 Elemental distribution manganese and ytterbium across the surface of a particle of MnO ₂ Yb-NP.	93
Figure 6-43 EDX Mapping of MnO ₂ Yb-NP showing the detection of manganese and ytterbium across the particle.....	93
Figure 6-44 Cyclic voltammetry of MnO ₂ Yb-NP collected over eight scan rates: 0.1 mV s ⁻¹ , 0.5 mV s ⁻¹ , 1 mV s ⁻¹ , 2 mV s ⁻¹ , 3 mV s ⁻¹ , 5 mV s ⁻¹ , 10 mV s ⁻¹ and 15 mV s ⁻¹ . Graph to the right shows the first three cycles at 0.1 mV s ⁻¹	94
Figure 6-45 Specific discharge capacity, specific charge capacity and Coulombic efficiency (CE) vs. Cycle number for MnO ₂ Yb-NP measured at 100 mA g ⁻¹ , 200 mA g ⁻¹ , 500 mA g ⁻¹ , and 2000 mA g ⁻¹ for 10 cycles each. The rate is then returned to	

- 100 mA g⁻¹ for the remaining 200 cycles. The coulombic efficiency per cycle is also show in the figure in blue.....95
- Figure 6-46** Galvanostatic charge-discharge of MnO₂Yb-NP showing the 240 cycles measured at current densities of 100 mA g⁻¹, 200 mA g⁻¹, 500 mA g⁻¹, and 2000 mA g⁻¹ for 10 cycles each before returning to 100 mA g⁻¹ for the remaining 200 cycles. Graph to the right shows the first 10 cycles at 100 mA g⁻¹.95
- Figure 7-1** The secondary building unit of Mn-formate synthesised as reported by Dybsteven et al. The figure shows the asymmetric unit, the symmetry plane, and the packing to showcase the porous nature of the MOF. Each formate anion is bound to three Mn^{II} ions in a syn-syn-anti mode.^[119]97
- Figure 7-2** TGA analysis of Mn-formate carried out under N₂ at a rate of 5 °C/min from 0 to 1000 °C showing the mass loss that leads to the decomposition of the MOF to the oxide.....98
- Figure 7-3** Stacked PXRD patterns of the simulated pattern Mn-formate Sim (black), synthesised Mn-formate-Exp (red) and the product of pyrolysis MnO:Mn₃O₄ (blue).99
- Figure 7-4** Rietveld analysis of MnO:Mn₃O₄ showing data points (red circles), calculated profile (black line), Bragg peak positions for MnO (black vertical lines) and Mn₃O₄ (grey vertical lines), and the difference profile (blue line). 100
- Figure 7-5** SEM images showing the difference in morphology of a) Mn-formate and b) MnO:Mn₃O₄. 101
- Figure 7-6 a, b, c** Magnified SEM images of MnO:Mn₃O₄ at 200 and 100 nm showing the surface morphology of the oxides.....101
- Figure 7-7** BET surface area (top) and isotherm (bottom) plots for MnO:Mn₃O₄. These graphs show insignificant uptake of the material and suggests the particles are non-porous. 102
- Figure 7-8** Cyclic voltammetry measured between 0.05 V and 3 V at 0.1 mV s⁻¹ highlighting the 1st, 2nd, and 3rd cycles shown in black, red, and blue, respectively. The remaining 100 cycles are shown in light grey..... 103
- Figure 7-9** Galvanostatic charge-discharge cycling between 0.05 V and 3 V showing both the changes in capacity and the voltage plateau profiles for the 101 cycles measured using MnO:Mn₃O₄ as the active electrode material in a lithium-ion battery. These cycles were measured at a current density of 100 mA g⁻¹. 104
- Figure 7-10** The reduction profile to the left shows that as MnO:Mn₃O₄ is reduced in the electrode from 3 V to 0.22 V a capacity is observed with a plateau at ~0.5 V. The inset shows the ex-situ PXRD measured at three voltages where the black pattern is the pristine sample, reducing to 1 V is shown in red, reducing further to 0.22 V is shown in blue and reducing fully to 0.01 V is shown in green. These patterns show there is no reduction of the crystalline Mn^{II} to Mn⁰ observed unless reducing to 0 V. Measured by Dr. Sylvio Indris..... 105
- Figure 7-11** (a) The electrochemical discharge data of the cell measured (b) In-situ PXRD measured at ALBA synchrotron during the delithiation cycle. The PXRD shows the first 40 patterns measured. Measured by members of Prof. Helmut Ehrenberg's group at ALBA synchrotron. 106
- Figure 7-12** (a) electrochemical discharge data of MnO:Mn₃O₄ showing the time taken to discharge the cell while in-situ PXRD patterns were measured. (b) indexed diffraction patterns used to determine the lattice parameters *a* for patterns 1 through

42. Measured by members of Prof. Helmut Ehrenberg's group at ALBA synchrotron.	106
Figure 7-13 Rietveld structural analysis of pattern 1 from the EC data measured at ALBA for MnO:Mn ₃ O ₄ showing the reflections associated to MnO, lithium and Cu-foil. Analysis by Dr. Björn Schwarz.	107
Figure 7-14 Rietveld structural analysis of pattern 40 from the in-situ EC data measured at ALBA for MnO:Mn ₃ O ₄ showing that the reflections for MnO do not change as the cell is delithiated. Analysis by Dr. Björn Schwarz.	108
Figure 7-15 (a) electrochemical discharge profile (b) In-situ EXAFs of the local environment around the Mn k-edge in the MnO:Mn ₃ O ₄ electrode material showing the isosbestic points (c) XANES region showing the phase transition occurring during the first discharge process (d) Fourier transform (FT) of the EXAFs and (e) a table to show the bond distances obtained from the FT. Measured at the DESY light source and analysed with the contributions of Dr. Angelina Sarapulova.	109
Figure 7-16 χ vs. T and χT vs T graphs of MnO:Mn ₃ O ₄ measured from 2K to 300K at 500 Oe. Measured and analysed with contributions from Dr. Björn Schwarz. ...	110
Figure 7-17 $1/\chi$ vs T plot for the inverse susceptibility with additional linear fitting calculating an R ² value of 99.99%. Analysed with the contributions of Dr. Björn Schwarz.	111
Figure 7-18 Magnetisation showing the open hysteresis at 2 K as well as ferromagnetic ordering above 25K. Measured and analysed with contributions from Dr. Björn Schwarz.	112
Figure 7-19 The molecular structure of Mn ₁₂ OAc where the Mn ^{IV} ions are shown in purple, Mn ^{III} in pink, O ²⁻ in red and C in grey. ^[123] The repeating unit shows there are no obvious interactions between the neighbouring clusters in the crystal structure.	113
Figure 7-20 Thermal analysis of Mn ₁₂ OAc from 75 °C to 900 °C in air at a rate of 5 K/min. (a) TGA, (b) DTA, (c) TGA 1 st derivative and (d) DTA 1 st derivative plots are shown.	114
Figure 7-21 Stacked X-ray powder diffractograms of the synthesised Mn ₁₂ OAc Exp (red) compared to the simulated pattern Mn ₁₂ OAc Sim (black), Mn ₁₂ OAc- α -MnO ₂ (blue) and Mn ₁₂ OAc- α -MnO ₂ + Na-Alg (pink).	115
Figure 7-22 Image of Mn ₁₂ OAc as synthesised showing the large crystals with needle-like morphologies.	116
Figure 7-23 SEM images taken of Mn ₁₂ OAc- α -MnO ₂ at scale bars of (a) 20 μ m and (b) 10 μ m (2x mag).	116
Figure 7-24 EDX mapping of the distribution of Mn, K and C across the surface of a Mn ₁₂ OAc- α -MnO ₂ particle. (a) electron microscope image (b) EDX layered image showing the overlapped of key elements (c) distribution of Mn (d) distribution of K and I distribution of C.	117
Figure 7-25 Elemental analysis calculated on Mn ₁₂ OAc- α -MnO ₂ showing the relative intensities of Mn, O, K and C across the surface of the particle shown in Figure 7-24	117
Figure 7-26 Cyclic voltammetry of Mn ₁₂ OAc- α -MnO ₂ measured on Cu-foil using multiple scan rates scan rates (a) 0.1 mV s ⁻¹ (b) 0.5 mV s ⁻¹ , 1 mV s ⁻¹ , 2 mV s ⁻¹ , 3 mV s ⁻¹ , 5 mV s ⁻¹ , 10 mV s ⁻¹ and 15 mV s ⁻¹	118

- Figure 7-27** Rate capability cycles were measured on $\text{Mn}_{12}\text{OAc-}\alpha\text{-MnO}_2$ at current densities of 100 mA g^{-1} , 200 mA g^{-1} , 500 mA g^{-1} , and 2000 mA g^{-1} for 10 cycles each before returning to 100 mA g^{-1} for the remaining 100 cycles. A region of fluctuating capacity is observed between the 90th and 130th cycle, which stabilises between the 130th and 140th cycle..... 119
- Figure 7-28** (a) Galvanostatic charge-discharge measurements including the rate capability cycles of $\text{Mn}_{12}\text{OAc-}\alpha\text{-MnO}_2$ at 100 mA g^{-1} , 200 mA g^{-1} , 500 mA g^{-1} , and 2000 mA g^{-1} for 10 cycles each before returning to 100 mA g^{-1} for the remaining 100 cycles. (b) Initial discharge curve and first 10 cycles measured at 100 mA g^{-1} 119
- Figure 7-29** χT vs T measured on freshly synthesised Mn_{12}OAc at an applied magnetic field of 100 Oe. Measured by and analysed with the contributions of Dr. Björn Schwarz. 120
- Figure 7-30** Field scans measured on Mn_{12}OAc at 2 K, 5 K and 300 K. Measured by and analysed with the contributions of Dr. Björn Schwarz. 120
- Figure 7-31** (a) χT vs T for ZFC and FC measurements. (b) Magnetic field scans of $\text{Mn}_{12}\text{OAc-}\alpha,\beta\text{-MnO}_2$ at 5 K and 300 K. Measured by and analysed with the contributions of Dr. Björn Schwarz. 121
- Figure 7-32** $1/\chi$ vs T for $\text{Mn}_{12}\text{OAc-}\alpha,\beta\text{-MnO}_2$. Measured by and analysed with the contributions of Dr. Björn Schwarz. 121
- Figure 7-33** The repeating unit of $\text{Mn}_3\text{Ca}_3\text{Na}_3$ to the right. The centroids between the phenyl rings are calculated as 4.917 \AA to the left. Mn^{III} ions are shown in purple, Ca^{II} in blue, O^{2-} in red, C in grey and Na^+ in yellow. The centroids between the phenyl rings are calculated as 4.917 \AA . Solvent molecules and hydrogen atoms are omitted for clarity. 122
- Figure 7-34** Stacked PXRD patterns of the synthesised $\text{Mn}_3\text{Ca}_3\text{Na}_3$ and simulated $\text{Mn}_3\text{Ca}_3\text{Na}_3$ Sim. Enlarged inserts on the graph show where the 'additional peaks' are seen as small bumps in the simulated pattern. 123
- Figure 7-35** Stacked PXRD of the pyrolysis products $\text{MnO}:\text{Mn}_3\text{O}_4\text{-400}$ (black), $\text{Mn}_3\text{O}_4\text{-600}$ (red), $\text{Mn}_3\text{O}_4\text{-800}$ (blue), and the simulated phases for Mn_3O_4 (pink), MnO (purple) and CaO (light blue). 124
- Figure 7-36** SEM images of the post pyrolysis products. a,b,c) $\text{MnO}:\text{Mn}_3\text{O}_4\text{-400}$ pyrolysed at $400 \text{ }^\circ\text{C}$ d,e,f) $\text{Mn}_3\text{O}_4\text{-600}$ pyrolysed at $600 \text{ }^\circ\text{C}$ g,h,i) $\text{Mn}_3\text{O}_4\text{-800}$ pyrolysed at $800 \text{ }^\circ\text{C}$ 125
- Figure 7-37** Cyclic voltammetry of the 100 cycles measured for $\text{Mn}_3\text{O}_4\text{-600}$ at 0.1 mV s^{-1} 126
- Figure 7-38** Specific capacity of the 150 cycles measured for $\text{Mn}_3\text{O}_4\text{-600}$ at 100 mA g^{-1} 126
- Figure 7-39** Molecular structure of $\text{Mn}_{21}\text{ClGlyc}$ showing the arrangement of manganese ions to create a 3d-framework.^[128] 127
- Figure 7-40** (a) TGA and (b) DTA analysis of $\text{Mn}_{21}\text{BrGlyc}$. First derivatives of (c) TGA and (d) DTA are provided for clarification of the thermal analysis processes. 128
- Figure 7-41** Stacked PXRD patterns showing the simulated pattern for $\text{Mn}_{21}\text{ClGlyc}$ (black), reported $\text{Mn}_{21}\text{ClGlyc}$ compound (blue) and $\text{Mn}_{21}\text{BrGlyc}$ analogue (red), with the circles highlighting the major reflections of the complex (green). 129

Figure 7-42 Stacked PXRD patterns of the oxides of Mn ₂₁ ClGlyc-MnO (black), Mn ₂₁ ClGlyc-MnO washed with water (red), MnO-500 (green), MnO-550 (blue), and MnO-600 (pink).	130
Figure 7-43 SEM images of pristine Mn ₂₁ BrGlyc at a,b) 10 μm, c) 20 μm, and d) 2 μm showing the smooth surface of the crystals.....	130
Figure 7-44 SEM images of MnO-500 after pyrolysis under N ₂ at 500°C.	131
Figure 7-45 SEM images of MnO-550 after pyrolysis under N ₂ at 550°C.	131
Figure 7-46 SEM images of MnO-600 after pyrolysis under N ₂ at 600°C.	131
Figure 7-47 CV showing the first 12 cycles of MnO-600 measured at a scan rate of 0.1 mV s ⁻¹	132
Figure 7-48 a-c) extracted directly from the publication by Nayak et al. ^[129] d) extracted from the corresponding supplementary information.....	133
Figure 7-49 Charge-discharge capacity of MnO-600 at a current density of 100 mA g ⁻¹	134
Figure 7-50 Specific capacity for MnO-600 measured at a scan rate of 0.1 mV s ⁻¹ for 10 cycles.	134
Figure 8-1 Synthetic route for the synthesis of Chnida through the Mannich reaction, using 3-hydroxy-2-naphthoic acid and iminodiacetic acid as the starting materials in an acidic solution.....	137
Figure 8-2 Molecular structure of the iron dinuclear complex, Na ₆ Fe ₂ chnida ₂ . ^[131, 132]	138
Figure 8-3 Repeating subunit of the dinuclear iron complex of Na ₆ Fe ₂ chnida ₂ showing the separated inorganic and organic areas within the ‘honeycomb’ structure. ^[131, 132]	138
Figure 8-4 Stacked PXRD of simulated K ₆ Fe ₂ chnida ₂ Sim (black), experimental K ₆ Fe ₂ chnida ₂ (red), experimental Na ₆ Fe ₂ chnida ₂ (blue) and the decomposed sample of 1 month old Na ₆ Fe ₂ chnida ₂ (green).	139
Figure 8-5 The PXRD pattern obtained after pyrolysis to NaFe _x O _y -500 shown in black. The simulated patterns for Fe ₃ O ₄ , Fe ₂ O ₃ , and NaFeO ₂ are provided respectively in red, green, and blue for comparison. Reflections related to Na ₂ CO ₃ are not visible. Introduction to Ramen spectroscopy given by Dr. Sergei Lebedkin.	140
Figure 8-6 SEM images of NaFe _x O _y -500 after pyrolysis at scale bar of 200 nm... ..	140
Figure 8-7 Raman spectra of NaFe _x O _y -500 showing the characteristic shifts associated to the presence of carbonates, Fe ₂ O ₃ and Fe ₃ O ₄ . The wavelength of the laser used was 532 nm. ^[133]	141
Figure 8-8 Current vs. Voltage (CV) diagram for NaFe _x O _y -500 in a Li-ion coin cell at multiple scan rates: 0.1 mV s ⁻¹ , 0.5 mV s ⁻¹ , 1 mV s ⁻¹ , 2 mV s ⁻¹ , 3 mV s ⁻¹ , 5 mV s ⁻¹ , 10 mV s ⁻¹ , and 15 mV s ⁻¹	142
Figure 8-9 Rate capability of NaFe _x O _y -500 showing cycle number vs capacity for the first 40 cycles measured at current densities of 100 mA g ⁻¹ , 200 mA g ⁻¹ , 500 mA g ⁻¹ , and 2000 mA g ⁻¹ , before returning back to 100 mA g ⁻¹ for long term cycling of over 200 additional cycles.	143
Figure 8-10 Galvanostatic charge/discharge measurements of NaFe _x O _y -500 used as the active electrode material in a Li-ion cell. 10 cycles were measured at each current density of 100 mA g ⁻¹ , 200 mA g ⁻¹ , 500 mA g ⁻¹ , and 2000 mA g ⁻¹ , before returning to 100 mA g ⁻¹ for the remaining 200 cycles measured.	143
Figure 8-11 ‘Differential Capacity’ dQ/dV vs. V plot for NaFe _x O _y -500.....	144

Figure 8-12 Cyclic voltammetry measured for NaFe _x O _y -500 in a Na-ion coin cell at multiple scan rates: 0.1 mV s ⁻¹ , 0.5 mV s ⁻¹ , 1 mV s ⁻¹ , 2 mV s ⁻¹ , 3 mV s ⁻¹ , 5 mV s ⁻¹ , 10 mV s ⁻¹ , and 15 mV s ⁻¹	145
Figure 8-13 Rate capability of NaFe _x O _y -500 showing cycle number vs capacity for the first 40 cycles measured at current densities of 100 mA g ⁻¹ , 200 mA g ⁻¹ , 500 mA g ⁻¹ , and 2000 mA g ⁻¹ , before returning to 100 mA g ⁻¹ for the long term cycling over 200 additional cycles.	146
Figure 8-14 Galvanostatic charge-discharge of a Na-ion cell using NaFe _x O _y -500 as the active electrode material. 10 cycles were measured at each current density of 100 mA g ⁻¹ , 200 mA g ⁻¹ , 500 mA g ⁻¹ , and 2000 mA g ⁻¹ , before returning to 100 mA g ⁻¹ for the long-term cycling over 200 additional cycles.....	146
Figure 8-15 dQ/dV for NaFe _x O _y -500 processed from the galvanostatic cycling....	147
Figure 8-16 The additional novel ligands synthesised: a) chnaida, b) chntoham, and c) omechnida.....	148
Figure 8-17 Overlap of the infrared spectra of chnida, omechnida, chnaida, and chntoham.....	149

12 Table of Tables

Table 1 The change in electrode processes and polarity across the discharge and charge cycles in batteries. Primary batteries only experience the discharge process while secondary batteries experience the discharge followed by the charge. ^[14]	15
Table 2 A list of terms and definitions used throughout this thesis taken from the Handbook of Batteries.	45
Table 3 Table of MnO ₂ Polymorphs: This table provides the mineral name, phase, space group, structure, a brief description on each of the most common polymorphs of MnO ₂ that are relevant to this thesis, and their thermal stabilities.	57
Table 4 Examples of natural Mn _x O _y minerals and their chemical formulae. Extracted from Bernardini et al. ^[91]	59
Table 5 Different phases of Mn _x O _y and their calculated effective magnetic moments.	111

13 Instruments Used

Most data were processed using Excel and/or Origin software. Mercury was used to simulate powder patterns. Fullprof was used for Rietveld analysis. Diamond was used to create crystal structures from cif files. Electrochemical cells were measured using EC-Lab software.

Powder X-Ray Diffraction, PXRD

X-Ray powder diffraction experiments were performed on the STOE STADI P diffractometer using a Cu-K α 1 radiation source with a wavelength of $\lambda = 1.5405 \text{ \AA}$ at room temperature. The data were processed using the software WinXPOW.

Synchrotron Powder X-Ray Diffraction, PXRD, (Alba)

Synchrotron PXRD measurements were carried out at beamline BL04 - MSPD at the Alba light source facility in Barcelona. This beamline operates between 8 and 50 keV.

Scanning Electron Microscopy, SEM

SEM studies were carried out using the LEO 1530 microscope operating between 200 V and 30 kV. This SEM was equipped with the EDX INCA 400 energy dispersive X-ray detector.

Attenuated Total Reflections Infrared Spectroscopy, ATR-IR

Infrared spectra were measured on the Perkin-Elmer Spectrum GX FT-IR. The following abbreviations were used to describe the intensities: vs, very strong; s, strong; m, medium; w, weak; vw, very weak; sh, shoulder; br, broad; vbr, very broad.

Raman Spectroscopy

Raman Spectroscopy were measured on the Bruker confocal Raman microscope using a 532 nm laser.

Synchrotron X-ray absorption spectroscopy, XAS (DESY)

Synchrotron XAS measurements were carried out at beamline P65 - Applied XAFS at the DESY facility in Hamburg. This beamline operates between 4 and 44 keV.

NMR

¹H-NMR spectra were recorded in a Bruker Ultrashield plus spectrometer at 500 MHz. Samples were run in deuterated solvents and peaks assignments are listed for each spectrum. Standard abbreviations for spectra: s, singlet; d, doublet; dd- doublet of doublets; t, triplet; m, multiplet; br, broad; J, coupling constant.

Thermogravimetric Analysis and Differential Thermal Analysis, TGA/DTA

TGA analysis was carried out using the Netzsch STA 409C-System under N₂ atmosphere at a rate of 5 K/min.

Vibrating Sample Magnetometer, VSM

The investigation of magnetic properties was carried out with a MPMS - XL7 SQUID from Quantum Design.

Elemental Analysis, EA

CHNS elemental analysis was performed on the Perkin Elmer Vario EL instrument.

14 Abbreviations

14.1 General Terms

A	Active component
BET	Brunauer-Emmett Teller surface area technique
C-rate	Charge-discharge rate
CV	Cyclic voltammetry
DTA	Differential thermal analysis
EA	Elemental analysis
EC data	Electrochemical data
EDX	Energy dispersive X-ray analysis
ESS	Energy storage system
EV	Electric vehicle
F	Faraday constant
FC	Field cooled
GCD	Galvanostatic charge-discharge
HF attack	Hydrofluoric acid attack
IR	Infrared spectroscopy
LIBs	Lithium-ion batteries
Ln	Lanthanide
M	Metal
NIBs	Sodium-ion batteries
NP	Nanoparticles
PXRD	Powder X-ray diffraction
R	Ideal gas constant
RC	Rate capability
rt	Room temperature
SEI	Solid electrolyte interphase
SEM	Scanning electron microscopy

Sim	Simulated
SOFC	Solid oxide fuel cells
TGA	Thermogravimetric analysis
TMO	Transition metal oxide
UV	Ultraviolet
V	Potential
vdW	van der Waals
z	Number of electrons
ZFC	Zero field cooled

14.2 Chemicals

DMC	Dimethyl carbonate
EC	Ethylene carbonate
Na-Alg	Sodium alginate
NMP	N-methylpyrrolidone
PVdF	Polyvinylidendifluoride